

# Controlling Light in Organic Microcavities

Dissertation  
zur Erlangung des wissenschaftlichen Grades  
Doctor rerum naturalium

vorgelegt von

Andreas Mischok  
geboren am 18.11.1987 in Bautzen

Institut für Angewandte Photophysik  
der Technischen Universität Dresden  
2015

Eingereicht am 16.12.2015

1. Gutachter: Prof. Dr. Karl Leo
2. Gutachter: Prof. Dr. Malte Gather

Verteidigt am 16.06.2016

## Abstract

This thesis deals with the use of microcavity resonators for the control of light in organic active materials. In addition to the vertical confinement provided by highly reflecting mirrors in a vertical cavity surface emitting laser (VCSEL), in-plane patterning facilitates additional ways to manipulate the cavity dispersion and enables the observation of novel photonic modes in highly confined systems and an improved performance of organic solid state lasers. Furthermore, organic microcavities are employed for efficient spectrally sensitive photodetection in the near infrared.

In microcavities comprising two dielectric distributed Bragg reflectors sandwiching an organic active blend of the matrix molecule Alq<sub>3</sub> and the laser dye DCM, optically pumped lasing is investigated, exhibiting a broad spectral tunability over 90 nm due to the large gain bandwidth of the laser dye. To directly influence the microcavity dispersion, different interlayers are introduced into the system, facilitating a red-shift of the cavity resonance due to the formation of Tamm-plasmon-polariton states (when using plasmonic Ag interlayers) or an increase of the optical cavity thickness (when using non-absorbing layers such as SiO<sub>2</sub>). Both concepts are explored and enable strong spectral shifts on the order of 10 meV-100 meV when using interlayers of only few tens of nm in thickness. In order to enhance the optical quality of metal-organic microcavities, the growth of noble metal layers on top of organic films can be improved by the use of diffusion barriers, stopping the diffusion of metal atoms into the organics, and seed layers which provide an improved surface wetting. Both concepts in total lead to an enhancement of the quality factor of such devices by a factor of two.

The manipulation of the cavity resonance using different interlayers provides the ability to structure the photon energy landscape in the device plane on the microscale. Using photolithography, photonic wires and dots are fabricated to laterally restrict the photons in potential wells, leading to the observation of discretised energy spectra in two and three dimensions. To facilitate an in-depth investigation, dispersion tomography is utilised and yields the angle resolved emission of multi-dimensionally confined photons in all directions. In metal-organic photonic dots and triangular wedges, such three-dimensional trapping is exploited to reduce parasitic modes, leading to reduced thresholds of an organic microlaser by one order of magnitude. Complex transversal modes are observed in the device emission as a result of the strong lateral confinement that is achieved by such patterning.

The manipulation of the photon energy landscape can not only be utilised for enhanced confinement but also for the introduction of photonic lattices. By adding periodic stripes of either Ag or SiO<sub>2</sub> into an organic microcavity, an optical Kronig-Penney potential is realised, directly showing the formation of photonic Bloch states in the microcavity dispersion. Utilising a modi-

fied Kronig-Penney theory, photons are assigned a polarisation-dependent effective mass, facilitating a quantitative allocation of calculated and observed modes and explaining the emergence of zero and  $\pi$ -phase coupling of spatially extended supermodes. Finally, by utilising an two-beam excitation geometry, direct control over lasing from multiple discretised states can be exerted, enabling spectral and angular tunability of devices on the microscale.

In an alternative concept, a full microcavity stack is deposited onto a periodic grating which couples the waveguided (WG) modes in the active cavity layer to the vertical emission. Coherent interaction between linear WG and parabolic vertical modes is indicated by anti-crossing points where the dispersion of both overlaps. In this hybrid system, novel lasing modes arise not only at the position of the VCSEL parabola apex but also at points of hybridization, showing a drastically enhanced in-plane spatial coherence of at least 50  $\mu\text{m}$ .

Finally, the concept of organic microcavities is applied towards efficient and spectrally sensitive photodetectors. Making use of the intermolecular charge transfer (CT) state in donor-acceptor blends of organic solar cells, the strong field enhancement of a microcavity is exploited to significantly increase the external quantum efficiency of the initially weak CT absorption at resonance. Consequently, near-infrared photodetection is enabled by cavity-enhanced CT state absorption, leading to devices showing competitive specific detectivities without the need of an external voltage and an EQE above 20% (18% at 950 nm) with a full width at half maximum of significantly below 50 nm. The detectors are shown to be tunable in a broad spectral range via the angular dispersion of the optical microcavity or a thickness variation of the electron and hole transport layers in the solar cell. These findings not only facilitate interesting applications but also enable the direct excitation and observation of the CT state that is integral to the working principles of organic solar cells.

## Kurzdarstellung

Die vorliegende Dissertation beschäftigt sich mit der Kontrolle über Emission und Absorption organischer aktiver Materialien mittels Mikrokavitätsresonatoren. Zusätzlich zum vertikalen Einschluss der Photonen zwischen hochreflektierenden Spiegeln in oberflächenemittierenden Mikrokavitäten (VCSEL, s.o.) werden Strukturierungen in der Bauteilebene hinzugefügt, um eine direkte Manipulation der Photonendispersion zu ermöglichen. Resultierend aus diesen Ergebnissen sind die Beobachtung neuartiger photonischer Moden sowie verbesserte Betriebseigenschaften von organischen Festkörperlasern. Desweiteren wird das Konzept der organischen Mikrokavität zur effizienten und spektral sensitiven Detektion von Nahinfrarot-Photonen angewendet.

In Mikrokavitäten aus zwei dielektrischen Bragg-Spiegeln (DBR), welche eine organische aktive Schicht aus dem Matrixmaterial  $\text{Alq}_3$  und dem Laserfarbstoff DCM einschliessen, wird optisch gepumptes Lasing beobachtet. Dabei ist die Emission spektral über einen weiten Bereich von 90 nm stufenlos einstellbar, was durch die hohe optische Gewinnbandbreite des Laserfarbstoffs ermöglicht wird. Um die Dispersion von Photonen in Mikrokavitäten direkt beeinflussen zu können, werden verschiedene Zwischenschichten in den Laser eingebracht, welche eine Rotverschiebung der Emission nach sich ziehen. In metall-organischen Kavitäten kann dieser Effekt durch die Bildung von Tamm-Plasmon-Polariton Quasiteilchen erklärt werden, die durch die Interaktion der optischen Moden mit den Plasmonen in einer dünnen Silberschicht entstehen. Alternativ werden nichtabsorbierende  $\text{SiO}_2$ -Zwischenschichten eingefügt, welche die optische Kavitätsdicke vergrössern und ähnliche starke Rotverschiebungen der Emission von 10 meV-100 meV nach sich ziehen. Um die optische Qualität metall-organischer Kavitäten zu verbessern, wird das Wachstum der edlen Ag-Schicht auf amorphen organischen Schichten mithilfe von Diffusionsbarrieren und Keimschichten kontrolliert. Die Kombination beider Konzepte ermöglicht eine Verbesserung des Qualitätsfaktors solcher Bauteile um den Faktor 2.

Durch die Manipulation der Photonendispersion mithilfe dielektrischer und plasmonischer Zwischenschichten wird eine Strukturierung der photonischen Potentiallandschaft in der Bauteilebene auf Mikrometer-Skala ermöglicht. Mittels Photolithographie werden photonische Drähte und Punkte hergestellt, welche das Licht auch lateral in Potentialtöpfen einschliessen und zur Beobachtung von diskretisierten Emissionsspektren in zwei und drei Dimensionen führen. Um diese Untersuchungen zu erweitern, wird eine tomographische Methode entwickelt, um die winkelaufgelöste Dispersion dieser mehrdimensional eingeschlossenen Photonen in allen Richtungen aufzunehmen. Die Ergebnisse dieser Untersuchung werden in metall-organischen photonischen Punkten und Dreieck-Strukturen ausgenutzt und führen dabei zu einer Verringerung der Laserschwelle von bis zu einer Grössenordnung. Die dabei entstehenden komplexen Transversalmoden sind ein Zeichen für die starke Konzentration des Lichts in solchen Strukturen.

Die laterale Strukturierung organischer Mikrokavitäten kann nicht nur für den vollständigen Einschluss von Licht ausgenutzt werden, sondern ermöglicht weiterhin die Beobachtung von photonischen Bandstrukturen in periodischen Gittern. Solch periodische Strukturen bestehend entweder aus Silber oder  $\text{SiO}_2$  ermöglichen die Realisierung eines optischen Kronig-Penney Potentials in Mikrokavitäten was schlussendlich zur Beobachtung optischer Bloch-Zustände in der Dispersion führt. Durch eine Modifizierung der Kronig-Penney Theorie, bei der unter anderem den Photonen eine polarisationsabhängige effektive Masse zugewiesen wird, ist eine quantitative Berechnung der Modenpositionen in solchen Systemen möglich. In Theorie und experimentellen Untersuchungen wird dabei das Auftreten von 0- oder  $\pi$ -phasengekoppelten räumlich ausgedehnten Supermoden erklärt. Mithilfe der Anregung durch zwei interferierende

Laserstrahlen kann desweiteren eine direkte Kontrolle über die Wellenlänge sowie den Auskopplungswinkel der stimulierten Emission ausgeübt werden.

In einem alternativen Konzept der lateralen Strukturierung werden organische Mikrokavitäten auf periodische Gitter aufgedampft, was zu einer kohärenten Kopplung von Wellenleitermoden der aktiven Schicht in die vertikale Emission führt. Diese Moden treten als lineare Dispersion in winkelaufgelösten Spektren auf und zeigen eine direkte Interaktion mit der parabolischen Dispersion der VCSEL-Mode an (Anti-)Kreuzungspunkten. In diesem hybriden System lassen sich neuartige Lasermoden beobachten, welche nicht nur am Scheitelpunkt der Kavitätsparell auftreten, sondern auch an Punkten, die durch die Hybridisierung beider Systeme entstehen. Diese Kopplung von vertikalen und lateralen Lasermoden zeigt eine drastisch erhöhte Kohärenzlänge von mindestens 50  $\mu\text{m}$  in der Probenebene.

Schließlich wird das Konzept einer organischen Mikrokavität noch in absorbierenden Systemen eingesetzt. Durch das Einbringen einer organischen Solarzelle in eine optische Kavität wird eine starke Erhöhung des Felds im spektralen Bereich des sonst nur schwach absorbierenden intermolekularen Ladungstransferzustands in Donator-Akzeptor Mischschichten ermöglicht. Die Ausnutzung dieses Zustands ermöglicht eine spektral scharfe (Halbwertsbreite deutlich unter 50 nm) Detektion von Nahinfrarotphotonen mit einer externen Quanteneffizienz von über 20% (18% für 950 nm) und einer konkurrenzfähigen spezifischen Detektivität. In weiteren Untersuchungen zeigen sich diese Detektoren als spektral durchstimmbare, zum Einen durch die parabolische Dispersion der Mikrokavität, zum Anderen durch die Variation der Dicken der Elektron- und Lochtransportschichten. Diese Ergebnisse ermöglichen nicht nur interessante Anwendungen, sondern auch die direkte Beobachtung und Anregung des Ladungstransferzustandes, welcher eine zentrale Rolle in der Funktion organischer Solarzellen spielt.

# Contents

<b>Publications</b>	<b>1</b>
<b>1 Introduction</b>	<b>7</b>
<b>2 Fundamentals</b>	<b>11</b>
2.1 Optics in Layered Media . . . . .	11
2.1.1 Maxwell Equations in Dielectric Media . . . . .	11
2.1.2 Optics in Metals . . . . .	15
2.1.3 Reflection and Transmission . . . . .	19
2.1.4 Transfer-Matrix Algorithm . . . . .	24
2.2 Optics of Microcavities . . . . .	25
2.2.1 Basics of Resonator Structures . . . . .	25
2.2.2 Distributed Bragg Reflector . . . . .	28
2.2.3 Microcavities . . . . .	30
2.2.4 Microcavity Dispersion . . . . .	32
2.2.5 Metal-Organic Microcavities: The Tamm-Plasmon-Polariton State . . . . .	35
2.2.6 Multi-Dimensional Photonic Confinement . . . . .	37
2.2.7 Basics of Laser Operation . . . . .	40
2.3 Basics of Organic Semiconductors and Devices . . . . .	44
2.3.1 Organic Small Molecule Semiconductors . . . . .	44
2.3.2 Charge-Transfer States in Blends of Organic Semiconductors . . . . .	47
2.3.3 Organic Lasers . . . . .	49
2.3.4 Organic Solar Cells and Organic Photodetectors . . . . .	52
2.4 Bloch States . . . . .	57
2.4.1 Electron and Photon Dispersion . . . . .	57
2.4.2 Kronig-Penney Model and Bloch States . . . . .	61
<b>3 Experimental Methods</b>	<b>65</b>
3.1 Sample Fabrication . . . . .	65

3.1.1	Resonator Materials . . . . .	65
3.1.2	Organic Molecules . . . . .	66
3.1.3	Physical Vapour Deposition . . . . .	68
3.1.4	Growth of Metal Layers . . . . .	70
3.2	Photo-Patterning of Interlayers . . . . .	72
3.2.1	Photolithography . . . . .	72
3.3	Optical and Electrical Characterisation . . . . .	75
3.3.1	Micro-Photoluminescence . . . . .	75
3.3.2	Further Methods . . . . .	77
<b>4</b>	<b>Planar Microcavities with Dielectric and Plasmonic Interlayers</b>	<b>79</b>
4.1	Microcavity Dispersion and Lasing . . . . .	79
4.1.1	Planar and Thickness-Gradient Microcavities . . . . .	79
4.1.2	Metal-Organic Microcavities . . . . .	82
4.1.3	Microcavities with SiO <sub>2</sub> Interlayers . . . . .	84
4.2	Growth of High-Quality Thin Silver Films for Microcavities . . . . .	86
<b>5</b>	<b>Multidimensional Photonic Confinement</b>	<b>91</b>
5.1	Dispersion Tomography of Multi-Dimensionally Confined Photons . . . . .	91
5.1.1	Setup for Dispersion Tomography . . . . .	92
5.1.2	2D - Photonic Confinement in Photonic Wires . . . . .	93
5.1.3	3D - Confinement in Metal-Organic Photonic Dots . . . . .	96
5.2	Exploiting Photonic Confinement in Laterally Patterned Metal-Organic Microcavities . . . . .	98
5.2.1	Mathieu-Modes in Elliptic Holes of Silver Interlayers . . . . .	99
<b>6</b>	<b>Photonic Bloch States</b>	<b>105</b>
6.1	Photonic Bloch States in Metal-Organic Microcavities . . . . .	106
6.1.1	Microcavity Dispersion and Kronig-Penney Model . . . . .	106
6.1.2	Photonic Bloch States . . . . .	107
6.1.3	Modified Kronig-Penney Model - Zero and $\pi$ -states . . . . .	109
6.2	Control of Lasing from Bloch States in SiO <sub>2</sub> -patterned Microcavities . . . . .	114
6.2.1	Coexisting of Confined and Extended Optical Bloch States in a SiO <sub>2</sub> Photonic Wire Array . . . . .	115
6.2.2	Photonic Bloch States in Metal- or SiO <sub>2</sub> -Patterned Cavities . . . . .	117
6.2.3	Quantitative Description of Coexisting Localized and Extended Bloch States . . . . .	119



6.2.4	Above-Threshold Investigation . . . . .	123
6.2.5	Control of Lasing by Selective Excitation . . . . .	126
6.2.6	Numerical Simulation of Selective Excitation . . . . .	128
6.3	Comparing Laser Modes in Periodically Patterned Microcavities . . . . .	130
<b>7</b>	<b>Hybrid Waveguide-VCSEL Resonators And Coherent Interaction</b>	<b>133</b>
7.1	Hybrid Device Architecture . . . . .	133
7.2	Emission of Hybrid WG-VCSEL Resonators . . . . .	134
7.3	Stimulated Emission of Hybrid Resonators . . . . .	137
<b>8</b>	<b>Cavity-Enhanced Charge-Transfer State Absorption for Highly Efficient NIR Detectors</b>	<b>141</b>
8.1	Design and Optical Simulation of Optimised Metallic Microcavities . . . . .	142
8.1.1	Concept of Cavity-Enhanced Charge-Transfer State Absorption . . . . .	142
8.1.2	Device Design and Optical Simulation . . . . .	143
8.2	Enhancing the Absorption of the C <sub>60</sub> :ZnPc Charge-Transfer State . . . . .	146
8.2.1	External Quantum Efficiency of CT-NIR Detectors . . . . .	146
8.2.2	Dependence on Top Mirror Thickness . . . . .	148
8.3	Spectral Tunability . . . . .	150
8.3.1	Angular Response . . . . .	150
8.3.2	Variation of Transport Layer Thicknesses for Spectral Tunability . . . . .	152
8.4	Distributed Bragg Reflector Cavities for High- <i>Q</i> Photodetectors . . . . .	155
<b>9</b>	<b>Conclusion and Outlook</b>	<b>161</b>
	<b>Bibliography</b>	<b>169</b>
	<b>Acknowledgements</b>	<b>195</b>



# Publications

## Articles

- [1] Andreas Mischok, Felix Lemke, Christoph Reinhardt, Robert Brückner, Alexander A. Zakhidov, Susanne I. Hintschich, Hartmut Fröb, Vadim G. Lyssenko, and Karl Leo, "Dispersion tomography of an organic photonic-wire microcavity", *Applied Physics Letters* **103**(18), 183302, (2013).
- [2] Andreas Mischok, Robert Brückner, Christoph Reinhardt, Markas Sudzius, Vadim G. Lyssenko, Hartmut Fröb, and Karl Leo, "Threshold reduction by multidimensional photonic confinement in metal-organic microcavities", *Proc. SPIE Photonics Europe* 91370D, (2014).
- [3] Andreas Mischok, Robert Brückner, Markas Sudzius, Christoph Reinhardt, Vadim G. Lyssenko, Hartmut Fröb, and Karl Leo, "Photonic confinement in laterally structured metal-organic microcavities", *Applied Physics Letters* **105**(5), 051108, (2014).
- [4] Andreas Mischok, Vadim G. Lyssenko, Robert Brückner, Franz J.F. Löchner, Reinhard Scholz, Alexander A. Zakhidov, Hartmut Fröb, and Karl Leo, "Zero-and  $\pi$ -States in a Periodic Array of Deep Photonic Wires", *Advanced Optical Materials* **2**(8), 746, (2014),  
also featured as cover art: "Photonics: Zero-and  $\pi$ -States in a Periodic Array of Deep Photonic Wires", *Advanced Optical Materials* **2**(8), 802, (2014).
- [5] Franz J.F. Löchner, Andreas Mischok, Robert Brückner, Vadim G. Lyssenko, Alexander A. Zakhidov, Hartmut Fröb, and Karl Leo, "Coexisting localized and extended optical Bloch states in a periodic deep wire array microcavity", *Superlattices and Microstructures* **85**, 646, (2015).
- [6] Andreas Mischok, Robert Brückner, Hartmut Fröb, Alexander A. Zakhidov, Vadim G. Lyssenko, and Karl Leo, "Control of Lasing from Bloch States in Microcavity Photonic Wires via Selective Excitation and Gain", *Physical Review Applied* **3**(6), 064016, (2015).

- [7] Andreas Mischok, Robert Brückner, Hartmut Fröb, Vadim G. Lyssenko, and Karl Leo, "Photonic lattices in organic microcavities: Bloch states and control of lasing", *Proc. SPIE Optics & Photonics* **9566**, 95660T, (2015),  
awarded with the Organic Photonics + Electronics Best Student Paper Award at SPIE Optics & Photonics San Diego (2015).
- [8] Irma Slowik, Yiyang Zhang, Andreas Mischok, Robert Brückner, Vadim G. Lyssenko, Hartmut Fröb, Nils Kronenberg, Malte C. Gather, and Karl Leo, "Fano-Like Interference in the Emission Spectra of a Multimode Organic Microcavity", *IEEE Journal of Selected Topics in Quantum Electronics* **22**(1), 1, (2016).
- [9] Christian Tzschaschel, Markas Sudzius, Andreas Mischok, Hartmut Fröb, and Karl Leo, "Net Gain in Small Mode Volume Organic Microcavities", *Applied Physics Letters*, **108**, 023304, (2016).
- [10] Andreas Mischok, Tim Wagner, Robert Brückner, Markas Sudzius, Hartmut Fröb, Vadim G. Lyssenko, and Karl Leo, "Lasing and Macroscopic Coherence of Hybridized Modes in Coupled 2D Waveguide-VCSEL Resonators", *Advanced Optical Materials*, DOI:10.1002/adom.201600282 (2016).
- [11] Tim Wagner, Markas Sudzius, Andreas Mischok, Hartmut Fröb, and Karl Leo, "Cross-coupled composite-cavity organic microresonators", *submitted*, (2016).
- [12] Tim Wagner, Markas Sudzius, Andreas Mischok, Hartmut Fröb, and Karl Leo, "Lasing from Hybrid DFB-VCSEL resonators", *in preparation*, (2016).
- [13] Bernhard Siegmund, Andreas Mischok, Johannes Benduhn, Donato Spoltore, Frederik Nehm, Hartmut Fröb, Christian Körner, Karl Leo, and Koen Vandewal, "Narrowband Near Infrared Detection via the Intermolecular Charge Transfer State", *in preparation*, (2016).
- [14] Frederik Nehm, Andreas Mischok, Jendrik Jördening, Sylvio Schubert, Hartmut Fröb, Vadim G. Lyssenko, Lars Müller-Meskamp, and Karl Leo, "Metal diffusion barriers for organic optoelectronics", *in preparation*, (2016).
- [15] Christian Kropla, Felix Lemke, Vadim Lyssenko, Andreas Mischok, Robert Brückner, Hartmut Fröb, and Karl Leo, "Laguerre-Gauss modes in organic VCSELs", *in preparation*, (2016).

## Patents

[16] Bernhard Siegmund, Koen Vandewal, Andreas Mischok, Johannes Benduhn, Donato Spoltore, Christian Körner, Karl Leo, "Verfahren zur Detektion und Umwandlung von infraroter elektromagnetischer Strahlung" DE 102015215581.1, *submitted*, (2015).

## Conference Contributions

(*presenting author is underlined*)

Andreas Mischok, Felix Lemke, Susanne Hintschich, Christoph Reinhardt, Vadim Lyssenko, Alexander Zakhidov, Robert Brückner, Hartmut Fröb, and Karl Leo, "Three-dimensional Dispersion Tomography of Photonic Wires in an Organic Microcavity", Poster Presentation, *International Conference on Superlattices, Nanostructures and Nanodevices, Dresden, Germany 2012*.

Andreas Mischok, Robert Brückner, Felix Lemke, Christoph Reinhardt, Markas Sudzius, Alexander Zakhidov, Susanne Hintschich, Vadim Lyssenko, Hartmut Fröb, and Karl Leo, "Far-Field Spectroscopy of Confined Modes in Laterally Structured Metal-Organic Microcavities", Poster Presentation, *Physics of Light-Matter Coupling in Nanostructures, Hersonnissos, Greece 2013*.

Andreas Mischok, Robert Brückner, Reinhard Scholz, Vadim Lyssenko, Markas Sudzius, Susanne Hintschich, Alexander Zakhidov, Hartmut Fröb, and Karl Leo, "Room-Temperature Lasing from Tamm Plasmon-Polaritons in an Organic Microcavity", Oral Presentation, *DPG Spring Meeting SKM, Regensburg, Germany 2013*.

Robert Brückner Markas Sudzius, Alexander Zakhidov, Andreas Mischok, Susanne Hintschich, Vadim Lyssenko, Hartmut Fröb, Mikhail Kaliteevski, and Karl Leo, "Macroscopic Coherence in Metal-Organic Microcavities", Oral Presentation, *10th International Conference on Optical Probes of Conjugated Polymers and Organic Nanostructures, Durham, UK 2013*.

Robert Brückner, Markas Sudzius, Alexander Zakhidov, Andreas Mischok, Susanne Hintschich, Vadim Lyssenko, Hartmut Fröb, Mikhail Kaliteevski, and Karl Leo, "Macroscopic Coherence in Metal-Organic Microcavities", Oral Presentation, *10th International Conference on Optical*

*Probes of Conjugated Polymers and Organic Nanostructures, Durham, UK 2013.*

Markas Sudzius, Tim Wagner, Andreas Mischok, Robert Brückner, Kai Schmidt, Vadim Lyssenko, Hartmut Fröb, and Karl Leo, "Vertical and Lateral DCM-Based Organic Microlasers", Oral Presentation, *European Optical Society Topical Meeting, Capri, Italy 2013.*

Robert Brückner, Andreas Mischok, Markas Sudzius, Alexander Zakhidov, Reinhard Scholz, Vadim Lyssenko, Hartmut Fröb, and Karl Leo, "Macroscopic Coherence in Metal-Organic Microcavities", Oral Presentation, *Optics of Excitons in Confined Systems, Rome, Italy 2013.*

Robert Brückner, Andreas Mischok, Markas Sudzius, Alexander Zakhidov, Vadim Lyssenko, Hartmut Fröb, and Karl Leo, "Bloch-like modes and macroscopic coherence in metal-organic microlasers", Oral Presentation *MRS Fall, Boston, USA 2013.*

Andreas Mischok, Robert Brückner, Reinhard Scholz, Vadim Lyssenko, Alexander Zakhidov, Hartmut Fröb, and Karl Leo, "Bloch-Like Photonic States in Laterally Structured Organic Microcavities", Oral Presentation, *DPG Spring Meeting SKM, Dresden, Germany 2014.*

Tim Wagner, Markas Sudzius, Andreas Mischok, Hartmut Fröb, and Karl Leo, "Organic microlasers in vertical and lateral geometry", Oral Presentation, *DPG Spring Meeting SKM, Dresden, Germany 2014.*

Christian Tzschaschel, Markas Sudzius, Andreas Mischok, Hartmut Fröb, and Karl Leo, "Direct Net Gain Measurements in Organic Microcavities", Oral Presentation, *DPG Spring Meeting SKM, Dresden, Germany 2014.*

Andreas Mischok, Robert Brückner, Christoph Reinhardt, Markas Sudzius, Vadim G. Lyssenko, Hartmut Fröb, and Karl Leo "Threshold Reduction by Multi-Dimensional Confinement in Metal-Organic Microcavities", Oral Presentation, *SPIE Photonics Europe, Bruxelles, Belgium 2014.*

Vadim Lyssenko, Andreas Mischok, Hartmut Fröb, and Karl Leo, "Coexisting of confined and Bloch-like extended states in a periodic array of organic photonic wires at room temperature", Poster Presentation, *Nonlinear Physics at the Nanoscale, Dresden, Germany 2014.*

Andreas Mischok, Robert Brückner, Reinhard Scholz, Vadim Lyssenko, Alexander Zakhidov, Hartmut Fröb, and Karl Leo, "Metal-Organic Microcavities: Device Concepts and Bloch-Like

States“, Oral Presentation, *Physics of Light-Matter Coupling in Nanostructures, Montpellier, France* 2014.

Tim Wagner, Markas Sudzius, Andreas Mischok, Robert Brückner, Vadim Lyssenko, Hartmut Fröb, and Karl Leo, ”Hybrid VCSEL and DFB organic microlasers“, Poster Presentation, *Physics of Light-Matter Coupling in Nanostructures, Montpellier, France* 2014.

Christian Tzschaschel, Markas Sudzius, Andreas Mischok, Michael Bretschneider, Hartmut Fröb, and Karl Leo, ”Direct Net Gain in Small Mode Volume Organic Microcavities“, Oral Presentation, *European Optical Society Annual Meeting, Capri, Italy* 2014.

Tim Wagner, Markas Sudzius, Andreas Mischok, Robert Brückner, Hartmut Fröb, Vadim Lyssenko, and Karl Leo, ”Hybrid VCSEL and DFB organic microlasers“, Oral Presentation, *ESREF, Berlin, Germany* 2014.

Andreas Mischok, Robert Brückner, Hartmut Fröb, Vadim G. Lyssenko, and Karl Leo, ”Disordered Photonic Structures in Organic Microlasers“, Poster Presentation, *DFG SPP 1839 Meeting, Berlin, Germany* 2015.

Andreas Mischok, Robert Brückner, Hartmut Fröb, Vadim G. Lyssenko, and Karl Leo, ”Disordered Photonic Structures in Organic Microlasers“, Oral Presentation, *DFG SPP 1839 Meeting, Berlin, Germany* 2015.

Andreas Mischok, Robert Brückner, Alexander Zakhidov, Hartmut Fröb, Vadim Lyssenko, and Karl Leo, ” Metal-Organic Microcavities: Utilizing Tamm-Plasmon-Polaritons for Observing Photonic Bloch States “, Oral Presentation, *DPG Spring Meeting SKM, Berlin, Germany* 2015.

Andreas Mischok, Robert Brückner, Alexander Zakhidov, Hartmut Fröb, Vadim Lyssenko, and Karl Leo, ” Control of Lasing from Bloch-States in Microcavity Photonic Wires via Selective Excitation and Gain“, Poster Presentation, *DPG Spring Meeting SKM, Berlin, Germany* 2015.

Tim Wagner, Markas Sudzius, Andreas Mischok, Hartmut Fröb, and Karl Leo, ”Characterisation of Hybrid VCSEL and DFB Organic Microlasers“, Oral Presentation, *DPG Spring Meeting SKM, Berlin, Germany* 2015.

Robert Brückner, Andreas Mischok, Franz Löchner, Stefan Meister, Vadim Lyssenko, Hartmut

Fröb, and Karl Leo, "Bloch States, Tamm Plasmons, and Coherence in Organic Microcavities", Oral Presentation, *Physics of Light-Matter Coupling in Nanostructures, Medellin, Colombia* 2015.

Tim Wagner, Markas Sudzius, Andreas Mischok, Hartmut Fröb, and Karl Leo, "Hybrid VCSEL and DFB Organic Microlasers", Oral Presentation, *11th International Conference on Excitonic and Photonic Processes in Condensed Matter and Nano Materials, Montreal, Canada* 2015.

Andreas Mischok, Robert Brückner, Alexander Zakhidov, Hartmut Fröb, Vadim Lyssenko, and Karl Leo, "Photonic Lattices in Organic Microcavities: Bloch States and Control of Lasing", Oral Presentation, *SPIE Optics & Photonics, San Diego, USA* 2015.

Robert Brückner, Andreas Mischok, Franz Löchner, Stefan Meister, Vadim Lyssenko, Hartmut Fröb, and Karl Leo, "Hybrid Microcavities: Interplay between metal and organics for electrically driven devices", Oral Presentation, *Optics of Excitons in Confined Systems, Jerusalem, Israel* 2015.

Christian Tzschaschel, Markas Sudzius, Andreas Mischok, Michael Bretschneider, Hartmut Fröb, and Karl Leo, "Net Gain Dynamics in Small Mode Volume Organic Microcavities", Oral Presentation, *European Optical Society Annual Meeting, Capri, Italy* 2015.

Bernhard Siegmund, Andreas Mischok, Johannes Benduhn, Donato Spoltore, Christian Koerner, Karl Leo, and Koen Vandewal, "Organic Near-Infrared Detectors Based on Charge-Transfer State Absorption", Oral Presentation, *MRS Fall, Boston, USA* 2015.

## Popular Science Talks

Andreas Mischok, "Licht und Laser aus Molekülen", 13. Physik-Spezialistenlager, Seifhennersdorf, Germany 17. November 2013.

Andreas Mischok, "Licht und Laser aus Molekülen", 3. Stufe der 16. Sächsischen Physikolympiade, Chemnitz, Germany 24. April 2015.



# 1 Introduction

Since Albert Einstein proposed the existence of stimulated emission in 1916 [17, 18], the realisation of a device based on this principle was a main goal of physicists worldwide. In 1953, Charles H. Townes and his students produced the first Maser (microwave amplification by stimulated emission of radiation), amplifying microwave radiation in the way Einstein described [19]. The first device working in the visible range (the Laser<sup>1</sup>) was finally realised by Theodore H. Maiman in a synthetic ruby crystal, periodically pumped by an intense flashtube [20]. Following this discovery, a multitude of materials were found to be capable of stimulated emission, including He-Ne and other noble gas mixtures, fluorescent laser dyes, and other solid state active materials such as doped yttrium aluminium garnet (YAG) crystals. Today, the laser is an integral technological instrument. Its characteristic properties such as monochromatic emission, spatial and temporal coherence and low beam divergence are used in a wide variety of applications including spectroscopy, material processing, or laser surgery in medicine. Recent research has shown lasing from a single biological cell [21] and intracellular microresonators [22], the realisation of a room temperature solid state organic maser [23], hybrid organic-inorganic perovskites [24, 25], or colloidal quantum dots [26, 27] and platelets [28], proving that the interest in the search for new materials is still high and that the end of new discoveries is far away.

Lasers consisting of inorganic semiconductor materials were quickly realised after Maiman's first ruby laser. In 1962 Robert N. Hall *et al.* presented the first coherent emission from a GaAs p-n-junction [29]. Nowadays, semiconductor laser diodes utilise a double hetero-structure, where a thin GaAs layer is sandwiched between two highly n- and p-doped  $\text{Al}_x\text{Ga}_{1-x}\text{As}$  layers. In the resulting band structure, the quasi Fermi-levels lie inside the conducting band and the valence band of the GaAs, respectively, thus creating the necessary population inversion. Today, laser diodes are the most commonly used laser type. In contrary to the usual edge-emitting designs, vertical cavity surface emitting lasers (VCSELs), as the name says, are able to emit on the device surface, yielding higher output aperture. They consist of two highly reflective distributed Bragg reflectors (DBRs), encasing a quantum well active region. Since the actual cavity thickness is on the scale of a few wavelengths of emitted light, single mode operation is possible, and the lasing threshold is reduced to a minimum. In the case of inorganic semiconductors, the mirrors

---

<sup>1</sup>light amplification by stimulated emission of radiation.

consist of doped GaAs blends (commonly AlGaAs), making electrical contacting over these mirrors possible. The design also allows an additional lateral structuring of the device, leading to a confinement of the developing transversal electromagnetic (TEM) modes and, thus, to a further reduction of the threshold. Such structuring is typically achieved by etching the entire stack into circular micropillars, called mesas [30]. Inorganic VCSELs suffer from certain disadvantages. Limited by the available laser transitions, their emission spectrum is restricted and not tunable in the device. The epitaxial growth of such structures under clean-room conditions is expensive and susceptible to disturbance in the process. Organic laser dyes can overcome those disadvantages with their broad emission spectrum and comparably easy fabrication by physical vapour deposition in a vacuum chamber.

Organic semiconductors have started to raise interest, when Ching Tang reported an efficiency of an organic solar cell of 1% in 1986 [31]. Recently, organic solar cells have exceeded efficiencies of 12% for small molecules (Heliatek [32]), 13% for dye-sensitized cells [33], and above 19% for hybrid organic-inorganic perovskite cells [34]. Other applications of organic semiconductors include organic light emitting diodes (OLEDs), already commonly used in displays and light sources [35, 36], or electronic devices such as field effect transistors [37]. Their high absorption cross sections in turn also facilitate efficient photodetection over a broad spectral range, making use of the advantages of organic materials such as tunability, flexibility and comparably cheap processing. An electrically driven organic solid state laser however, has not been achieved yet.

The VCSEL design is suitable for devices with an organic active layer (organic VCSEL or OVCSEL). Here, the DBR mirrors typically consist of alternating stacks of dielectric materials encasing the cavity that consists of a matrix material doped with an organic laser dye. The first working, optically excited device was realised in 1996 [38, 39, 40, 41]. The fabrication of OVCSELs is easily and cheaply done by evaporation techniques in a vacuum chamber.

One main obstacle on the road to an electrically driven device lies in the contacting of the organic cavity for charge carrier injection. Since the dielectric mirrors are highly isolating, a conductive material has to be introduced into the structure. Free charge carriers, however, are commonly sources of high absorption, usually fatal for optical applications. The introduction of a thin silver layer next to the active material can nevertheless yield a functioning cavity, as recently shown by Brückner *et al.* [42], and leads to the formation of two coupled hybrid optical Tamm states. Structuring techniques such as photolithography can be applied to shape the silver layer and thus create photonic confinement comparable to aforementioned micropillars, so called photonic dots [43], or more intricate structures.

Due to their versatility, organic microlasers offer an interesting playground for sophisticated photonic systems. In high-quality vertical microcavities, large coherence lengths persist even

below the lasing threshold [44] and thus facilitate the formation of complex lateral modes. This effect raises interest in the investigation of in-plane structures, where isolated photonic wires and dots effectively confine photons in more than one dimension [45, 46, 47, 48], while periodic arrays of structures enable observation of the coherent interaction of light in separated areas. Interestingly, such behaviour follows analogies from other areas of physics, where especially interesting quantum effects are more directly accessible on the length scale of visible photons. In addition, it is possible to couple such microcavity photons strongly to excitons in the active material by emission and re-absorption in a high-quality microcavity, creating exciton-polaritons [49]. These quasiparticles offer a direct pathway for experiments on light-matter coupling at the micro and nanoscale and exhibit bosonic behaviour, most prominent their ability to undergo Bose-Einstein condensation [50, 51]. Complex photonic structures play a great role in manipulating such particles and facilitate further experiments regarding quantum information transport, spin optics [52], the investigation of magnetic properties [53, 54, 55], propagation of excitons in such potential landscapes [56], their detailed understanding being key aspects for applications e.g. in Spin-Optronics such as the optical spin Hall effect [57] and the recent proposal of a Z polaritonic topological insulator [58].

This dissertation is structured as follows: Chapter 2 provides the physical fundamentals of this work, with a focus on microcavity optics. The transfer-matrix algorithm is derived and utilised to describe different microcavity systems, including conductive materials. The fundamentals of organic semiconductors are presented and their application towards lasers, solar cells, and photodetectors are introduced. Finally, the theoretical concept of electronic and photonic Bloch states is provided. Chapter 3 describes the experimental methods and materials used throughout this thesis, focusing on the fabrication of organic microcavities including micrometre-scale photolithography as well as spectroscopy and imaging. In Chapter 4, the emission properties of planar microcavities are explored in terms of tunable lasing and the influence of plasmonic or dielectric interlayers in the system. For this purpose, avenues for improved growth of thin silver films with high optical quality are presented. Chapter 5 deals with two- and three-dimensional photonic confinement of photons in microcavities with added photonic wires and dots. Here, a powerful dispersion tomography technique is utilised to highlight the multidimensional confinement in momentum space. Furthermore, lasing modes in such highly confined systems are investigated regarding their input-output behaviour, lasing thresholds, and transversal mode patterns. Photonic Bloch states are explored in detail in Chapter 6, showcasing their observation in periodic arrays of both plasmonic and dielectric photonic wires and providing a detailed theoretical model. A high degree of control over different lasing modes in those systems is demonstrated, including multimode- and tunable lasing. To conclude the investigation on organic microlasers, a

different kind of patterning is introduced in Chapter 7, where a periodic grating on the substrate facilitate coherent coupling between waveguided and vertical modes in an organic microcavity evaporated on top. Spontaneous and stimulated emission from hybrid modes is observed in spatially and angle-resolved spectroscopy demonstrating a macroscopic increase of the coherent mode extension. Finally, the concept of organic microcavities is expanded towards absorbing systems in Chapter 8. Here, the charge transfer state absorption in a donor-acceptor blend of an organic solar cell is optically enhanced by a microcavity to facilitate efficient photodetection in the near infrared. The resulting detectors are characterised and pathways for further improvement are given.

## 2 Fundamentals

### 2.1 Optics in Layered Media

*This section gives an introduction to the principles of optics as utilized in this work, the goal being the derivation of the Fresnel formulae and their application in the transfer-matrix algorithm which will become invaluable for the description of optical fields inside multilayer systems later.*

*Starting with the Maxwell equations in media in Section 2.1.1, the principle fields are introduced and continuity conditions at material interfaces are found. After the derivation of the wave equation for the electric field, the polarisation of light in relation to a material boundary is introduced. As the use of metals inside resonator systems is of special interest to this work, the optical properties of metals are briefly discussed using the free electron model starting in Section 2.1.2, and in particular surface plasmon resonances are derived, which will be of importance when investigating the optical properties of ultra thin metal films later.*

*Finally, the Fresnel formulae are derived in Section 2.1.3 and the reflection and transmission at material interfaces is discussed and quantified as the corresponding coefficients, with their ultimate application for the transfer-matrix algorithm in Section 2.1.4.*

#### 2.1.1 Maxwell Equations in Dielectric Media

To describe the propagation of light as an electromagnetic wave in layered media, one has to start at Maxwell's equations (JAMES CLERK MAXWELL<sup>1</sup>) describing the electric field  $\vec{E}$ , the magnetic induction  $\vec{B}$ , the electric displacement  $\vec{D}$ , and the magnetic field  $\vec{H}$  in a medium. The electromagnetic field as described by the vectors  $\vec{E}$  and  $\vec{B}$  is connected to the fields inside a dielectric medium  $\vec{D}$  and  $\vec{H}$  via the orientation of electrical and magnetic dipoles described by the polarisation  $\vec{P}$  and magnetisation  $\vec{M}$  as follows:

$$\vec{D} = \epsilon_0 \vec{E} + \vec{P} = \epsilon_0 \epsilon \vec{E} \quad (2.1)$$

$$\vec{H} = \frac{1}{\mu_0} \vec{B} - \vec{M} = \frac{1}{\mu_0 \mu} \vec{B} = \quad . \quad (2.2)$$

---

<sup>1</sup>James Clerk Maxwell, 1831-1879, Scottish physicist, his equations lay the foundation for electromagnetism as it is known today.

Here, we introduce the permittivity of free space ( $\epsilon_0$ ) and material ( $\epsilon$ ) as well as the permeability of free space ( $\mu_0$ ) and material ( $\mu$ ), which are the basis for the universal constant of the speed of light

$$\begin{aligned} \text{in vacuum: } c_0 &= \frac{1}{\sqrt{\epsilon_0\mu_0}} \\ \text{in materials: } c &= \frac{1}{\sqrt{\epsilon\mu \cdot \epsilon_0\mu_0}} = \frac{1}{\tilde{n} \cdot \sqrt{\epsilon_0\mu_0}} = \frac{c_0}{\tilde{n}} \quad . \end{aligned} \quad (2.3)$$

With  $\tilde{n} = n + i\kappa$  we denote the complex refractive index of the material with its real part  $n$ , the linear refractive index, and the extinction coefficient  $\kappa$ . As magnetic materials are not investigated in this thesis, the magnetic permeability  $\mu$  is set to unity in the following.

Having these relations in mind, and allowing for external charges  $\rho_{\text{ext}}$  and currents  $j_{\text{ext}}$ , one can formulate Maxwell equations in media [59]:

$$\text{div } \vec{D} = \rho_{\text{ext}} \quad (2.4)$$

$$\text{div } \vec{B} = 0 \quad (2.5)$$

$$\text{curl } \vec{E} = -\frac{\partial \vec{B}}{\partial t} \quad (2.6)$$

$$\text{curl } \vec{H} = \vec{j}_{\text{ext}} + \frac{\partial \vec{D}}{\partial t} \quad . \quad (2.7)$$

## Material Interfaces

In layered media, the behaviour of electromagnetic fields at interfaces is especially of importance. Let two materials with differing permittivity and permeability be aligned with their interface in the  $x - y$  plane and growth direction  $z$ . Considering the interface between these two media, we can apply Gauss' theorem (JOHANN CARL FRIEDRICH GAUSS<sup>2</sup>) to the second Maxwell equation (2.5) in a volume including the interface with surfaces in both material 1 and 2 ( $S_1$  and  $S_2$ ) and infinitely small height to obtain:

$$\int \text{div } \vec{B} dV = \int \vec{B} \cdot \vec{e}_z (dS_1 + dS_2) = 0 \quad , \quad (2.8)$$

where  $\vec{e}_z$  is the unit vector normal to the surface. As both surfaces differ only in orientation, we obtain:

$$(\vec{B}_1 \cdot \vec{e}_{z1} + \vec{B}_2 \cdot \vec{e}_{z2})dS = \vec{e}_z \cdot (\vec{B}_2 - \vec{B}_1)dS = 0 \quad , \quad (2.9)$$

<sup>2</sup>Johann Carl Friedrich Gauss, 1777-1855, German mathematician, with important contributions to many mathematical and physical fields, he is lauded as one of history's greatest mathematicians.

which consequently means that the normal component of the magnetic induction is continuous across the surface. Similar considerations can be done for the first Maxwell equation (2.4), leading to:

$$\vec{e} \cdot ({}_z\vec{B}_2 - \vec{B}_1)dS = 4\pi\rho_{\text{surface}} \quad , \quad (2.10)$$

showing that the normal component of the electric displacement field changes according to a surface charge density  $\rho_{\text{surface}}$ .

For the behaviour of the tangential component, we utilise the Stokes theorem (SIR GEORGE GABRIEL STOKES<sup>3</sup>), applied to the third Maxwell equation (2.6) across a closed loop with two tangents to and two normals crossing the interface:

$$\int \text{curl } \vec{E} \cdot \vec{e}_x dS = \oint \vec{E} \cdot d\vec{r} = -\frac{1}{c} \int \dot{\vec{B}} \cdot \vec{e}_t dS \quad , \quad (2.11)$$

where  $\vec{e}_x$  is a unit vector tangential to the material interface. In the limit of infinitely small vectors normal to the surface, we obtain:

$$(\vec{E}_1 \cdot \vec{e}_{x1} + \vec{E}_2 \cdot \vec{e}_{x2})d\vec{r} = \vec{e}_x(\vec{E}_2 - \vec{E}_1)d\vec{r} = 0 \quad . \quad (2.12)$$

As  $\vec{e}_x = \vec{e}_y \times \vec{e}_z$ , we follow:  $\vec{e}_z \times (\vec{E}_2 - \vec{E}_1) = 0$ , leading to the conclusion that the tangential component of the electric field is continuous across the surface. Again, similar derivations for Maxwell equation (2.7) yield:

$$\vec{e}_z(\vec{H}_2 - \vec{H}_1)d\vec{r} = \frac{4\pi}{c} \vec{j}_{\text{surface}} \quad , \quad (2.13)$$

showing that the tangential component of the magnetic field changes according to a surface current density  $\vec{j}_{\text{surface}}$ . Following this, under the consideration that the velocity of light is depending on the medium in which the fields propagate, one can derive Snell's law (WILLEBRORD SNELLIUS<sup>4</sup>), relating the angles of incident ( $\vartheta_1$ ) and transmitted ( $\vartheta_2$ ) field at the interface between dielectric media  $\tilde{n}_1$  and  $\tilde{n}_2$ :

$$\frac{\sin \vartheta_1}{\sin \vartheta_2} = \frac{c_1}{c_2} = \frac{\tilde{n}_2}{\tilde{n}_1} \quad . \quad (2.14)$$

## Wave Equation

While the Maxwell equations describe the behaviour and interaction of different electric and magnetic fields, one can derive differential equations describing each field separately. To derive

<sup>3</sup>Sir George Gabriel Stokes, 1819-1903, Irish mathematician and physicist, most notably known for his works in fluid dynamics (the Navier-Stokes equations) and mathematical physics (the here mentioned Stokes theorem).

<sup>4</sup>Willebrord Snellius, 1580-1626, Dutch astronomer and mathematician, rediscovered the law of refraction in 1621.

the wave equation for the electric field  $\vec{E}$ , we take the curl of the third Maxwell equation (2.6):

$$\text{curl}(\text{curl } \vec{E}) = \text{grad}(\text{div } \vec{E}) - \Delta \vec{E} = -\text{curl} \frac{\partial \vec{B}}{\partial t} = -\mu_0 \frac{\partial(\text{curl } \vec{H})}{\partial t} .$$

Under the absence of external charges  $\rho_{\text{ext}} = 0$ , the electric displacement is free of sources ( $\text{div } \vec{D} = 0$ ), making the electric field ( $\vec{E} = \varepsilon \varepsilon_0 \vec{D}$ ) free of sources, if the material permittivity  $\varepsilon$  changes only slightly over small distances. Finally, by inserting the fourth Maxwell equation (2.7), under the assumption that no external currents are present, we arrive at the wave equation for the electric field:

$$\Delta \vec{E} - \frac{1}{c_0^2} \varepsilon \frac{\partial^2 \vec{E}}{\partial t^2} = 0 . \quad (2.15)$$

This equation relates the spatial distribution  $\Delta \vec{E}$  of a field to its time propagation  $d^2 \vec{E}/dt^2$  and thus gives access to the dispersion relation of an electromagnetic wave  $\omega(\vec{k})$ , which relates its momentum or propagation vector  $\vec{k}$  to its oscillation frequency in time  $\omega$ .

The easiest solution of the wave equation for the electric field is the plane wave with harmonic time dependence:

$$\vec{E} = \vec{E}_0 \cdot \exp(i(\vec{k} \cdot \vec{r} - \omega t + \varphi)) , \quad (2.16)$$

with the constant phase factor  $\exp(i\varphi)$ . Inserting the plane wave into the wave equation, we arrive at the dispersion relation of photons in media:

$$-k^2 \vec{E} + \frac{\varepsilon \omega^2}{c_0^2} \vec{E} = 0 \quad \Rightarrow \quad \omega = \tilde{n} c_0 k . \quad (2.17)$$

This relation holds true in most cases, where effects such as interference do not play a major role. However, in more complex structures such as thin films and their multilayer structures, conductive media, or metamaterials, the photon dispersion can severely alter and has to be treated individually.

Following analogous steps, the wave equation for the magnetic field  $\vec{H}$  can be derived as well:

$$\Delta \vec{H} - \frac{1}{c_0^2} \varepsilon \frac{\partial^2 \vec{H}}{\partial t^2} = 0 . \quad (2.18)$$

## Polarisation

The polarisation of light in general describes the oscillation direction of the electromagnetic fields (by convention mostly described by the electric field oscillation), which can be linear (oscillating in a plane along the direction of propagation), circular (rotating at constant amplitude), or elliptical (rotating and oscillating). Here, the polarisation of light in relation to material inter-



faces will prove to be of special importance. As already evidenced above, the field components in relation to an interface between media play an important role when electromagnetic waves cross or reflect from such an interface. To derive the polarisation, we assume again an interface between media  $\tilde{n}_1$  and  $\tilde{n}_2$  in the  $x$ - $y$  plane, such that  $\tilde{n} = \tilde{n}(z)$ . For a plane wave propagating in  $x$ -direction ( $\vec{k} = (k_x, 0, 0)$ ), the Maxwell equations (2.6) and (2.7) reduce to their components:

$$\begin{aligned} \frac{\partial E_y}{\partial z} &= -i\omega\mu_0 H_x & , & \quad \frac{\partial E_x}{\partial z} - ik_x E_z = i\omega\mu_0 H_y & , & \quad ik_x E_y = i\omega\mu_0 H_z \\ \frac{\partial H_y}{\partial z} &= i\omega\epsilon_0 \epsilon E_x & , & \quad \frac{\partial H_x}{\partial z} - ik_x H_z = -i\omega\epsilon_0 \epsilon E_y & , & \quad ik_x H_y = -i\omega\epsilon_0 \epsilon E_z \quad . \end{aligned} \quad (2.19)$$

It can be shown that this system allows two sets of solutions [60]. The first set requires  $E_y = H_x = H_z = 0$  to be zero and only  $E_x, E_z, H_y$  have a nonzero value and is called transverse magnetic (TM- or p-) waves. The second set requires  $E_x = E_z = H_y = 0$  to be zero and  $E_y, H_x, H_z$  have a nonzero value and is called transverse electric (TE- or s-) waves. The full set of equations for either case includes the corresponding wave equations and leaves a full set of equations:

$$\begin{aligned} \text{TM:} \quad 0 &= \frac{\partial^2 H_y}{\partial z^2} + (k_0^2 \epsilon - k_x^2) H_y \\ E_x &= -i \frac{1}{\omega \epsilon_0 \epsilon} \frac{\partial H_y}{\partial z} \\ E_z &= -\frac{k_x}{\omega \epsilon_0 \epsilon} H_y \end{aligned} \quad (2.20)$$

$$\begin{aligned} \text{TE:} \quad 0 &= \frac{\partial^2 E_y}{\partial z^2} + (k_0^2 \epsilon - k_x^2) E_y \\ H_x &= -i \frac{1}{\omega \mu_0} \frac{\partial E_y}{\partial z} \\ H_z &= -\frac{k_x}{\omega \mu_0} E_y \quad . \end{aligned} \quad (2.21)$$

The interaction of electromagnetic waves and matter strongly depends on the polarisation, which has to be very carefully treated and taken into account for all kinds of application.

### 2.1.2 Optics in Metals

The behaviour of light in conductive media differs fundamentally from the propagation of light in dielectrics. In the presence of free charge carriers, an oscillating electromagnetic field induces an oscillation of charged particles also, leading to an interaction between electromagnetic wave and oscillation of charge carrier density.

### Free Electron Gas

To derive the behaviour of light in metals, we describe the motion of free charge carriers (electrons) by the model of the free electron gas. Here, free electrons in the conduction band of the metal move according to the differential equation:

$$m\ddot{\vec{r}} + m\gamma\dot{\vec{r}} = -e\vec{E} = -e\vec{F}(\vec{r}) \cdot e^{-i\omega t} \quad , \quad (2.22)$$

where  $m$  is the material specific effective electron mass, and  $\gamma$  is the collision frequency with which the electrons scatter and lose all momentum inside the material, dampening the oscillation. The electron is then subject to an external stimulation in form of an electric field oscillating harmonically  $-e\vec{E}(\vec{r}, t) = -e\vec{F}(\vec{r}) \cdot \exp(-i\omega t)$ . Solving this equation, we can calculate the material polarisation by multiplying the charge carrier position vector with the electron density  $\rho$ :

$$\vec{P}(t) = -e\rho \cdot \vec{r}(t) = -\frac{\rho e^2}{m(\omega^2 + i\gamma\omega)} \vec{E}(t) \quad , \quad (2.23)$$

and thus also calculate the dielectric displacement field to extract the permittivity  $\epsilon$ :

$$\begin{aligned} \vec{D}(t) &= \vec{P}(t) + \epsilon_0 \vec{E}(t) = \epsilon_0 \left( 1 - \frac{\frac{\rho e^2}{m\epsilon_0}}{\omega^2 + i\gamma\omega} \right) \vec{E}(t) \\ \epsilon &= 1 - \frac{\omega_p^2}{\omega^2 + i\gamma\omega} = \left( 1 - \frac{\omega_p^2 \tau^2}{\omega^2 \tau^2 + 1} \right) + i \left( \frac{\omega_p^2 \tau}{\omega(\omega^2 \tau^2 + 1)} \right) \quad , \end{aligned} \quad (2.24)$$

with the plasma frequency  $\omega_p = e\sqrt{\rho/m\epsilon_0}$ . This frequency describes the oscillation of the plasma of electron density inside a metal, its quantisation being the plasmon. For low frequencies of light  $\omega \ll \gamma$ , the permittivity becomes  $\epsilon \approx 1 + i\omega_p^2/\gamma\omega$ , exhibiting a significant imaginary part, and thus leading to a large extinction coefficient  $\kappa$ . In this region, conductive media are largely absorbing. For the high frequency limit  $\omega \gg \gamma$ , the permittivity becomes  $\epsilon \approx 1 - \omega_p^2/\omega^2$ . Here, the imaginary part vanishes, and the metal behaves like a transparent dielectric. In real materials however, interband transitions result in an increased absorption and thus raise the imaginary part of the permittivity again at higher frequencies [61]. For common metals, the plasma frequency lies typically in the ultraviolet regime.

Conductivity and permittivity are closely connected, as free charge carriers always interact with oscillating fields around them. Consequently, by linking the dielectric constants of the free electron gas to the Drude model (PAUL DRUDE<sup>5</sup>), one can relate the conductivity  $\sigma$  to the complex

<sup>5</sup>Paul Drude, 1863-1906, German physicist specializing in optics, most famous for his work relating optical and electrical properties and the structure of substances.

permittivity:

$$\varepsilon = \varepsilon' + i\varepsilon'' = \varepsilon' + i\frac{\sigma(\omega)}{\omega\varepsilon_0} \quad , \quad (2.25)$$

where the complex conductivity becomes  $\sigma = \varepsilon_0\omega_p^2/(\gamma - i\omega)$ .

### Surface Plasmon Polaritons

The oscillating fields of electromagnetic radiation cause an oscillation of charge carrier density in conductive media which, in turn, causes the emission of electromagnetic waves. In special cases, this back and forth coupling between two oscillating waves, described by their quantisations plasmon (charge carrier density) and polariton (electromagnetic field or material polarisation) will travel along the surface of a conductive medium, such as a metal. The condition for the observations of such surface plasmon polaritons shall be laid out in the following.

Considering similar boundary conditions to Section 2.1.1, we assume a material interface in the  $x - y$  plane between a dielectric  $\varepsilon_1$  and a metal  $\varepsilon_2$ . Sufficiently below the plasma frequency, the real part of  $\varepsilon_2$  becomes negative, as evidenced by Equation (2.24). To first consider the case of TM-polarised light, we calculate Equations (2.20):

$z > 0$ , Dielectric:

$$\begin{aligned} H_y &= A_1 \cdot \exp(ik_x x - k_1 z) \\ E_x &= iA_1 \frac{1}{\omega\varepsilon_0\varepsilon_2} k_1 \cdot \exp(ik_x x - k_1 z) \\ E_z &= -A_1 \frac{k_x}{\omega\varepsilon_0\varepsilon_2} \cdot \exp(ik_x x - k_1 z) \end{aligned} \quad (2.26)$$

$z < 0$ , Metal:

$$\begin{aligned} H_y &= A_2 \cdot \exp(ik_x x + k_2 z) \\ E_x &= -iA_2 \frac{1}{\omega\varepsilon_0\varepsilon_2} k_1 \cdot \exp(ik_x x + k_2 z) \\ E_z &= -A_2 \frac{k_x}{\omega\varepsilon_0\varepsilon_2} \cdot \exp(ik_x x + k_2 z) \end{aligned} \quad . \quad (2.27)$$

According to the continuity conditions (2.13), (2.12) and the wave equation, we obtain:

$$A_1 = A_2, \quad \frac{k_1}{k_2} = -\frac{\varepsilon_2}{\varepsilon_1}, \quad k_x^2 - k_0^2\varepsilon_i = k_i^2, \quad (2.28)$$

which leads to the dispersion relation of the surface plasmon polariton travelling along the  $x$ -direction:

$$k_{x, \text{spp}} = \frac{\omega}{c} \sqrt{\frac{\varepsilon_1 \varepsilon_2}{\varepsilon_1 + \varepsilon_2}} \quad . \quad (2.29)$$

Following the same steps of calculating the surface plasmon polariton resonance as Equations (2.26) and (2.27) in TE-polarisation, we arrive at the only possible solution of:

$$A_1 = A_2 = 0 \quad , \quad (2.30)$$

i.e. surface plasmon polaritons do not exist in TE-polarisation. Figure 2.1 (a) shows the dispersion relation of surface and bulk plasmon in relation to a surrounding medium of  $\varepsilon = 1$ . As the frequency approaches the surface plasmon resonance  $\omega_{\text{sp}}$ , the in plane propagation diverges. The field amplitude extends into both metal as well as dielectric and exhibits an exponential decay as a function of the distance to the interface.

### Localized Surface Plasmons

As derived, surface plasmon polaritons propagate along the surface between conductive and dielectric media, when both materials are extended films. However, if small conductive islands on the order of or smaller than the wavelength of light are present, all electrons of the conduction band oscillate with the driving field. This non-propagating resonance is called a localized surface plasmon (LSP) and exhibits strong extinction of the field depending on optical constants, size, shape, and aspect ratio of the conductive nanoparticles. In the quasi-static approach, it can be shown that the extinction cross section  $C_{\text{ext}}$  of spherical nanoparticles behaves as follows [60, 62]:

$$C_{\text{ext}}(\lambda, V) = \frac{18\pi\varepsilon_1^{3/2}V}{\lambda} \frac{\varepsilon_2''}{(\varepsilon_2' + 2\varepsilon_1)^2 + \varepsilon_2''^2} \quad , \quad (2.31)$$

where  $V$  is the particle volume and  $\varepsilon_{1/2}$  represent dielectric (1) and metal (2), as above. It becomes clear, that a maximum arises at the Fröhlich condition (HERBERT FRÖHLICH<sup>6</sup>)  $\varepsilon_2' = -2\varepsilon_1$ . A more rigorous approach requires the use of Mie theory (GUSTAV MIE<sup>7</sup>), see e.g. [60, 63], where it can be seen, that LSP resonances broaden and shift to the red with increasing particle size [64]. Figure 2.1 shows the main extinction wavelength for gold nanospheres of different radii, with maxima in the green to red regions of the spectrum. For small nanoparticles, large linewidths on the order of 200 nm to 1000 nm are expected, leading to a broad extinction in the

<sup>6</sup>Herbert Fröhlich, 1905-1991, English physicist, known for his work on the theory of electrons in solid state materials as well as for contributions to superconductivity, particle physics, and biophysics.

<sup>7</sup>Gustav Adolf Feodor Wilhelm Ludwig Mie, 1869-1957, German physicist, most known for his work on scattering of electromagnetic waves at small particles.

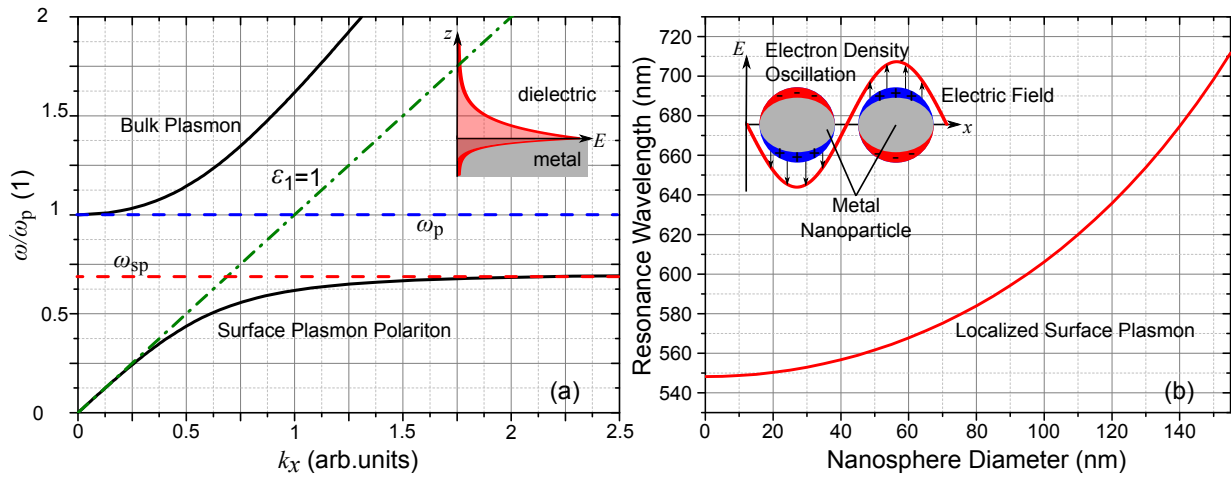


**Figure 2.1:** (a) Surface plasmon polariton dispersion at a metal-dielectric interface. Below the surface plasmon resonance  $\omega_{sp}$ , the surface plasmon propagates along the  $x$ -axis with arbitrarily high wavenumber. Above the plasma frequency, bulk plasmon dispersion is visible. The linear dispersion of the dielectric with  $\epsilon = 1$  is added for comparison as dash-dotted line. Inset shows the field distribution at the interface. (b) Absorption peak wavelength of localized surface plasmons in gold nanospheres of varying diameter. Inset shows schematic depiction of the LSP inside of sub-wavelength sized metal nanospheres.

visible. To fully include all effects, the interaction and coupling between different nanoparticles plays an important role and has to be taken into account [60] but shall not be discussed in detail here.

Noble metals such as silver tend to show island-like growth (see Section 3.1.4), so the formation of LSPs and in turn their absorption will play an important role there. As cavity-based systems strongly decrease their performance in presence of parasitic absorption, island-like growth and LSP absorption have to be avoided at all costs for the purpose of this work.

### 2.1.3 Reflection and Transmission

For practical purposes, the exact knowledge of field propagation through multilayer systems is not of interest, instead more accessible values such as the overall reflection, transmission, and absorption of the system are utilized to describe its behaviour under illumination. In general, one distinguishes dielectric reflection and refraction, as observed at the interface between dielectric media of differing refractive indices  $n$ , and metallic reflection at the surface of a conductor for light below the plasma frequency. When entering a conductor, light is quickly absorbed due to their high extinction coefficient, and conductors such as metals thus mainly exhibit (very good) reflection of light. For very thin films of absorbing medium, however, there remains a finite transmission, which can be enhanced by interference in multilayer systems, as will be discussed

in the following Section.

Considering the continuity conditions at material interfaces, already Snell's law has been given in Equation (2.14), detailing the angle of refraction in a medium as a result of the material polarisation and thus the change of the speed of light in the medium. In similar fashion, the relation between the angle of incident (i) and reflected (r) light can be found [59]:

$$\frac{\sin \theta_i}{\sin \theta_r} = \frac{c_i}{c_r} = \frac{c_i}{c_i} = 1 \quad \text{and} \quad \cos \theta_i = -\cos \theta_r \quad , \quad (2.32)$$

showing that the reflected angle and the incident angle are the same when mirrored at the interface normal:  $\theta_i = \pi - \theta_r$ .

By considering the incident, reflected and transmitted fields  $\vec{E}^i$ ,  $\vec{E}^r$ , and  $\vec{E}^t$ , the Fresnel equations (AUGUSTIN-JEAN FRESNEL<sup>8</sup>) can be found.

### Fresnel Equations

Let a plane wave be incident on a material interface in the  $xy$ -plane as above. The fields can then be split into their TE- and TM- polarised parts:

Incident Field:

$$\begin{aligned} E_x^i &= -A_{\text{TM}} \cos \theta_i \exp(-i\omega(t - (x \sin \theta_i + z \cos \theta_i)/c_1)), \\ E_y^i &= A_{\text{TE}} \exp(-i\omega(t - (x \sin \theta_i + z \cos \theta_i)/c_1)), \\ E_z^i &= A_{\text{TM}} \sin \theta_i \exp(-i\omega(t - (x \sin \theta_i + z \cos \theta_i)/c_1)) \end{aligned} \quad (2.33)$$

Transmitted Field:

$$\begin{aligned} E_x^t &= -T_{\text{TM}} \cos \theta_t \exp(-i\omega(t - (x \sin \theta_t + z \cos \theta_t)/c_2)), \\ E_y^t &= T_{\text{TE}} \exp(-i\omega(t - (x \sin \theta_t + z \cos \theta_t)/c_2)), \\ E_z^t &= T_{\text{TM}} \sin \theta_t \exp(-i\omega(t - (x \sin \theta_t + z \cos \theta_t)/c_2)) \end{aligned} \quad (2.34)$$

Reflected Field:

$$\begin{aligned} E_x^r &= -R_{\text{TM}} \cos \theta_r \exp(-i\omega(t - (x \sin \theta_r + z \cos \theta_r)/c_1)), \\ E_y^r &= R_{\text{TE}} \exp(-i\omega(t - (x \sin \theta_r + z \cos \theta_r)/c_1)), \\ E_z^r &= R_{\text{TM}} \sin \theta_r \exp(-i\omega(t - (x \sin \theta_r + z \cos \theta_r)/c_1)), \end{aligned} \quad (2.35)$$

<sup>8</sup>Augustin-Jean Fresnel 1788-1827), French engineer and physicist, established in part the theory of wave optics.

and the corresponding magnetic fields can be calculated:

$$\vec{H}^l = \sqrt{\epsilon_l} \vec{e}^l \times \vec{E}^l \quad . \quad (2.36)$$

Demanding continuity of the in plane components, we can split the fields into their TE- and TM-polarised parts and calculate the amplitudes of the reflected and transmitted waves under application of Snell's law:

$$R_{\text{TM}} = \frac{\tan(\theta_i - \theta_t)}{\tan(\theta_i + \theta_t)} A_{\text{TM}}, \quad R_{\text{TE}} = -\frac{\sin(\theta_i - \theta_t)}{\sin(\theta_i + \theta_t)} A_{\text{TE}} \quad (2.37)$$

$$T_{\text{TM}} = \frac{2 \sin \theta_t \cos \theta_i}{\sin(\theta_i + \theta_t) \cos(\theta_i - \theta_t)} A_{\text{TM}}, \quad T_{\text{TE}} = \frac{2 \sin \theta_t \cos \theta_i}{\sin(\theta_i + \theta_t)} A_{\text{TE}} \quad . \quad (2.38)$$

These are the Fresnel equations for the reflection and transmission of fields regarding their polarisation. As becomes immediately obvious, under normal incidence ( $\theta_l = 0$  for all  $l$ ), the amplitudes of reflected and transmitted light are no longer dependent on polarisation (apart from a phase shift of the reflected TM-wave), while under oblique incidence the polarisation strongly influences the corresponding amplitudes. This will be of importance in the case of microcavities later and will, among others, lead to the polarisation splitting of the microcavity dispersion. Furthermore, a special case emerges when  $\theta_i + \theta_t = \pi/2$ , the so-called Brewster angle (D. BREWSTER<sup>9</sup>). Here, the TM-polarised part of the reflected light vanishes, and the reflected light becomes exclusively TE-polarised.

When talking about the fraction of energy reflected or transmitted through an interface, one needs to consider the Poynting vector (J. POYNTING<sup>10</sup>), or its absolute value  $S = c/(4\pi) \cdot \vec{E} \cdot \vec{H}$ . By calculating the energy of the waves incident and reflected/transmitted at the boundary, the reflectivity  $\mathcal{R}$  and transmittivity  $\mathcal{T}$  can be calculated:

$$\mathcal{R}_{\text{TM}} = \frac{\tan^2(\theta_i - \theta_t)}{\tan^2(\theta_i + \theta_t)}, \quad \mathcal{R}_{\text{TE}} = \frac{\sin^2(\theta_i - \theta_t)}{\sin^2(\theta_i + \theta_t)} \quad (2.39)$$

$$\mathcal{T}_{\text{TM}} = \frac{\sin 2\theta_i \sin 2\theta_t}{\sin^2(\theta_i + \theta_t) \cos^2(\theta_i - \theta_t)}, \quad \mathcal{T}_{\text{TE}} = \frac{\sin 2\theta_i \sin 2\theta_t}{\sin^2(\theta_i + \theta_t)} \quad . \quad (2.40)$$

These values provide the ratios of reflected and transmitted light at a boundary and are often discussed as reflectance and transmittance (in percent). Following energy conservation, their sum must be unity:

$$\mathcal{T}_{\text{TM}} + \mathcal{R}_{\text{TM}} = 1 \quad , \quad \mathcal{T}_{\text{TE}} + \mathcal{R}_{\text{TE}} = 1 \quad , \quad (2.41)$$

<sup>9</sup>David Brewster, 1781-1868, Scottish physicist, influential in experimental optics and inventor of many optical applications (such as the kaleidoscope).

<sup>10</sup>John Henry Poynting, 1852-1914, English physicist.

In conducting media these relations still hold, however all values become complex, leading to the observation of absorption, greatly diminished transmission, and phase changes at the interface.

### Reflection and Transmission in Conductive Media

While the Fresnel equations do not require any assumptions on part of the refractive indices or permittivities of the materials and are thus universal in that regard, a few effects of conductive media in particular shall be discussed here. A main difference when observing conductive compared to dielectric media is the complex value of the permittivity and thus a complex valued refractive index  $\tilde{n} = n + i\kappa$ , which is closely related to the material absorption coefficient  $\alpha$  following the Beer-Lambert law (AUGUST BEER, JOHANN HEINRICH LAMBERT<sup>11</sup>) for the transmitted intensity  $I_T$ :

$$I_T = I_0 \cdot \exp(-\alpha r) = I_0 \cdot \exp\left(-2\kappa(\omega)\frac{\omega}{c}r\right) \quad . \quad (2.42)$$

Here we see, that extended conductive media exhibit a vanishing transmission after only small distances. The calculation of reflection and transmission of fields follows analogously to Equations (2.37), (2.38), by allowing for complex angles as obtained from the complex law of Snell. This leads not only to a splitting of light in parts reflected and refracted at the medium, but also to a phase change  $\delta_j^r$  of the reflected amplitude:

$$r_{\text{TM/TE}} = \frac{R_{\text{TM/TE}}}{A_{\text{TM/TE}}} = \rho_{\text{TM/TE}} \exp(i\delta_{\text{TM/TE}}^r) \quad . \quad (2.43)$$

As especially metals below the plasma frequency exhibit very high extinction coefficients (e.g. silver at 600 nm,  $\kappa \approx 4$ ), light can only transmit through films much smaller than its wavelength. The transmission through a thin conductive film of  $\varepsilon_2$  and thickness  $d$  sandwiched between dielectric media  $\varepsilon_1$  and  $\varepsilon_3$  is then calculated as the product of the interface transmissions and the propagation through the film [59]:

$$\mathcal{T}_{\text{TM}} = \frac{n_1 \cos \theta_3}{n_3 \cos \theta_1} \frac{\mathcal{T}_{\text{TM},12} \mathcal{T}_{\text{TM},23} \exp(-2\kappa d\omega/c)}{\left[ 1 + \mathcal{T}_{\text{TM},12} \mathcal{T}_{\text{TM},23} \exp(-4\kappa d\omega/c) + 2\sqrt{\mathcal{T}_{\text{TM},12} \mathcal{T}_{\text{TM},23}} \exp(-2\kappa d\omega/c) \cos(\delta_{12} + \delta_{23} + 2\kappa d\omega/c) \right]} \quad (2.44)$$

$$\mathcal{T}_{\text{TE}} = \frac{n_3 \cos \theta_3}{n_1 \cos \theta_1} \frac{\mathcal{T}_{\text{TE},12} \mathcal{T}_{\text{TE},23} \exp(-2\kappa d\omega/c)}{\left[ 1 + \mathcal{T}_{\text{TE},12} \mathcal{T}_{\text{TE},23} \exp(-4\kappa d\omega/c) + 2\sqrt{\mathcal{T}_{\text{TE},12} \mathcal{T}_{\text{TE},23}} \exp(-2\kappa d\omega/c) \cos(\delta_{12} + \delta_{23} + 2\kappa d\omega/c) \right]} \quad (2.45)$$

<sup>11</sup>August Beer, 1825-1863, German physicist and mathematician; Johann Heinrich Lambert, 1728-1777, Swiss mathematician, physicist, philosopher and astronomer, the modern Beer-Lambert's law was derived as a combination of both Beer's and Lambert's laws concerning the absorbance of transparent samples.



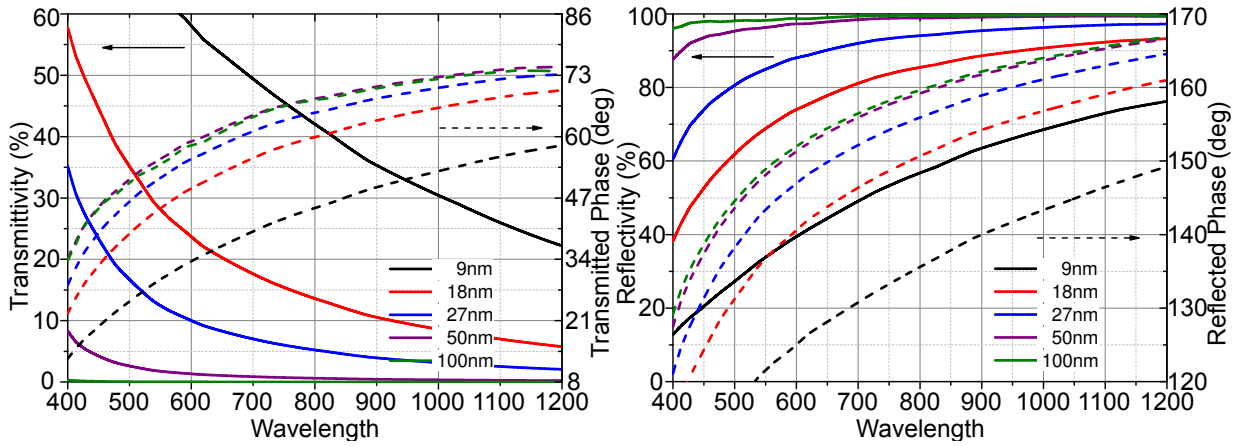


**Figure 2.2:** Calculated reflection and transmission of thin silver films between air ( $n = 1$ ) and a dielectric substrate ( $n = 1.5$ ). The optical constants of silver are taken from reference [61] (a) Transmittivity and transmitted phase of silver films of thicknesses 9 nm to 100 nm. Below thicknesses of about 40 nm, silver still exhibits a significant amount of transmission, while virtually no light is transmitted for films above 100 nm. The transmitted light also experiences a phase shift as a sum of the phase shifts at the air-silver and silver-dielectric interfaces and the phase of propagation through the layer. (b) Reflectivity and reflected phase of silver films of thicknesses 9 nm to 100 nm. Above 50 nm film thickness silver exhibits very high reflectivities in the visible and near-infrared part of the spectrum. Approaching the blue side of the spectrum, the reflectivity drops closer to the plasma frequency of silver in the ultraviolet. Due to the imaginary part of the permittivity, the reflected phase however does not amount to multiples of  $\pi$ , instead for thin films a significant phase shift of the reflected light is observed.

consisting mainly of the interface transmission  $\mathcal{T}_{12}$  and  $\mathcal{T}_{23}$  and the attenuation after Beer-Lambert:  $\exp(-2\kappa d\omega/c)$ . The total transmitted phase can be approximated as a sum of the interface phase change and the phase collected while travelling through the conductive medium:

$$\delta_{\text{TE/TM}}^t = \delta_{\text{TE/TM},12}^t + \delta_{\text{TE/TM},23}^t + n_2 d \cos \theta_2 \omega / c \quad . \quad (2.46)$$

Figure 2.2 shows the reflection and transmission of silver films of varying thicknesses from 9 nm to 100 nm, going from partly transparent to completely opaque and highly reflecting in the visible spectrum. In addition, one observes an uneven phase shift when reflecting at thin silver films, which becomes of immense interest for the realisation of metal-mirror-based resonators and shall be kept in mind. The transmission through silver films causes a change in phase not only by the optical path through the metal, but in addition also due to phase jumps at material interfaces. In more complex thin film systems, the transmittivity of thin conductive films can be strongly enhanced by interference effects in multilayer systems such as photonic crystals, where the electromagnetic field will produce a field node at the position of the metal. An example of

this is the formation of Tamm-plasmons (IGOR YEVGENYEVICH TAMM<sup>12</sup>) at the interface between periodic dielectric layer stacks and a metal film, which will be detailed later in this work.

### 2.1.4 Transfer-Matrix Algorithm

While the Fresnel equations provide all the tools necessary to describe multilayer systems of thin films, applications often require the consideration of many layers (e.g. 43 layers for a standard organic microcavity), demanding a formalism easily implemented into simulation. The treatment of multilayer systems with  $i$  layers is possible via the transfer-matrix algorithm, relating plane waves travelling forward (A) and backward (B) through an optical system:

$$E_z^i = \tilde{A}_i e^{-ikz} + \tilde{B}_i e^{ikz} = A_i(z) + B_i(z) \quad . \quad (2.47)$$

Then, the crossing of the interface between the  $(i - 1)$ -th and  $i$ -th layer can be described by the interface matrix ( $D_{i-1}$ ):

$$\begin{pmatrix} A_{i-1} \\ B_{i-1} \end{pmatrix} = D \begin{pmatrix} A_i \\ B_i \end{pmatrix} \quad , \text{ with } \quad D_{i-1} = \frac{1}{t_{i-1,i}} \begin{pmatrix} 1 & r_{i-1,i} \\ r_{i-1,i} & 1 \end{pmatrix} \quad , \quad (2.48)$$

where the reflection ( $r$ ) and transmission ( $t$ ) coefficients are acquired as the square root of Fresnel equations (2.39) and (2.40). Light also has to travel through a layer  $i$ , which can be described by the propagation matrix  $P_i$ :

$$P_i = \begin{pmatrix} \exp(-i\delta_i) & 0 \\ 0 & \exp(i\delta_i) \end{pmatrix} \quad . \quad (2.49)$$

Here, light acquires a phase  $\delta_i$  during propagation through the layer given by  $\delta_i = n_i d_i \cos \theta_i \omega / c$ . In total, travelling through a multilayer system with  $N$  layers is given by the multiplication of transfer matrices  $M_i := D_{i-1} P_i$ :

$$\begin{pmatrix} A \\ B \end{pmatrix} = D_0 P_1 D_1 \dots P_N D_N \begin{pmatrix} A'_{N+1} \\ B'_{N+1} \end{pmatrix} = \left( \prod_{i=1}^N M_i \right) D_N \begin{pmatrix} A'_{N+1} \\ B'_{N+1} \end{pmatrix} =: M \begin{pmatrix} A'_{N+1} \\ B'_{N+1} \end{pmatrix} \quad . \quad (2.50)$$

If we assume a wave incident from the left side of the structure ( $B'_{N+1} = 0$ ), the reflection and transmission coefficients of the multilayer stack are then derived using the components of the transfer matrix  $M$ :

$$|r| = \left| \frac{A_{N+1}}{A_0} \right| = \left| \frac{M_{21}}{M_{11}} \right|, \quad |t| = \left| \frac{B_0}{A_0} \right| = \left| \frac{1}{M_{11}} \right| \quad . \quad (2.51)$$

<sup>12</sup>Igor Yevgenyevich Tamm, 1895-1971, Soviet physicist, received the Nobel Prize in Physics jointly for the discovery of Cherenkov radiation.

While the transfer-matrix algorithm is analytic, in practice it is implemented in a simulation software that numerically solves for the transfer matrices of a large number of layers. In this work, self-written algorithms are used alongside commercial software<sup>13</sup>. Note, that all calculations made by the transfer matrix method consider only a one-dimensional sequence of layers and typically do not include roughness, material variation, and patterning in plane.

## 2.2 Optics of Microcavities

*The behaviour of light in resonator structures lies the fundamental principles investigated and employed in this work. After having introduced the basic concepts in the previous section, here follows a closer look into the optics of microresonators, with the vertical microcavity as its central point.*

*After a brief introduction to microresonators in Section 2.2.1, the working principle of the distributed Bragg reflector (2.2.2) and a microcavity comprising two of these mirrors follows (2.2.3). Special interest here lies in the dispersion of microcavities and its behaviour under non-ideal conditions, where detuning and phase shifts lead to changes in the resonant wavelength and polarisation splitting (2.2.4). Subsequently, the concept of Tamm-plasmon-polaritons in metal-organic microcavities is introduced (2.2.5) and the behaviour of multidimensional confinement in photonic wires and dots is explored (2.2.6).*

*Finally, the basic processes in active laser media are surveyed and rate equations describing the occurrence of lasing in microcavities are found (2.2.7).*

### 2.2.1 Basics of Resonator Structures

Microresonators in use today may take many forms [65], where optical feedback is provided either by highly reflective mirrors (plane-parallel such as Fabry-Pérot or confocal resonators), or by means of trapping modes via total internal reflection in distributed feedback (DFB) or whispering-gallery mode (WGM) resonators. The basic principle demands that light of a certain (resonant) wavelength is enhanced, while non-resonant wavelengths are diminished and leave the system. Vertical resonators typically consist of two highly reflecting plane, confocal, concentric, or other optically stable mirrors, facing each other. The optical feedback is provided by the mirrors and the finite resonator length, selecting only resonant standing waves in between. Typical examples include the Fabry-Pérot resonator and its special application, the vertical cavity surface emitting laser (VCSEL) [66]. In waveguided systems, optical feedback can be provided by an added grating as in DFB-resonators [67], where only resonant modes stay trapped and

<sup>13</sup>FilmWizard by Scientific Computing International and RSoft by RSoft Design Group inc.

non-resonant modes leave the system due to the grating, or by means of continuous total internal reflection in spherical WGM structures [68, 69]. Further types include photonic crystal resonators [70, 71], where defects in periodic wavelength-size microstructures can confine light in analogy to trap states in defects of crystal lattices. The spectral behaviour of all microresonator structures strongly depends on their size, and resonance conditions directly relate to the micro-scale dimensions of either vertical or lateral patterns. Often, some form of periodicity plays a role in creating forbidden bands of photon energies, while defects such as a cavity layer in a VCSEL or the defect in a photonic crystal form the cavity mode depending mainly on size and position of the defect. Typical applications of those resonators range from interference measurements, to wavelength-selective optical filters and monochromators, as well as laser cavities and other systems where strong field-enhancement is desired.

In this work, special interest lies in plane-parallel Fabry-Pérot resonators as well as DFB resonators, which will be discussed in the following sections.

### Planar Fabry-Pérot Resonator

The type of resonator most commonly employed in this work is the coplanar Fabry-Pérot resonator, where two mirrors facing each other create standing waves between them. This leads to a strongly altered behaviour of light, when (i) the optical distance  $n \cdot d$  between mirrors is on the order of magnitude of the wavelength of interest, (ii) the wavelength obeys the resonance condition  $\lambda = m \cdot d/2$ , ( $m \in \mathbb{N}$ ), and (iii) the coherence length of said light is larger than the dimension of the resonator. If a plane wave of resonant wavelength  $\lambda$  inside of the resonator is reflected and travels inside the resonator, it interferes with itself according to:

$$E(x) = E_0 \cdot \exp(i(kx + \omega t)) + E_0 \cdot \exp(i(k(x) - \omega t)) = E_0 \cdot \exp(ikx) \cdot 2 \cos(\omega t) \quad , \quad (2.52)$$

creating a wave that is stationary in space ( $\exp(ikx)$ ) and oscillating only in time ( $\cos(\omega t)$ ), when interference conditions are met.

In particular, the electric field of resonant modes is enhanced between the mirrors due to the formation of this standing wave. If the mirrors are not perfectly reflecting and in fact exhibit even a minimal transparency, the field enhancement will then lead to an enhancement of transmission of resonant wavelengths, in a loss free system up to a transmission of 100%. Consequently, the field amplification of resonant wavelengths reaches large numbers. Active materials inside of such resonators can show a number of effects benefitting from an increased field strength, such as lasing, higher harmonic generation, or other non-linear behaviour. Furthermore, the angular distribution of these effects is interesting. The dispersion of such a resonator is given by its angle-dependent variation of the resonance wavelength. Under oblique angles, the  $\vec{k}$  vector receives a

lateral component  $k_{\parallel}$  in addition to its vertical component  $k_z$ . Consequently, the wavelength of resonant modes shift to the blue, changing the resonance condition to:

$$\lambda = \frac{2\pi}{\sqrt{k_z^2 + k_{\parallel}^2}} = md/2 \cdot \cos \vartheta = md/2 \cdot \sqrt{1 - \sin^2 \vartheta} \quad . \quad (2.53)$$

If the angle of incidence  $\vartheta$  is small and thus the lateral  $k$  component is small compared to the total wavevector, the dispersion of the resonator becomes parabolic  $\lambda = md/2 \cdot (1 - \vartheta^2)$ . The Fabry-Pérot resonator is the basic principle behind the vertical microcavity, which will be discussed in detail in the following sections.

### Distributed Feedback Resonator

Instead of relying on high reflectivity of various mirrors, one can make use of the inherently perfect total internal reflection in dielectric media. As discussed above, the reflection of light travelling from an optically dense medium of high refractive index  $n_1$  to a less dense medium of lower refractive index  $n_2$  exhibits total internal reflection at angles above the critical angle. If an optically dense layer is then sandwiched between two less dense coplanar layers, modes radiating in directions below the critical angle become trapped inside the optical waveguide. Such behaviour can be exploited e.g. for optical telecommunication or illumination through wires utilizing in- and outcoupling at the ends or via dedicated coupling structures in the system, where the coplanar nature of the waveguide is interrupted by a structure that allows modes below the critical angle to escape. A particular structure is the distributed feedback (DFB) structure, employing a periodic modulation of the waveguide height or direction. In such systems, only a small amount of modes, obeying the Bragg condition:

$$m \cdot \lambda_C = 2n_C \Lambda \quad , \quad (2.54)$$

remain trapped. Here,  $n_C$  denotes the active layer refractive index, while  $\Lambda$  denotes the grating period and  $m$  the scattering order. This can be exploited, as optical feedback is made possible by such a periodic corrugation and distributed feedback resonators are among the most widely employed laser resonators in applications. The nature of the resonator also means that in first-order structures ( $m = 1$ ), resonant wavelengths can only be coupled out in lateral direction, e.g. at the end of the resonator, while in higher order structures, the additional higher order grating facilitates a possible outcoupling in vertical direction. For example, second order structures ( $m = 2$ ) offer a pathway for modes to couple out normal to the surface. This can be utilized in small areas of second order grating to allow emission of coherent light perpendicular to the

waveguide. The theory of distributed feedback systems in multilayer systems quickly becomes complicated and shall not be detailed here. Further information can be found in references [72, 73, 74, 75].

### 2.2.2 Distributed Bragg Reflector

To facilitate a high quality of Fabry-Pèrot resonator and thus a large field enhancement, mirrors of exceptionally high reflectivity and low loss are needed. While metallic mirrors provide sufficient reflection for common applications, dielectric mirrors offer supreme performance for high-end uses such as laser microresonators. These mirrors consist of periodically alternating layers of dielectric materials with high ( $n_1$ ) and low ( $n_2$ ) refractive index, where each layer thickness corresponds to  $\lambda_D/(4n_i)$  of the so called design wavelength  $\lambda_D$ , starting and ending with the higher  $n_1$  always. Such distributed Bragg reflectors (DBRs) provide very high reflectivity in a spectrally selective area, exhibiting minimal losses if the materials used has only minimal intrinsic absorption.

The working principle of these dielectric mirrors can be understood by examining the propagation of phase  $\varphi$  inside such a multilayer system. If light of the design wavelength  $\lambda_D$  hits the interface between low ( $n_2$ ) and high ( $n_1$ ) refractive index material, it splits into a transmitted and a reflected wave. Upon reflection at the interface to an optically denser material, the light receives an additional phase of  $\pi$ . This reflected wave now travels back through the low refractive index material, receiving an additional propagation phase of  $\varphi = (d_{n_2})/\lambda_D \cdot 2\pi = (\lambda_D/4)/\lambda_D \cdot 2\pi = \pi/2$ . Upon reflecting at the back interface of the layer, an additional phase of  $\pi$  and subsequently an additional propagation phase of  $\pi/2$  are acquired, adding up to:

$$\varphi_{T \text{ total } n_2} = \varphi_{r21} + \varphi_{\text{prop}2} + \varphi_{r21} + \varphi_{\text{prop}2} = \pi + \pi/2 + \pi + \pi/2 = 3\pi \quad . \quad (2.55)$$

Comparing this phase to the initially transmitted light ( $\varphi = 0$ ), it becomes clear that destructive interference occurs in layer  $n_2$  in transmission geometry. Waves propagating in layer  $n_1$  do not receives additional phases on reflection at the interface, so the total phase of a wave travelling back and forth in this layer amounts to:

$$\varphi_{T \text{ total } n_1} = \varphi_{r12} + \varphi_{\text{prop}1} + \varphi_{r12} + \varphi_{\text{prop}1} = 0 + \pi/2 + 0 + \pi/2 = \pi \quad . \quad (2.56)$$

Again, destructive interference can be observed in transmission through layer  $n_1$ . The uneven phase change adds up at every interface of the periodic system, leading to a strong suppression of the transmission through destructive interference for large numbers of layers.

In reflection, the phase behaves differently. Comparing light initially reflected at the interface

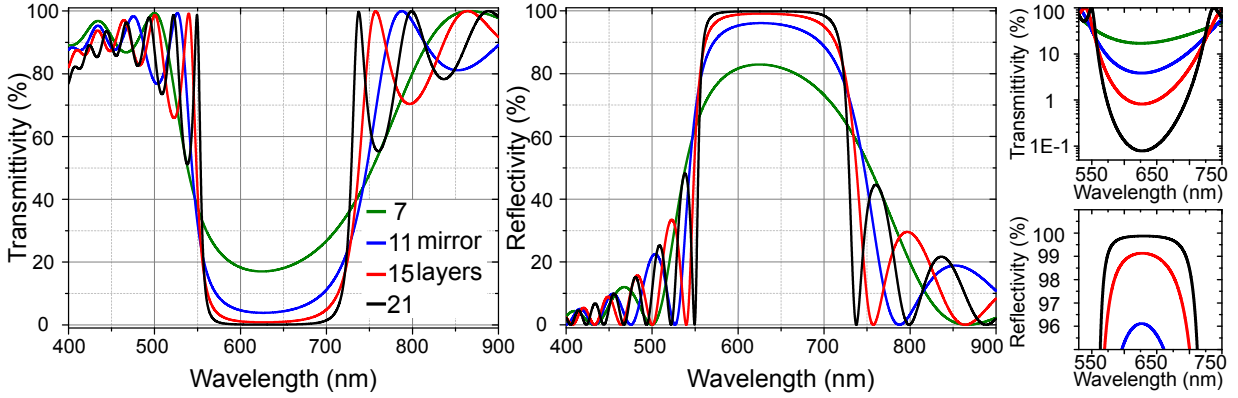


**Figure 2.3:** (a) and (c) Simulated transmission spectrum of a distributed Bragg reflector made of 21 (7, 11, 15) alternating layers of  $\text{TiO}_2$  and  $\text{SiO}_2$  and design wavelength 630 nm. Around the design wavelength, a  $\approx 150$  nm wide photonic stopband exhibits very low transmission, below 1% for 21 layers. (b) and (d) Simulated reflection spectrum of the DBRs. As almost no absorption is present,  $R + T \approx 1$ . For 21 layers, reflectivities above 99.9% are achieved.

from low to high refractive index ( $\varphi = \varphi_{r21} = \pi$ ) to light initially transmitted, propagating through the optically dense material, reflected at the interface from high to low refractive index and propagating back:

$$\varphi_{R \text{ total } n_2} = \varphi_{\text{prop}1} + \varphi_{r12} + \varphi_{\text{prop}1} = 0 + \pi/2 + 0 + \pi/2 = \pi \quad , \quad (2.57)$$

we see that the waves constructively interfere in reflection. In layer  $n_1$ , the initially reflected wave receives no change in phase, while the wave that is first transmitted and then reflected back receives a total change in phase of:

$$\varphi_{R \text{ total } n_1} = \varphi_{\text{prop}2} + \varphi_{r21} + \varphi_{\text{prop}1} = \pi + \pi/2 + 0 + \pi/2 = 2\pi \quad , \quad (2.58)$$

again constructively interfering ( $0\pi$  vs  $2\pi$ ) in reflection. This seems obvious as, when transmission is strongly suppressed, reflection must be strongly enhanced if no parasitic absorption takes place.

In total, this behaviour results in the formation of a photonic stopband of very high reflection and very low transmission around the design wavelength  $\lambda_D$  of the mirrors. Figure 2.3 showcases the reflection and transmission spectra of such a distributed Bragg reflector made of 21 (7, 11, 15) alternating layers of  $\text{TiO}_2$  and  $\text{SiO}_2$ . Here, a maximum reflectivity of  $R = 99.96\%$  can be observed even in experiment. The width of this stopband depends mainly on the difference in

refractive index of materials 1 and 2:

$$\Delta\lambda \approx \lambda_D \cdot \frac{4}{\pi} \arcsin\left(\frac{n_1 - n_2}{n_1 + n_2}\right), \quad (2.59)$$

leading to a width of  $\Delta\lambda \approx 150$  nm for  $\lambda_D = 630$  nm,  $n_1 = 2.1$ , and  $n_2 = 1.45$ , nicely coinciding with the calculated spectra above.

If the refractive index dispersion and intrinsic losses of the materials stay favourable, such mirrors can be arbitrarily tuned to any wavelength by changing the optical thickness of the layers. The combination of  $\text{TiO}_2$  and  $\text{SiO}_2$  is especially suited for the visible and near-infrared spectral regions.

### 2.2.3 Microcavities

Microcavities are resonators on the micron-scale, in particular on the scale of a few multiples of  $\lambda_D/2$ , and thus strongly influence the light travelling in such structures. Typical Fabry-Pèrot type cavities employ two coplanar metallic or dielectric mirrors encasing an active layer of  $\lambda_D/2$  thickness. Here, a standing wave forms inside of the resonator, exhibiting strong field enhancement depending on the type of mirror. For high-performance microlasers, the microcavity consists of two DBRs encasing an active material, which in this case is an organic emitter.

The introduction of a  $\lambda_C/2$  layer in a DBR, with  $\lambda_C$  in the stopband of the DBR ( $\lambda_D - \Delta\lambda < \lambda_C < \lambda_D + \Delta\lambda$ ), modifies the phase of light propagating through such a device. Here, the conditions for constructive and destructive interference are switched at the cavity-DBR interfaces due to the longer propagation through the cavity layer:

$$\varphi_{\text{prop, C}} = \varphi = (d_C)/\lambda_C \cdot 2\pi = (\lambda_C/2)/\lambda_C \cdot 2\pi = \pi \quad . \quad (2.60)$$

Consequently, a cavity mode of high transmission and low reflection appears at  $\lambda_C$  inside the optical stopband. The electric field of this wavelength is strongly enhanced in the cavity, facilitating the field density necessary for laser operation or enhancing absorption in a spectrally narrow range. Both cavity spectrum and field distribution are depicted in Figure 2.4, for a cavity comprising two 21 (7, 11, 15) layer DBRs as above and an  $\lambda/2$  cavity, where we see a cavity mode arising in the center of the DBR stopband.

Resonant light travels inside the cavity from mirror to mirror, strongly enhancing the interaction of light with the active material and thus artificially increasing the cavity thickness. The number of round-trips a photon travels before being absorbed or leaving the cavity via the mirrors can be estimated via the quality factor  $Q$  of the microcavity. It is defined as  $2\pi$  times the number of oscillations before the field decays to  $1/e$  of the initial value, and is connected to the



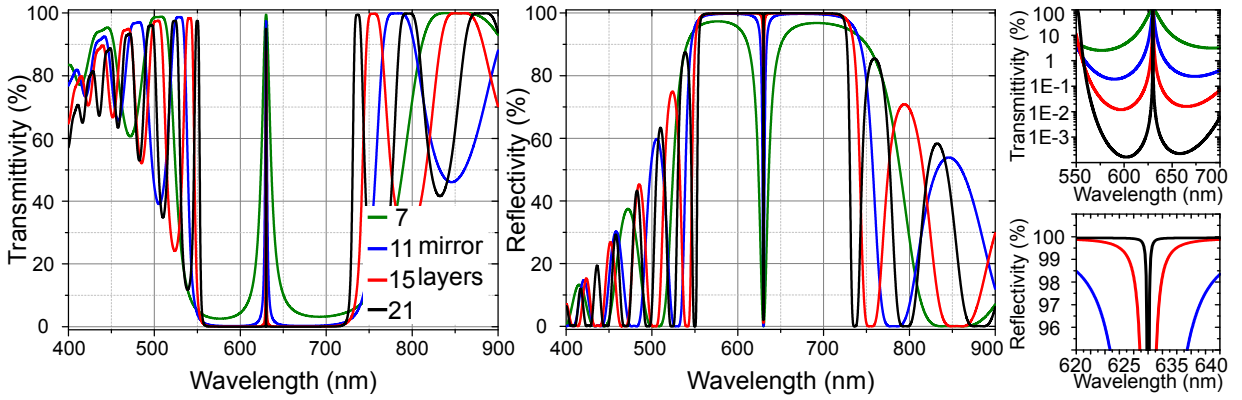


**Figure 2.4:** (a) and (c) Simulated transmission spectrum of a microcavity comprising two 21 (7, 11, 15) layer DBRs and a  $\lambda/2$  cavity layer at a design wavelength of 630 nm. A sharp cavity mode arises in the center of the photonic stopband, exhibiting quality factors of  $Q \approx 8000$  (21 layers),  $Q \approx 1200$  (15 layers),  $Q \approx 260$  (11 layers),  $Q \approx 50$  (7 layers). (b) and (d) Simulated reflection spectra of the microcavities.

linewidth  $\Delta\lambda_C$  of the resonant mode in the cavity:

$$Q = 2\pi \times \frac{\text{\# of Oscillations}}{\text{until decay}} = \frac{\omega_C \epsilon}{-d\epsilon/dt} = \frac{\omega_C \tau_{RT}}{L} = \frac{\omega_C}{\Delta\omega_C} \approx \frac{\lambda_C}{\Delta\lambda_C} \quad , \quad (2.61)$$

with  $\epsilon$  the energy stored in the cavity, the power dissipation  $d\epsilon/dt$ , the round-trip time  $\tau_{RT}$ , the fractional power loss per round trip  $L$ , and the resonance frequency  $\omega_C = 2\pi c/\lambda_C$ . All these relations are equivalent definitions of the  $Q$ -factor.

Microcavities with high quality dielectric mirrors can reach  $Q$ -factors in the range of  $10^4$ . For the organic laser systems in this work, typical  $Q$ -factors are in the range of  $10^2 \dots 7 \cdot 10^3$ , while in all-metal cavities, values of  $10^1 \dots 2 \cdot 10^2$  are obtained. In Figure 2.4, a different number of DBR layers and thus a different reflectivity leads to a drastic change in quality factor, from below 100 (7 mirror layers) to several thousand ( $>15$  mirror layers).

## Spontaneous Emission Enhancement

Microcavities enable strong enhancement of resonant wavelengths by suppressing non-resonant modes and thus decreasing the total mode number in the system. When putting an emitting dipole into such a system, it feels the enhanced field, leading to a strong interaction of both and an enhancement of spontaneous emission at the resonant wavelength. In 1946, Purcell (EDWARD PURCELL<sup>14</sup>) described the "Enhanced Spontaneous Emission Probabilities at Radio Frequencies" [76], detailing this interaction and describing the Purcell factor comparing the spontaneous emis-

<sup>14</sup>Edward Mills Purcell, 1912-1997, American physicist, awarded the Nobel Prize in 1952 for the discovery of the nuclear magnetic resonance, leading also to his discovery of the Purcell effect.

sion rate in free space  $\Gamma_f$  to that in a resonant cavity  $\Gamma_C$ :

$$F_P = \frac{\Gamma_C}{\Gamma_f} = \frac{3\lambda_C^3 Q}{4\pi^2 n_C^3 V_{\text{eff}}} \quad , \quad (2.62)$$

where  $V_{\text{eff}}$  is the effective mode volume of the resonant mode. Following this equation, the ratio  $Q/V_{\text{eff}}$  becomes especially important to improve microcavity performance. However, this is not trivial to achieve, as a reduction in mode volume, e.g. by laterally confining photons in addition to the vertical confinement, sets limitations on the  $Q$  factor that can be reached. The Purcell effect enhances the performance of microcavity lasers by spectrally redistributing emission and thus helps to increase important laser characteristics, enabling ultra-low nonlinear thresholds.

### 2.2.4 Microcavity Dispersion

In a microcavity, photons are confined in vertical direction between highly reflecting mirrors, strongly altering their dispersion behaviour. The emission of the excited cavity layer with a thickness  $d_C$  propagates in (growth-)  $z$ -direction with a resonant wavevector  $k_z = \pi/(n_C d_C)$  and can propagate at an oblique angle  $\vartheta$  with a longitudinal wavevector  $k_{\parallel}$ . Such a microcavity then exhibits a parabola-like dispersion  $E(k_{\parallel})$  in agreement to the Fabry Pèrot resonator discussed above:

$$E(k_{\parallel}) = \hbar c_0 |\vec{k}| = \hbar c_0 \sqrt{k_z^2 + k_{\parallel}^2} = \hbar c_0 \sqrt{\left(\frac{\pi}{n_C d_C}\right)^2 + k_{\parallel}^2} \approx \frac{\hbar c_0 \pi}{n_C d_C} + \frac{\hbar c_0 d_C}{2\pi n_C} k_{\parallel}^2 \quad . \quad (2.63)$$

Here, the fundamental mode energy - or the apex of the parabola - is given by the energy  $E(0) = \hbar c_0 \pi / (n_C d_C)$ , while for higher  $k_{\parallel}$  the energy increases and the wavelength decreases, correspondingly. The parallel component can be more readily accessed by the outcoupling angle of the microcavity:  $\sin \vartheta = k_{\parallel} / k_z = k_{\parallel} n_C d_C / \pi$ . The dispersion relation of such a microcavity is depicted in Figure 2.5 (a).

The discussion of the microcavity dispersion in this case is made under the assumption that the field always has a node at the cavity-mirror interfaces. However, under real circumstances this is not always the case. The two main influences that change this condition are the behaviour of the phase at the interface and the penetration of light into the mirrors. As detailed in Section 2.1.3, the introduction of conductive, and thus absorptive, media introduces a phase shift of light upon reflection and thus alter the resonance condition of the microcavity drastically. Depending on the thickness of the absorptive mirror, and thus on the phase shift, the mode position shifts accordingly, e.g. metal cavities exhibit a blueshift of the resonance for increasing mirror thickness (not to confuse with the redshift of metal compared to DBR mirrors). Here, an effective cavity

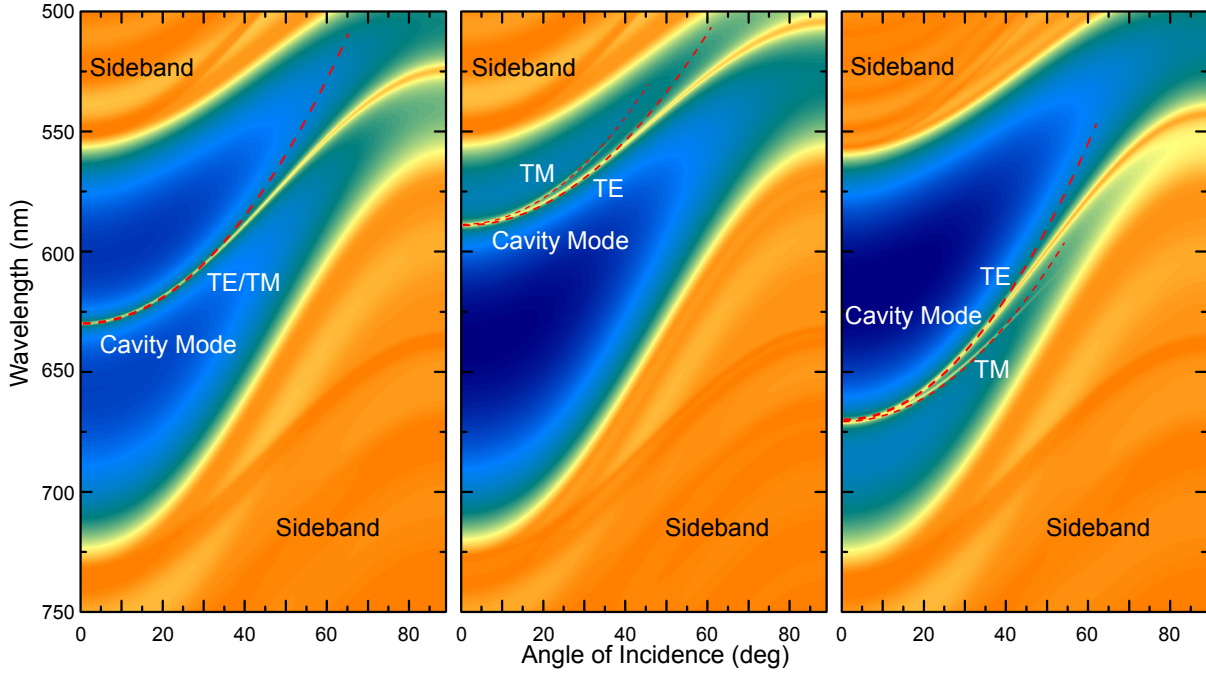


**Figure 2.5:** Calculated angle-resolved transmission spectra of microcavities with  $\text{SiO}_2\text{-TiO}_2$  DBRs and cavity layers of thicknesses  $\lambda/2$  (a),  $3\lambda/8$  (b), and  $5\lambda/8$  (c). While the  $\lambda/2$ -cavity in (a) exhibits a single narrow cavity mode comprising both polarisations, the positively (b) and negatively (c) detuned cavities show broadening of the cavity mode and splitting into TE and TM polarisations. The sign of TE-TM splitting changes going from positive to negative detuning. Dashed red lines show parabolic approximations, valid for angles up to  $\approx 45^\circ$ .

thickness can be determined, taking into account the effectively increased cavity thickness:

$$d_{\text{C,eff}} = d_{\text{C}} + \frac{|\delta_{\text{L}}^r|d_{\text{C}}}{\pi} + \frac{|\delta_{\text{R}}^r|d_{\text{C}}}{\pi} , \quad (2.64)$$

with  $\delta_{\text{L,R}}^r$  the phase change (in radians) at the left/right interface of the cavity. To preserve the spectral position of the cavity resonance in metal cavities, the actual cavity thickness thus has to be reduced compared to the dielectric case. In the case of a combination of thin metal films with dielectric mirrors, additional interaction leads to the formation of a Tamm-plasmon-polariton state which will be discussed in detail in the following section.

The second influence towards the microcavity resonance is the penetration of light into the neighbouring mirrors. While in perfect microcavities ( $\lambda_{\text{C}} = \lambda_{\text{D}}$ ), the field exhibits always a node at the interfaces of the active layer and the DBRs and the calculation (2.63) is valid, a detuning of the cavity resonance in respect to the DBR design wavelength (i.e.  $\lambda_{\text{C}} \neq \lambda_{\text{D}}$ ) leads to a penetration of light into the first dielectric layers. The resonance energy  $E_{\text{eff,TE/TM}}$  has to be

modified [5, 77]:

$$E_{\text{eff,TE/TM}} = \hbar \frac{d_C \omega_C + d_{\text{DBR}}^{\text{TE/TM}} \omega_D}{d_C + d_{\text{DBR}}^{\text{TE/TM}}} , \quad (2.65)$$

with the polarisation-dependent penetration depth of light into the DBRs  $d_{\text{DBR}}^{\text{TE/TM}}$  and the DBR design frequency  $\omega_D = 2\pi c/\lambda_D$ . By expanding the transfer-matrix of this system, the expression for the penetration depths can be found for the system  $n_1 > n_2$  [77, 78, 79]:

$$\begin{aligned} d_{\text{DBR}}^{\text{TE}}(\vartheta) &= \frac{2}{n_1^2 - n_2^2} (n_1^2 d_{n_1} \cos^2 \vartheta_1 + n_2^2 d_{n_2} \cos^2 \vartheta_2) \\ d_{\text{DBR}}^{\text{TM}}(\vartheta) &= \frac{2 \cos^2 \vartheta_1 \cos^2 \vartheta_2 (n_1^2 d_{n_1} + n_2^2 d_{n_2})}{\cos^2 \vartheta_C (n_1^2 \cos^2 \vartheta_2 - n_2^2 \cos^2 \vartheta_1)} , \end{aligned} \quad (2.66)$$

with the DBR layer thicknesses  $d_{n_i}$ , and  $\vartheta_i$  the angle inside a DBR layer of refractive index  $n_i$ . As the penetration depth is dependent on the polarisation of light, this leads to a pronounced polarisation splitting of resonator modes in detuned cavities at higher observation angles. If the optical layer thicknesses  $n_1 d_{n_1}$ ,  $n_2 d_{n_2}$  of either DBR material differ from the ideal case of  $\lambda_D/4$ , the DBR design frequency also has to be parametrised:

$$\begin{aligned} \omega_D^{\text{TE}}(\vartheta) &= \frac{\pi c_0 (n_1 \cos \vartheta_1 + n_2 \cos \vartheta_2)}{n_1^2 d_{n_1} \cos^2 \vartheta_1 + n_2^2 d_{n_2} \cos^2 \vartheta_2} \\ \omega_D^{\text{TM}}(\vartheta) &= \frac{\pi c_0 (n_1 \cos \vartheta_2 + n_2 \cos \vartheta_1)}{2(n_1^2 d_{n_1} + n_2^2 d_{n_2}) \cos \vartheta_1 \cos \vartheta_2} . \end{aligned} \quad (2.67)$$

Figure 2.5 (b) and (c) shows the dispersion for cavities with different detuning towards their optimal conditions. While for positive detuning (b), the TM polarised resonance lies energetically higher than the TE polarised one, the splitting changes sign for negative detuning (c). As in both cases the resonance is shifted away from the stop band center, a reduction of  $Q$ -factor is observed in detuned cavities. Figure 2.6 (a)-(d) shows the distribution of electric field inside various cavities. Only for perfectly tuned DBR microcavities (at  $\lambda_C = 630$  nm) do the field nodes coincide with the interface between cavity and adjacent DBR layers. While for positively detuned cavities, the field penetrates the DBR layers, for negative detuning (b) the field nodes lie inside the cavity. Both cases lead to a spectral shift of the resonance (e.g. in (b) to 676 nm) and polarisation splitting. The inclusion of absorptive mirrors such as 100 nm Ag leads to a phase shift at the cavity-mirror interface as can be seen in (c) and (d) for full and half metal cavities. Here, the field at the interface starts at an uneven phase and the imaginary field nodes lie far outside the cavity. The inclusion of metal typically causes a significant red-shift and cavity thicknesses have to be adjusted to preserve the spectral position of the resonance. Fig. 2.6 (e) and (f) show the inclusion of a thin metal layer inside of a two-DBR microcavity, leading to the

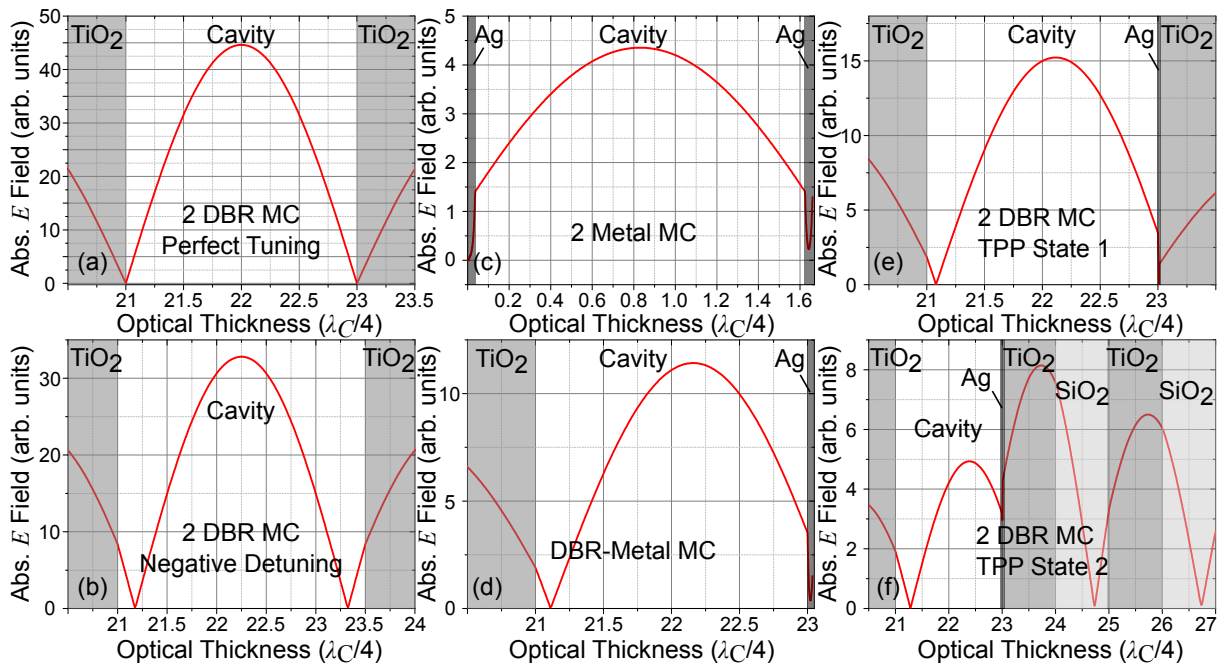


**Figure 2.6:** Field distribution in the cavity layer for different types of MC. (a) Perfectly tuned MC with two DBRs. Field nodes are located exactly at cavity-mirror interface. (b) Negatively detuned MC with two DBRs. Increased thickness of the cavity red-shifts the resonance. Field nodes are located inside the cavity layer. For positive detuning, field nodes lie in the DBR layers. (c) Two metal mirror cavity ( $2 \times 100$  nm Ag). Phase shift at metal-cavity interface leads to strong red-shift of resonance. Imaginary field nodes lie far outside the cavity and thus the resonant mode is red-shifted. (d) DBR-Metal MC. The field node at DBR side lies inside the cavity, while the imaginary node at metal side is outside the cavity. (e) and (f) Two-DBR MC with added 30 nm silver layer. Both TPP states exhibit phase shifts at the interface to the metal layer.

formation of two Tamm-plasmon-polariton states. Also here, phase shifts at the metal interfaces occur.

### 2.2.5 Metal-Organic Microcavities: The Tamm-Plasmon-Polariton State

Introducing thin absorptive layers such as metals into a DBR-based microcavity leads to a fundamental change of the cavity behaviour, described as the formation of Tamm-plasmon-polariton (TPP) states [42, 80, 81]. As detailed in Section 2.1.3, the high absorption and vanishing optical thickness of the metal (e.g.  $n_{\text{Ag}} \approx 0.1$ ) induce a change of phase of light at the interface to the adjacent layers and two coupled modes are generated, the TPP state 1, which resides mainly in the cavity layer still, and the TPP state 2, which resides in the first high refractive index layer of the DBR next to the metal[42]. Both of these states are red-shifted compared to the original

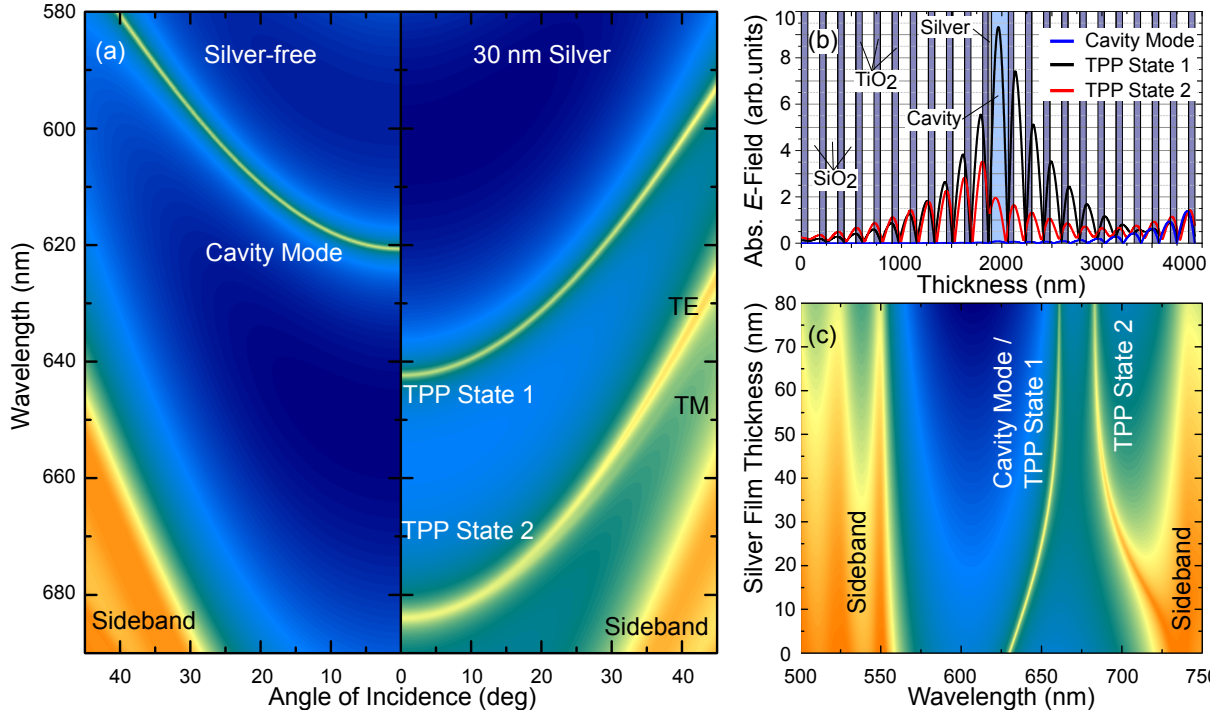


**Figure 2.7:** (a) Dispersion of a microcavity with and without an additional 30 nm silver layer. On the right, parabolic Tamm-plasmon-polariton (TPP) states appear, red-shifted compared to the original cavity mode. TPP state 2 exhibits a pronounced polarisation splitting due to its detuning from the DBR design wavelength. (b) Electric field distribution in a microcavity with 30 nm of silver next to the cavity layer. The original cavity mode (620 nm) is not resonant, while two TPP states (642 nm and 685 nm) emerge on either side of the metal film. (c) Change of microcavity transmission for increasing silver thickness. TPP state 1 stems from the red-shifted original cavity resonance, while TPP state 2 emerges from the red sideband of the DBR.

cavity mode. The distribution of the electric field can be calculated using the transfer matrix method and is depicted in Figure 2.7 (b) (and for the cavity layer in Fig. 2.6 (e) and (f)).

Calculating the spectral position of modes in such a metal-DBR cavity requires solving the coupled resonator equation [82]:

$$-\frac{t^2}{r^2} = (1 - (r_{\text{DBR,A}} r e^{2i\phi_{\text{DBR,A}}})^{-1})(1 - (r_{\text{DBR,C}} r e^{2i\phi_{\text{DBR,C}}})^{-1}), \quad (2.68)$$

where  $r$  and  $t$  are the reflection and transmission coefficients of the metal layer,  $r_{\text{DBR,A}}$  and  $r_{\text{DBR,C}}$  the reflection coefficients of the adjacent DBRs on the side facing away from (A) and towards (C) the active layer.  $\phi_{\text{DBR,A}}$  and  $\phi_{\text{DBR,C}}$  represent the phases of propagation through the adjacent layers, respectively. A full calculation of these properties can be found at Brückner et al. in [82]. The mode positions can then be determined analytically by a transfer matrix algorithm, while for

practical purposes a numerically solved algorithm including all microcavity layers is used. Of interest is the polarisation splitting that also occurs here, similarly to Equation (2.65) for similar detuning of modes, due to the polarization-dependent reflectivities of the DBRs.

The effect of introducing a thin silver film of 30 nm thickness into an organic microcavity is shown in Figure 2.7 (a). The original cavity mode at 620 nm redshifts and splits up into two TPP states 1 (642 nm) and 2 (684 nm). The states still follow a parabolic dispersion as in the case of metal-free cavities. Similarly to detuned cavities, polarisation splitting becomes clearly visible for TPP state 2. Furthermore, the behaviour of resonant modes for increasing silver thicknesses can be understood from Fig. 2.7 (c), where the origins of the TPP states become clear. While TPP state 1 shifts from the position of the original cavity mode to the red, TPP state 2 emerges from the red side band of the DBR and shifts towards the blue. At thicknesses  $>50$  nm, the resonances decouple and preserve their spectral distance [42].

Here, we are interested in the TPP 1 state, which resides mainly in the active layer and enables a strong interaction with the active material. Although the TPP states are strongly influenced by the metal layer, this state still exhibits a considerably high quality factor for thin silver films, profiting from the high quality DBR behind. Utilizing this property, lasing from Tamm plasmon polariton states has been recently demonstrated in inorganic [83] and organic [84] microcavities. The strong interaction of cavity photons and metal plasmons and the resulting large spectral shift for very thin silver films further opens up the possibility to structure the cavity dispersion laterally by patterning the silver film.

### 2.2.6 Multi-Dimensional Photonic Confinement

Confining light in  $z$ -direction inside of a microcavity strongly affects its dispersion, going from the typical linear dispersion  $E(k) = \hbar ck$  to the parabolic dispersion observed in the preceding sections. Consequently, even further manipulation can be achieved by trapping photons in more dimensions.

Typically, such confinement is reached by laterally etched MCs into micron-size photonic wires [85, 86] or micropillars [87, 88], leading to an additional trapping of modes inside of the device and thus facilitating reduced mode volumes or ultra-high quality factors [89] as well as the ability to control the modes in lateral direction. Other types of structuring include the deposition of metal stripes on top of the full microcavity stack [90] or the use of surface acoustic waves [91, 92]. Photonic boxes [3, 45, 93, 94] and wires [1, 4, 5, 6, 95], and arrays of these are investigated regarding their confining properties and exhibit more complex mode dispersions.

Interestingly, large coherence lengths in microcavity systems allow the investigation of the formation of photonic bands in various photonic crystal structures patterned into the device.

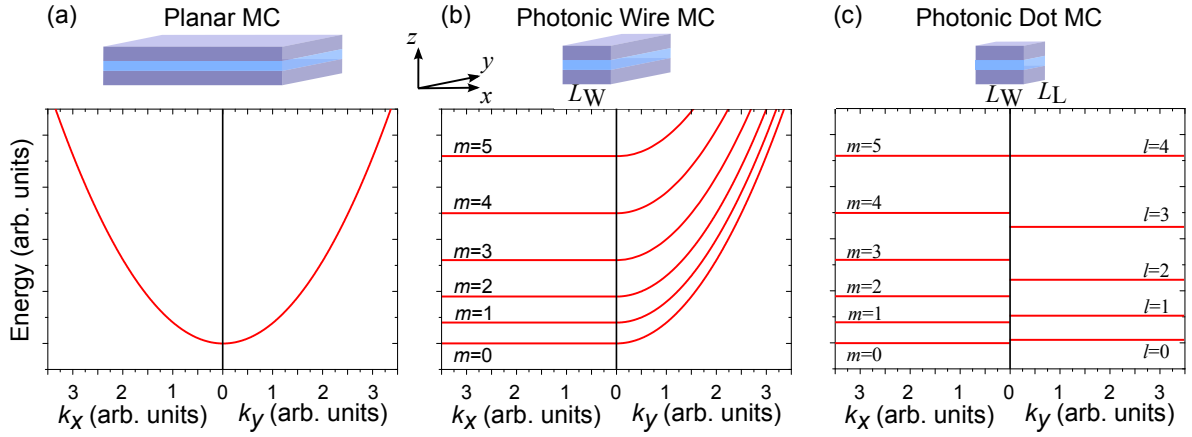


**Figure 2.8:** In-plane dispersion of microcavities with multi-dimensional confinement. (a) 1D-confined microcavity with infinite extension in  $x$ - and  $y$ -direction showing isotropic parabolic dispersion. (b) Photonic wire microcavity with infinite extension in  $y$ -direction, confined in  $x$ -direction to  $x = L_W$ . Due to the 2D confinement, the momentum in  $x$ -direction is discretised according to  $k_x = q_m$  with mode number  $m$ . (c) Photonic dot microcavity, confined in  $x$ -direction to  $L_W$  and in  $y$ -direction to  $L_L$ . In full 3D confinement, both in-plane wavenumbers are confined to  $k_x = q_m$ ,  $k_y = p_l$ .

Periodic photonic wires[96] are investigated as well as square-[56, 97, 98] or hexagonal[99] lattices leading to clear band structures as commonly observed in solid-state physics. Typically, a weak modulation of the cavity facilitates the formation of extended bands, while deep potentials lead to mode localization and confinement in lateral direction. Both types will be studied in detail in the course of this work.

The confining properties of singular wires and dots lead to differing dispersion properties as depicted in Figure 2.8 for 1D, 2D, and full 3D photon confinement.

### Photonic Wires

While the confinement in  $z$ -direction traps photons in two dimensions and leads to an isotropic dispersion paraboloid, the creation of photonic wires and thus the reduction to a one-dimensional system leads to an anisotropy of the system, splitting the parallel  $k$ -component. Let the wires be aligned along the  $y$ -direction, leading to a confinement in  $x$ -direction and consequently a discretisation of those states, as standing waves form in the confined region. The dispersion in photonic wires of width  $L_W$  and thickness  $d_W$  then changes to [45]:

$$E_m(k_y) = \hbar c_0 |\vec{k}| = \hbar c_0 \sqrt{k_z^2 + k_x^2 + k_y^2} = \hbar c_0 \sqrt{\left(\frac{\pi}{n_C d_C}\right)^2 + \left(\frac{\pi(m+1)}{n_C L_W}\right)^2 + k_y^2}, \quad (2.69)$$



where the index  $m$  describes the index of discrete states from ground ( $m = 0$ ) towards higher excited states, exhibiting  $m + 1$  antinodes of the standing wave. In  $y$ -direction, the photons propagate unhindered and thus still a parabolic dispersion is observed regarding  $k_y$ , following the same arguments as Section 2.2.3. Again, a full analysis includes also the penetration of light into DBR layers, as discussed in Equation (2.65).

The spatial field distribution  $F(x)$  can now be expressed as standing waves with discrete wavenumbers  $q_m = \pi(m + 1)/(n_C L_W)$ :

$$F(x) \propto \cos(q_m x) \quad \text{or} \quad \sin(q_m x) \quad , \quad (2.70)$$

for symmetric (cos) and asymmetric (sin) modes. Subsequently, the angular distribution of the emission intensity  $I_m(k_x)$  can be obtained by the Fourier transformation of the spatial distribution [48]:

$$I_m(k_x) \propto \cos^2\left(\frac{L_W k_x}{2} - \frac{m\pi}{2}\right) \cdot \frac{q_m^2}{(q_m^2 - k_x^2)^2} \quad . \quad (2.71)$$

Figure 2.8 (b) shows the dispersion in both  $k_x$  and  $k_y$  directions, comparing the unconfined, continuous parabolic dispersion along the wire to the discretised flat dispersion of standing waves perpendicular to the wire orientation.

## Photonic Dots

Structuring the dispersion further consequently requires the reduction of dimensionality to a fully three-dimensionally confined photonic dot. Possible geometries include circular and elliptic dots, leading to the formation of Mathieu-modes [3, 100] with radial and angular mode numbers, which will be detailed in Chapter 5. Here, the simplified case of a rectangular photonic box of width  $L_W$  and length  $L_L$  shall be briefly discussed. Naturally, the full confinement leads to a discretisation in both parallel directions with discrete wavenumbers  $q_m = \pi(m + 1)/(n_C L_W)$  and  $p_l = \pi(l + 1)/(n_C L_L)$ [48]:

$$E_{ml} = \hbar c_0 |\vec{k}| = \hbar c_0 \sqrt{k_z^2 + k_x^2 + k_y^2} = \hbar c_0 \sqrt{\left(\frac{\pi}{n_C d_C}\right)^2 + \left(\frac{\pi(m + 1)}{n_C L_W}\right)^2 + \left(\frac{\pi(l + 1)}{n_C L_L}\right)^2} \quad , \quad (2.72)$$

with integer mode numbers  $m$  in  $k_x$ -direction and  $l$  in  $k_y$ -direction. Figure 2.8 (c) shows the discrete dispersion in both directions, where for differing dimensions of the box ( $L_W \neq L_L$ ), different intermode spacing is observed.

### 2.2.7 Basics of Laser Operation

The basic principle of the laser is based on the interaction of strong light fields with active luminescent media exhibiting two or more energy levels. The name-giving principle<sup>15</sup> of stimulated emission directly couples the external light field to the internal energy distribution of the medium, where typically excited electrons, electron-hole plasmas, or bound excitons can be stimulated to annihilate under emission of photons showing the same frequency, directionality, polarisation, and phase as the initial stimulator. A basic laser consists of this active medium inside of an optical resonator, providing the optical feedback necessary for stimulated emission to completely take over. The active medium needs to be pumped in order to supply the necessary amount of excited states, typically by optical or electrical excitation. A multitude of laser media are in use and application, starting from mixtures of gases (e.g. He-Ne laser, CO<sub>2</sub> laser [101]), liquids (e.g. dye-lasers [102]), solid state materials (e.g. doped alumina crystals such as Ti:Sa [103]) to semiconducting materials (e.g. GaAs microcavities [104]) and more exotic systems such as biological (e.g. single cell laser [21]) and organic emitters.

#### Basic Processes in Active Media

In active media, three fundamental processes influence the distribution of unexcited and excited states and transitions between them, as depicted in Figure 2.9 (a)-(c). Considering a two-level system of a ground state ( $E_G$ ) filled with electrons (population number  $N_G$ ) and an empty excited state ( $E_E$ ,  $N_E$ ), the absorption of light with a frequency  $\hbar\omega_0 = E_E - E_G$  allows an electron to populate the excited state. This transition is described by the Einstein coefficient (A. EINSTEIN<sup>16</sup>)  $B_{\text{Abs}}$ :

$$\left(\frac{dN_G}{dt}\right) = -\left(\frac{dN_E}{dt}\right) = -B_{\text{Abs}}N_G \cdot \rho_\omega(\omega_0) \quad , \quad (2.73)$$

where  $\rho_\omega(\omega_0)$  is the radiation density of the surrounding field at  $\omega_0$ . An excited electron is able to spontaneously decay to the ground state under the emission of a photon of  $\omega_0$  after the mean decay time  $\tau_{\text{Sp}}$ , described by the Einstein coefficient  $A_{\text{Sp}} = 1/\tau_{\text{Sp}}$ :

$$\left(\frac{dN_E}{dt}\right) = -\left(\frac{dN_E}{dt}\right) = -A_{\text{Sp}}N_E \quad . \quad (2.74)$$

Here, the surrounding field does not influence the transition. An alternative way for an excited electron to decay is provided, if a photon of  $\omega_0$  can stimulate the transition before spontaneous emission occurs. Here, the photon emitted by this stimulated transition is an exact copy of the

<sup>15</sup>LASER - light amplification by stimulated emission of radiation

<sup>16</sup>Albert Einstein, 1879-1955, German theoretical physicist, revolutionized many fields of physics. Among his many achievements is the first description of stimulated emission in “Quantentheorie der Strahlung”[18].

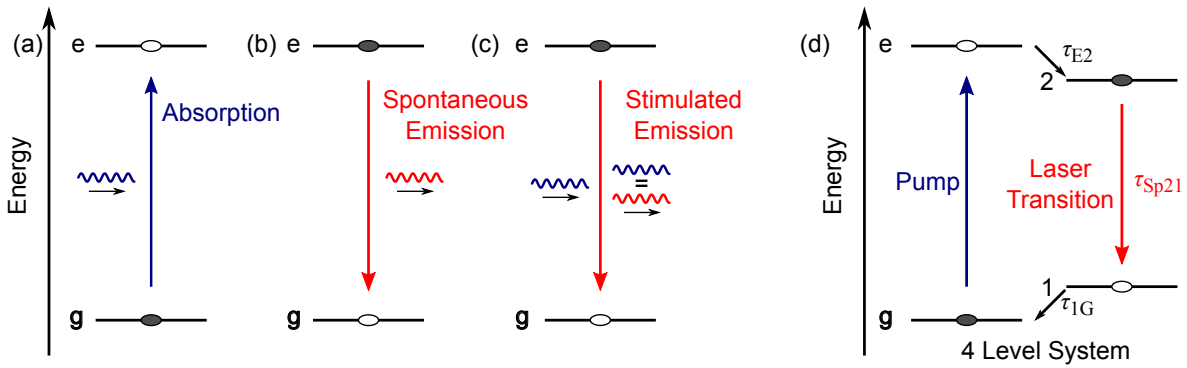


**Figure 2.9:** Energy level schemes for physical processes in active media. (a) Absorption of a photon promotes an electron to the excited state. (b) Spontaneous decay of an excited electron to the ground state under emission of a photon  $\hbar\omega = E_E - E_G$ . (c) Photon stimulates an excited electron to decay under emission of a second, similar, photon. (d) Schematic energy scheme of a 4-level laser system, where  $\tau_{Sp21} \gg \tau_{1G}, \tau_{E2}$ .

initial photon. The transition is described by the Einstein coefficient  $B_{St}$ :

$$\left(\frac{dN_E}{dt}\right) = -\left(\frac{dN_E}{dt}\right) = B_{St}N_E\rho_\omega(\omega_0) \quad . \quad (2.75)$$

Einstein showed that in thermodynamic equilibrium, where Boltzmann's law (L. BOLTZMANN<sup>17</sup>) for the distribution of excited electrons is valid, the coefficients relate to one another and especially  $B_{Abs} = B_{St}$ . In order for stimulated emission to dominate the system, as is wanted for laser operation, the system therefore has to be inverted, i.e. the population of the excited state has to surpass the population of the ground state. In equilibrium however, Boltzmann statistics describe the population of a two level system as:

$$\frac{N_E}{N_G} = \exp\left(-\frac{\hbar\omega_0}{k_B T}\right) \leq 1 \quad , \quad (2.76)$$

with Boltzmann's constant  $k_B$  and the temperature  $T$ . In a two level system in thermal equilibrium, population inversion can thus never occur even for infinite temperatures. For real laser operation, one either has to leave the equilibrium or utilize systems with further energy levels, the example of the 4 level system shall be given here.

### The 4 Level System

One of the most commonly employed systems in laser operation is the 4 level system which, in addition to ground and excited state has two intermediate levels ( $N_2$  and  $N_1$ ) between which the

<sup>17</sup>Ludwig Eduard Boltzmann, 1844-1906, Austrian physicist, laid the groundwork for statistical mechanics.

laser transition occurs. Figure 2.9 (d) schematically shows the energy scheme. This way, the pumping mechanism from  $E_G$  to  $E_E$  is separated from the actual laser transition. Desirable are fast decay rates  $\tau_{E2}$  and  $\tau_{IG}$ , populating the upper laser level from the excited state and quickly depopulating the lower laser level to the ground state. This way, population inversion  $N_2 > N_1$  is reached much more easily and re-absorption of emitted photons is minimised. However, intrinsic loss is introduced in this system as the transitions to and from the laser levels can not be harnessed - in certain lasers (e.g. the HeNe-laser) this constitutes a major part of energy loss in the system.

The interaction between laser field and active 4 level system can be described by the rate equations:

$$\begin{aligned}\frac{\partial n_2}{\partial t} &= R_P - \frac{\sigma c q n_2}{V} - \frac{n_2}{\tau_{Sp21}} \\ \frac{\partial q}{\partial t} &= \frac{\sigma c}{V}(q+1)n_2 - \frac{q}{\tau_\gamma} \quad ,\end{aligned}\quad (2.77)$$

where  $n_2$  is the population density of the upper laser level,  $q$  is the photon density in the system,  $\sigma$  is the stimulated emission cross section, and  $\tau_\gamma$  is the photon decay rate, describing optical losses in the cavity. Plotting this behaviour in Figure 2.10 (a), we see the emergence of two linear regimes, where the output intensity increases linearly with the input intensity in the spontaneous emission regime at first, before a strongly non-linear transition to the stimulated emission regime, where again a linear behaviour is observed. The input power necessary to reach this stimulated emission regime is denoted as the lasing threshold of the system. Here, the external electric field is intense enough that photons stimulate the energy transition faster than spontaneous emission can occur and thus almost all emission from excited states contributes to the laser mode. The resulting emission shows all properties of stimulated emission, such as monochromaticity, directionality, polarisation, and coherence.

### Input-Output Behaviour of Microcavity Lasers

The input-output behaviour of a lasing 4 level system behaves differently if put into a microcavity. A direct interaction between the optical cavity and the active medium leads to enhancing effects such as the Purcell effect (see above) and increases spontaneous emission of light into the laser mode as opposed to other modes in the system. The rate equations are modified to [105, 106, 107]:

$$\begin{aligned}\frac{\partial n_2}{\partial t} &= R_P - (1 - \beta)\Gamma_I n_2 - \beta\Gamma_C q n_2 - \Gamma n_2 \\ \frac{\partial q}{\partial t} &= \beta\Gamma_C(q+1)n_2 - \frac{q}{\tau_\gamma} \quad ,\end{aligned}\quad (2.78)$$

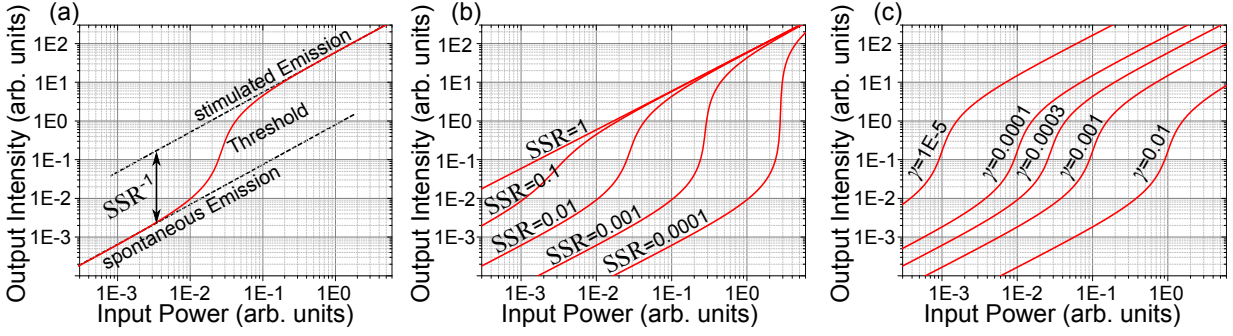


**Figure 2.10:** (a) Input-output characteristics of a microcavity laser for  $SSR = 0.01$  and  $\gamma = 0.0003$ . After a linear increase of the spontaneous emission intensity, a strong nonlinear increase of output intensity occurs at the threshold, followed by again a linear increase of stimulated emission intensity. Dashed lines with slope 1 are guides to the eye. (b) Input-output characteristics for  $\gamma = 0.0003$  and varying  $SSR$ . With increasing  $SSR$ , the threshold decreases drastically. When no non-radiative losses are present,  $SSR = \beta$ . (c) Input-output characteristics for  $SSR = 0.01$  and varying  $\gamma$ . For decreasing  $\gamma$ , losses in the system decrease, leading to a decrease in threshold and an increase in output intensity. The stimulated emission threshold follows  $P_{\text{thr}} \propto \gamma/SSR$ .

where  $\Gamma_f$  is the emission into free space,  $\Gamma_C = \Gamma_f \cdot F_P$  is the spontaneous emission into the cavity mode,  $\Gamma$  is the non-radiative loss of population, and  $\beta = \Gamma_C/\Gamma_{\text{Tot}}$  is the spontaneous emission coupling factor, the ratio of emission into the laser mode to the sum of emission into all modes. In practice, it becomes obvious, that the lasing threshold of the system strongly depends on the factor  $\beta$ , to the point that a "thresholdless" laser may be obtained, if  $\beta$  reaches unity [108]. In small mode volume microcavities, a finite number of exciteable emitters furthermore modifies the rate equations, as the pumping of an absorbing level  $n_g$  to  $n_e$  has to be taken into account. Resulting from this effect, the laser emission saturates above the threshold, when all absorbers in the system are excited [105].

While these rate equations describe a 4 level microcavity system very well, the situation becomes more difficult, when significant non-radiative losses are present. Here, the  $\beta$  factor can no longer be directly obtained from the fit of the rate equation model to the experimentally measured input-output behaviour. Such losses are often introduced by absorptive layers such as metals and therefore make an quantified analysis of the rate equation difficult. To fit experimental data, the empirical formula [3, 107]:

$$\tilde{q} = (2\gamma)^{-1} \left[ P - \frac{\gamma}{SSR} + \sqrt{\left( P - \frac{\gamma}{SSR} \right)^2 + 4\gamma P} \right] \quad (2.79)$$

is used. Here,  $\tilde{q}$  and  $P$  are dimensionless parameters corresponding to the output and input intensity, respectively. The cavity decay rate, including all losses, is denoted by  $\gamma$ , while  $SSR$

denotes the spontaneous-to-stimulated emission ratio, which can be obtained from the distance between linear fits to the spontaneous and stimulated emission regimes in the double-logarithmic input-output plot.

In the ideal case without non-radiative losses, the SSR approaches the  $\beta$ -factor. In the presence of non-radiative losses however,  $\beta$  becomes more insensitive to the lasing threshold and cannot directly be obtained from the relation between spontaneous and stimulated emission intensity. Such a laser may even show threshold behaviour for  $\beta = 1$  [109]. Since for our system, it is not possible to easily quantify the additional absorption, we can not directly extract  $\beta$ . The lasing threshold is mainly dependent on this ratio, as well as the cavity photon lifetime  $1/\gamma$ , in the way that the threshold pump intensity  $P_{\text{thr}} \propto \gamma/\text{SSR}$ . This dependence is depicted in Figure 2.10 (b) and (c), where both parameters are varied over several orders of magnitude. While increasing the SSR shifts the spontaneous closer to the stimulated emission and thus reduces the threshold, an increase of  $\gamma$  drastically decreases the overall output intensity of the system and in turn increases the threshold power.

## 2.3 Basics of Organic Semiconductors and Devices

*Here, I will introduce the basic principles of organic semiconductors, their composition, and physical properties as well as the working principles of standard organic devices featured in the thesis. I will provide the basis for all active materials and device concepts employed throughout this work.*

*In Section 2.3.1, I start with the general structure of organic materials, their basic properties and energetic and electronic composition and give a special focus on the formation of charge-transfer states in blends of organic materials in Section 2.3.2. Following this, I will introduce organic lasers in Section 2.3.3, detailing the working principle of an active organic material in resonator structures. Finally, in Section 2.3.4, I will feature organic solar cells and organic photodetectors as device concepts.*

### 2.3.1 Organic Small Molecule Semiconductors

The class of organic materials comprises molecules made up of the building blocks carbon (C) and hydrogen (H), where typically other atoms such as nitrogen (N), oxygen (O), sulphur (S) or various metals are added, changing elementary properties. The basic working principle encompasses the energetic setup of the valence electrons in the carbon atoms. Exemplarily, the benzene molecule that is made of a ring of six carbon atoms shows a  $sp^2$ -hybridization of three of the molecular s and p orbitals, which form strong  $\sigma$  bonds between the atoms in the plane.

The free  $p_z$  orbital then lies orthogonal to this plane and can form  $\pi$  bonds with neighbouring atoms. Here, this  $\pi$  system is not localised on a single bond, but instead all orbitals form a conjugated system delocalised over the entire molecule (see Figure 2.11 (a)). The coupling gives rise to the formation of a binding  $\pi$  and an antibinding  $\pi^*$  orbital, which fundamentally influences the optical properties of the molecule. Energetically, the  $\pi$  orbital is the highest occupied level in the system and thus is called highest occupied molecular orbital (HOMO). Consequently, the lowest unoccupied molecular orbital (LUMO) is the antibinding  $\pi^*$  level. The delocalisation of the  $\pi$  orbital gives rise to high polarisability and thus strong interaction with external fields. The energetically small HOMO-LUMO transition (few eV) is in turn exploited to absorb (or emit) light in the visible range, creating charge carriers in the system. Due to weak intermolecular coupling, excited charge carriers stay strongly localised benefiting low dielectric constants in the organic solid, and consequently lead to a Coulomb-interaction between excited electron in the LUMO and leftover hole in the HOMO, forming a bound quasiparticle - the neutral exciton. In contrast to inorganic semiconductors, where large dielectric constants efficiently screen the charge and thus lead to low exciton binding energies ( $\approx 10$  meV) and large exciton radii (larger than the lattice spacing) creating the Wannier-Mott exciton (G. WANNIER, N. MOTT<sup>18</sup>), in organic semiconductors tightly localised (one molecule) and strongly bound (few 100 meV to  $> 1$  eV [110]) Frenkel excitons (Y. FRENKEL<sup>19</sup>) dominate. The high binding energies facilitate excitons also at room-temperature, where inorganic semiconductors typically operate with electron-hole plasmas and exhibit exciton formation under very low temperatures. Furthermore, the strong localisation of the Frenkel exciton gives rise to large oscillator strengths, which together with potentially large photoluminescence quantum yields, make them ideal emitters in a wide range of applications. The large size of organic molecules and involvement of many bound atoms gives rise to a multitude of vibronic modes, with typical separations of few hundred meV. Strong structural disorder in amorphous organic films leads to different polarisation environments and finally causes a wide inhomogeneous broadening of the transition spectra of non-crystalline organic solids.

As the intermolecular van der Waals interaction (J. VAN DER WAALS<sup>20</sup>) in organic solids is weak, comparably low processing temperatures can be utilised for the fabrication of organic devices. Furthermore, very high grades of purity can be achieved by repeated vacuum sublimation, as is necessary for highly efficient devices.

---

<sup>18</sup>Gregory Hugh Wannier, 1911-1983, Swiss physicist and Sir Nevill Francis Mott, 1905-1996, English physicist, known for their work on crystals and semiconductors and excitons therein.

<sup>19</sup>Yakov Il'ich Frenkel, 1894-1952, Soviet physicist, well known for his work in condensed matter physics and discovery of the exciton.

<sup>20</sup>Johannes Diderik van der Waals, 1837-1923, Dutch physicist, most famous for his work of the equation of state for ideal gases and liquids and his contributions to forces between molecules.

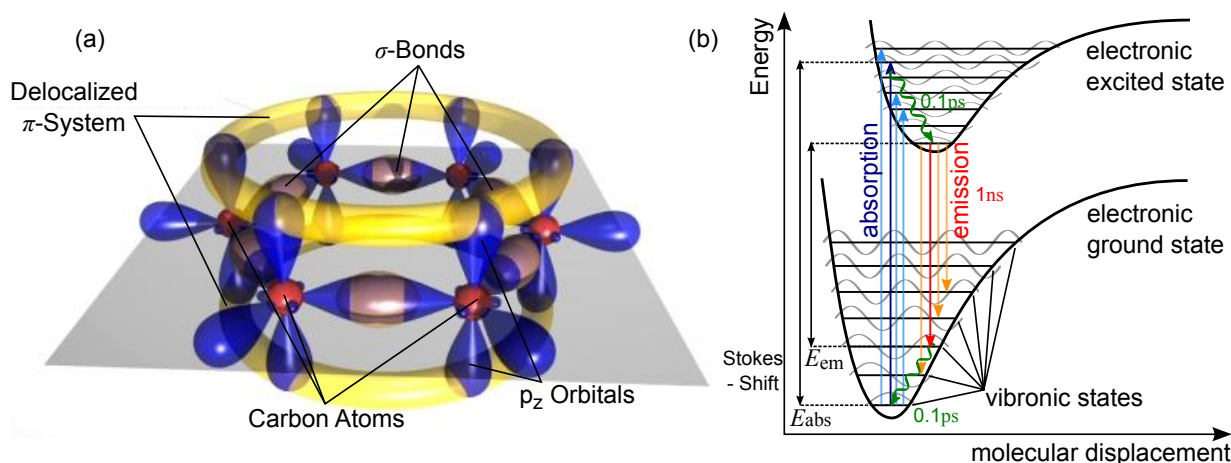


**Figure 2.11:** (a) Illustration of benzene molecule, where the free  $p_z$ -orbitals form a conjugated  $\pi$ -system, delocalised over the molecule. Adapted from [111]. (b) Illustration of the optical transitions in molecules. The Franck-Condon principle demands that optical transitions occur only vertically in the energy-space diagram, giving rise to a Stokes-shift ( $E_{\text{abs}} - E_{\text{em}}$ ) of absorption (blue) and emission (red) after fast nonradiative transitions (green).

### Optical Transitions

The absorption and emission of photons and corresponding electronic transitions leads to a displacement of charges on the molecule and a resulting shift of atomic coordinates. In Born-Oppenheimer approximation however, electronic transitions happen orders of magnitude faster ( $10^{-15}$  s) than vibronic relaxations ( $10^{-13}$  s), and atomic positions can be regarded as constant for the processes of absorption and emission [112]. This Franck-Condon principle is visualised in Figure 2.11 (b), where electronic transitions can occur only vertically in the plot of energy over atomic position. The relaxation of nuclei to the vibronic ground state happens subsequently and is still fast compared to the radiative transition (emission,  $10^{-9}$  s) of electrons from the excited state into the vibronic modes of the ground state. Resulting from this principle is the Stokes-shift, a red-shift of emitted wavelengths compared to absorbed wavelengths. Typically, absorption and emission spectra appear nearly mirrored and can exhibit Stokes shifts ranging from tens to hundreds of nm, aiding laser operation as self-absorption of emitted photons is minimized. The process of absorption - fast vibronic relaxation - slow fluorescence - fast vibronic relaxation to ground state facilitates an ideal intrinsic 4-level system in fluorescent organic thin films.

### Molecular Doping

One of the main drawbacks of organic semiconductors is their low conductivity, going down to values as low as  $10^{-10}$  S/cm (zinc-phtalocyanine in vacuum, [113]). For electrically oper-



ated devices, the charge carrier concentration has to be increased to facilitate efficient transport, typically achieved by molecular n- and p-doping. Similarly to doping of inorganic semiconductors, dopand molecules exhibit energy levels close to the transport levels of the host (n-doping:  $\text{HOMO}_{\text{Dopand}} > \text{LUMO}_{\text{Host}}$ ; p-doping:  $\text{HOMO}_{\text{Host}} > \text{LUMO}_{\text{Dopand}}$ ), facilitating the creation of free charge carriers at room temperature. As very high HOMO levels are required for n-dopands, they easily oxidize under ambient conditions and have to be handled and protected carefully. Utilising molecular doping, the conductivity can be increased by several orders of magnitude to  $10^{-5}$  S/cm...1 S/cm. Compared to inorganic semiconductors, where doping concentrations are typically much lower than 0.01%, doping concentrations for organics lie in the range of one to few tens of percent.

In contrast to electrical doping, different guest molecules can be introduced that predominantly affect the optical properties of the film. A typical example is the inclusion of a highly efficient laser dye in a matrix grid, as will be detailed in Section 2.3.3 or the mixing of electron donor and acceptor in bulk heterojunctions of solar cells. Here, another optical effect becomes visible, as the formation of an intermolecular charge transfer state at the interface between such molecules enables additional optical transitions.

### 2.3.2 Charge-Transfer States in Blends of Organic Semiconductors

In neat layers of organic molecules, excitons are mostly generated by band to band absorption of photons, exciting electrons from the HOMO to the LUMO of the same material. Here, the band gap of the material determines the energy of allowed transitions, i.e. only photons with sufficient energy can be absorbed and generate excitons in the material. In organic solar cells, these excitons diffuse to the interface between donor and acceptor material, where the charge separation takes place. An intermediate state is formed, when the exciton is not located on a single material, but instead comprises the hole on the donor and the electron on the acceptor, forming an intermolecular charge-transfer (CT) state [114, 115]. From there, charge separation takes place as the charges move further away from each other and finally free charge carriers are transported to the electrodes, generating the photocurrent. Here, the CT state still allows an optical transition to the ground state, on the one hand leading to a loss of excitons while on the other hand enabling the direct excitation of CT excitons at the interface. As the band gap between LUMO of the acceptor and HOMO of the donor is smaller than the band gaps of the single materials, energies of the CT state manifold lie lower than typical absorption bands and may extend into the NIR for standard donor:acceptor blends. Consequently, this state can be optically excited by illumination of light in that spectral range, exhibiting low but measurable absorption due to the restriction of CT exciton generation to the interface and low oscillator strengths.

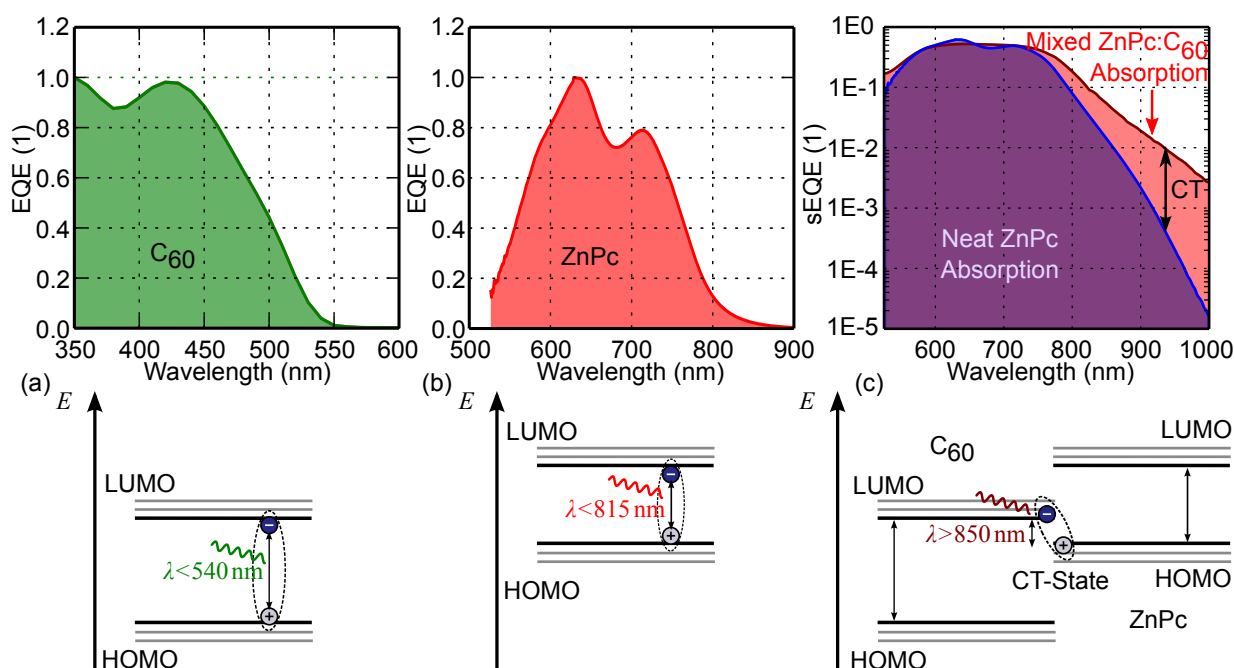


**Figure 2.12:** (a) EQE and energy diagram of a neat layer of  $C_{60}$ . Above the band gap of 540 nm, excitons are generated by band to band absorption of light in the green, blue, and ultraviolet part of the spectrum. (b) EQE and energy diagram of neat ZnPc. Here, the smaller band gap at of 815 nm allows the generation of excitons via band to band absorption peaking in the red part of the visible spectrum. (c) Sensitive EQE spectrum and energy diagram of a blend of  $C_{60}$ :ZnPc at a volume mixing ratio of 1:1. Apart from the contributions of the constituents of the blend, a low energy absorption shoulder arises due to intermolecular charge-transfer state absorption, where excitons are formed at the interfaces between  $C_{60}$  (electron) and ZnPc (hole). Figure adapted from [13].

Compared to direct band to band absorption of organic molecules, the absorption coefficients for CT absorption are up to two orders of magnitude lower and range from  $10^4 \text{ cm}^{-1}$ ... $10^3 \text{ cm}^{-1}$  [115].

### The Charge-Transfer State in the Blend $C_{60}$ :ZnPc

The blend of fullerene ( $C_{60}$ ) as electron acceptor and zinc-phtalocyanine (ZnPc) as electron donor is commonly employed in bulk heterojunction organic solar cells as the complementary absorption spectra of  $C_{60}$  ( $< 540 \text{ nm}$ ,  $E_{\text{Gap}} = 2.3 \text{ eV}$ ) and ZnPc ( $500 \text{ nm}$ ... $815 \text{ nm}$ ,  $E_{\text{Gap}} = 1.5 \text{ eV}$ ) cover the whole visible range and both materials show preferable mixing in the final film. While the neat materials exhibit only their direct band to band absorption and the EQE drops drastically above 815 nm, sensitive EQE measurements [115, 116, 117] reveal the appearance of another broad absorption band reaching far into the NIR when blending both materials by thermal co-evaporation in a volume ratio of 1:1. Here, CT excitons are generated directly at the  $C_{60}$ :ZnPc

interface as the difference  $\text{LUMO}_{\text{C}_{60}} - \text{HOMO}_{\text{ZnPc}}$  is lower than the band gaps of neat layers. Figure 2.12 compares the absorption spectra (recalculated to EQE, see Section 2.3.4) of the neat materials  $\text{C}_{60}$  and ZnPc to the sensitive EQE measured in a ZnPc: $\text{C}_{60}$  bulk heterojunction. Here, for the mixed layer a broad shoulder at low energies ( $>800$  nm) extends above the values for neat materials and shows an additional absorption facilitated by the interaction of both molecules. In correlation to the energy levels of ZnPc and  $\text{C}_{60}$ , their intermolecular CT state energies lie above 850 nm and thus extend into a range typically not covered but very interesting for application.

### 2.3.3 Organic Lasers

Organic semiconductors offer significant advantages for laser operation as the Frenkel excitons in organic semiconductors inherently exhibit large binding energies on the order of few hundred meV to more than 1 eV [110], making them stable under room-temperature conditions and thus facilitating lasing without the formation of an electron-hole plasma as in inorganic semiconductors. There, Wannier-Mott excitons typically offer binding energies below 20 meV and are easily dissociated at room-temperature. Large binding energies furthermore strongly localise the exciton on one molecule, giving rise to large oscillator strengths and susceptibilities  $g$ . Consequently, the  $\beta$  factor is enhanced [107]:

$$\beta = \frac{2g^2}{\gamma_{\parallel}\gamma_{\perp}}, \quad (2.80)$$

where  $\gamma_{\parallel}$  and  $\gamma_{\perp}$  are the longitudinal and transverse relaxation rates of the organic emitters, directly leading to lower lasing thresholds  $P_{\text{Thr}} \propto 1/\beta$ . In addition, the fluorescence spectra are broadened by vibronic transitions, enabling high optical gain in a wide continuous spectral range and allowing tunable lasing from organic molecules [118], in addition to the previously mentioned advantages in fabrication. Consequently, these properties attracted considerable interest in the investigation of organic lasers.

#### State of the Art of Organic Microlasers

Organic dyes have been employed for lasing only a short time [119] after the first report of lasing action in a ruby crystal by Maiman [20] due to their high photoluminescence quantum yield, albeit in liquid form. Here, the formation of long-lived triplet states requires a constant pumping of the solution, bringing unexcited molecules in the focus of the pump spot [120]. However, advantages such as the broad spectrum have made them an important part of research and, among other, make them ideal for ultrashort pulse generation. Despite early interest, it took until the 1990s [38, 39, 40, 41] before a solid state organic laser was realised. Those lasers were and still are optically excited, despite efforts towards electrical pumping. At most, mono-

lithic devices can achieve lasing from an organic microlaser while being optically pumped by an integrated inorganic light emitting diode [121]. Nevertheless, solid state organic lasers show interesting properties and applications such as tunable lasing achieved by changing the resonator [122, 123, 124, 125], the pump spot [118] or the geometry of pumping conditions [6]. In microlaser systems, lasing thresholds can be extremely low [3, 125, 126, 127, 128], especially when taking into account additional confinement. Here, the broad gain spectrum enables fabrication within a certain margin of error, typically not possible in inorganic quantum well or dot lasers, and low threshold lasing over a large spectral range will be presented in Chapter 4.

Organic microlasers are employed for Raman spectroscopy [129], being able to compete with conventional HeNe lasers, in biological systems [22], where they enable the observation and tracking of cell movement, in sensing [130, 131], reacting strongly to the presence of explosives or illegal drugs in air, or for the integration in photonic circuits [132]. Future prospects lie also in short range optical data transfer [133], and current fields of application for solution-based dye lasers, such as spectroscopy and ultrafast investigation, especially due to the possibility of miniaturisation.

Recently, organic media also have been utilised to facilitate strongly coupled systems, where excitons strongly couple to cavity photons, forming a polariton quasiparticle [134, 135, 136, 137] and are able to show Bose-Einstein condensation of such particles even at room-temperature [138, 139, 140].

### **The Host:Guest System Alq<sub>3</sub>:DCM**

In organic microcavity lasers, the host:guest system Alq<sub>3</sub>:DCM is widely employed and has been known for a long time [141, 142, 143]. Here, the matrix molecule Tris-(8-hydroxyquinolino)-aluminium (Alq<sub>3</sub>) is doped by 2 wt% with the laser dye Dicyanomethylene-2-methyl-6-p-dimethylaminostyryl-4H-pyran (DCM) by thermal coevaporation of the molecules under ultra-high vacuum. Both molecular structures can be found in Figure 2.13 (a). The low concentration of guest molecules inhibits their aggregation and luminescence quenching, enabling high photoluminescence quantum efficiencies [144] and large stimulated emission cross sections. The absorption and emission spectra of both molecules are shown in Fig. 2.13 (b). Both molecules exhibit significant Stokes shifts of more than 100 nm. Due to a large overlap of emission from Alq<sub>3</sub> and absorption from DCM, a highly efficient Förster resonant energy transfer (FRET) between both molecules facilitates a direct transfer of excitation from the matrix to the lasing dye. In this system, the Förster radius, i.e. the radius in which the FRET is efficient, lies in the range of  $\approx 30 \text{ \AA}$ , which at typical doping concentrations of around makes this transition preferable (transition rate  $5 \cdot 10^{10} \text{ s}^{-1}$ ) to the direct fluorescence of Alq<sub>3</sub> ( $7 \cdot 10^7 \text{ s}^{-1}$ ). Consequently, upon excitation of the matrix around 400 nm, almost all energy is transferred to the DCM [145]. Al-

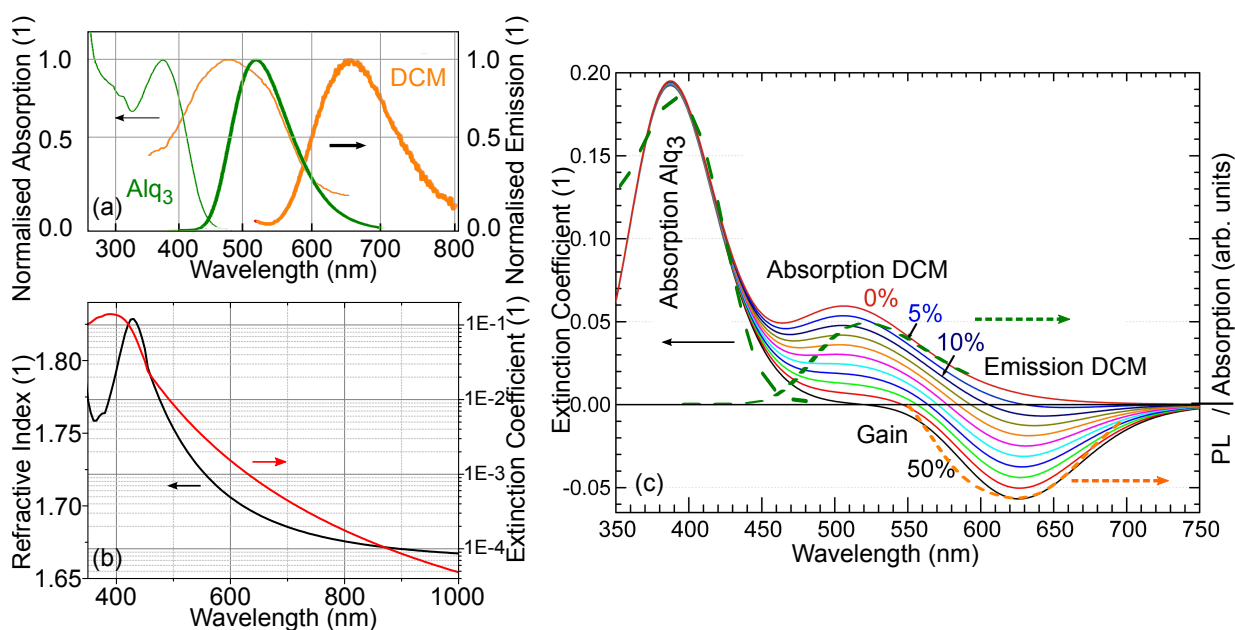


**Figure 2.13:** (a) Absorption and emission spectra of neat materials Alq<sub>3</sub> and DCM. Large overlap between Alq<sub>3</sub> emission and DCM absorption facilitates efficient FRET between both. (b) Optical constants of neat Alq<sub>3</sub>. (c) Calculated extinction coefficient of the organic emitter system for different fractions of excited DCM molecules. Apart from the absorption of Alq<sub>3</sub>, centered at 400 nm and the absorption of DCM at 510 nm, we see the occurrence of gain (negative absorption) around 630 nm, for higher fractions of excited molecules. Dashed lines: measured absorption of pure Alq<sub>3</sub> and DCM (green); photoluminescence intensity of 2wt% DCM in Alq<sub>3</sub> (orange). Figure (c) reprinted with permission from reference [6].

ternatively, a direct excitation of DCM is possible via illumination around 500 nm. Here, Alq<sub>3</sub> acts only as matrix, diluting and preventing aggregation of the laser dye.

## Gain

A key factor for active laser media is the optical gain, as lasing starts precisely when the gain of the system is able to overcome the total of losses. The calculated extinction coefficient in Fig. 2.13 (c) shows the transformation of absorption into gain even for small percentages of excited DCM molecules. From previously published data (e.g. [146]) and our own experimentally obtained spectra, we estimate the oscillator strengths of the corresponding transitions per DCM molecule. An excitation at power  $P$  of a fraction  $N(P)/N(0)$  of the DCM molecules then proportionally decreases the absorption spectrum and increases the emission spectrum assuming roughly equal oscillator strengths, resulting in normalized absorption/net gain spectra with a maximum on the order of  $\sim 400 \text{ cm}^{-1}$ - $600 \text{ cm}^{-1}$  in the bare film [9, 146]. At higher excitation, this gives access to a gain-spectrum spanning over 150 nm, allowing for tunable devices and

direct observation of the full cavity emission spectrum in real- and  $k$ -space. By off-resonantly exciting either the AlQ<sub>3</sub> matrix at 405 nm or the laser dye DCM at 532 nm, a broad gain spectrum forms around 630 nm in an inherent 4 level system of the organic dyes in the weak coupling regime.

As the reverse process of absorption, gain occurs as the absorption coefficient (or extinction coefficient  $\kappa$ ) turns negative when the material is pumped. Characterising the optical gain in a medium is thus of importance for lasing applications and typical methods to measure gain in thin films are the variable stripe length method [147, 148] and the method of Hakki and Paoli [149] in Fabry Perot geometry. However, neither of these methods can reliably be applied to study losses and gain in strongly confined systems such as microcavities, as the number of optical modes is severely limited and thus an enhanced coupling of spontaneous emission into these modes is observed. The radiative transition is further influenced by the Purcell effect, making a measurement of in situ optical gain in microcavities desirable. A novel method to characterise the net gain coefficient in small mode volume microcavities has been developed by us and is detailed in reference [9], but shall not be the focus of this work. From this method, we estimate the peak net gain of AlQ<sub>3</sub>:DCM inside a VCSEL configuration to be at least larger than 380 cm<sup>-1</sup>, establishing a very good basis for laser operation.

### 2.3.4 Organic Solar Cells and Organic Photodetectors

Since the first report of a working organic solar cell by Ching Tang in 1986 [31], they have attracted considerable interest, reaching record efficiencies of 12% for small molecules (Heliatek [32]), 13% for dye-sensitized cells [33], and above 19% for hybrid organic-inorganic perovskite cells [34]. Here, the focus lies on small molecule cells which typically comprise a small molecule absorber layer sandwiched between organic transport materials and a transparent and an opaque electrode in a planar thin film geometry. Usually, the organic layers are evaporated under ultra-high vacuum on a substrate with an indium tin oxide (ITO) transparent electrode, forming an amorphous or nanocrystalline thin film stack in vertical direction that is finished with a thermally evaporated opaque metal electrode. Typically, organic molecules exhibit extremely large absorption coefficients around 10<sup>5</sup> cm<sup>-1</sup>, compared to silicon (50 cm<sup>-1</sup>-100 cm<sup>-1</sup>) or direct inorganic semiconductors such as Ge (10<sup>3</sup> cm<sup>-1</sup>-10<sup>4</sup> cm<sup>-1</sup>) at their corresponding absorption edges [150], making them ideal for ultra-thin device production, where typical solar cells range in few hundred nm in thickness and are able to be produced with less than 1 g/m<sup>2</sup> of active material.

### The p-i-n Concept

The basic small molecule organic solar cell follows the p-i-n concept [151, 152, 153], where an intrinsic absorber layer (i) is sandwiched between electron- (n) and hole- (p) transporting materials. Under illumination of the device, excitons form by absorption of photons, lifting an electron from the LUMO to the HOMO of an absorbing molecule. To facilitate the dissociation of bound, neutral excitons, the absorber layer often comprises an electron donating (such as ZnPc) and an electron accepting (such as C<sub>60</sub>) material, where an exciton formed in either material can be separated at their interface. While flat heterojunctions provide such an interface in the center and efficient transport of the free charge carriers to the transport layers, the diffusion length of excitons typically is not large enough to reach the interface here. Instead, a bulk heterojunction (BHJ) is employed, where both donor and acceptor are co-evaporated at comparable volume ratios, creating islands of both molecules and strongly increasing the area of, while decreasing the distance to, an interface. At this interface, an exciton formed on the donor molecule is able to dissociate, as the HOMO and LUMO levels of the donor lie energetically higher than those of the acceptor. Thus, electrons are prompted to move onto the acceptor, while the hole prefers to stay on the donor to minimize the energy of the system. An intermolecular charge-transfer state is formed in the process of fully separating the charge carriers, and finally the free charge carriers can be transported towards their respective transport layers. Forming an exciton on the acceptor follows a similar route, as the hole is prompted to move onto the donor, while the electron remains on the acceptor. At the electrodes, the free charge carriers can be collected as the photocurrent of the device.

The schematic of a typical organic solar cell is depicted in Figure 2.14 (a), comprising a transparent electrode of either ITO or a thin metal film, a p-doped hole transport layer (HTL), a photo-active BHJ, n-doped electron transport layer (ETL), and an opaque Al electrode on top. In the dark, the device exhibits a current-voltage (IV) characteristic of a pn-diode - in backwards direction (negative voltage) no current is flowing, while in forward direction (positive voltage) the current increases exponentially. Under illumination, the IV-curve shifts negative current as free charge carriers are created in the device, building up either an open circuit voltage  $V_{OC}$  at zero current or flowing as a short circuit current density  $j_{SC}$  at zero voltage. The real operating conditions of the solar cell then lie somewhere in between these values, at the maximum of  $j \cdot V$ , the so-called maximum power point (MPP). The ratio of  $j_{MPP} V_{MPP} / (j_{SC} V_{OC})$  is then called the fill factor (FF) of the device as a measure for the efficiency of charge carrier transport, exhibiting values around 40% – 70% in organic solar cells - depending strongly on the device architecture and quality. To determine the efficiency of absorption and charge carrier transport, the external quantum efficiency relates the number of photons at a given wavelength shining onto a solar cell (via the incident light power  $P_{illu}(\lambda)$ ) to the number of collected charge carriers (the photocurrent

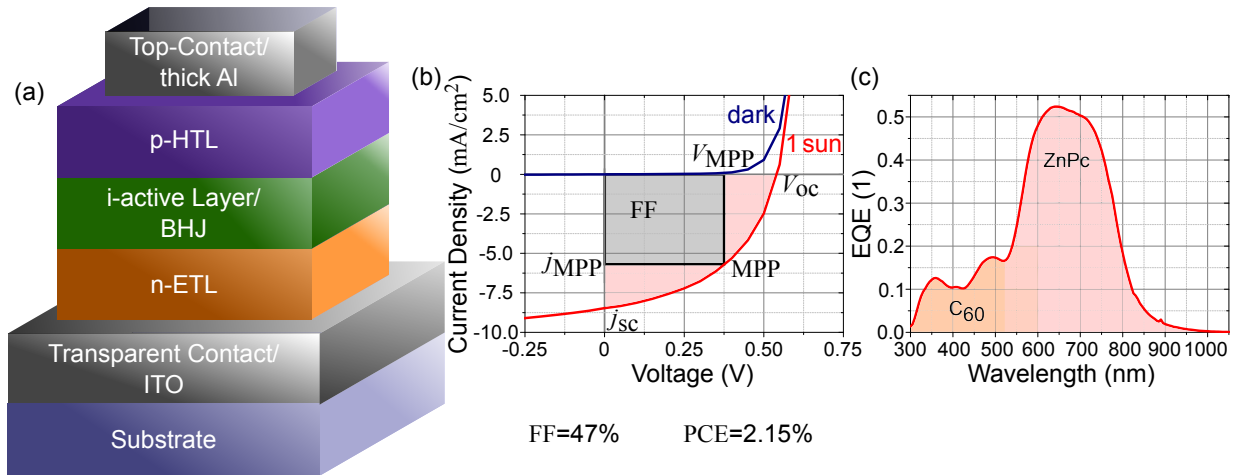


**Figure 2.14:** (a) Schematic structure of a p-i-n organic solar cell. On top of a glass substrate, a transparent contact is deposited, followed by an n-doped electron transport layer (ETL), an intrinsic absorber blend of donor and acceptor molecules, and a p-doped hole transport layer (HTL). The solar cell is commonly finished by an opaque top electrode such as a thick ( $\sim 100$  nm) aluminium layer. Adapted from [13]. (b) Current-voltage characteristics and characteristic quantities of an organic solar cell with and without illumination of a Xenon lamp ( $1000 \text{ W/m}^2$ ). The inverted stack contains: 100 nm Ag bottom contact | 35 nm Bis-HFI-NTCDI:W<sub>2</sub>(hpp)<sub>4</sub> n-ETL | 60 nm ZnPc:C<sub>60</sub> i-active layer | 32 nm BF-DPB:NDP9 p-HTL | 10 nm Ag top contact. (c) External quantum efficiency (EQE) of the cell from (b).

$I(\lambda)$ :

$$EQE(\lambda) = \frac{hc \cdot I_{PC}(\lambda)}{q\lambda \cdot P_{illu}(\lambda)} = \frac{hc}{q\lambda} R(\lambda) \quad , \quad (2.81)$$

where  $q$  is the elementary charge and  $R$  is the spectral responsivity. Finally, the power conversion efficiency (PCE) of a solar cell gives the ratio of electrical power produced under MPP conditions to the total power of light illuminating the cell:  $PCE = P_{el,MPP}/P_{illu}$ .

Figure 2.14 (b) shows the  $jV$  curve for a cell comprising a ZnPc:C<sub>60</sub> active layer, exhibiting a FF of 47% and a PCE of 2.15% at an illumination of  $1000 \text{ W/m}^2$ . The spectrally resolved external quantum efficiency can be seen in Fig. 2.14 (c), where the absorption of C<sub>60</sub> provides EQE at the lower wavelengths, while ZnPc gives a maximum EQE of 50% in the red spectral region.

## Photodetectors

In contrast to solar cells, the power conversion efficiency is not of primary interest for photodetectors, where the detection of a wide range of intensities is required. High external quantum efficiencies are desired and often achieved by applying a negative bias voltage that aids in charge carrier collection. The basic composition is similar to a solar cell, where an active absorber layer



is sandwiched between transport layers and electrodes. The important and optimised parameters however can differ, as detectors require a high signal to noise ratio ( $S/N = j_I/j_D$ ), high external quantum efficiencies, fast time response, and in the best case spectral selectivity. The NIR range is especially important for applications such as optical data transmission, medical diagnostics, food quality control and many more. Due to their high absorption coefficients, organic materials can be utilised for photodetectors [154, 155] and offer all advantages of organic semiconductors and low conductivities can be overcome by thin film production and bias voltages. Today, printable [156, 157, 158], flexible [159], transparent [157, 160], and highly responsive [158, 161, 162] detectors based on small molecules or polymers are available, as well as wavelength-tunable devices based on hybrid organic-inorganic perovskites [163, 164]. The spectrum that is covered by different molecules reaches from ultraviolet [161, 165] and x-ray [166] detection, over the whole visible (VIS) spectrum [167] into the near infrared (NIR)[160]. However, organic NIR detectors still can not reach far into longer wavelengths and typically offer only broadband detection, including sensitivity in the VIS. Wavelength-selectivity is often achieved by adding a spectrometer setup including a grating or prism in front of the detector, or might be achieved by adding filters but is usually not inherent to the device.

An important parameter is the specific detectivity  $D^*$  in units of Jones ( $\text{cm} \cdot \sqrt{\text{Hz}}/\text{W}$ , ROBERT CLARK JONES<sup>21</sup>), combining important properties such as EQE and noise [160, 168]:

$$D^* = \frac{R \sqrt{A}}{S_N} = \frac{\text{EQE} \cdot q \sqrt{A}}{\hbar\omega S_N} = \frac{\text{EQE} \cdot \sqrt{q}}{\hbar\omega \sqrt{2j_D}}, \quad (2.82)$$

with the responsivity  $R = \text{EQE} \cdot q/(\hbar\omega)$ , electron charge  $q$ , the noise spectral density  $S_N$ , the detector area  $A$ , and the dark current density  $j_D$ . Typically, large bias voltages (up to the order of 100 V) can be applied to enhance EQE even in regions of low absorption, however leakage currents might limit the application of those. Good detectors reach values of  $D^* > 10^{12}$  J.

In this work, detectors mimic the composition of an organic solar cell, where two electrodes sandwich a stack of ETL, active absorber layer, and HTL in the typical diode configuration. Consequently, under illumination the diode curve shifts downwards and an intensity-dependent current can be measured at zero or negative bias voltage, as long as leakage currents remain low. As the total power conversion efficiency is no longer important, and layer thicknesses as well as electrodes can be more freely varied, wavelength selectivity as well as an enhanced detectivity can be inherently realised by creating an optical microcavity where metal electrodes (or additional DBRs) provide highly reflective mirrors and variable thick transport layers are utilised to spectrally tune the cavity resonance.

<sup>21</sup>Robert Clark Jones, 1916-2004, American physicist, known for his work on polarisation of coherent light and photodetection.

### Cavity-Enhanced Detectors

Optical microcavities may strongly increase the electric field density inside and thus not only benefit emitting devices such as lasers, but can be utilised to increase field density to enhance nonlinear effects, or in this case enhance low absorption. First cavity enhanced detectors have been realised a long time ago [169, 170] and today inorganic semiconductor devices employ this principle to great effect [171, 172]. More recently, graphene has been utilised as active absorber material in a AlAs/AlGaAs DBR microcavity, leading to strong enhancement of the inherently weak absorption of graphene [173].

An inherent property of microcavities is their aversion to absorption, which means that highly absorptive layers will severely inhibit the cavity resonance and thus such devices can not profit from their advantages. A weakly absorbing material can however benefit greatly from cavity enhancement as the increased field leads to high EQE even for very low absorption coefficients. The selectivity enables wavelength multiplexing, as non-resonant modes are inhibited at the mirrors, while a finely tunable resonance is enabled by either a variation of cavity thickness or tuning the angle of incidence according to the microcavity dispersion.

In cavity-enhanced devices, the waves propagating forwards ( $E_F$ ) and backwards ( $E_B$ ) in the device result from the incident field  $E_i$  transmitted through the illuminated side and the feedback from one round trip in the cavity:

$$E_F = t_1 E_i + r_1 r_2 E_F \exp\left(-\frac{\alpha_{\text{ETL}}}{2} d_{\text{ETL}} - \frac{\alpha_{\text{HTL}}}{2} d_{\text{HTL}} - \frac{\alpha_{\text{Abs}}}{2} d_{\text{Abs}}\right) \exp(ikd_{\text{Tot}} + \delta_1 + \delta_2) \quad (2.83)$$

$$E_B = r_2 E_F \exp\left(-\frac{\alpha_{\text{ETL}}}{2} d_{\text{ETL}} - \frac{\alpha_{\text{HTL}}}{2} d_{\text{HTL}} - \frac{\alpha_{\text{Abs}}}{2} d_{\text{Abs}}\right) \exp(-ikd_{\text{Tot}} + \delta_2) \quad (2.84)$$

with transmission  $t$  and reflection  $r$  coefficients and phase changes  $\delta$  from mirrors 1 and 2 and absorption coefficients  $\alpha$  and thicknesses  $d_{\text{Tot}} = d_{\text{ETL}} + d_{\text{HTL}} + d_{\text{Abs}}$  of the transport layers and active absorber layer (Abs). With these fields, the absorbed power in the active layer  $P_{\text{Abs}}$  can be calculated [174]:

$$P = (P_F \exp(-\alpha_{\text{ETL}} d_{\text{ETL}}) + P_B \exp(-\alpha_{\text{HTL}} d_{\text{HTL}}))(1 - \exp(-\alpha_{\text{Abs}} d_{\text{Abs}})) = \eta_{\text{Abs}} P_i \quad , \quad (2.85)$$

with the absorption efficiency  $\eta_{\text{Abs}}$ :

$$\eta_{\text{Abs}} = (1 - r_1^2)(1 - \exp(-\alpha_{\text{Abs}} d_{\text{Abs}})) \cdot \left( \frac{\exp(-\alpha_{\text{ETL}} d_{\text{ETL}}) + r_2^2 \exp(-\alpha_{\text{HTL}} d_{\text{HTL}} + \alpha_{\text{Tot}} d_{\text{Tot}})}{1 - 2r_1 r_2 \exp(\alpha_{\text{Tot}} d_{\text{Tot}}) \cos(2kd_{\text{Tot}} + \delta_1 \delta_2) + r_1^2 r_2^2 \exp(-2\alpha_{\text{Tot}} d_{\text{Tot}})} \right), \quad (2.86)$$

where  $\alpha_{\text{Tot}} = (\alpha_{\text{ETL}} d_{\text{ETL}} + \alpha_{\text{HTL}} d_{\text{HTL}} + \alpha_{\text{Abs}} d_{\text{Abs}})/d_{\text{Tot}}$ . This formula gives the efficiency of ab-

sorbing an incident photon in the active layer of the detector. A sharp and high resonance arises for large reflectivities  $r_1, r_2$ , and low parasitic absorption  $\alpha_{\text{ETL}}, \alpha_{\text{HTL}}$ . However, mirror 1 still needs to exhibit some transmission (see factor  $1 - r_1^2$ ) to allow for incident light to enter the device. Furthermore, the absorption in the active layer needs to be small in comparison to typical absorption in solar cells as large absorption coefficients or layer thicknesses strongly inhibit the cavity effect. Absorber materials in OPV exhibit absorption coefficients of  $\alpha > 10^5 \text{ cm}^{-1}$ , requiring layer thicknesses below 2 nm to achieve  $Q$ -factors on the order of 100 for reasonable mirror reflectivities of  $r_1^2 r_2^2 = 0.97$ . The charge-transfer state absorption (Section 2.3.2) however exhibits coefficients in the range of  $10^4 \text{ cm}^{-1} > \alpha > 10^3 \text{ cm}^{-1}$ , where viable layer thicknesses of  $> 50 \text{ nm}$  result. In this range, the thickness is large enough to avoid shunts, but small enough to result in full carrier collection. Improving the CT absorption by microcavity field enhancement thus provides a way to extend the sensitivity of organic absorber materials into the infrared, to wavelengths of important applications.

## 2.4 Bloch States

*This section delivers a theoretical basis for eigenstates of particles with a parabolic dispersion inside of a periodic potential. While the most famous application of this principle is the description of electrons in a crystal lattice, I will show that similar effects can be observed for photons and polaritons inside microcavities.*

*Starting with the dispersion relations of both electrons in media and photons in planar cavities in Section 2.4.1, introducing the realisation of periodic potentials for both particles. Finally, the one-dimensional case is solved in the famous Kronig-Penney model and the formation of Bloch states is discussed in Section 2.4.2. The observation of photonic Bloch states in patterned microcavities will then be discussed in Chapter 6.*

### 2.4.1 Electron and Photon Dispersion

In vacuum, electrons and photons behave quite differently, especially regarding their dispersion relations  $E(k)$ , that govern many physical properties of the particles. Electrons obey Schrödinger's equation (ERWIN SCHRÖDINGER<sup>22</sup>), leading to a dispersion relation for free electrons:

$$E_{\text{el}}(k) = \frac{\hbar^2 k^2}{2m_{\text{el}}} \quad , \quad (2.87)$$

<sup>22</sup>Erwin Rudolf Josef Alexander Schrödinger, 1887-1961, developed the basics for wave mechanics in quantum physics. Awarded the Nobel prize in physics for his Schrödinger equation in 1933.

with  $m_{\text{el}}$ , the free electron mass.

Photons on the other hand obey Maxwell's equations and the corresponding wave equation (2.15) leading to a linear photon dispersion:

$$E_{\text{phot}}(k) = \hbar ck \quad . \quad (2.88)$$

However, when the boundary conditions change for both particles, their dispersive behaviour is strongly influenced as a result of a direct interaction between particle and surrounding medium. Surprisingly, the interaction between an electron in an atomic crystal lattice reveals many analogies to the behaviour of cavity photons in a photonic crystal and enables the transfer of basic experimental and theoretical concepts from one system to the other.

### Electrons in Solid State Materials and their Effective Mass

In a crystal lattice, electrons are influenced by a rigid formation of positive atomic cores. Their wave function alters in a way, that unhindered propagation through such a lattice becomes possible. Resulting from this behaviour is the formation of energy bands as described further in this section. In particular, charge carriers change their mass as the dispersion differs from the free parabola and thus the effective mass  $m^*$  is defined as:

$$m_{ij}^{*-1} = \frac{1}{\hbar^2} \frac{\partial^2 E}{\partial k_i \partial k_j} \quad . \quad (2.89)$$

As the dispersion might differ in directions  $i, j$ , the effective mass depends on the orientation of interest. Here, the one-dimensional case is mainly of interest, so that  $m^* = \hbar^2 \cdot 1/(\partial^2 E/\partial k^2)$ . The effective mass may vary strongly in different materials and show values greater or lower than the free electron mass, in special cases the effective mass can become very light (e.g. GaAs  $m^* \approx 0.07m_{\text{el}}$ ). In semiconductors, missing electrons in the valence band can be described as holes, which exhibit negative effective mass as the dispersion curves downward there.

### Microcavity Photons

For photons inside of a microcavity, the linear dispersion alters. Assuming the growth direction of the microcavity to be in  $z$ -direction, the wavevector splits in its  $k_z$ - and parallel  $k_{\parallel}$  components. As the  $z$ -component is fixed in the cavity, we obtain an altered dispersion relation for cavity photons:

$$E_{\text{cav}}(k) = \hbar c \left| \vec{k} \right| = \hbar \frac{c_0}{n_C} \sqrt{k_z^2 + k_{\parallel}^2} \quad , \quad (2.90)$$

where  $k_z$  is fixed and  $k_{\parallel}$  is typically small in comparison. If the cavity is not detuned with respect to the DBR design wavelength, the  $z$ -component can be expressed as  $k_z = \pi/L_C$ . Then, the dispersion can be approximated by:

$$E_C(k_{\parallel}) = \sqrt{\left(\frac{\pi\hbar c}{n_c L_C}\right)^2 + \frac{\hbar^2 c^2}{n_c^2} k_x^2} \approx E_C(0) + \frac{\hbar^2 k_x^2}{2m_x} \quad (2.91)$$

assuming a photon effective mass:  $m_x = \pi\hbar n_c/cL_C$ , and the photonic ground state energy:  $E_C(0) = \pi\hbar c/n_c L_C$ . The introduction of an effective mass for photons here is just a mathematical tool for simplification, but it showcases the strong analogy between electrons and cavity photons. They exhibit similar parabolic dispersion relations, where cavity photons experience a finite constant ground state potential  $E_C(0)$ , above which they propagate like free electrons.

When the cavity is detuned with respect to the DBR design wavelength, still a parabolic dispersion will be observed, however the expressions for the photon effective mass, corresponding to the curvature of the parabola, and the ground state energy will be affected. In particular, the effective mass will become depended on the polarisation of light, as to correctly reflect the polarisation splitting observed in detuned microcavities at larger angles. When adding additional interlayers, a detuning is impossible to avoid and in fact desired, so for a quantitative mode allocation, this needs to be taken into account. To derive the correct effective mass, we need the cavity thickness, as well as thickness and penetration depth of light into the adjacent DBR layers, as discussed in Section 2.2.4. The effective mass can then be written as:

$$m^* = \frac{\hbar\omega_0^2}{2\omega_1 c^2} \quad \text{with} \quad \omega_1 = \frac{\partial^2 \omega_{\text{eff,TE/TM}}}{2\partial(\sin\vartheta)^2} \quad (2.92)$$

Here,  $\omega_1$  is the coefficient of the second-order Taylor approximation of the effective frequency  $\omega_{\text{eff,TE/TM}} = (d_C \omega_C + d_{\text{DBR}}^{\text{TE/TM}} \omega_D)/(d_C + d_{\text{DBR}}^{\text{TE/TM}})$ , as defined in Equation (2.65). Effective photon or polariton masses are incredibly light compared to electron masses in different materials and reside around  $10^{-5} \cdot m_{\text{el}}$ , which results in interesting properties such as low nonlinear thresholds. Note that the effective mass is dependent on the polarisation of light and depending on the sign of detuning, either TE or TM -polarised photons can be ‘‘heavier’’.

It becomes clear, that both the photon effective mass as well as the photonic ground state strongly depend on the cavity thickness. The ground state energy in particular shifts toward lower energies for an increasing cavity thickness and higher energies for smaller thicknesses. Adding a low refractive index interlayer that is otherwise optically inactive, such as almost non-absorbing  $\text{SiO}_2$ , can in turn increase the cavity thickness and thus lower the ground state energy significantly for only very small interlayer thicknesses. Adding a plasmonic interlayer such as silver does not significantly increase the optical thickness of the cavity, but causes a phase shift

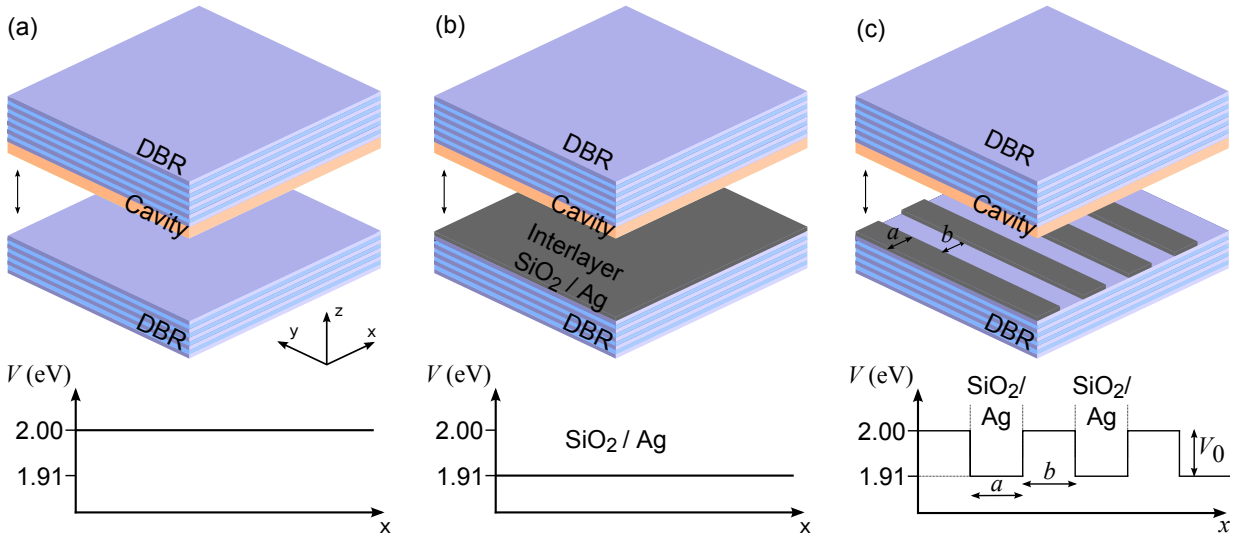


**Figure 2.15:** Sample schematics and photonic potential for (a) standard microcavity, (b) microcavity with added interlayer and (c) microcavity with periodically patterned interlayer. An added interlayer shifts the photonic potential to the red by  $V_0$ , creating a periodic Kronig-Penney potential for periodically patterned layers.

of the light at the cavity-silver interface. Here, again the addition of a thin silver film into a cavity will lead to a decrease in the ground state energy of the system, albeit smaller for comparable film thicknesses in the purely dielectric case. Taking into account the phase shift at the metal-cavity interface, an effective cavity thickness can be defined as follows:

$$d_{\text{TPP,eff}} = d_C + \frac{|\delta_{\text{Ag}}^r| d_C}{\pi} \quad , \quad (2.93)$$

with  $\delta_{\text{Ag}}^r$ , the phase change at the metal-cavity interface. A full calculation requires solving the coupled resonator equation for both Tamm plasmon polariton states as detailed in Section 2.2.5, utilizing the transfer matrix algorithm. For practical purposes, this algorithm is solved numerically and the ground state energy, or effective cavity thickness, are obtained empirically from there.

In total, the ground state energy of a modified cavity can be given as:

$$E_C(0) = \frac{\pi \hbar c}{n_C d_C + n_I d_I + |\delta_I^r| d_C / \pi} \quad , \quad (2.94)$$

where  $d_I$  and  $\delta_I^r$  are the thickness of the added interlayer and the phase change at the interface between this layer and the original cavity. Figure 2.15 gives the sample structures and photonic potential for microcavities without (a), with (b) and with a patterned (c) interlayer.

When describing the photonic potential in a patterned system, the lowest energy, correspond-

ing to areas with additional interlayers, will be arbitrarily set to zero, while areas of higher energies, corresponding to the pure cavity, will be described by an additive potential  $V_0$ . In the case of infinitely high barriers, the solutions of photonic wells from Section 2.2.6 are valid, for the real case of finite potentials, the dispersion transforms into electronic or photonic Bloch states.

## 2.4.2 Kronig-Penney Model and Bloch States

### Schrödinger Equation for Parabolic Particles in a Periodic Potential

Calculating the dispersion relation of electrons - and via analogy photons or polaritons in microcavities - requires solving the Schrödinger equation in the potential of interest. The time independent Schrödinger equation for the wave function  $\psi$  in a rectangular potential as shown in Figure 2.15 (c) is given by:

$$\begin{aligned} \frac{\partial^2}{\partial x^2} \psi + \frac{2m^*E}{\hbar^2} \psi &= 0 & \text{for } 0 + l \cdot (a + b) < x < a + l \cdot (a + b) \\ \frac{\partial^2}{\partial x^2} \psi + \frac{2m^*(E - V_0)}{\hbar^2} \psi &= 0 & \text{for } -b + l \cdot (a + b) < x < 0 + l \cdot (a + b). \end{aligned} \quad (2.95)$$

This equation holds true for both cases of either electronic or photonic wave functions, if the corresponding effective masses are used. In fact, an equivalence between both Schrödinger equation and the wave equation derived from Maxwell's equations can be shown [175]. If all assumptions made prior are followed (in particular small outcoupling angles and small cavity detuning), this derivation will give correct results for photonic modes in microcavities.

Utilizing the Kronig-Penney model (RALPH KRONIG<sup>23</sup> and WILLIAM PENNEY<sup>24</sup>), the equations for both areas can be solved by the ansatz of plane waves with the propagation constants  $\alpha, \beta$  for both areas (1) and (2):

$$\begin{aligned} \psi_1 &= Ae^{i\alpha x} + Be^{-i\alpha x}; & \text{with } \alpha &= \frac{\sqrt{2m^*E}}{\hbar} \\ \psi_2 &= Ce^{-i\beta x} + De^{i\beta x}; & \text{with } \beta &= \frac{\sqrt{2m^*(E - V_0)}}{\hbar}. \end{aligned} \quad (2.96)$$

For solving this set of equations for the amplitudes  $A, B, C,$  and  $D,$  we employ further boundary conditions.

<sup>23</sup>Ralph Kronig, 1904-1995, German physicist, discovered the particle spin and developed a theory for x-ray absorption.

<sup>24</sup>William George Penney, 1909-1991, English mathematician, provided fundamental applications of quantum mechanics to crystal physics.

### The Bloch Theorem and Continuity Conditions

It can be shown that the eigenfunctions describing waves in a periodic potential have to satisfy the Bloch theorem (F. Bloch<sup>25</sup>):

$$\psi(x) = u(x) \exp(ikx) \quad \text{with} \quad u(x + (a + b)) = u(x) \quad , \quad (2.97)$$

i.e. the wavefunction has to satisfy the condition  $\psi(x+(a+b)) = \exp(ik(a+b))\psi(x)$ . In particular, this leads to the following boundary conditions for the functions (2.96) and their derivatives (denoted by  $u'$ ):

$$u(-b) = u(a) \quad \text{and} \quad u'(-b) = u'(a) \quad . \quad (2.98)$$

As the full wavefunction shall be continuous and smooth, we obtain further continuity conditions for the wavefunctions in areas (1) and (2):

$$\psi_1(0) = \psi_2(0) \quad \text{and} \quad \psi'_1(0) = \psi'_2(0) \quad . \quad (2.99)$$

Equations (2.98) and (2.99) provide now four equations to solve for the amplitude vector  $\hat{A} = (A, B, C, D)$ , and can be written in the form of a coefficient matrix  $\hat{M}$ :

$$\hat{M} = \begin{pmatrix} 1 & 1 & 1 & 1 \\ \beta & -\beta & i\alpha & -i\alpha \\ \exp(i(k-\beta)b) & \exp(i(k+\beta)b) & \exp(-i(k-\alpha)a) & \exp(i(k+\alpha)a) \\ \begin{pmatrix} -i(k-\beta) \cdot \\ \exp(i(k-\beta)b) \end{pmatrix} & \begin{pmatrix} -i(k+\beta) \cdot \\ \exp(i(k+\beta)b) \end{pmatrix} & \begin{pmatrix} -i(k-\alpha) \cdot \\ \exp(-i(k-\alpha)a) \end{pmatrix} & \begin{pmatrix} -i(k+\alpha) \cdot \\ \exp(i(k+\alpha)a) \end{pmatrix} \end{pmatrix} \quad (2.100)$$

$$\text{where} \quad \hat{M} \cdot \hat{A} = \hat{0} \quad . \quad (2.101)$$

### Solving the Transcendental Equation of the Dispersion Relation

If a nontrivial solution of Equation (2.101) shall exist, the determinant of the coefficient matrix (2.100) has to be zero:

$$|\hat{M}| = 0 \quad , \quad (2.102)$$

leading to the equation:

$$\frac{\beta^2 - \alpha^2}{2\alpha\beta} \sinh(\beta b) \sin(\alpha a) - \cosh(\beta b) \cos(\alpha a) = \cos((a+b) \cdot k) \quad , \quad (2.103)$$

<sup>25</sup>Felix Bloch, 1905-1983, Swiss physicist, known for his contributions towards explaining the behaviour of electrons in crystal lattices.



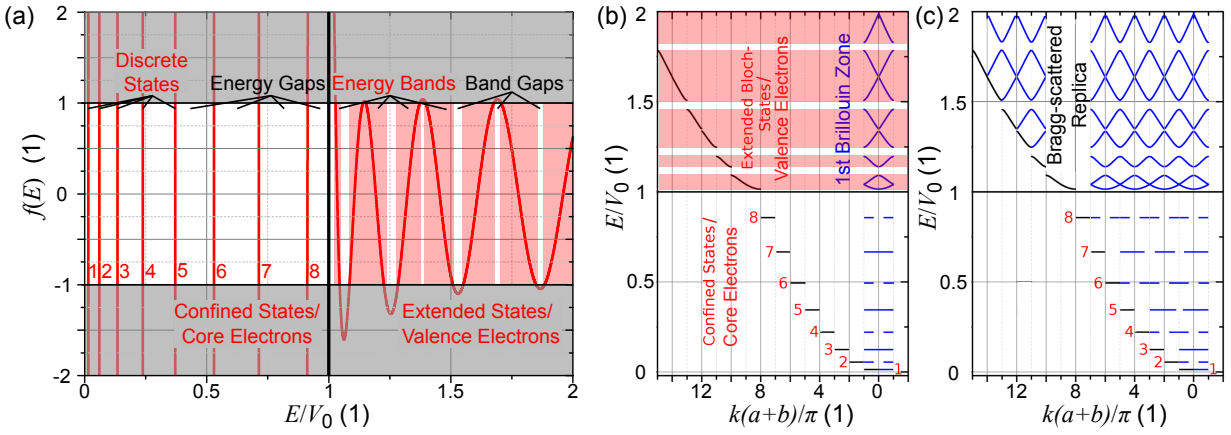


**Figure 2.16:** (a) Left side of transcendental Equation (2.103) as  $f(E)$  over  $E/V_0$ . As the right side of the equation,  $\cos((a+b)k)$  has only solutions between  $-1 \dots +1$  and values outside are forbidden (grayed out area), gaps in the dispersion appear. (b) Dispersion of waves in a periodic potential. Below  $V_0$ , discrete states represent the particles confined in the potential well, e.g. core electrons in solid state crystal. Above  $V_0$ , a more extended dispersion showcases allowed energy bands of extended particles such as valence electrons. (c) Bragg-scattered replica at  $k_l = k + l \cdot \pi / (a + b)$  fill the whole momentum-resolved spectrum.

directly describing the dispersion relation  $E(k)$ , as the particle energy is included in the propagation constants  $\alpha(E), \beta(E)$ . This equation, while being the analytical formula for the dispersion, is transcendental, i.e. can not be solved in terms of algebra. A correct solution can be obtained graphically as visualised in Figure 2.16 (a), where the left side of Equation (2.103) is plotted as  $f(E)$  over the particle energy. As the equation's right side can only have values between  $-1 < \cos((a-b)k) < +1$ , the dispersion exhibits gaps in energy, where no eigenstates of the system exist. In particular, below the potential barrier ( $E/V_0 < 1$ ), almost dispersion-free discrete states are obtained, while above the barrier ( $E/V_0 > 1$ ) more extended ranges of energies become allowed, leading to the formation of energy bands and their corresponding band gaps. For practical purposes, the transcendental equation is calculated numerically.

## Bloch States

As mentioned above, Equation (2.103) already delivers the desired dispersion relation, which can be calculated numerically for a certain set of parameters and is depicted in Figure 2.16 (b). Here, we observe a set of discrete states below the potential barrier, exhibiting a flat dispersion and large energy gaps in between. These states represent localized solutions of the system, residing mainly in the wells of the potential used. In a solid state system, they represent the core electrons bound to the ionic cores of the crystal lattice, while in a photonic system they appear localized at the position of the photonic well created by a patterned interlayer. Here, they form

standing waves inside their confining potential. The states above the barrier however exhibit much stronger dispersion, albeit interrupted by energy gaps. These states form the band structure of the material with their corresponding band gaps and are extended over larger areas above the potential wells. Both form the Bloch states of the one-dimensional periodic potential, as an accessible description of many physical properties such as the formation of energy bands, the origin of band gaps in the energy spectrum, or the dispersion of electrons and holes in semiconductors. In the photonic system, the formation of such states will be shown later in this thesis, fundamentally altering the behaviour of light, creating forbidden energies for photons and providing a high density of states at points of low dispersion as ideal condensation cores for lasing. The full description of the microcavity dispersion will include a more complex treatment of the photon effective mass leading to, among other effects, a dependence of photonic Bloch states on the polarisation and will be detailed in Chapter 6. It shall be noted that adding an additional linear potential  $V = V_1 \cdot x$ , such as applying a voltage to a crystal, leads to many new observations such as Bloch oscillations of charge carriers, which have been experimentally demonstrated for semiconductor superlattices [176], but also for photonic lattices [177, 178, 179] as well.

### Bragg-Scattering in Periodic Optical Gratings

In periodic systems, the scattering points repeat after every period and thus the scattered momentum vectors repeat periodically also in reciprocal space. To describe the dispersion in a crystal lattice, usually only the first Brillouin zone (L. BRILLOUIN<sup>26</sup>) is given, as all necessary information are included there. In optics, Bragg scattering (W.H. BRAGG, W.L. BRAGG<sup>27</sup>) leads to a repetition of features at wavenumbers

$$k' = k + l \cdot \frac{\pi}{a + b} \quad , \quad (2.104)$$

with  $l$  as an integer, leading to a periodic repetition of all features observed in the far field spectrum in every Brillouin zone. However, Bragg scattering can only occur if the coherence length  $d_{\text{Coh}}$  is larger than the  $l$ -th spacing of the grating  $d_{\text{Coh}} > |l|\pi/(a + b)$ . When observing the full momentum space, this behaviour leads to the observation of extended states filling the whole dispersion as shown in Figure 2.16 (c). After every  $\pi/(a + b)$ , features repeat and energy bands with distinct band gaps become visible above the potential.

<sup>26</sup>Léon Nicolas Brillouin, 1889-1969, french physicist, known for his theoretical contributions to solid state quantum physics.

<sup>27</sup>William Henry Bragg, 1862-1942, British physicist; and his son William Lawrence Bragg, 1890-1971, Australian/British physicist, they were awarded the Nobel price in physics "For their services in the analysis of crystal structure by means of X-ray", jointly.

## 3 Experimental Methods

*This chapter serves as an overview over different experimental methods used to fabricate, structure, and investigate organic microcavities. The first part focuses on device fabrication, detailing different evaporation methods, such as electron beam- and thermal physical vapour deposition, as well as the materials that are utilised in Sections 3.1.1 and 3.1.3. Special care is given to the thermal evaporation of the noble metal silver and steps to increase the quality of thin silver films in microcavities.*

*Section 3.2 gives an overview over the photo-patterning of interlayers in the microcavity, presenting different methods centered around photolithography and structuring techniques, such as lift-off and etching processes. The optical characterisation of the patterned layers is presented, as the micron-scale optical quality is decisive for the performance of the final samples, and different challenges in high-resolution structuring are discussed.*

*The final Section 3.3 presents different characterization methods important for the investigation of organic microcavities and gives a brief overview over spectroscopic and imaging methods, the confocal microphotoluminescence setup, and the electrical characterisation of photodetectors.*

### 3.1 Sample Fabrication

#### 3.1.1 Resonator Materials

For the production of high-quality organic microlasers, a multitude of different methods have to be employed, optimized for each constituent of the device. For the resonator mirrors, typically dielectric DBRs are utilised which here consist of the optically favourable oxides of silicon ( $\text{SiO}_2$ ) and titanium ( $\text{TiO}_2$ ), exhibiting low absorption in the red spectral region and a high refractive index difference, needed for a broad and deep stopband. For lasing, these mirrors are essential and provide ultra-high reflectivity in the spectral design window as well as enable transmission of the pump laser to excite the system.

As an ideal material to influence and structure the microcavity dispersion, silver has proven to be widely applicable as well as easily patterned using various etching methods. For applications

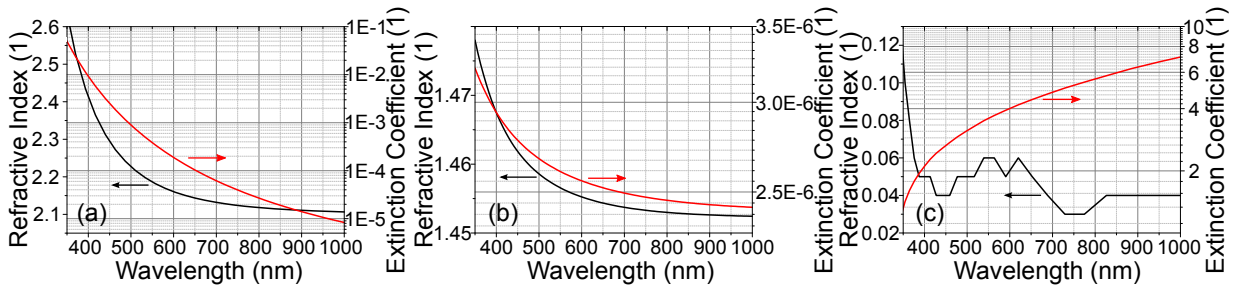


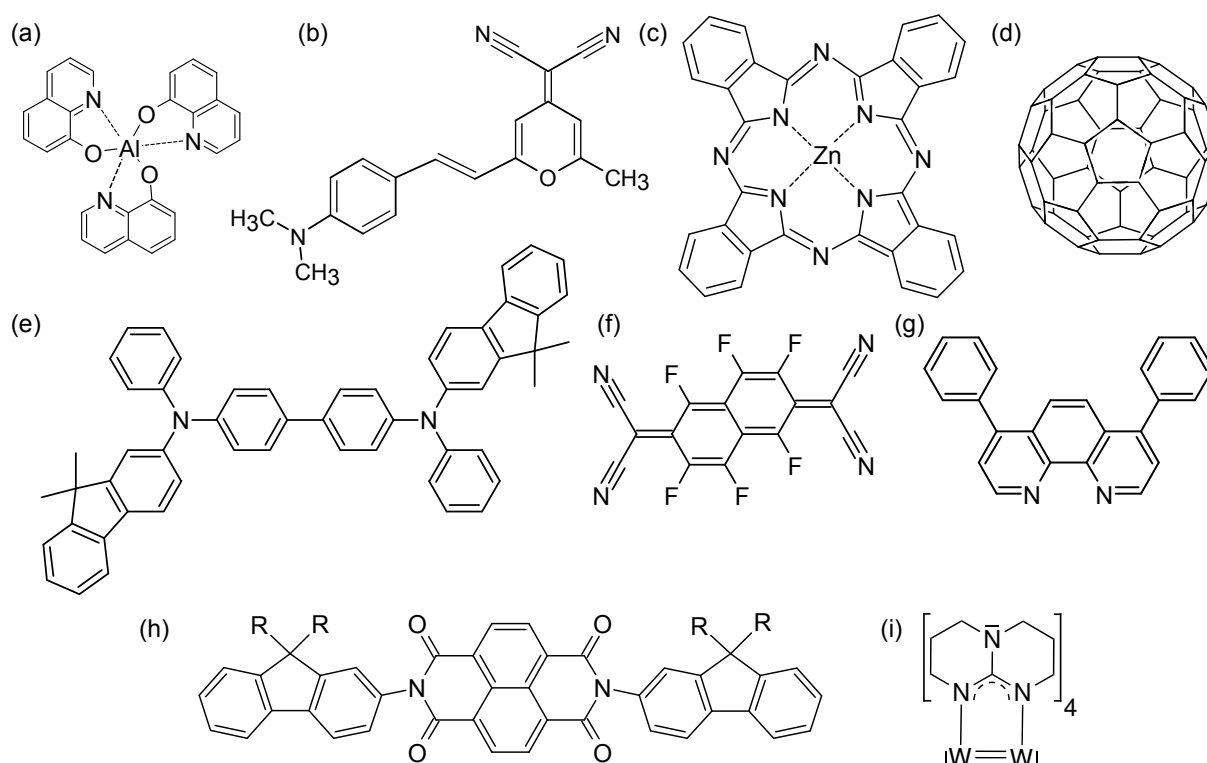
**Figure 3.1:** Optical constants (refractive index  $n$  - black, extinction coefficient  $\kappa$  - red) of (a)  $\text{TiO}_2$ , (b)  $\text{SiO}_2$ , (c) bulk silver.

requiring lower reflectivities, silver itself can serve as the microcavity mirror on one or both sides of the devices, additionally providing high conductivity for electrical contacting. To obtain very high qualities of thin silver films, various sublayers such as aluminium, molybdenum oxide, or gold are employed (see Section 3.1.4).

Figure 3.1 provides the optical constants of the mirror materials. For the dielectric mirrors,  $\text{TiO}_2$  provides a very high refractive index and reasonably low extinction ( $n = 2.15$ ,  $\kappa = 1.35 \cdot 10^{-4}$  at 630 nm), while  $\text{SiO}_2$  provides a low refractive index and exceptionally low extinction ( $n = 1.45$ ,  $\kappa = 2.53 \cdot 10^{-6}$  at 630 nm). While  $\text{SiO}_2$  is feasible in the whole VIS and NIR range, care has to be taken for  $\text{TiO}_2$  in the blue part of the visible spectrum, as the extinction coefficient increases strongly there. For DBRs in the blue, other dielectrics such as zirconium oxide or tantalum oxide prove useful, albeit exhibiting lower refractive indices. Silver exhibits a vanishing refractive index and very high extinction coefficient ( $n = 0.05$ ,  $\kappa = 4.2$  at 630 nm, [61]), as most metals below the plasma frequency. Compared to other metals, silver exhibits favourable optical properties, such as reflectivities above 95% in the red for thicknesses above 50 nm (compare 100 nm Ag:  $\mathcal{R} \approx 98\%$ ; 100 nm Au:  $\mathcal{R} \approx 90\%$ ; 100 nm Al:  $\mathcal{R} \approx 88\%$ ).

### 3.1.2 Organic Molecules

The organic materials used in devices in this work comprise only small molecules and can be categorised into active emitters, absorbers, transport layers, and p- and n-dopands. While the active emitter system  $\text{Alq}_3\text{:DCM}$  is already discussed in Section 2.3.3, and the absorbing bulk heterojunction  $\text{ZnPc:C}_{60}$  is briefly discussed in Section 2.3.4, all optical properties shall be presented here for sake of completion. As constituents of the cavity layer, all organic molecules are required to show low absorption at the design wavelength, if the optical quality of the cavity shall not suffer. As an exception, the absorbing layer in cavity-enhanced photodetectors has to exhibit a minimum of absorption (see Section 2.3.4), albeit still orders of magnitude lower than for typical absorbers at their maximum.



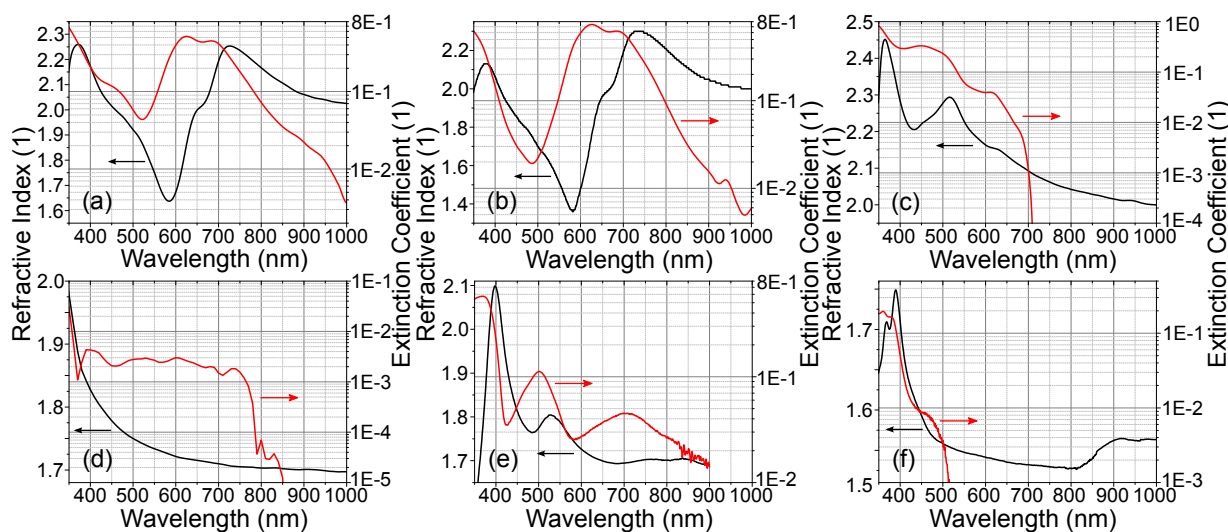
**Figure 3.2:** Molecular structures of (a) tris (8-hydroxy-quinolinato)-aluminium (**Alq<sub>3</sub>**), (b) 4-(dicyanomethylene)-2-methyl-6-[p-(dimethylamino)-styryl]-4H-pyran (**DCM**), (c) zinc-phthalocyanine (**ZnPc**), (d) buckminster fullerene (**C<sub>60</sub>**), (e) N,N'-(Diphenyl-N,N'-bis(9,9-dimethyl-fluoren-2-yl))-benzidine (**BF-DPB**), (f) 2,2'-(perfluoronaphthalene-2,6-diylidene)dimalononitrile (**F<sub>6</sub>TCNNQ**), (g) 4,7-diphenyl-1,10-phenanthroline (**BPhen**), (h) N,N-Bis(fluoren-2-yl)-naphthalenetetracarboxylic diimide (**Bis-HFI-NTCDI**), and (i) ditungsten-tetra(hpp) (**W<sub>2</sub>(hpp)<sub>4</sub>**). Not shown is the proprietary dopand NDP9.

Figure 3.2 shows the molecular structures and full names of the emitter system of Alq<sub>3</sub> and DCM, the absorber materials ZnPc and C<sub>60</sub> the hole transport material BF-DPB and p-dopand F<sub>6</sub>TCNNQ, the electron transport materials Bis-HFI-NTCDI and BPhen, and the n-dopand W<sub>2</sub>(hpp)<sub>4</sub><sup>1</sup>. Note, that ZnPc and C<sub>60</sub> can be additionally utilised as hole transport and electron transport materials, respectively, if their parasitic absorption is not detrimental to the device, or even desired for visible blind detectors. Not shown is the proprietary p-dopand NDP9<sup>2</sup>

Figure 3.3 in turn presents the optical constants of the organic layers utilised for detectors, considering dopands, where possible. The optical constants for the laser matrix and dye are presented in Section 2.3.3 for varying fractions of excited DCM molecules. These values are of

<sup>1</sup>Alq<sub>3</sub> - Sigma Aldrich, 2× sublimated IAPP; DCM - Radiant Laser dyes, 2× sublimated IAPP; ZnPc - TCI Europe, 3× sublimated IAPP; C<sub>60</sub> - CreaPhys; BF-DPB - synthesised and purified IAPP; F<sub>6</sub>TCNNQ - Novald AG; Bis-HFI-NTCDI - synthesised and purified IAPP; BPhen - Sigma Aldrich; W<sub>2</sub>(hpp)<sub>4</sub> - Novald Ag.

<sup>2</sup>NDP9, Novald AG.



**Figure 3.3:** Optical constants (refractive index  $n$  - black, extinction coefficient  $\kappa$  - red) of (a) bulk heterojunction ZnPc:C<sub>60</sub> (volume ratio 1:1), (b) neat ZnPc, (c) neat C<sub>60</sub>, (d) caesium-doped BPhen (1:1), (e) NDP9-doped BF-DPB (10 wt%), (f) Bis-HFI-NTCDI.

great importance for the design of microcavities and the distribution of electric field inside the cavity, and are employed in transfer matrix simulation to optimize all layer thicknesses.

### 3.1.3 Physical Vapour Deposition

Physical vapour deposition describes the thin film deposition of materials from vapour by physical processes, such as thermal evaporation. All evaporation techniques for the fabrication of samples are contained in a single multi-purpose vacuum chamber (LAB500), as schematically depicted in Figure 3.4. For small molecule organic microcavities, two methods are used for the deposition of small molecules on the one hand and DBR oxides on the other. Organic molecules exhibit much lower sublimation points and are not suited for electron beam evaporation as they are potentially damaged and fragmented by high kinetic energies of the accelerated particles. The purified organic materials are instead sublimated in a heated crucible (e) under ultra high vacuum, at base pressures in the range of  $5 \cdot 10^{-7}$  mbar to  $8 \cdot 10^{-8}$  mbar. Under these conditions, the organic small molecules form amorphous or nanocrystalline films on the substrate (d)[180], ideally suited for application. Evaporation rates and film thicknesses are controlled by a quartz crystal microbalance (f)<sup>3</sup> and evaporation is started and stopped by opening or closing a shutter. For microlasers, the host:guest system Alq<sub>3</sub>:DCM is co-evaporated at  $10 \text{ \AA/s}$  and  $0.2 \text{ \AA/s}$ , respectively, to achieve the desired weight ratio. Here, the crucial optical thickness is additionally

<sup>3</sup>QCM CNT-06IG, Beamtec

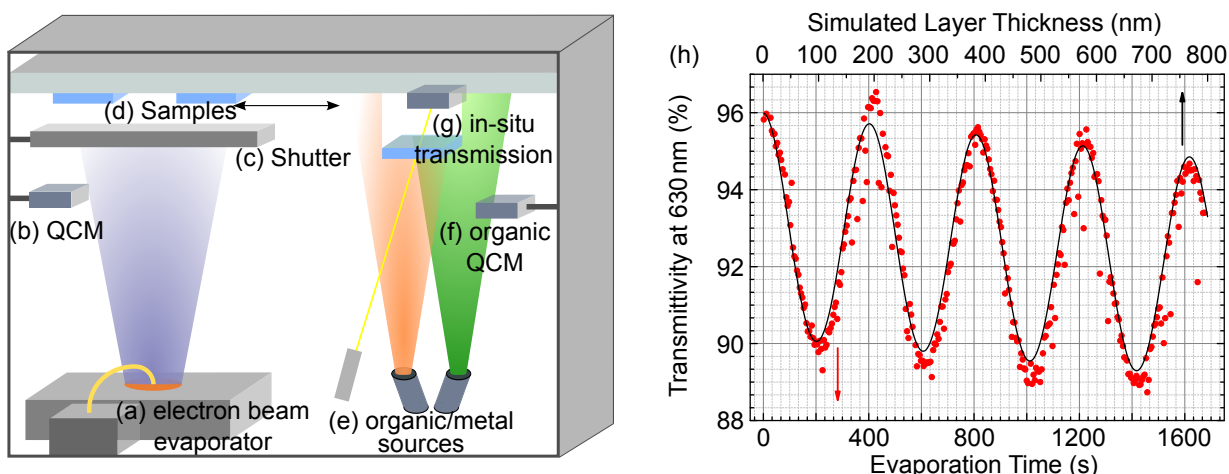


**Figure 3.4:** Schematic of the Lab500 evaporation chamber. (a) Electron beam evaporator. A tungsten filament emits electrons that are accelerated and guided into a crucible containing raw materials. (b) Quartz crystal microbalance controlling the oxide rate and thickness. (c) Shutter or rotating shutter. (d) Samples, movable above different evaporation sources. (e) Thermal crucibles for sublimation of organic materials and evaporation boat for thermal evaporation of metals. (f) QCM for thermal sources. (g) In-situ light transmission measurement. An optical fibre sends the light collected here to a spectrometer, controlling the transmission spectrum during evaporation. (h) In-situ transmission at 630 nm during evaporation of 800 nm Alq<sub>3</sub>:DCM (red circles) and corresponding simulation of layer thickness (black line).

controlled by an in-situ transmission measurement (g), where the transmission at a given wavelength is monitored during the whole evaporation process. Here, thin-film interference leads to a characteristic transmission behaviour over time that accurately can be assigned to the film thickness, as depicted in Figure 3.4 (h). To obtain wedged layers, a rotating shutter is placed in front of the sample, that partially shadows the evaporation source and thus enables varying film thicknesses on one sample. For photodetectors, organic layers are evaporated at rates of 0.3 Å/s to 0.6 Å/s, or by thermal co-evaporation of matrix and dopant for transport layers, or thermal co-evaporation of donor and acceptor for the bulk-heterojunction. Often, devices containing organic molecules are encapsulated by adding an encapsulation glass in nitrogen atmosphere, as the influence of water vapour and oxygen prove detrimental to their performance.

As oxides such as SiO<sub>2</sub> and TiO<sub>2</sub> require high temperatures of several thousand Kelvin[181], they are typically evaporated from liquid (TiO<sub>2</sub>) or sublimated (SiO<sub>2</sub>) under ultra high vacuum using an electron or ion beam. Here, the oxide films are prepared in a vacuum chamber via electron beam evaporation (a) under a base pressure of  $5 \times 10^{-7}$  mbar and a partial oxygen pressure of  $2 \times 10^{-4}$  mbar. Here, the additional oxygen pressure prevents the formation of unwanted suboxides in the TiO<sub>2</sub> vapour, as these leads to uncontrolled changes of the refractive index and

parasitic absorption in the mirror. A heated tungsten filament emits an electron current which is accelerated to 8 kV and guided via magnetic fields into the different crucibles, containing the oxides in purified granulates or pellets<sup>4</sup>. On the substrate (d), the oxides form amorphous thin films. A constant rate of 2 Å/s for both oxides is again controlled by a QCM (b).

Metal thin films can be produced by either thermal or electron beam PVD, under a base pressure of  $1 \times 10^{-6}$  mbar. For the evaporation of silver films, high deposition rates (2 Å/s to 6 Å/s) are desirable, as the remaining kinetic energy of silver atoms at the sample surface enables a random walk and promotes aggregation and clustering of silver into small islands [63, 182], which is counteracted by a high evaporation rate [183].

### 3.1.4 Growth of Metal Layers

For the application in microcavities, the optical quality of all layers involved determines the device performance and requires careful optimisation. Here, especially the thin film behaviour of metal layers can make the difference between high reflectivity or high absorption and thus has to be carefully examined for achieving best devices. The growth of incomplete layers or islands of conductive materials gives rise to the formation of localised surface plasmons (LSP) that cause strong extinction of light in the visible range and thus are often undesired in optical devices (see Section 2.1.2).

The growth of thin films can be categorised into three mechanisms strongly depending on the materials and conditions involved: In *Frank van der Merwe* growth (Figure 3.5 (a)), the material forms a closed monolayer, filling all gaps before the growth of a second layer starts. Resulting from this mechanism are very low roughness and minimal parasitic optical absorption by LSPs. Conductive paths through layers are reached at very low thicknesses here. On the contrary, *Volmer-Weber* growth (Fig. 3.5 (c)) features the clustering of material and the formation of isolated islands, giving rise to high roughness and less favourable optical conditions among which is the pronounced excitation of LSPs. Furthermore, as metal- or TPP-based cavities strongly depend on the thickness of the metal film involved [7, 42], high surface roughness on the micro-scale (where typical laser mode volumes reside) leads to a broadening of the optical resonance and thus a decrease of quality factor. An intermediate process is the *Stranski-Krastanov* growth (Fig. 3.5 (b)), where the material forms a closed monolayer first, when the wetting of the surface is energetically desirable, and continues with island growth on top. Typically, all processes take place in different magnitudes, depending on the experimental conditions.

To promote the desired *Frank van der Merwe* growth where possible, favourable evaporation conditions have to be found as well as the substrate or underlying layer have to be considered

---

<sup>4</sup>TiO<sub>2</sub>, 99.9% Prof. Feierabend GmbH; SiO<sub>2</sub>, 99.997% Prof. Feierabend GmbH.



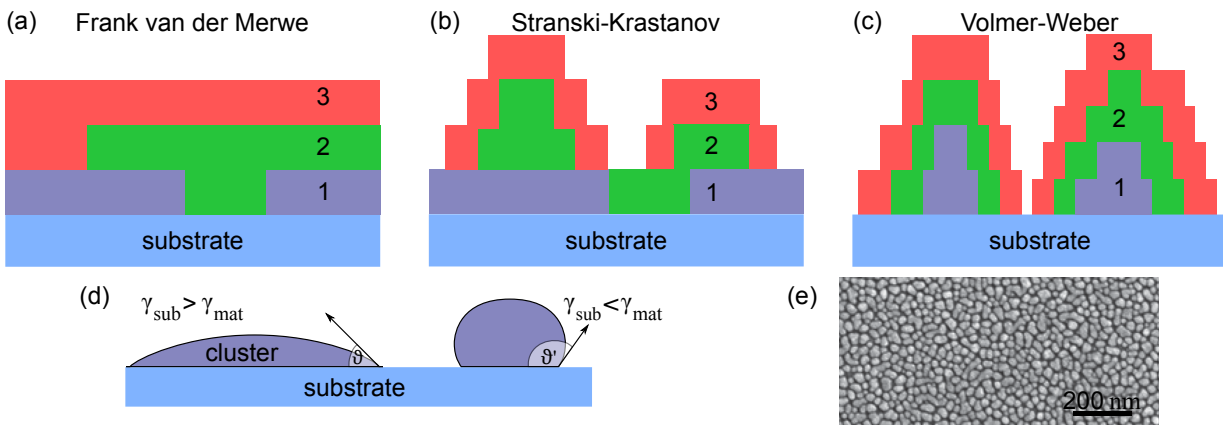


**Figure 3.5:** Illustrations of monolayers (blue, green, red) showing (a) *Frank van der Merwe* growth with smooth and closed layers, (b) *Stranski-Krastanov* growth with islands after a closed monolayer, and (c) *Volmer-Weber* growth with predominantly island formation. (d) Cluster formation of material on a substrate depending on their surface energies. (e) SEM micrograph of 7 nm silver on a low surface energy substrate, showing pronounced island growth. Figure (e) adapted from [185].

for optimisation. During growth, evaporated atoms hit the sample surface with a remaining kinetic energy and propagate along the surface towards places with lowest energy. To influence this behaviour, either the ability of atoms to perform this random walk has to be inhibited, or the energetic landscape of the surface must be considered. Ostwald-ripening (WILHELM OSTWALD<sup>5</sup>) describes the formation of clusters in presence of a saturated gas of atoms utilising the Kelvin equation [63]. Here, a low temperature favours the formation of smaller and more densely packed islands, which tend to coalesce earlier than large, spread-out ones. Additionally, a low substrate temperature inhibits diffusion, as the diffusion coefficient decreases. Furthermore, a high deposition rate proves favourable for an early point of percolation [184], the point where a closed layer is formed.

### Seed-Layer and Diffusion Barrier

Finally, the energetic landscape of the surface, especially the surface energy  $\gamma$ , needed to create a new unit of surface area  $A$  plays an important role:

$$\gamma = \lim_{dA \rightarrow 0} dW/dA \quad , \quad (3.1)$$

where  $W$  is the work done creating a new surface. When evaporating thin films, it is important how the surface energy of the substrate or underlying layer  $\gamma_{\text{sub}}$  relates to the surface energy

<sup>5</sup>Wilhelm Ostwald, 1853-1932, German chemist, received the Nobel Prize in Chemistry in 1909 for his work on catalysis, chemical equilibria and reaction velocities.

of material clusters  $\gamma_{\text{mat}}$ . Figure 3.5 (d) showcases that if  $\gamma_{\text{sub}} < \gamma_{\text{mat}}$ , the energy needed for the material to wet the substrate is greater than the energy needed to attach to a cluster of material. Islands that form under this condition cover little area and show large contact angles  $> 90^\circ$ . If  $\gamma_{\text{sub}} > \gamma_{\text{mat}}$  however, the wetting of the surface is favourable and islands grow exhibiting small contact angles and cover large areas. As silver exhibits a large surface energy  $\gamma \approx 1.25 \text{ J/m}^2$ , compared to the typical layers and substrates in organic microcavities such as  $\text{SiO}_2$  ( $\gamma \approx 0.31 \text{ J/m}^2$ ),  $\text{TiO}_2$  ( $\gamma \approx 0.38 \text{ J/m}^2$ ) [186] and most organics ( $\gamma < 0.1 \text{ J/m}^2$ ), it tends to show unfavourable growth on those materials, and thin film formation is inhibited, as shown in a scanning electron micrograph (SEM) in Figure 3.5 (e). Instead, thin high surface energy seed-layers such as Al ( $\gamma \approx 1.15 \text{ J/m}^2$ ) and Au ( $\gamma \approx 1.8 \text{ J/m}^2$ ) [187] are utilised below the silver to improve the optical and electrical quality of the thin film [185, 188].

In addition, noble metals often do not react strongly with surfaces of organic thin films [188, 189] and tend to diffuse into the organic layer. Here, a diffusion barrier layer of either base metals such as Al or thin oxides such as  $\text{MoO}_3$  ( $\gamma \approx 0.06 \text{ J/m}^2$ ) can be utilised below the metal layer, and strongly improve the layer formation and device performance [190].

## 3.2 Photo-Patterning of Interlayers

Controlling the photon dispersion in more than one dimension requires the patterning of microcavities also in-plane. Here, thin interlayers of either  $\text{SiO}_2$  or Ag are used in conjunction with photolithography to create micron-scale patterns and thus facilitate photonic confinement in the lateral direction. While maskless photolithography<sup>6</sup> proves a flexible way to expose the photoresist, creating patterns  $> 10 \mu\text{m}$ , for most applications a mask aligner<sup>7</sup> with corresponding contact photomask<sup>8</sup> is required for highest resolution exposure.

### 3.2.1 Photolithography

On top of the bottom DBR, a patterned interlayer is produced by two types of photolithography. For metal layers, an etching process is feasible to use, as depicted in Figure 3.6. A thin metal layer is deposited on the mirror via thermal deposition in vacuum, under a base pressure of  $1 \times 10^{-6}$  mbar. A commercial negative tone photoresist<sup>9</sup> of  $2 \mu\text{m}$  thickness is spin-cast on top and annealed for 1 min at  $110^\circ \text{C}$ . After UV-exposure through a chrome contact-mask, the exposed parts of the resist crosslink, which is further enhanced by the post-exposure bake at  $100^\circ$  for 1

<sup>6</sup>Maskless Exposure System SF-100 Extreme, Intelligent Micropatterning LLC

<sup>7</sup>Mask Aligner MJB4, SUESS Microtec AG.

<sup>8</sup>Photronics Dresden GmbH and Compugraphics Jena GmbH.

<sup>9</sup>AZ nLOF2020, MicroChemicals

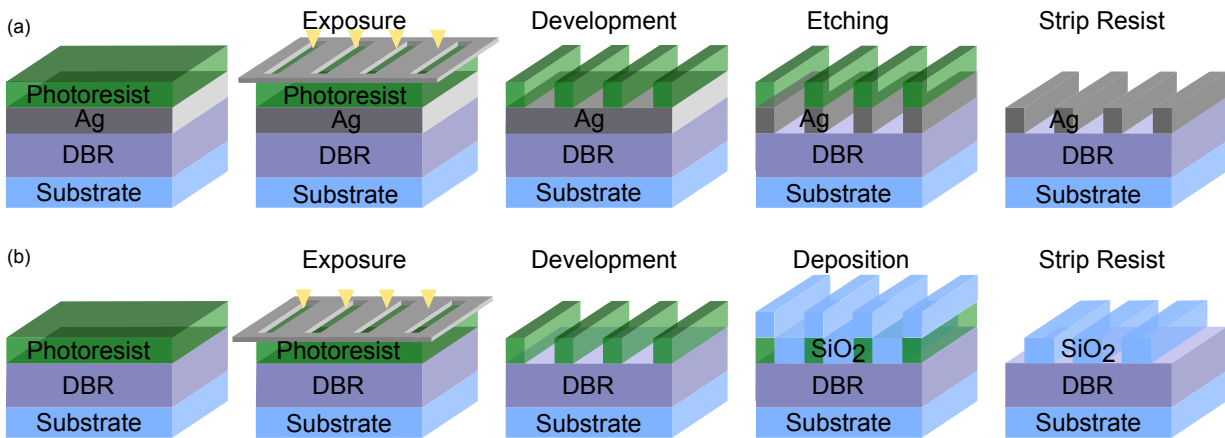


**Figure 3.6:** Photopatterning of interlayers. (a) Photolithographic etching process used for metal layers. After deposition of a bottom DBR and a thin metal layer, a photoresist layer is deposited on top via spin-casting and exposed by i-line UV light (365 nm) through a contact shadow mask. After development, the resist serves as a protection for the underlying metal during the etching process. Finally, the resist is stripped after structuring. (b) Photolithographic lift-off process. Here, the resist is deposited on the DBR itself and, after exposure and development, serves as a lift-off resist for material deposited on top. The resulting image will be the negative compared to process (a). Reprinted from [7].

minute. For very high resolutions, and thus small structure sizes, care has to be taken during exposure to avoid unwanted interference of light refracted at the mask. Here, an unwanted substructure can appear and influence the final pattern (see Figure 3.8 (b)). Subsequently, the non-crosslinked parts can be dissolved during development in tetramethylammonium hydroxide (TMAH). For wet-etching, the remaining resist is further fixed by heating at 120°C for 3 minutes in a hardbake step to increase its resistance to the etchants. The patterned resist layer serves as a protection of the underlying silver which can now be wet-etched using either in nitric acid (HNO<sub>3</sub>), or plasma-etched using Ar ions. Finally, the remaining resist can be removed in various solvents, such as N-methyl-2-pyrrolidone (NMP), leaving the DBR with patterned silver on top for further deposition of the cavity. Figure 3.8 (c) shows a silver layer on top of a DBR, patterned into an array of 2×2 μm wide squares, showing excellent quality over the whole macroscopic structure.

Here, wet etching proves successful for larger patterns >5 μm, while smaller patterns suffer as the etchant can creep below the resists and leads to significant damage of the protected area as well. Etching with an accelerated Ar ion beam proves a superior method for the high-resolution patterning of silver, as the directed nature of the ion beam makes the pre-patterned photoresist an ideal aperture. Here, a direct transfer of the pattern from resist to underlying layer is provided. However, the ion beam exposure leads to increased temperatures, which becomes especially no-

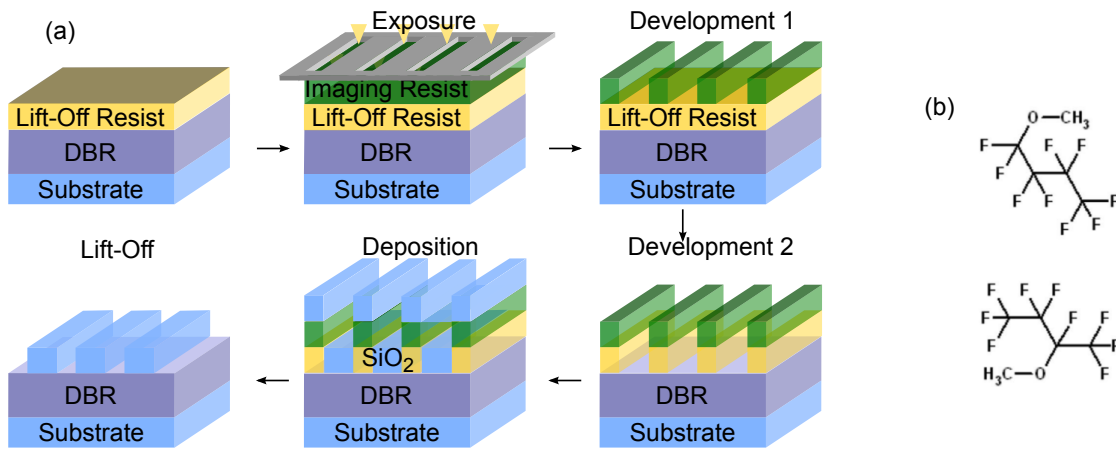


**Figure 3.7:** (a) Lift-off process utilising additional lift-off resist. Before the deposition of the imaging resist, a non-photoactive lift-off resist (e.g. a highly fluorinated resist) is deposited via spin-casting. After deposition, exposure and development of the imaging resist on top, the lift-off resist is developed through the imaging resist. (b) Molecular structure of the HFE comprising two isomers of C<sub>5</sub>H<sub>3</sub>F<sub>9</sub>O. Figure (b) adapted from [191].

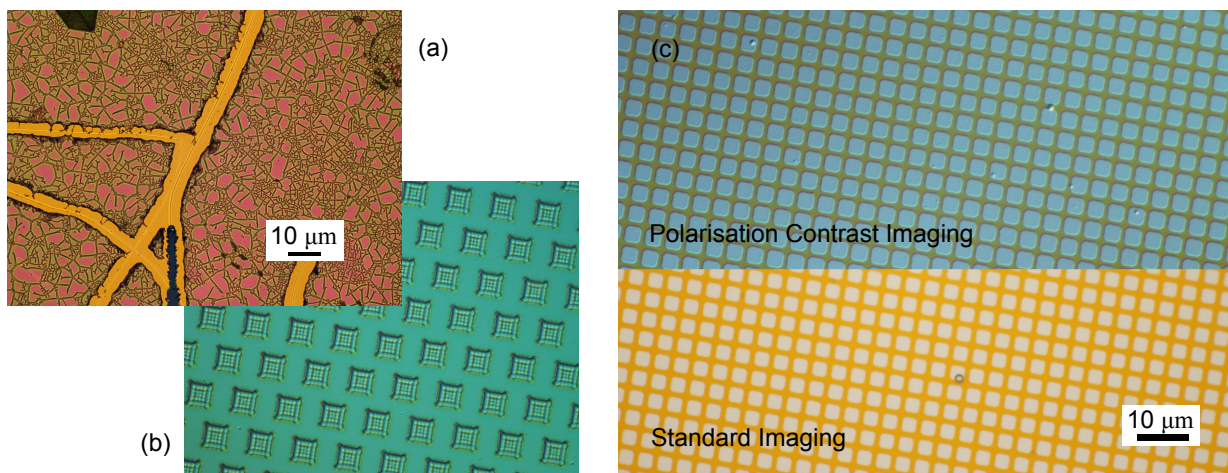


**Figure 3.8:** (a) Unsuccessful lift-off of SiO<sub>2</sub> on a single resist layer. The layer deposited on top cracks but does not lift off completely. (b) Interference effects in developed photoresist. For small structures in high resolution lithography, an additional sub-structure may appear in the photoresist due to interference during the exposure step. (c) Micrograph of 2 μm square-patterned Ag on a DBR made by standard (bottom) and polarisation contrast imaging (top).

ticeable on the edges of the photoresist, where high peak temperatures lead to a hardbake of the resist, as the grade of crosslinking increases. The highly crosslinked resist becomes increasingly difficult to strip, requiring the use of additional mechanical forces (such as ultrasonic bath) or higher process temperatures in the final solvent which may lead to damage of the essential microcavity layers. As dielectric materials such as  $\text{SiO}_2$  are not easily etched, especially without damaging the DBR, a lift-off process is used for them (Fig. 3.6 (b)). The photoresist is cast directly onto the DBR and, after development, serves as a deposition mask for the  $\text{SiO}_2$  layer. After deposition, the resist and  $\text{SiO}_2$  on top of it can be lifted off in appropriate solvents. As this step is less controllable and prone to errors, lift-off processes are not used for the metal layer. Additionally, layers deposited on top of the imaging resist and high process temperatures during electron beam evaporation can again lead to a strong crosslinking and hardening of the resist. Figure 3.8(a) shows the unsuccessful lift-off of a  $\text{SiO}_2$  layer on a DBR, where the resist is only removed in a small area overall but remains as a cracked layer together with the oxide film on top. To improve the lift-off, a double resist system with a fluoropolymer layer as bottom resist can be used [191], which is soluble in hydrofluoroethers (HFEs, [192]). As detailed in Figure 3.7, the highly fluorinated resist<sup>10</sup> is cast directly on the DBR. After annealing at 80° C for 1 minute, the imaging resist is cast on top and annealed for 1 minute at 110° C. The imaging resist can then be exposed and developed as usual, as the fluorinated resist is inert to TMAH and is subsequently etched by an HFE<sup>11</sup>. Similarly to the lithographic etching process above, the imaging resist serves as a protection layer to the SL1 in this step. The pattern transfer between the resists has to be carefully controlled, as for the final lift-off an undercut is required, i.e. the fluorinated resist has to be etched below the edges of the imaging resist also. Here, an insufficient etching will not yield the necessary undercut and lead to problems in the final lift off, while an overestimated etching can lead to a folding down of the imaging resist, which can attach to the sample surface and leave unwanted residue. After lift-off, we obtain a DBR with patterned  $\text{SiO}_2$  layer for further use.

## 3.3 Optical and Electrical Characterisation

### 3.3.1 Micro-Photoluminescence

For below and above threshold investigations of our microcavities, we use either a 405 nm cw laser diode<sup>12</sup>, or a pulsed 532 nm solid state laser (1.5 ns pulse length @ 2 kHz, (a))<sup>13</sup>. In our mea-

---

<sup>10</sup>SL1, Orthogonal Inc.

<sup>11</sup>HFE 7100, Orthogonal Inc.

<sup>12</sup>Coherent CUBE 405-50C

<sup>13</sup>CryLas, FDSS-532-Q2

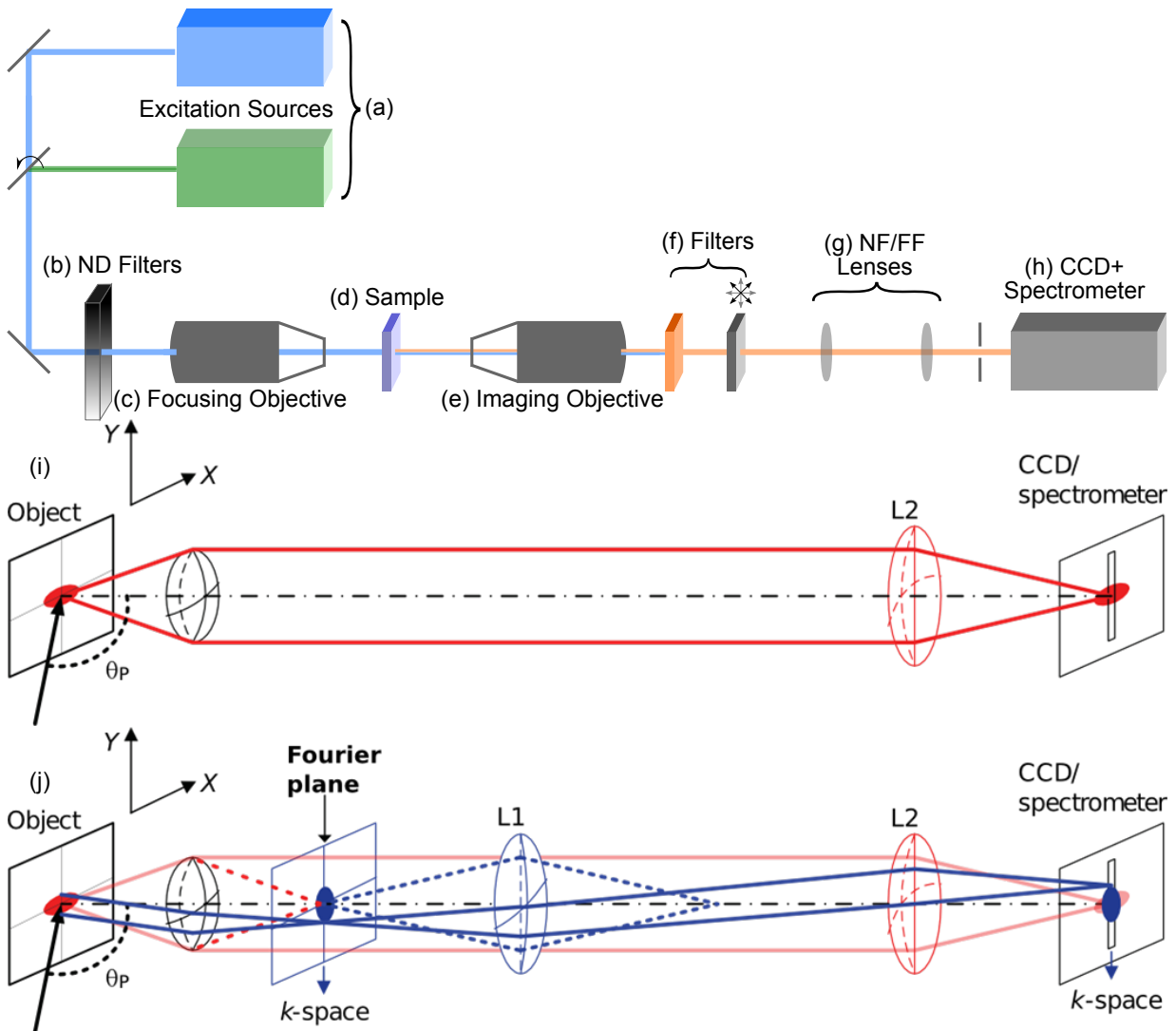


**Figure 3.9:** Micro-photoluminescence setup. (a) Excitation sources 405 nm cw laser; 532 nm pulsed ns laser. (b) ND filters to decrease excitation pulse energy. (c) Objective (25 $\times$ , NA=0.5) focusing the excitation onto the sample to spot sizes 2  $\mu\text{m}$  to 20  $\mu\text{m}$ . (d) Sample in movable  $x - y$  stage. (e) Imaging objective (63 $\times$ , NA=0.8) collecting emission/transmission from the sample. (f) Excitation light filter and polarisation filter. (g) Near-field and far-field lenses, imaging either the spatially (NF) or angularly (FF) resolved emission onto the entrance slit of (h) 0.6 m imaging spectrometer. Additionally, the direct image can be recorded via a CCD. Figure reprinted with permission from reference [7]. (i) and (j) Ray sketches of near-field and far-field spectroscopy, respectively. Adapted from [90].

surement setup in Figure 3.9, they are focused onto the sample (d) in spot diameters from 2  $\mu\text{m}$  to several tens of  $\mu\text{m}$  to observe photoluminescence (PL) and lasing of the organic microcavity. Using either the near-field or the far-field lens (g), we get access to the spatially or angularly resolved spectrum, respectively, by focusing either the image plane or its Fourier-distribution[90] onto the entrance slit of a 0.6 m imaging spectrometer recorded by a cooled charge-coupled device (CCD) camera (h). The spectra are recorded unpolarized or in different polarizations using the filter (f). The excitation intensity can be tuned via a neutral density filter wheel (b). All experiments are performed at room-temperature under ambient conditions.

To observe the cavity dispersion, the far-field lens images the Fourier space instead of the image space (see Fig. 3.9 (i) and (j)) onto the spectrometer and in turn allows an angle-resolved measurement, up to angles according to the numerical aperture of the imaging objective. Here, a NA of 0.8 corresponds to a maximum angle of  $\vartheta = \arcsin(\text{NA}/n_{\text{air}}) \approx 53^\circ$ .

### 3.3.2 Further Methods

#### Imaging and Spectroscopy

In addition to the micro-photoluminescence setup, samples are investigated regarding their optical properties and transmission as well as reflection spectra. To investigate the quality of photolithographic structuring, an inverted confocal microscope<sup>14</sup> is used in either transmission or reflection geometry. Furthermore, the use of polariser, analyser and Wollaston prism allows for the observation of thin films in polarisation contrast imaging [193], creating differently coloured images depending on film thickness. Here, it is especially useful to distinguish the lithography photoresist or thin patterned layers from the sample surface as these provide a good contrast in the micrograph. Figure 3.8 (c) shows the comparison between standard and polarisation contrast imaging.

To investigate the transmission and reflection of samples, a two-beam UV-VIS-NIR spectrometer<sup>15</sup> is utilised. Here, three different detectors enable the detailed spectral investigation in the UV and visible range (photomultiplier) and the near infrared (InGaAs and PbS detectors).

While Fourier-space imaging gives easy access to the angle resolved spectrum, the angle is restricted by the numerical aperture of the imaging objective. To observe large angles, a goniometer<sup>16</sup> is utilised, where two arms for illumination and detection are rotated around the sample.

---

<sup>14</sup>Nikon Eclipse Ti LV100D

<sup>15</sup>SolidSpec-3700/3700DUV, Shimadzu

<sup>16</sup>HZG-3, Freiburger Präzisionsmechanik

**External Quantum Efficiency in Solar Cells and Photodetectors**

While microlasers are investigated optically, the characterisation of photodetectors requires measuring the current-voltage characteristics and external quantum efficiency of the devices. The IV-curve is measured under no illumination (dark), under the illumination of a sun simulator at  $1000 \text{ W/cm}^2$  with the spectrum of a Xe lamp, and under monochromatic illumination of an infrared light emitting diode. As the solar cell behaviour of samples investigated here is not of importance, the IV characteristics are not mismatch-corrected.

To obtain the EQE, the solar cell is illuminated by monochromatic light modulated by a chopper wheel and the resulting photocurrent is preamplified by a transimpedance amplifier and recorded with a lock-in amplifier [194]. All EQE measurements are carried out under short-circuit conditions without additional bias illumination. To characterise a large number of devices, the measurement is carried out with the help of a specially configured robot.



# 4 Planar Microcavities with Dielectric and Plasmonic Interlayers

*This chapter serves as an introduction into the experimental part of this work, detailing the behaviour of planar and wedged microcavities and the manipulation of the cavity resonances via different interlayers. In Section 4.1.1, lasing of an organic microcavity with a thickness gradient is investigated, showing tunability of the laser mode over 90 nm.*

*In the following, plasmonic (Section 4.1.2) and dielectric (Section 4.1.3) interlayers are introduced next to the cavity layer, facilitating a shift of the microcavity resonance as the result of either the manipulation of the cavity layer thickness or the behaviour of the phase at the cavity-interlayer interface.*

*In the final Section 4.2 of this chapter, the growth of high quality thin silver films in organic microcavities is investigated, leading to the use of both a diffusion barrier and seed layer to double the optical quality of silver desposited on top of an organic cavity layer.*

## 4.1 Microcavity Dispersion and Lasing

### 4.1.1 Planar and Thickness-Gradient Microcavities

Planar microcavities have been investigated for a long time and apart from their inorganic counterparts, microcavities comprising an organic active layer exhibit interesting properties. The large spectral width of the photoluminescence provides a large gain bandwidth, exploited in different types of resonators. A way of realising a continuously tunable single device was provided by Schütte *et al.* [118], comprising not a planar but wedge-shaped active layer. Such architectures can be realised by evaporation under oblique substrate positioning, but a more elegant and controllable way is to use of rotating partially covering shutter mask [195], restricting the amount of material passing through based on spatial position on the sample and shutter geometry. Resulting from this technique is a thickness gradient dependent on the type of mask used. Here, an Alq<sub>3</sub>:DCM cavity layer with varying thickness from 485 nm to 650 nm is fabricated on top of a high quality DBR. The thicknesses correspond to  $3\lambda/2$  for differing cavity mode

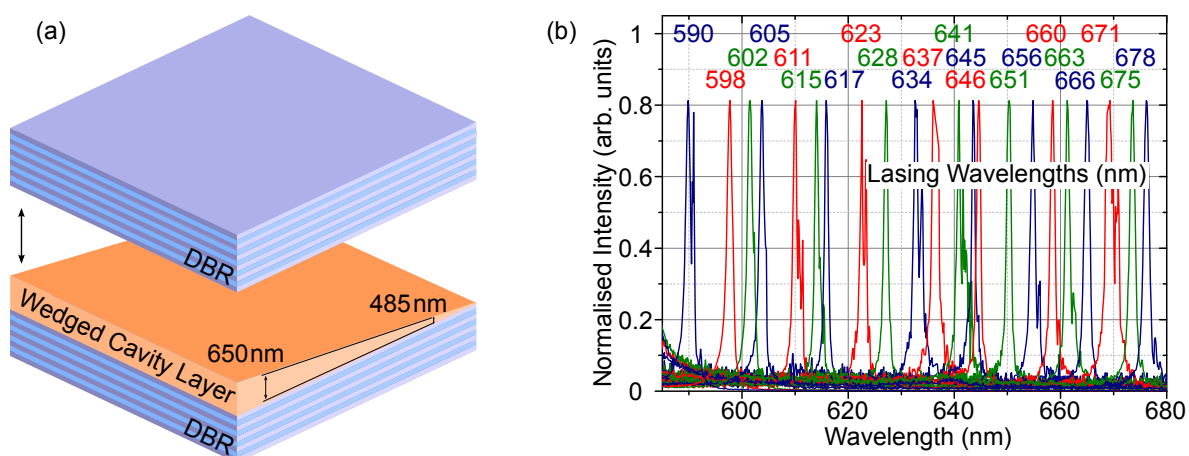


**Figure 4.1:** (a) Schematic for the wedged organic cavity with a  $3\lambda/2$  cavity layer for continuously varying cavity wavelengths. Shifting the excitation spot over the sample enables cavity lasing in a wide range of different wavelengths. (b) Emission spectra of lasing from different tunable wavelengths covering almost 90 nm from 590 nm to 678 nm.

wavelengths. To achieve the largest spectral range of lasing in the system, highest gain values and lowest lasing thresholds are sought. It has been shown that  $3\lambda/2$  cavities outperform  $1\lambda/2$  cavities in this regard [9, 196] although higher material usage results. Fabricating a high quality DBR on top, the finished microlaser, depicted in Figure 4.1, exhibits quality factors ranging from  $Q = 450 \dots 1050$  (limited by spectral resolution) for different wavelengths. As the DBR design wavelength is fixed for the whole device, the lasing mode shifts within the stop band, resulting in different degrees of confinement due to varying DBR reflectivity and thus decreasing  $Q_y$  factors when approaching the stop band edge.

Here, the wedge introduced in the active and top DBR layer is comparatively small on the full scale of the 2.5 cm wide sample (on the order of  $10^{-5}$  rad) and thus does not negatively influence the performance of the device on the lateral length scale of lasing modes [9, 118, 197] which can be described as locally planar. Exciting the DCM directly with a 2 ns laser pulse at 532 nm, the stimulated emission regime can be reached for a wide range of emission wavelengths at different pump positions over the full spatial width of the device. Figure 4.1 shows laser mode spectra from 590 nm to 678 nm for a multitude of different excitation spots. This ultra-wide range spanning over almost 90 nm is achieved on a single device comprising the same emitting molecules and completely covered by the DBR stop band. Continuous tuning is realised by small shifts of the pump spot, 22 different lasing wavelengths are exemplarily shown here. While the DBR in principle allows an even wider range of wavelengths, decreasing quality factors, increasing self-absorption, and, most of all, the limited gain band width of the dye restrict further tunability. A fabrication of wedged DBR layers can facilitate a tunable mirror stop band and thus

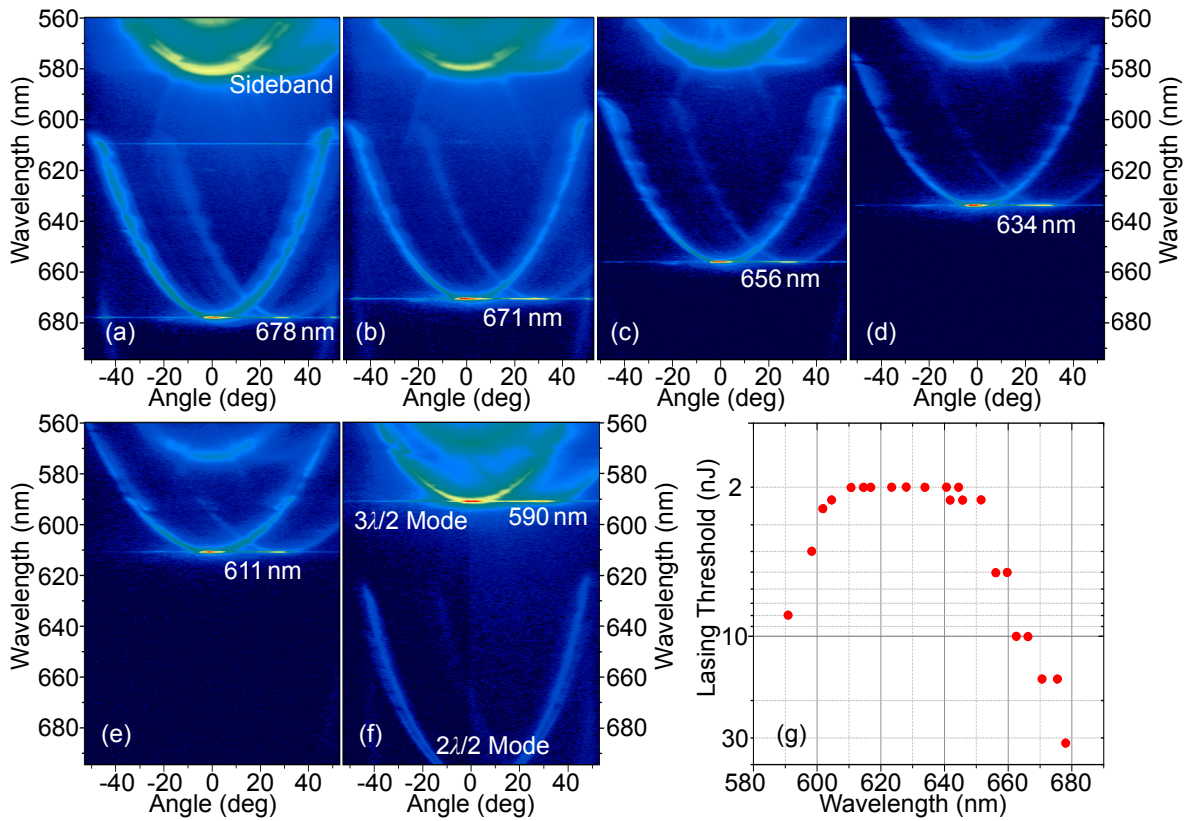


**Figure 4.2:** (a)-(f) Far field emission spectra of tunable lasing from a wedged organic microcavity. The cavity mode shifts according to the changing cavity thickness at different points of excitation. Lasing can be observed as the intensity concentrates at the dispersion parabola apex in all figures. The copy of the dispersion curves at larger positive angles is an artifact of the measurement setup. (g) Lasing thresholds for different wavelengths in the same sample. Lasing threshold decreases towards the gain maximum of Al<sub>q</sub>:DCM around 630 nm.

further widen the spectral range, although additional emitters for longer/shorter wavelengths might be required.

For all tunable wavelengths, a parabolic cavity mode dispersion can be observed in angle-resolved spectroscopy. The varying cavity thickness leads to a shift of the full cavity parabola within the spectral range observed. Figure 4.2 (a)-(f) shows just-above-threshold spectra of different cavity wavelengths. For comparison, lasing thresholds of all modes are presented in Figure 4.2 (g). Here, it becomes obvious that the threshold decreases towards the wavelength of optimum photoluminescence of the active system at 630 nm, where a threshold pulse energy of 2 nJ is observed. Between 610 nm and 650 nm, a plateau forms (in the limited resolution of the threshold measurement) beyond which the threshold drastically increases by up to more than one order of magnitude compared to best conditions. Nevertheless, stable operation is achieved for all wavelengths and excitation energies at repetition rates of 2 kHz, corresponding to total

excitation powers of  $4 \mu\text{W}$  to  $70 \mu\text{W}$  focused in a spot of few  $\mu\text{m}$  in diameter (corresponding to  $\approx 100 \text{ W/cm}^2 \dots 2000 \text{ W/cm}^2$ ).

In addition to changing the apex wavelength of dispersion for different active layer thicknesses, the shape of the parabola differs as well. For decreasing wavelengths, an increase of the opening angle can be seen in the far field spectra, especially visible in Fig. 4.2 (f), where the  $3\lambda/2$  mode at  $590 \text{ nm}$  and the  $2\lambda/2$  mode at  $700 \text{ nm}$  are visible in the same spectrum. The large wavelength parabola appears significantly narrower than the one at smaller wavelengths. This observation is a direct result of the shift of the mode inside the DBR stop band and thus varying penetration of the laser mode from the active into the DBR layers. As detailed in Section 2.2.4, this penetration is especially important when the cavity mode approaches the edge of the stop band, and in turn modifies emission wavelength and dispersion of the microcavity. While in typical devices a large detuning is not desired, it has to be taken into account here. This effect alters the dispersion relation in Equation (2.63), where ideal conditions are assumed, according to the calculations of Panzarini *et al.* [77]. Thus, care has to be taken when leaving such ideal conditions and a more dramatic manipulation of the cavity dispersion is desired. Such manipulation is manifested in the introduction of various interlayers of plasmonic or dielectric nature, as a change in cavity thickness or phase distribution in the cavity lead to significant spectral shifts.

### 4.1.2 Metal-Organic Microcavities

The first method to influence the cavity spectrum is the inclusion of thin metal films into the microcavity. While it seems counterintuitive to include a highly absorbing layer into a high-performance DBR microcavity, the use of a highly conductive layer promises interesting investigations on the interaction of light and plasmons, as well as pathways for future electrical excitation in direct applications. Here, silver is used due to its favourable properties of high reflectivity in comparison to other noble metals in the VIS and the possibility to structure thin films under ambient conditions. As detailed in Section 2.2.5, adding a thin metal film into a microcavity leads to the formation of Tamm-plasmon-polariton (TPP) states, as the interaction of light in the cavity and plasmons in the metal layer facilitates a phase shift at the interface of the organic active layer to the silver film. In the experiment, a standard organic microcavity with  $2 \times 21$  layer DBRs and an organic active layer is fabricated. In addition, half of the cavity is covered by a  $30 \text{ nm}$  thick silver film to directly compare the bare cavity mode to the TPP states in the same sample. In Figure 4.3, we clearly see the parabolic cavity mode with a high quality factor, starting at  $620 \text{ nm}$  in the silver-free area in both simulation and experiment. Adding  $30 \text{ nm}$  of silver, the cavity state shifts by approximately  $70 \text{ meV}$  ( $22 \text{ nm}$ ) to the red, forming the TPP state 1, still exhibiting significant quality factors of about 700. Furthermore, a second TPP

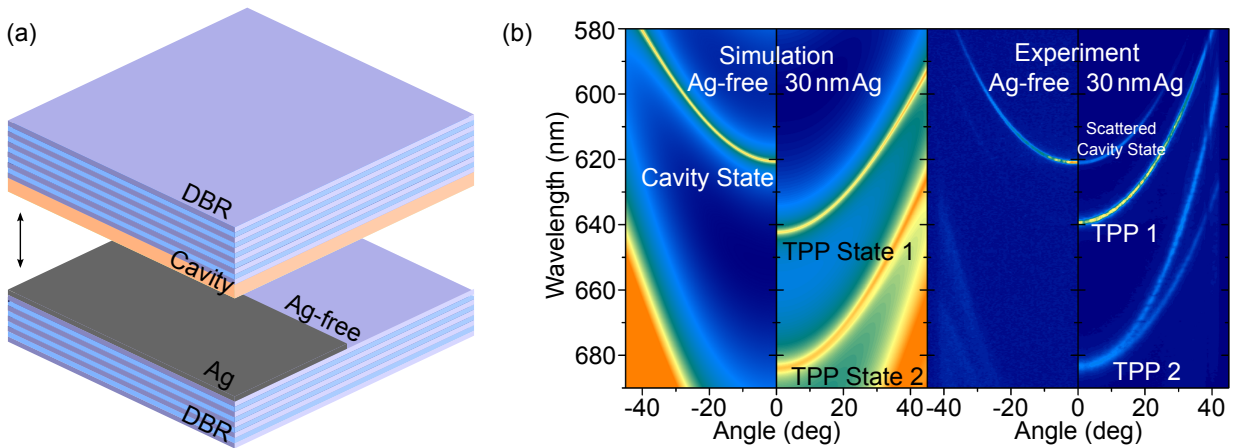


**Figure 4.3:** (a) Schematic of sample with and without metal layer in the cavity. (b) Simulated transmission (left) and experimental emission (right) spectrum of the microcavity at excitation in and outside of the metal-covered area. Tamm-plasmon-polariton states appear when adding a thin metal film, in agreement with theory. TPP state 2 shows a pronounced polarisation splitting.

state appears at 685 nm, showing pronounced polarisation splitting [82] and much lower quality factors due to its origin in the adjacent DBR layer (Section 2.2.5) and detuning towards the DBR stop band.

It is important to note that the resonances of either area are suppressed in their corresponding non-resonant area, e.g. the TPP modes are not resonant in the metal-free section of the sample. Although in the experiment, emission from the cavity mode is visible in the metal-covered area as well, this signal represents light scattered into lateral direction, showing up as cavity state emission from the metal-free part even tens of  $\mu\text{m}$  away from the silver edge, and does not originate from the TPP area.

This spectral shift opens up the possibility to manipulate the cavity dispersion on a small lateral scale. Instead of utilising a wedged cavity, which by its nature is restricted to very small gradients, the resonance can be shifted on the micro-scale by adding a thin silver film. Patterning said film can thus lead to much higher degrees of optical control and facilitate optical confinement (Chapter 5) and the formation of photonic lattices (Chapter 6).

For the formation of TPP states, the thickness of the silver film plays an important role [42]. Here, different thicknesses of laterally extended ( $> 200 \times 200 \mu\text{m}^2$ ) metal patches are deposited in a single organic microcavity to directly study the dependence of the far field emission spectra. Figure 4.4 shows such spectra for varying thicknesses from  $\approx 10$  nm to 40 nm, taken at the edge of the metal patch and the metal-free area. Here, emission into negative angles represents the cavity state emission into the metal-free side, while positive angles are directed into the metal patch and thus show emission of the TPP state 1. The variation of metal films facilitates a

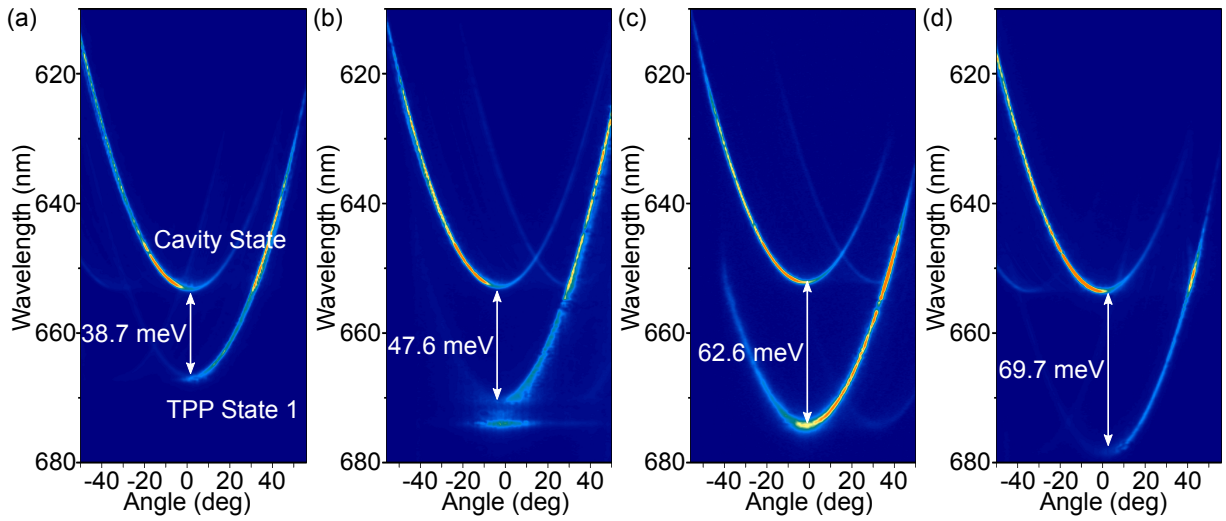


**Figure 4.4:** Far field emission spectra at the edges of metal layers of differing thicknesses ((a)  $\approx 10$  nm (b) 20 nm (c) 30 nm (d) 40 nm). While the cavity state retains its spectral position, the TPP state 1 red-shifts for increasing metal thicknesses, according to expectation.

variation in coupling strength, shifting the mode by 39 meV ( $\approx 10$  nm metal), 48 meV (20 nm metal), 63 meV (30 nm metal), and 70 meV (40 nm metal). As expected, an increase in silver film thickness leads to a stronger red shift of the TPP state compared to the constant position of the cavity state emission. Here, the shift observed strongly depends on a multitude of factors, including design of the DBRs, position and detuning of the original cavity mode, and optical quality of the silver film. Each variation requires solving the coupled resonator equation (2.68) using transfer matrix methods, for the exact thicknesses of each layer involved, while the general trends observed here are valid.

The inclusion of thin metal films proves a reliable and controllable way to manipulate the microcavity dispersion on the micro-scale. While small losses in optical quality are unavoidable, the rich physics of coupling to plasmons as well as pathways to application make this nevertheless an important area of investigation. When a loss-free manipulation is sought, dielectric interlayers such as  $\text{SiO}_2$  can be used, influencing the dispersion in a similar way although through fundamentally different properties.

### 4.1.3 Microcavities with $\text{SiO}_2$ Interlayers

The formation of a microcavity can be explained optically by the introduction of a  $l \times \lambda/2$  layer of a low refractive index material into a periodic DBR structure, where the breaking of the periodicity introduces an optical trap state much like the formation of trap states between energy bands in condensed matter. Following this analogy, the position of the trap state can be altered by

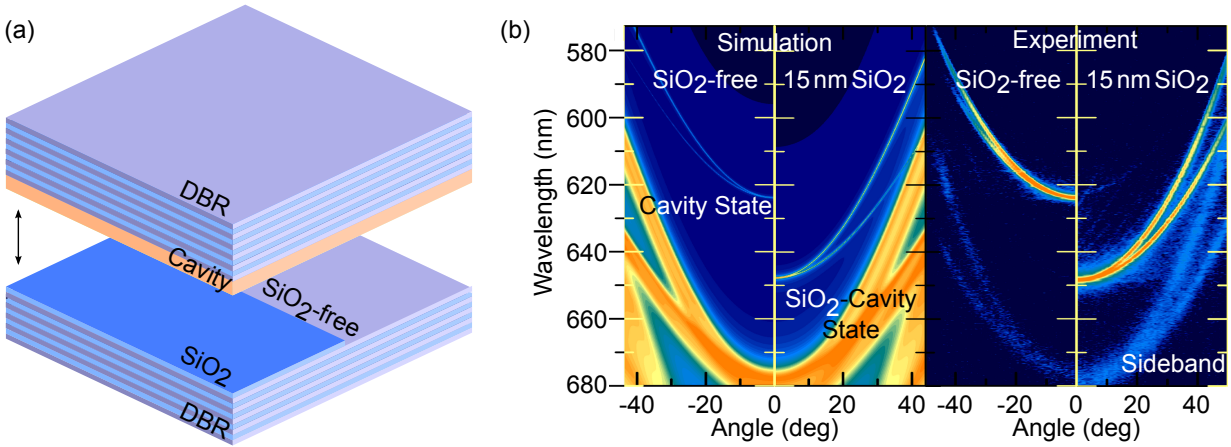


**Figure 4.5:** (a) Schematic of sample with and without SiO<sub>2</sub> interlayer in the cavity. (b) Simulated transmission (left) and experimental emission (right) spectrum of the microcavity at excitation in- and outside of the SiO<sub>2</sub>-covered area. The added interlayer locally increases the cavity thickness and red-shifts the original resonance from 623 nm to 649 nm. The combined SiO<sub>2</sub>-organic cavity state exhibits pronounced polarisation splitting, as expected from far-detuned modes.

changing the shape of the defect, such as the thickness of the cavity layer. As shown in Section 2.2.3, a variation in thickness of the cavity layer only can move the position of the resonance inside the mirror stop band and thus enable again the direct manipulation of dispersion by adding a patterned interlayer in the system. While a microstructuring of the organic active layer is possible [191, 192], inserting a non-absorbing low refractive index dielectric film provides the same optical effect (except for optical net gain) and can locally increase the cavity thickness.

Here, the low index mirror material SiO<sub>2</sub> is utilised as a thin interlayer between bottom DBR (with TiO<sub>2</sub> as topmost layer) and organic layer, creating a combined SiO<sub>2</sub>-organic cavity with an effective thickness

$$d_{C,\text{eff}} = n_{\text{Alq}_3}d_{\text{Alq}_3} + n_{\text{SiO}_2}d_{\text{SiO}_2} \quad , \quad (4.1)$$

leading to an approximate resonance shift of  $E_0 \approx \pi\hbar c / (n_{\text{Alq}_3}d_{\text{Alq}_3} + n_{\text{SiO}_2}d_{\text{SiO}_2})$ . The resulting far field spectra can be seen in Figure 4.5, showcasing the significant spectral shift induced by adding only 15 nm of SiO<sub>2</sub> in the cavity. Optically increasing the cavity thickness leads to a very efficient manipulation, decreasing the resonance by  $\approx 85$  meV for such a thin interlayer. The detuning of the cavity furthermore leads to a penetration of light into the DBR layers. For far-detuned cavities, the resonance energy is strongly influenced by this effect which has to be taken into account for a correct mode description. Here, the resonance condition alters according to Equation 2.65 in Section 2.2.4, leading to additional spectral shifts and a splitting of the cavity mode into its two polarisations at higher angles. The combined SiO<sub>2</sub>-cavity mode in Fig. 4.5 (b) exhibits a very strong polarisation splitting, the upper branch belonging to TE, the lower branch

to TM polarisation. Such effects have been observed and explained in detuned cavities [198] and metal-organic cavities [82] before.

Nevertheless, the introduction of thin SiO<sub>2</sub> layers proves a very successful way to manipulate the cavity dispersion with a loss-free material capable of retaining high quality factors for lasing in patterned and unpatterned areas. While the result of both plasmonic and dielectric interlayers is very similar, the nature of the resonance shift is fundamentally different. While SiO<sub>2</sub> increases the cavity thickness and thus facilitates the change in cavity dispersion, plasmons at the interface to metal layers generate a change of phase and form red-shifted TPP states. Both methods prove useful for controlling light in microcavities and shall be used throughout this work to facilitate different types of applications.

## 4.2 Growth of High-Quality Thin Silver Films for Microcavities

In order to fully utilise the potential of metal-organic microcavities, the optical quality of the silver layer is of critical importance. Previous work has shown that the growth of very thin silver films is not ideal when deposited on organic layers [199]. The high surface energy of the metal promotes island growth upon thermal evaporation, leading to a rough layer with open holes. Additionally, the noble nature of silver inhibits interactions with the surface of the underlying organics and thus facilitates diffusion of metal atoms or clusters into the active materials. Both these properties are potentially fatal for the realisation of high-quality microresonators. Apart from the rough nature of such silver films and the resulting lowered optical quality, the growth of nano-scale islands leads to strong parasitic absorption, as conductive nanoparticles enable the excitation of localised surface plasmons (LSPs) under direct illumination of light in the VIS. As detailed in Section 3.1.4, the use of a high surface energy seed layer can improve the quality of a silver film deposited on top. For this purpose, very thin layers (1 nm...3 nm) of gold can be utilised, benefitting the silver film on top without having a significant influence on the optical properties.

The morphology of thin conductive films can be observed in scanning electron microscopy as depicted in Figure 4.6 (a)-(d). Here, 25 nm of silver are deposited on a 3 layer DBR (TiO<sub>2</sub>|SiO<sub>2</sub>|-TiO<sub>2</sub>, (a) and (b)) with and without the use of a seed layer of 2 nm Au. While usually the percolation behaviour of ultra thin films (< 10 nm silver) is of interest, here the optical quality of much thicker films is addressed. While for the deposition on top of a TiO<sub>2</sub> layer, the difference of using a seed layer is not significant and not clearly resolved on this scale of SEM measurements, the deposition on top of organics shows a more explicit effect. Here, even for 40 nm of silver on



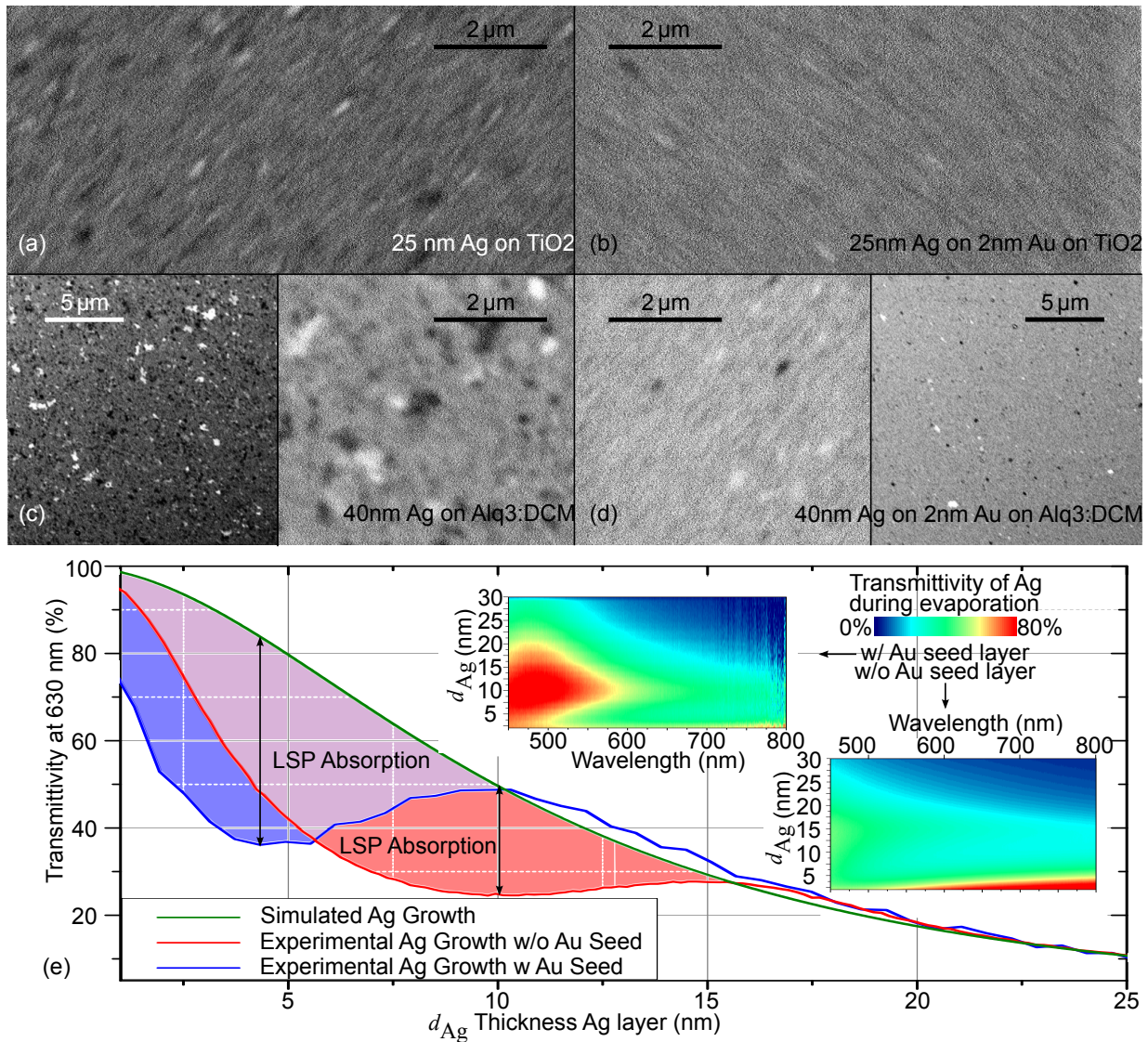


**Figure 4.6:** (a)-(d) SEM micrographs of silver films on different substrates. (a) 25 nm Ag on a 3-layer DBR (TiO<sub>2</sub>|SiO<sub>2</sub>|TiO<sub>2</sub>). (b) 25 nm Ag on a 3-layer DBR with a 2 nm Au seed layer. (c) 25 nm Ag on a 3-layer DBR and 50 nm of Alq<sub>3</sub>:DCM. (d) 25 nm Ag on a 3-layer DBR and 50 nm of Alq<sub>3</sub>:DCM with a 2 nm Au seed layer. The addition of a gold seed layer promotes a more uniform and closed silver film on top. SEM micrographs are taken at similar settings, providing a qualitative comparability of the images. (e) In-situ transmission spectra of Ag on glass during evaporation (red, blue) and calculated transmission of different silver film thicknesses (green). Compared to the simulated spectrum, pronounced dips in transmission stem from parasitic absorption by localised surface plasmons. The addition of an Au seed layer promotes a closed layer at lower thicknesses > 10 nm. Insets show the full transmission spectra during Ag growth.

top of Alq<sub>3</sub>:DCM (Fig. 4.6 (c) and (d)), a clear difference on film quality can be observed on the few-wavelength length scale. While a more in-depth analysis is not possible in this resolution, a tendency of the film quality is made possible.

In-situ optical transmission measurements allow more insight into the growth of such layers by monitoring the transmission through a thin silver film on a glass substrate during evaporation. Here, in Fig. 4.6 (e), the absorption of LSPs becomes directly visible when comparing the observed transmission data (red, blue, and insets) to the simulated spectrum (green) of a perfect silver layer. During growth, nano-scale islands of silver form on the surface of the substrate, leading to a very pronounced deep dip in the transmittivity. While a decrease of transmittivity is expected for an increased thickness of metal, such sharp drops as observed can only be attributed to additional parasitic absorption. Remarkably, the transmittivity in the experimental spectra even increases again during silver growth when islands connect, the whole layer closes up and LSP absorption is inhibited again as the film becomes conductive as a whole. While for the sample without seed layer (red), this point is reached at 15 nm and the transmission curve coincides with the simulated spectrum, the use of a 2 nm Au seed layer improves silver growth, and a closed layer can be expected at 10 nm already. Other investigations have shown that under perfect experimental conditions even lower thickness are possible [189, 200, 201]. While the initial dip is even higher when using the seed layer, for thicknesses above 10 nm a better growth behaviour can be expected here.

When processing noble metals on top of organics, individual metal atoms can easily diffuse into the organic film as they are not reactive enough to strongly interact with the surface [199, 202]. This leads to an increased parasitic extinction of light inside the organic layer and provides recombination centers for different molecules. A diffusion barrier can be utilised to prohibit this behaviour. Its atoms or molecules impede diffusion by binding themselves chemically to the organic molecules of the layer below and promote metal growth on top [203]. Here, a thin 4 nm MoO<sub>3</sub> layer is utilised as a diffusion barrier between the Alq<sub>3</sub>:DCM cavity layer and a seed and silver layer on top. In a full microcavity stack, their impact on the formation of TPP states and the overall optical quality of metal-organic devices are investigated. Figure 4.7 shows far field emission spectra of such cavities without (a) and with (b) additional diffusion barrier and seed layers. While both cavities show the formation of TPP states, their separation differs significantly even though the same silver thickness is used for both. The much smaller separation of the device with seed and barrier layer suggests the formation of a much thicker complete silver film on top of the organic layer, as both TPP states spectrally approach each other for increasing metal layer thickness (see Chapter 2 Fig. 2.7). While the added 2 nm of gold certainly enhance the TPP, they are not sufficient to explain the strong spectral difference alone. A diffusion of metal into the organics and impaired growth without the seed layer therefore negatively effects the formation

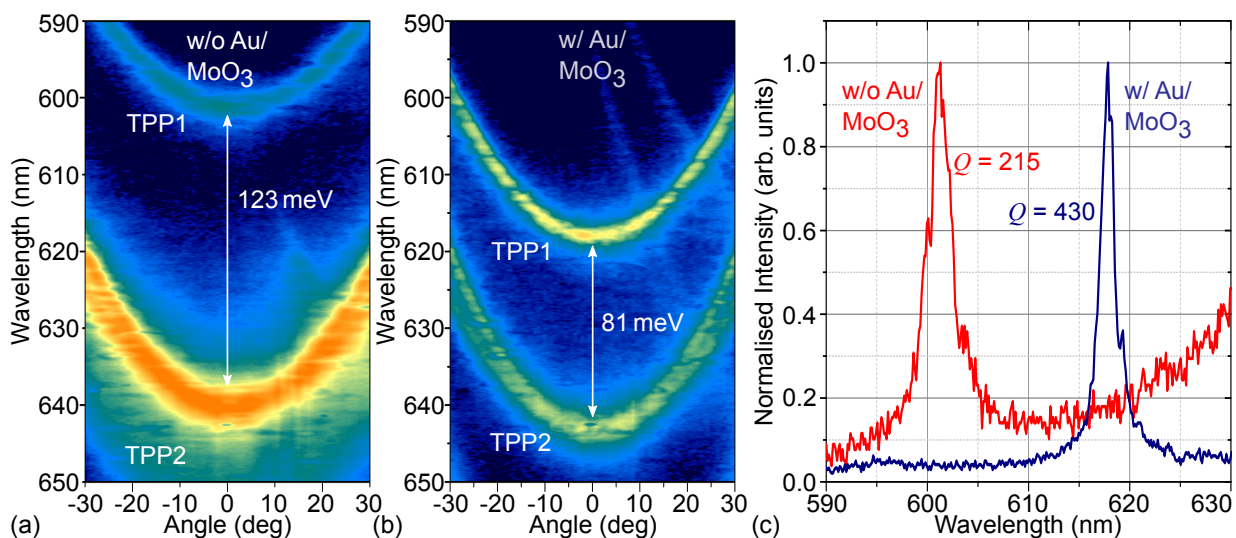


**Figure 4.7:** (a) Far field emission spectrum of an organic microcavity with 20 nm silver on top of the active Alq<sub>3</sub>:DCM cavity layer. (b) Far field emission spectrum of an organic microcavity with 20 nm silver, a 4 nm MoO<sub>3</sub> diffusion barrier and a 2 nm Au seed layer on top of the active Alq<sub>3</sub>:DCM cavity layer. The added barrier and seed layers drastically improve the quality of the TPP states and indicate a more homogeneous and thicker layer on top of the organics. (c) Cross sections of both spectra at 0° showing TPP state 1. Utilising seed and barrier layers doubles the quality factor.

of TPP states, in addition to a significant broadening of resonances. Parasitic absorption of both LSPs and diffused metal atoms strongly decrease the quality factor of organic microcavities. Here, the use of a 4 nm MoO<sub>3</sub> and 2 nm of Au can effectively double the quality factor from  $Q = 215$  (without seed or barrier) to  $Q = 430$  (with seed and barrier). This is to date the highest reported quality factor of a top metal layer on an organic microcavity. Both barrier and seed layers will be used, where appropriate, throughout all further devices in this work.



# 5 Multidimensional Photonic Confinement

*In this chapter, the addition of a laterally patterned interlayer is used to facilitate photonic confinement in photonic wires and dots of both metal and SiO<sub>2</sub> structures. As this experiment arises interest in the full in-plane dispersion for both  $k_x$  and  $k_y$  direction, a tomography method is employed in Section 5.1 to map emission into all angles. This method finds application in both the investigation of photonic wires in Section 5.1.2 as well as photonic dots in Section 5.1.3, where full three-dimensional confinement of photons is experimentally demonstrated.*

*The mode confinement in such photonic patterns furthermore facilitates a strong reduction of lasing threshold in elliptic holes and triangular wedges in an additional metal layer. In Section 5.2, such structures are investigated regarding the formation of confined modes in the near-field and drastically reduced lasing threshold in their input-output behaviour.*

*The contents of this chapter have in part been published in reference [1] © 2013 AIP Publishing LLC; in reference [3] © 2014 AIP Publishing LLC; and in reference [2] © 2014 Society of Photo Optical Instrumentation Engineers.*

*Parts of the data presented in Figures 5.2, 5.3, and 5.6 - 5.8 have been obtained and used for the author's diploma thesis work entitled "Resonator Modes in Organic Microcavities with Patterned Metal Layers" and are presented here within the greater context of the doctoral work.*

## 5.1 Dispersion Tomography of Multi-Dimensionally Confined Photons

The inclusion of different interlayers into a microcavity facilitates a spatially-selective resonance shift of the main optical mode in the system. If the in-plane extension of the interlayer then approaches the order of magnitude of the wavelength of resonant light, a further manipulation of the MC energy landscape becomes possible. Such confinement breaks the in-plane symmetry of the system and leads to discretisation of modes perpendicular to the wire orientation. State of the art nanofabrication techniques facilitate an almost arbitrary three-dimensional device design. In

single[204] and coupled[205] photonic dots or photonic crystals[47], increasingly complex mode engineering is realised. Besides, spectroscopy of such photonic trap structures provides fundamental insight into the optical confinement of photons or exciton-polaritons[94] and, by analogy, into the quantum confinement of other particles. Patterning of the optically active area can be achieved by various means. Full cavity stacks are etched into inorganic micropillars via electron-beam lithography and subsequent reactive ion etching, resulting in ultra-high quality ( $Q$ )-factors [85, 89] and very low lasing thresholds. Furthermore, organic small molecules can be structured by shadow mask evaporation, showing reduced threshold and substantially enhanced  $\beta$ -factors [195]. Due to the large photonic stop-band created by DBRs, a manipulation of only the cavity layer is sufficient to shift the cavity mode out of the original resonance. A micron-scale topography can be created for the active region, by photolithographic structuring of the cavity layer or bordering mirror layers, which is sufficient to confine light and show discretization of modes [1]. Here, it will be demonstrated how full spectral and momentum coverage is obtained via  $\mu$ -PL tomography by mapping the mode dispersion of MC photonic wires in both lateral dimensions. To investigate the complex mode structure in microcavities with multidimensional confinement, the energy dispersion for one  $\vec{k}$  vector component is directly recorded while the second lateral  $\vec{k}$  component is scanned, obtaining a detailed dispersion tomogram of the cavity resonances.

### 5.1.1 Setup for Dispersion Tomography

In far field geometry, an additional lens images the Fourier plane of the collecting objective onto the vertical entrance slit of a spectrometer, which selects the outcoupling angle along the  $y$ -axis and, thereby,  $k_y$ . After wavelength dispersion in the spectrometer, a cooled charge coupled device (CCD) records the emission wavelength versus the outcoupling angle,  $\vartheta$ , along the  $x$ -axis ( $\sin \vartheta \propto k_x$ ). The far field lens is moved along the  $y$ -axis by an offset,  $h$ , to scan the  $k_y$  component of the  $\vec{k}$ -vector across the spectrometer slit (see Fig. 5.1 (b)), again ultimately limited by the numerical aperture of the outcoupling objective. The  $k_y$  component scanned can be obtained by a simple geometrical consideration and is only dependent on the offset  $h$ :

$$k_y = k_z \tan \left( \arcsin \left( \frac{1}{n_0} \sin \left( \arctan \left( \frac{h}{f_1'} \right) \right) \right) \right) = \frac{k_z \times h}{\sqrt{(n_0^2 - 1)h^2 + n_0^2 f_1'^2}} \quad (5.1)$$

with the focal length  $f_1'$  as indicated in Fig. 5.1 (a).

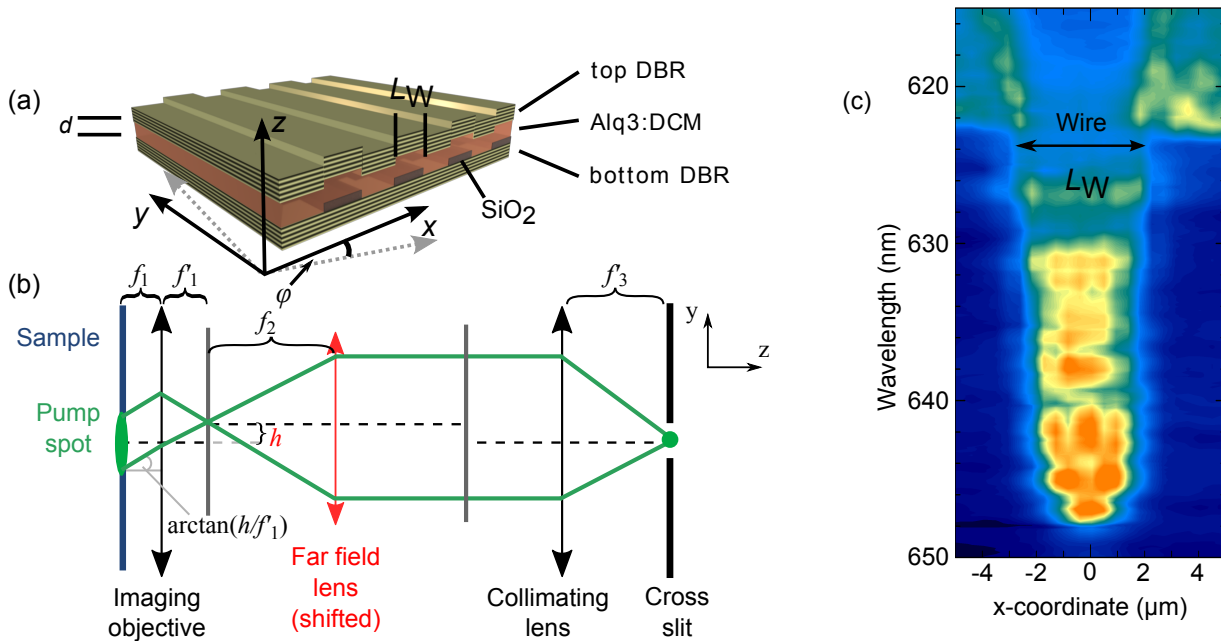


**Figure 5.1:** (a) Scheme of the sample and the relevant dimensions.  $d$  is the thickness of the cavity layer,  $L$  the width of the SiO<sub>2</sub> stripes (thicknesses not to scale). (b) Ray scheme demonstrating how the optical axis is shifted by moving the farfield lens. The focal lengths of the lenses are indicated as  $f_i$  for the front and  $f'_i$  the back focal length. From the focal lengths of the lenses and the offset from the optical path,  $h$ , we derive the  $k_y$  vector shift. (c) Spatially resolved emission spectrum of a photonic wire. Both, strong spatial confinement and mode discretisation can be directly observed. Intensity is colour-coded as in Fig. 5.3. Reprinted with permission from reference [1].

### 5.1.2 2D - Photonic Confinement in Photonic Wires

To exhibit the confinement of photons, the spatially resolved PL-spectrum is presented in Figure 5.1 (c). The addition of SiO<sub>2</sub> wires next to the cavity layer results in the formation of photonic potential wells, according to the thickness of such a wire. Neglecting the very small absorption of the wires, this potential can be easily calculated as by Equation (6.8). As seen in Fig. 5.1 (c), light in the spectral range of 645 nm...620 nm (1.91 eV...2.00 eV) is effectively laterally trapped and develops standing waves with discrete energy gaps. This will be even clearer in the far field spectrum below. Only photons with sufficient energy ( $\gtrsim 2$  eV,  $\lambda < 620$  nm) can exist above the barrier and form a continuous mode spectrum there. Such easily obtainable photonic structures may be utilized, with possibly more sophisticated lateral patterning, to suppress losses by waveguiding in the system and decrease mode volume with the prospect of lower lasing thresholds.

Accessing the dispersion of such laterally inhomogeneous cavities requires multidimensional angle-resolved measurements. With Fourier-space spectroscopy and tomography[90, 206] as deployed in this work, these features are readily accessible as demonstrated in the following.

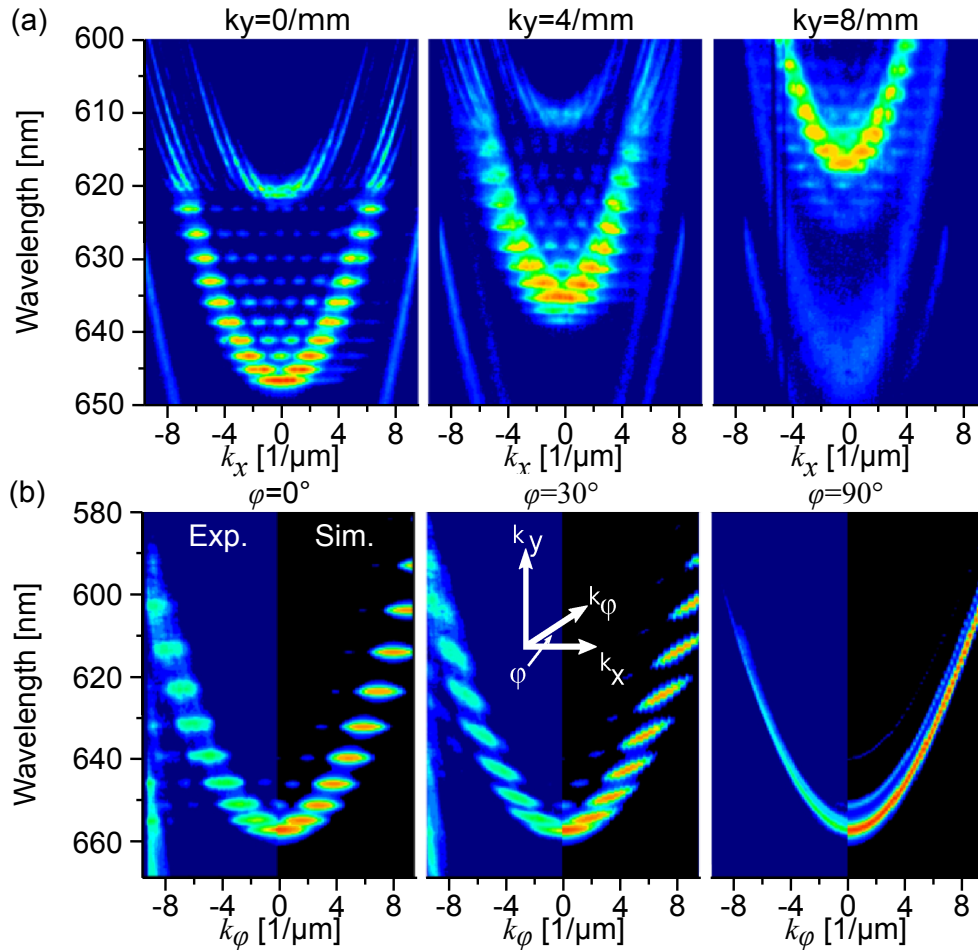


**Figure 5.2:** (a) Tomography sections from a  $k_y$  scan of the photoluminescence from a photonic wire. (b) Tomography sections made by rotating the sample by an angle  $\varphi$ , about the axis perpendicular to the  $x - y$  plane. Left panels show the measurement and right panels the corresponding simulation. Intensity is color-coded as in Fig. 5.3. Reprinted with permission from reference [1].

Figure 5.2 (a) shows the  $\mu$ -PL measurement for the microcavity containing periodic  $\text{SiO}_2$  wires. The emission follows the typical parabolic dispersion seen in unstructured MCs, albeit broken up into discrete resonances by the optical confinement in  $k_x$ -direction, i.e. perpendicular to the stripes of the grating. On the  $k_y$ -axis, i.e. with the entrance slit parallel to stripes, the parabolae remain continuous due to the lack of optical confinement. This is revealed by scanning the  $k_y$ -axis as described above (Fig. 5.2 (a)). The spectral distance between the discrete states is directly connected to the stripe width  $L$ , as equation (5.3) shows. Utilizing the broadband and unpolarized emission of the laser dye, further optical properties like polarisation splitting at higher  $k$ -values[82] can be mapped as well.

For a theoretical description of the mode structure, we assume standing waves between wires (comparable to perfect reflectivity) for confinement in  $x$ -direction, which will prove to be suffi-



cient for the fit to the experimental data. The boundary condition for the electric field therefore is  $F_x(0) = F_x(L_W) = 0$ . With  $L_W = Ln_O$  as optical stripe width and  $n_O \approx 1.75$  the constant refractive index of the active layer, we obtain  $F_{x,m} \sim \sin[x/L_W\pi(m+1)]$  with  $m \in \mathbb{N}_0$  as the mode number. For the unconfined  $y$ -direction, the mode decays exponentially within  $5 \mu\text{m}$  [207], much larger than the  $2 \mu\text{m}$  Gaussian excitation spot. Therefore, the electric field is  $F_y \sim \exp(-|y|/a)$ , where  $a$  is the extent of the field in  $y$ -direction. Fourier transformation of these electric fields leads to the field distribution in  $\vec{k}$  space and thus to the intensity distribution  $I$ :

$$I_m(k_x, k_y) \sim \left[ \frac{L_W a \times (m+1)}{L_W^2 k_x^2 - \pi^2 (m+1)^2} \right]^2 \times \left[ 1 - (-1)^{m+1} \times \cos(k_x L_W) \right] \times \left[ \frac{\sqrt{2/\pi} \times a}{a^2 k_y^2 + 1} \right]^2 \quad (5.2)$$

This intensity distribution is calculated along the energy dispersion relation  $E_m(k_x, k_y)$  in the right halves of the panels in Figure 5.2 (b), in excellent agreement with the experimental data. The dispersion relation is gained from the relation  $E(k) = \hbar c_0 |\vec{k}|$  with appropriate expressions for the  $|\vec{k}|$  components leading to

$$E_m(k_y) = \hbar c_0 \sqrt{\frac{k_y^2}{n^2} + \left( \frac{(m+1) \times \pi}{L_W} \right)^2 + \left( \frac{\pi}{d_M} \right)^2}, \quad (5.3)$$

where  $c_0$  is the vacuum speed of light and  $d_M = n_O d_O + n_{\text{SiO}_2} d_{\text{SiO}_2}$  [45].

An alternative way of slicing the two dimensional dispersion relation into planes is facilitated by rotating the sample by the angle  $\varphi$  around the optical axis, or, more adeptly, rotating the image of the sample by use of a Dove prism [208]. Then, the entrance slit of the spectrometer selects a line in the  $k_x - k_y$  plane, indicated by  $k_\varphi$  in Fig. 5.2 (b), related via geometrical consideration.

Figure 5.2 (b) shows the resulting tomography images, which finally lead to an identical composite dispersion tomogram as obtained via the  $k_y$  scan. The theoretical model for this rotation scan is in analogy to the procedure above, albeit transformed into spherical coordinates including the sample rotation angle  $\varphi$  and the outcoupling angle  $\vartheta$ . Clearly, the rotational scan offers a more gradual view at the transition from continuous parabolae (entrance slit parallel to wires) to discrete states (entrance slit perpendicular to the wires), illustrating that the type of scan (rotation or translation) should be chosen appropriate for the sample geometry.

The above tomography images for fixed  $k_y$  are combined into a dispersion tomogram in Figure 5.3, giving illustrative access to the full dispersion relation. Since the complete dispersion relation is measured, detailed information can easily be extracted using any program capable of three-dimensional visualization. The multidimensional view can be understood better in a rotating animation (see <http://dx.doi.org/10.1063/1.4827820.1> © 2013 AIP Publishing LLC).

The tomographic scanning of a non-isotropic photon dispersion reveals the discretisation of

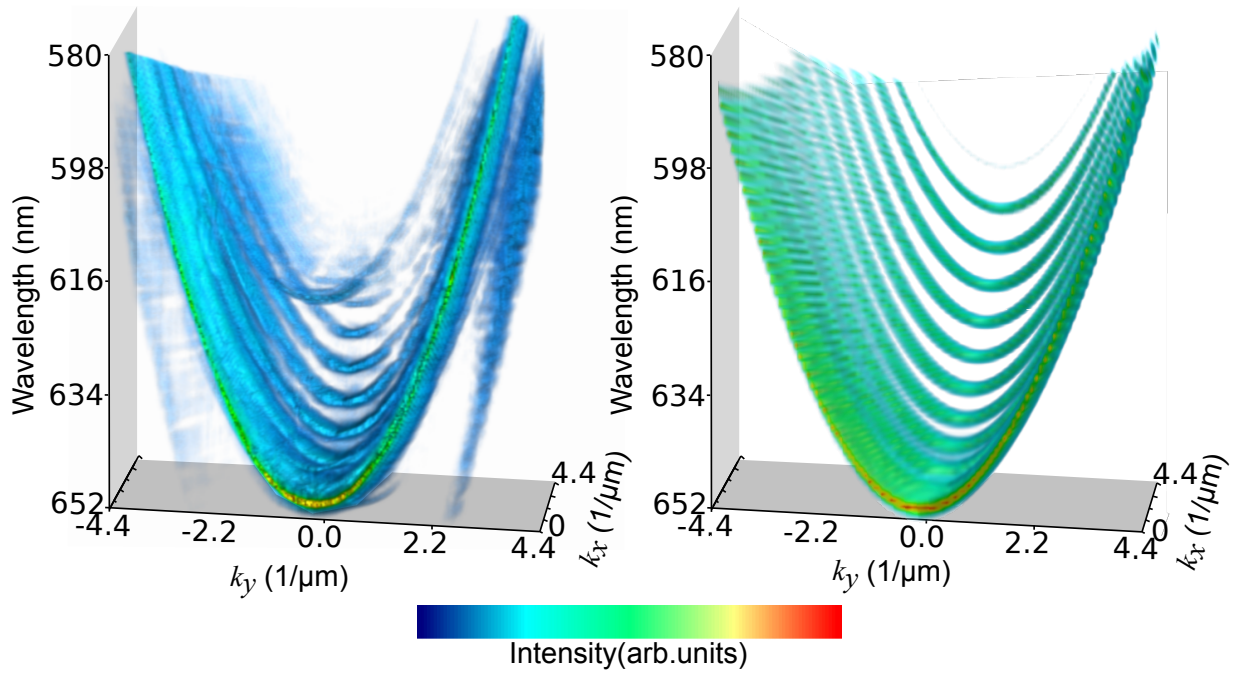


**Figure 5.3:** Reconstructed dispersion tomogram gained from  $k_y$  scan method shown in Figure 5.2 (left) and theoretical model (right). Reprinted with permission from reference [1]. Enhanced in the online version of the published article, see <http://dx.doi.org/10.1063/1.4827820.1>.

states in  $\vec{k}$ -space by translating the far field lens out of the optical axis or by rotating the sample image using a Dove prism. Thereby, mode dispersions of a high quality are visualised, depicting the emission of an organic photonic wire microcavity in a single tomogram. The strong optical confinement shown here is not restricted to the wire geometry, but may be exploited further in sophisticated designs to decrease the lasing threshold or expanded towards a fully three-dimensionally confined system.

### 5.1.3 3D - Confinement in Metal-Organic Photonic Dots

In addition to the  $z$  - confinement in vertical direction by the highly reflective DBRs, photonic wires facilitate another restriction of the mode formation in one lateral direction. Consequently, the fabrication of photonic dots should provide a complete three-dimensional trapping of photons and in turn result in a quantum-like discretisation of modes in all directions of momentum. Such patterning provides highly localised standing waves with discrete propagation angles in all directions.

Similar to the photonic wires above, such photonic dots are fabricated by lithographically patterned interlayers. In this experiment, 25 nm of silver (on 2 nm of gold) are added on top of the bottom DBR and patterned into rectangular patches of  $1.8 \mu\text{m} \times 2.2 \mu\text{m}$  size, before finishing the

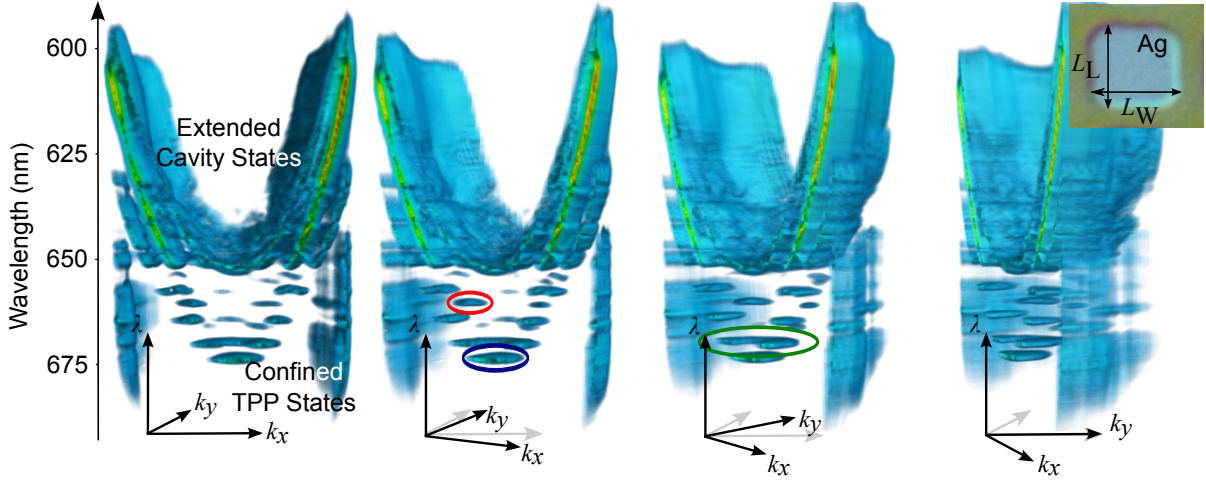


**Figure 5.4:** Reconstructed dispersion tomogram of a three-dimensionally confined metal-organic photonic dot. The confined Tamm-plasmon-polariton states show discretisation in both  $k_x$  and  $k_y$  direction. The ground state of the system (blue circle) forms a disk with extension into both components of in-plane momentum. Different spatial extensions lead to differing positions of discrete states in  $k_x$  and  $k_y$  and facilitate the formation of fully 3D confined modes (e.g. red circle) in the system. When discrete levels of  $x$  and  $y$  confinement overlap, a ring-like mode formation is observed (green circle). Wavevector scale is similar to Fig. 5.3. Inset shows a micrograph of the photonic dot.

microcavity as usual. As discussed in the previous Chapter 4, this introduction of silver facilitates the formation of red-shifted Tamm-plasmon polariton (TPP) states locally at the position of the metal patches. Due to the small lateral extension of the silver area, the TPP states in turn experience a strong confinement to the position of the metal-organic photonic dot that is created. Consequently, TPP states discretise into standing waves in both planar directions. Corresponding to Equation (2.72), in rectangular dots both directions can be handled independently and lead to the formation of fully confined modes also in momentum space with discrete wavevector components:  $k_x = q_m = \pi(m+1)/(n_C L_W)$  and  $k_y = p_l = \pi(l+1)/(n_C L_L)$ [48]. Both confined wavevectors now combine to the discretised energy dispersion of Equation (2.72):

$$E_{ml} = \hbar c_0 |\vec{k}| = \hbar c_0 \sqrt{k_z^2 + k_x^2 + k_y^2} = \hbar c_0 \sqrt{\left(\frac{\pi}{n_C d_C}\right)^2 + \left(\frac{\pi(m+1)}{n_C L_W}\right)^2 + \left(\frac{\pi(l+1)}{n_C L_L}\right)^2}. \quad (5.4)$$

The fully confined nature of these modes raises interest in the measurement of the full momentum space via dispersion tomography. Figure 5.4 shows the reconstructed dispersion tomograph of such metal-organic photonic dots as viewed under different angles. Here, the full extent of mode discretisation becomes apparent. While in photonic wires, the parallel component stays unconfined and still shows a continuous parabola with discrete multiples in the

perpendicular  $k$ -component, in photonic dots no continuous modes remain in the TPP states. Instead, different types of discrete modes appear. Starting at the ground state of the system, at  $k_x = k_y = 0, \lambda = 675 \text{ nm}$  (blue circle in Fig. 5.4), a disk-like flat mode is visible, which extends in both momentum directions. Compared to a planar cavity, this ground state is raised by the contributions of both wavevector components  $q_0, p_0$ , which hold finite values. As the width and length of the dots differ only by a small amount, the first excited state of the system is degenerate to represent both the  $q_1, p_0$  and  $q_0, p_1$  states (green circle). Here, this combined state forms a donut-like mode at 670 nm. If the dots is less square, i.e.  $|L_W - L_L|$  is larger, no degenerate states may appear. The separation between discrete states increases with increasing mode number  $m$  or  $l$ , facilitating full confinement of non-degenerate modes at higher quantum numbers  $q > 1, p > 1$ . These fully discrete states fill the rest of the spectrum below the potential barrier at 650 nm. As an example, mode  $q_2, p_1$  is highlighted by a red circle. This mode exists only at an oblique angle in both directions and would otherwise not be present, when observing independent  $k_x$  or  $k_y$  spectra. The dispersion tomogram proves the existence of such fully confined modes, which is facilitated by an only weak intervention into the whole sample composition, and further manifests the analogies of such confined photonic systems as a playground to directly observe quantum behaviour. Furthermore, such strong three-dimensional confinement can aid in the improvement of microcavity performance.

## 5.2 Exploiting Photonic Confinement in Laterally Patterned Metal-Organic Microcavities

Creating fully three-dimensionally confined modes in structured silver layers can severely impact the lasing threshold in organic microcavities. Here, the lasing of Mathieu-modes in elliptic holes and more complex transversal modes in triangular wedges is investigated. The input-output characteristics are modelled using a set of rate equations (see Section 2.2.7), fitting perfectly to the measured data. As previously discussed, adding thin metal layers into such a MC leads to a coupling of cavity photons to plasmons in the metal and thus the formation of Tamm-plasmon-polaritons (TPP) [42, 82, 209] showing TPP lasing [83] as well as macroscopic coherence in structured silver layers implemented into a cavity [210]. Fabricating elliptic holes in such a metal layer shows strong transversal confinement into Mathieu-modes, in perfect agreement with theoretical prediction [43, 211]. The effect of such confinement on the lasing action however has not been investigated previously. Similar confining effects are observed for nanoscale deformations of one DBR mirror, investigated theoretically [212], and realized by focused ion beam milling of such deformations on a substrate [213].

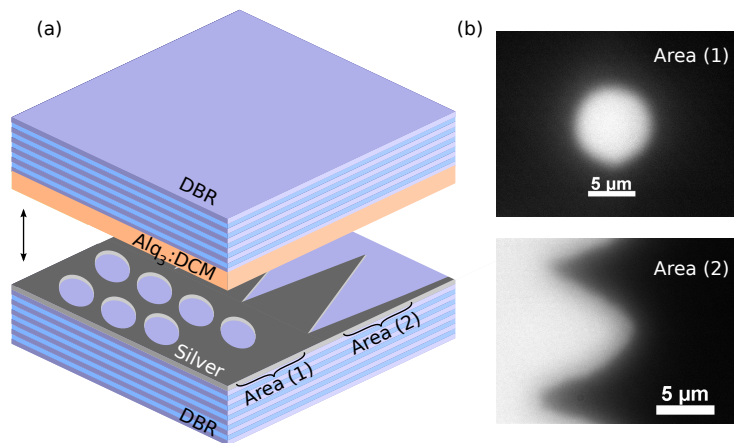


**Figure 5.5:** (a) Sample schematic. An organic cavity layer of the host:guest system Alq<sub>3</sub>:DCM is encased between two dielectric distributed Bragg reflectors (DBR). A thin silver layer is added onto the bottom DBR and structured by photolithography to yield metal free holes (Area (1)) and metal free lateral wedges (Area (2)) on the micrometer-scale. The same sample also contains extended metal free areas for comparison. The layer thicknesses are shown not to scale. (b) Transmission micrographs of the silver structures in a MC. Reprinted with permission from reference [3].

### 5.2.1 Mathieu-Modes in Elliptic Holes of Silver Interlayers

The metal layer leads to the formation of Tamm-plasmon-polariton (TPP) modes [42]. The first one is red-shifted (639 nm) in comparison to the original cavity mode (621 nm), a second TPP state emerges from the red side band, shifting to the blue with increasing silver thickness. In a structured cavity, three modes are observable, the original cavity mode and the two TPP modes, albeit spatially separated in transversal direction.

To describe laser transitions in microcavity devices, the data are fitted with commonly used rate equation models, such as the Maxwell-Bloch model described by Rice and Carmichael [107] or the rate equations described by Björk and Yamamoto [109] (see also Section 2.2.7).

The presence of silver causes splitting of the original cavity to TPP modes [42]. This leads to a strong light confinement inside of elliptic holes in the silver layer, incorporated into the cavity as shown in Figure 5.5. The solution of the Helmholtz-equation in elliptic coordinates gives even or odd Mathieu functions (for the angular part) and even or odd modified Mathieu functions (for the lateral part) [214]. Assuming lateral boundary conditions, i.e. the electric field has a node at the metal edge, these functions and the corresponding energetic spectrum discretize with angular ( $l$ ) and radial ( $n$ ) mode numbers [43]. Figure 5.6 (a)-(c) shows these transversal modes for different mode numbers as observed in the samples. These perfectly clear and confined modes already give an impression of the lateral optical trapping achieved in a perforated silver layer MC.

Selective excitation of these modes can be achieved by a two-beam interference experiment.

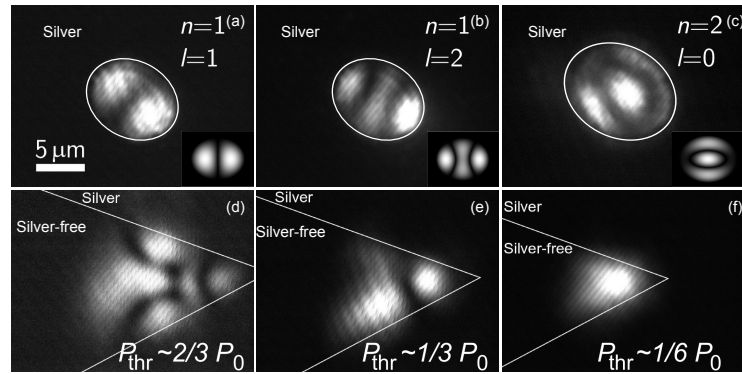


**Figure 5.6:** (a)-(c) Even Mathieu-modes in elliptic holes of the metal layer in the sample. Via selective excitation, modes of different radial ( $n$ ) and angular ( $l$ ) mode number can be excited. Insets show calculated Mathieu-modes. (d)-(f) Emission from confined modes in lateral wedges of the sample's metal layer. The modes form according to the spot of excitation (in the image center) in relation to the wedge tip. Different modes exhibit significantly different lasing thresholds, decreasing towards the tip, down to  $1/6$  of the unstructured cavity's threshold  $P_0$ . White lines illustrate the edges of the metal layer. Reprinted with permission from reference [3].

Via movable mirrors, two beams can be focused onto the sample under an oblique angle towards each other. The resulting interference pattern is then used to selectively excite only certain areas inside a metal hole. Such a tunable pattern favors certain transversal modes in terms of lasing action, by tuning the interference angle of the excitation spots, different Mathieu-modes can therefore be obtained (see Fig. 5.6).

Apart from the change in transversal mode behaviour, the confinement also leads to an intensity concentration due to standing waves inside such holes as well as a suppression of modes traveling in the cavity plane. Such waveguided or leaky modes are usually undesired and lead to significant losses in microlasers with vertical geometry, transporting photons away from the excitation center, leading to a reduction in spectral field density and a direct increase of the lasing threshold.

Figure 5.7 shows a comparison of the input-output characteristics on metal-free and metal-near areas, measured in elliptic- (a) and triangle- (b) shaped structures. The investigated areas lie only  $50\ \mu\text{m}$  apart from each other. This allows a direct comparison of lasing characteristics in two areas with different amounts of lateral confinement.

The input-output characteristics show a linear increase both below and above threshold in either case, with increasing excitation power. The stimulated emission threshold is clearly reduced at least three times for the confined mode ( $P_{\text{Thr}} = 0.6\ \text{nJ}$ ), in comparison to a metal-free area ( $P_{\text{Thr}} = 1.8\ \text{nJ}$ ). The data for unconfined emission is verified in several spots on the sample to ensure that no artificial influence of fabrication impurities or scattering effects on specific sample positions takes place.

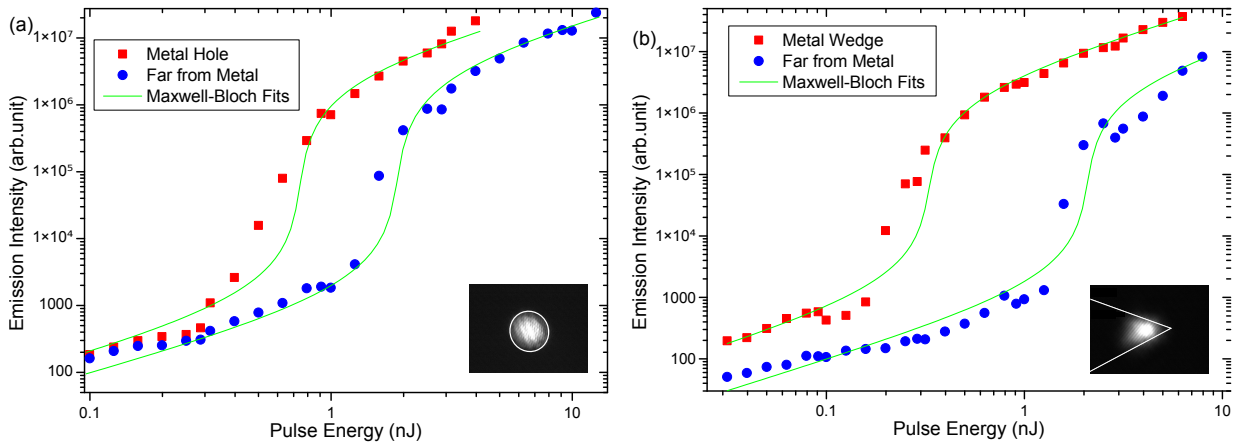


**Figure 5.7:** (a) Input-Output curve of emission from a metal-free hole and a corresponding extended metal-free area on the same sample. The lateral confinement leads to a significant decrease of lasing threshold in the hole. (b) Input-Output comparison of a triangle-structure and an unstructured area on the same sample with corresponding rate-equation model. The lateral confinement at the tip of the triangle improves the lasing threshold by 6 times. In both cases, the behaviour can be approximated well by a standard rate equation model. Reprinted with permission from reference [3].

A standard rate equation model (detailed in Section 2.2.7) describes these input-output curves very well, confirming the nonlinear transition into the laser regime (solid lines in Fig. 5.7). From this measurement, one can extract the spontaneous to stimulated emission ratio (SSR). The approximation of the input-output curves in Figure 5.7 yields a comparable ratio for both experiments, with  $SSR = 4.9 \times 10^{-4}$  for the confined and  $SSR = 5.0 \times 10^{-4}$  for the unconfined excitation. In the ideal case without nonradiative losses, the SSR approaches the  $\beta$ -factor, while in the presence of nonradiative losses,  $\beta$  becomes more insensitive to the lasing threshold and cannot directly be obtained from the relation between spontaneous and stimulated emission intensity. As for the investigated system it is not possible to easily quantify the additional absorption,  $\beta$  can not be directly extracted. However, clearly the formation of discrete modes can be observed in Figure 5.6, which leads to the conclusion that a definite improvement of mode confinement can be achieved. The reduction is supported by  $k$ -space spectroscopy, where gaps in the energy dispersion are observed for similar structures [43]. A clear experimental distinction can be seen in the lasing threshold, where  $P_{\text{thr, unconfined}}/P_{\text{thr, confined}} \approx 3$ . This behaviour is confirmed for different sizes of the excitation spot, where always the same reduction in threshold is observed.

The use of elliptic holes for multidimensional confinement shows an improvement in device characteristics, however other geometries are also of interest. The field enhancement at the tip of triangular structures is well known, and utilized for example in plasmonic nanostructures

[215, 216]. Such triangular cuts are fabricated into a metal layer (see Fig. 6.1(b)) via the same photolithographic etching technique to investigate transversal mode development and the influence of positioning on the emission characteristics of the sample.

Figure 5.6 (d)-(f) shows the formation of transversal modes of the cavity state, bordered by silver, illustrated by the continuous white line. As already experienced in the previous measurement, a strong confinement of the mode creates a complex standing wave. Tuning between different states is achieved by an exact positioning of the pump spot. Starting at around 12  $\mu\text{m}$  distance to the triangle tip, an extended transversal mode becomes visible, exhibiting at least five distinct antinodes in the field distribution. Shifting the excitation towards the apex of the cut, the spatial extension as well as complexity of the mode decreases, until we arrive at a strongly confined state extended only 5  $\mu\text{m}$  in each direction.

The input-output characteristics of these wedges again reveal a strong decrease of lasing threshold for the confined mode. In the best case scenario, these structures show a threshold reduction of one order of magnitude, depending on the inclination angle of the triangle. A representative curve, showing emission from the modes presented above, can be seen in Fig. 5.7 (b), and is again modelled via the Maxwell-Bloch equations. A higher inclination here still provides an improvement of the lasing threshold by six times in comparison to a completely unconfined spot on the same sample. Although the transition from the spontaneous emission regime to lasing is again very similar in both cases ( $\text{SSR}_{\text{unconfined}} \approx 7.3 \times 10^{-4}$ ) despite additional nonradiative losses, the lasing threshold shows a decrease of almost one order of magnitude in a near-metal cavity region.

The geometry of this structure also allows the investigation of the development of confinement in detail. As already seen in Fig. 5.6 (b), the lasing mode switches for different pump positions moving from unstructured to most confined area. The lasing threshold behaves accordingly, as apparent in Figure 5.8. In connection to the distance from the apex of the triangle  $x$ , modes with different emission energy are excited. While the wavelength changes stepwise between the unconfined area ( $\lambda = 624.2 \text{ nm}$ ) and three distinct modes ( $\lambda_1 \approx 624.6 \text{ nm}$ ,  $\lambda_2 \approx 625.7 \text{ nm}$ ,  $\lambda_3 \approx 626.6 \text{ nm}$ ), each mode shows a minimum in the lasing threshold ( $x_1 \approx 12.5 \mu\text{m}$ ,  $x_2 \approx 7.0 \mu\text{m}$ ,  $x_3 \approx 2 \mu\text{m}$ ) for ideal excitation conditions. Looking again on the intensity distribution in Fig. 5.6 (d)-(f), mode  $\lambda_1$  corresponds to (d), mode  $\lambda_2$  to (e), and mode  $\lambda_3$  to (f). In total, the lasing threshold drops by a factor of six, with several preferred mode positions in between.

This result demonstrates the engineering of the photonic field distribution by structuring thin silver films utilising photolithography. The formation of Tamm-plasmon-polaritons in the silver is exploited to confine lasing modes and significantly reduce losses by leaky modes in the system. Such confined modes exhibit discrete energy levels, and the confinement leads to the formation of distinct transversal modes and a reduction of lasing threshold up to one order of magnitude.



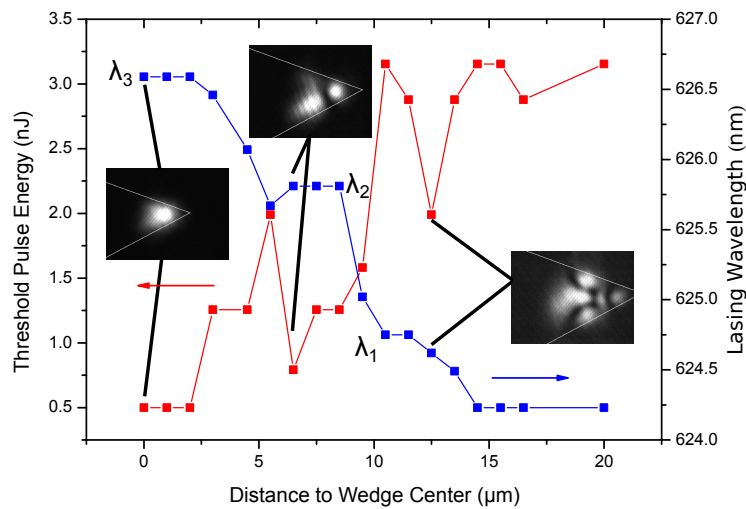


**Figure 5.8:** Lasing threshold and wavelength of microcavity emission depending on the distance to the triangle tip. Approaching the tip, the threshold decreases with several local minima at  $12.5\mu\text{m}$ ,  $6.5\mu\text{m}$  and  $0\mu\text{m}$ . They correspond to the standing waves observed in Fig. 5.6 (d)-(f). The lasing wavelength changes stepwise between these modes and the free cavity mode at distances  $\geq 15\mu\text{m}$ . Reprinted with permission from reference [3].

The transition into the laser regime is supported by the fit with standard rate equations and even though highly absorptive silver is introduced into the cavity, the spontaneous to stimulated emission ratio remains unchanged. The introduction of highly conductive - but highly absorptive - silver and subsequent patterning via comparably simple techniques proves useful and, in future, can help in the realization of an electrically driven organic laser diode.



## 6 Photonic Bloch States

*In the previous chapter, it was shown how the microcavity photon dispersion can be manipulated using different interlayers to create a micrometre-scale confinement in single photonic wires and dots. Based on these results, the concept of lateral structuring is continued towards periodic lattices of plasmonic and dielectric photonic wires.*

*Starting with silver photonic wires in Section 6.1, the formation of the corresponding Kronig-Penney potential landscape is observed and explained by modifying the theory towards photonic systems. Section 6.1.2 provides the observation of photonic Bloch states in both spatially and angle-resolved  $\mu$ -photoluminescence spectroscopy, showing the formation of localised discrete states and extended minibands in the microcavity dispersion. The modified analytical Kronig-Penney theory is first introduced in Section 6.1.3, accompanied by numerical simulations, and applied to explaining the emergence of zero- and  $\pi$ -states above the potential barrier.*

*Similar observations of Bloch states can be made in photonic wires of non-absorptive  $\text{SiO}_2$  wires, as introduced in Section 6.2. Here, the high optical quality of the resulting modes allows an in-depth characterisation of arrays with different wire widths and periods in Section 6.2.2. Based on these results, the modified Kronig-Penney theory is extended by the concept of a polarisation-dependent effective photon mass in Section 6.2.3, allowing a quantitative allocation of mode positioning including effects such as mode penetration into DBRs and the resulting polarisation splitting.*

*The high optical quality of  $\text{SiO}_2$  wires allows for the application of photonic Bloch states towards a more direct control of lasing in the system. In first above-threshold investigations in Sections 6.2.4, the dependence of lasing on the spatial positioning of the excitation beam is established and the ability to screen the gain distribution of the active layer is demonstrated. By exciting the sample with two interfering excitation beams, creating a fixed in-plane momentum, a full control over the stimulated emission is demonstrated in Section 6.2.5.*

*Finally, Section 6.3 serves a comparison of lasing modes in both plasmonic and dielectric systems.*

*The contents of this chapter have been published in parts in reference [4] © 2014 John Wiley and Sons; in reference [6] © 2015 American Physical Society; in reference [5] © 2015 Elsevier; and in reference [7] © 2015 Society of Photo Optical Instrumentation Engineers.*

## 6.1 Photonic Bloch States in Metal-Organic Microcavities

A one-dimensional periodic rectangular potential, also known as the Kronig-Penney (KP) potential, transforms the parabolic dispersion of a free particle into a set of bands separated by bandgaps. In the case of deep wells, the lowest bands converge into a set of single discrete states, enumerated by  $j = 1$  to  $j = j_{\max}$ , representing states confined of the position of the well. Such states can be found for example in the core electrons in condensed matter crystals, or confined photons as discussed in the previous section. Above the well potential, continuous extended states form the bands of valence electrons or extended photonic modes in laterally patterned microcavities. Due to the microscopic nature of electronic confinement, the KP potential and resulting mode structure is difficult to observe in experiments. Here, the formation of such a potential and the experimental observation of discrete and continuous KP states is presented within a periodically modulated metal-organic microcavity. The large coherence length of the vertically confined system facilitates the observation of photonic energy bands resembling localised and extended Bloch states in such deep potential wells. Depending on the width of the photonic wires, the thickness of the cavity layer and the additional metal grating, the parity of the highest localised state  $j_{\max}$  can be either even or odd, leading to a complementary parity of the first continuous mode. Such modification in turn effects the apex of the first extended Bloch-like state above potential, which in turn either starts at  $k = 0$ , or a  $\pi$ -state at the edges of the Brillouin zone formed by the periodic metallic wires.

### 6.1.1 Microcavity Dispersion and Kronig-Penney Model

Microcavity photons exhibit a dispersion relation similar to electrons, due to their confined nature between highly reflective mirrors. If the cavity is not detuned with respect to the DBR design wavelength, the  $k_z$ -component can be expressed as  $k_z = \pi/L_c$ . Then, the dispersion can be approximated by Equation (2.91):

$$E_C(k_{\parallel}) = \sqrt{\left(\frac{\pi\hbar c}{n_c L_c}\right)^2 + \frac{\hbar^2 c^2}{n_c^2} k_x^2} \approx E_C(0) + \frac{\hbar^2 k_x^2}{2m_x}, \quad (6.1)$$

where  $\pi\hbar c/n_c L_c = E(0)$  is the energy of the fundamental mode,  $m_x = \pi\hbar n_c/cL_c$ , while  $k_x = \omega \sin(\theta)/c$  is related to the angle  $\theta$  of the emitted light [217]. In angle-resolved reflection, transmission, or emission spectra of MCs, one can thus restore the true dispersion curves of cavities or e.g. exciton-polaritons and their nature. Bringing together several confined modes enables a coupling between spatially overlapping photons and polaritons in a periodic chain of square photonic boxes [218, 219, 220], showing the creation of photonic bands and bandgaps at the

Brillouin zone boundaries, resembling crystalline solids.

In subsequent investigations of such periodic arrays, new extraordinary features of the polariton dispersion were observed experimentally [86, 92, 221, 222]. In particular, the spontaneous build-up of coherent in-phase zero- and anti-phase  $\pi$ -states was observed in an exciton-polariton condensate array and explained as the result of coupling with weak periodic potential barriers within a semiconductor MC [49, 90]. Further investigations of polaritons in 2D square- [46, 97], triangular- [223], and honeycomb [99, 224] lattice potentials confirmed the coherent emission of  $\pi$ -states at edges of the Brillouin zones (including d-waves and K-states), and formations of Bogoliubov [225, 226] and Dirac [223] dispersions were observed. Note that the most of the investigated [49, 90, 97, 223, 224, 225] shallow periodic arrays are produced by thin, patterned metal structures with periods of a few  $\mu\text{m}$ , evaporated on top of the full MC stack. This cavity manipulation produces a weak potential of 200  $\mu\text{eV}$ , resulting in typical 1D or 2D Bloch waves.

In this experiment, a periodic array of one-dimensional photonic wires is created by the deposition of periodic 40 nm thick silver stripes at the interface between the organic cavity layer and the top surface of the bottom DBR. As discussed previously, this leads to the formation of the Tamm-plasmon-polariton states (TPPs), red-shifted by  $\sim 77$  meV to lower energies. Such patterned metallic stripes create deep photonic wires, unlike the shallow potentials observed before (Refs [90, 97, 223, 224, 225]), which demonstrate the simultaneous existence of discrete modes confined in photonic wells, and extended Bloch waves from high-index photonic bands, propagating above the barrier potential. The large exciton binding energy in combination with broad emission spectra of organic semiconductor dyes allow an observation of a broad energetic range of states at room temperature. The KP model can be used to analytically describe the peculiarities of the MC modes and, in particular, the phase-locking of the laser modes to either zero- or  $\pi$ -phase.

Structured metallic wires are of interest for future electrical excitation of organic microcavities and semitransparent conductive wires for display applications. The understanding of the complex modes formed in such a device seems integral for the optimal design, regarding directionality, confinement, and the optical and electrical excitation of luminescence in the system.

### 6.1.2 Photonic Bloch States

In the investigated sample (see Fig. 6.1) an array of silver stripes of  $\sim 40$  nm thickness, with different periods  $L_p = 7.4 \mu\text{m}$  or  $11.1 \mu\text{m}$ , is created by a photolithography lift-off process (Fig. 6.1 (a)). Due to limitations in precision, the resulting periodicity may vary by few percent. Here, silver is used due to its high reflectivity of  $R \approx 0.96$  in the spectral region of interest. The resonant wavelength  $\lambda_c \approx 656$  nm, ( $E_c(0) = 1.8895$  eV) of the metal-free cavity is deter-

mined by the optical thickness  $n_c L_c$  and the penetration depth of light into the DBRs [77, 198]. The embedding of the 40 nm silver layer between the cavity and the bottom DBR red-shifts the cavity resonance by  $V = E_c(0) - E_{\text{TPP}}(0) \approx 77$  meV to  $\lambda_{\text{TPP}} \approx 684$  nm, ( $E_{\text{TPP}}(0) = 1.8121$  eV) due to the additional shift of phases at the interfaces between the metal, the adjacent organic cavity, and  $\text{TiO}_2$  layers of the DBR[42].

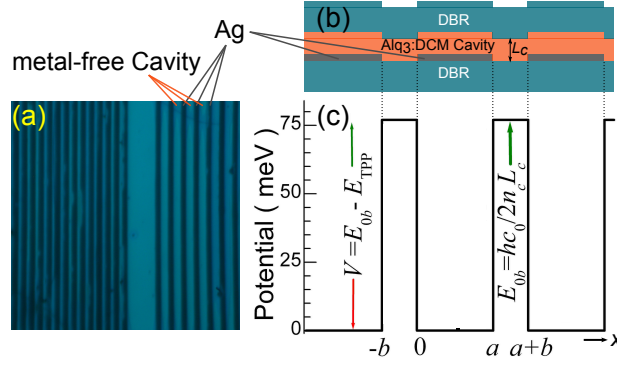


**Figure 6.1:** (a) Top view micrograph of the microcavity with the periodic array of metal-organic photonic wires, consisting of silver stripes of  $\sim 40$  nm thickness, the width  $a$  from  $\sim 2$  to  $\sim 10$   $\mu\text{m}$ , patterned by photolithography (periods  $L_P = 11.1$   $\mu\text{m}$ ) between the bottom DBR and the organic cavity layer. (b) Sample schematic cross section. (c) Spatial distribution of the 1D periodic rectangular potential, consisting of potential barriers of height  $V$  of the  $\text{Alq}_3:2\%\text{DCM}$  organic layer (with the refractive index  $n_b = 1.75$  and thickness  $h_b = 186$  nm) and potential wells of Ag stripes (with thickness 40 nm and width  $a$  from  $\sim 2$  to  $\sim 10$   $\mu\text{m}$ ). Reprinted with permission from reference [4].

Fig. 6.2 (a) shows the spatially-resolved emission spectra of a periodic structure measured by PL spectroscopy at 405 nm cw excitation. These NF spectra consist of two qualitatively different distributions: discrete TPP modes are confined within the photonic wires above silver of width  $a \sim 3$   $\mu\text{m}$ , emitting in the spectral range of 684–656 nm (1.8121–1.8895 eV) below the barrier. Above the barrier, extended continuous Bloch-like modes propagate at shorter wavelengths  $\lambda \leq 656$  nm (1.8895 eV), with comparable intensities. Figure 6.2 shows spectra with a higher spatial resolution. In Fig. 6.2 (c), the discrete modes (at 684–656 nm) start from the localized ground state centered at  $k = 0$  and go up to  $j_{\text{max}} = 9$  (highest “odd” localized mode). This highest mode localized below the barrier has 9 extrema, including the weakest satellite maximum at  $k = 0$ . The dispersion of the extended modes, starting at  $\lambda \approx 656$  nm, splits into subbands, separated by small bandgaps, or a set of anticrossing parabolas with much steeper slopes. The estimated period of the dispersion curves - as visible by the separation between shifted parabolas - is inverse to the spatial period  $L_P$ , decreasing when  $L_P$  changes from 7.4 to 11.1  $\mu\text{m}$ .

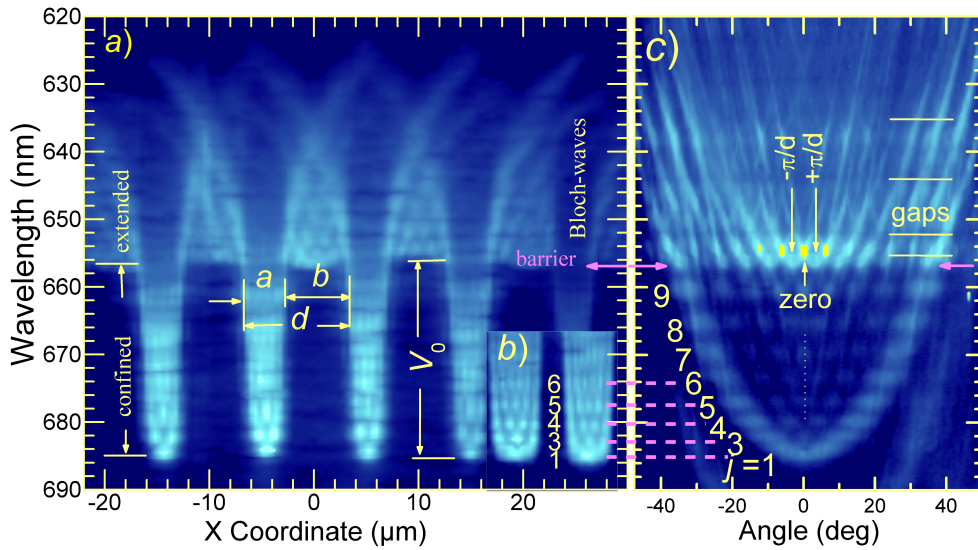


**Figure 6.2:** Spatially-resolved below-threshold (a, b) and angle-resolved above-threshold (c) emission spectra of the organic MC with an embedded 1D grating of metal stripes. The spectra were taken from two different areas with ( $a = 4.0 \mu\text{m}$  (a) and  $a = 7.7 \mu\text{m}$  (b, c)). For both areas the grating period is  $L_P = 11.1 \mu\text{m}$ . Both NF and FF images reveal discrete TPP modes (localized in the photonic wires and separated by potential barriers), emitting in spectral range 684 nm...656 nm. Bloch-like extended modes, periodic in real and k-spaces, propagate above ( $< 656 \text{ nm}$ ) the periodic array of metal-organic potential wells and organic-dielectric potential barriers. Reprinted with permission from reference [4].

### 6.1.3 Modified Kronig-Penney Model - Zero and $\pi$ -states

It is important to note that the (energetically) lowest Bloch-like extended mode from the lowest above-barrier ( $j_{\text{max}} + 1$ )-subband depends on the parity of the highest below-barrier mode. The apex of the extended dispersion parabola is therefore located at either  $k = 0$  or at the edge of the first Brillouin zone, at  $k = \pi/d$ , opposite to the parity observed for the mode  $j_{\text{max}}$ . At high excitation intensities (above lasing threshold), the coherent emission arises from several apex points of these parabolas of the lowest ( $j_{\text{max}+1}$ ) subband, marked in Fig. 6.2 (c) as yellow spots. Similar coherent phenomena were presented earlier [82], resembling the coherent emission of zero- or  $\pi$ -states in a periodic array of an inorganic MC [49]. Here, the aim is to explain which type of phase-locking will occur and how to analytically describe the formation of zero or  $\pi$ -states.

In the following, a simple KP-calculation according to Section 2.4 is used to derive analytical criteria for the  $j_{\text{max}+1}$  state. According to the KP model, in a 1D rectangular periodic potential

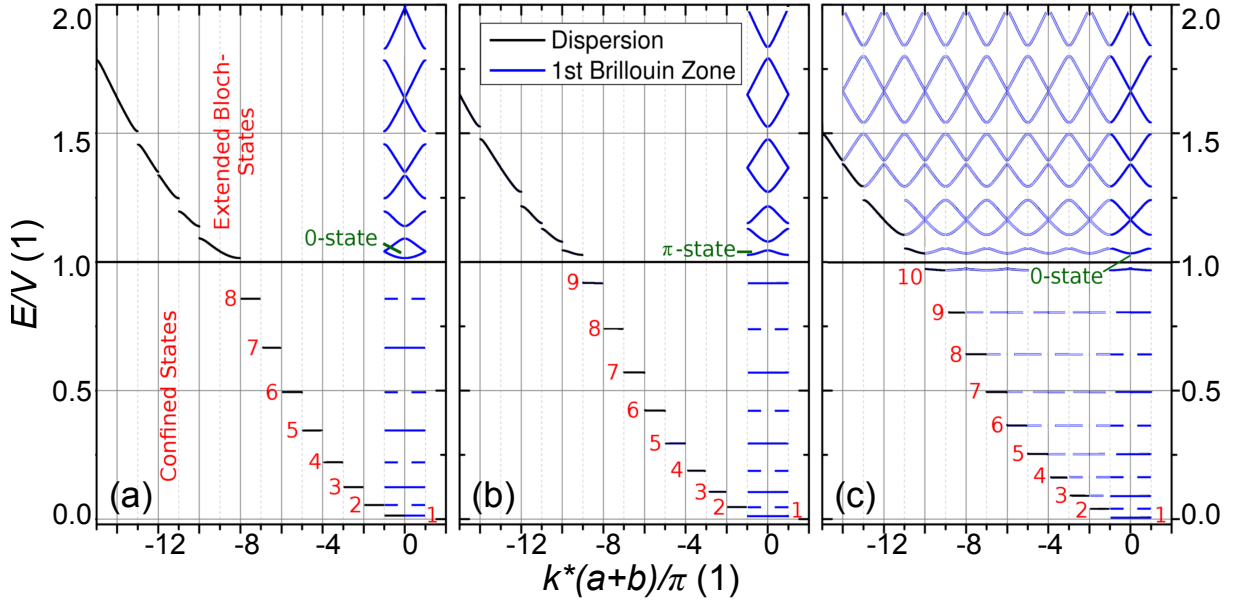


**Figure 6.3:** Analytical calculation of localized and extended Bloch states for potential widths 5.2  $\mu\text{m}$ , 5.5  $\mu\text{m}$ , and 5.8  $\mu\text{m}$  and periods 8.7  $\mu\text{m}$ , 9.0  $\mu\text{m}$ , and 9.3  $\mu\text{m}$ . The increasing potential width increases the number of below-barrier states from 8 to 10, switching the first extended state from zero- to  $\pi$ - to zero-type. The number of extended states is conserved due to the constant barrier width of 3.5  $\mu\text{m}$ , their appearance however changes due to the shift of parity in the below-barrier states. The third graph shows dispersion replica, Bragg-scattered at the Brillouin zone boundaries for comparison with the experimental data. Reprinted with permission from reference [4].

the dispersion relation transforms into Equation (2.103) [227]:

$$\frac{\beta^2 - \alpha^2}{2\alpha\beta} \sinh(\beta b) \sin(\alpha a) - \cosh(\beta b) \cos(\alpha a) = \cos(kd) \quad (6.2)$$

where  $\alpha = (2m_a^*E)^{1/2}/\hbar$  and  $\beta = (2m_a^*(V - E))^{1/2}/\hbar$ . The “wavevector”  $\alpha$  is real, while  $\beta$  is real for the eigenvalue energies  $E \leq V$  or imaginary for  $E > V$ . Eq. (6.2) implicitly relates the eigenvalues  $E$  in the left-hand side, via  $\alpha$  and  $\beta$ , with the corresponding wavevector  $k$ . It follows from Eq. (6.2) that the eigenvalues  $E_j(k) = E_j(k + 2\pi/d)$  are periodic in momentum space, with a reciprocal wavevector  $2\pi/d$ . The energies  $E_j(k)$  associated with the  $j$ th-subband vary continuously with the wavevector  $k$ , spanning within the first Brillouin zone  $-\pi/d \leq k \leq \pi/d$ . For a large potential height  $V$  and/or wide barrier width  $b$ , each subband in a photonic well collapses to an energy level  $E_j$  with vanishing bandwidth, similar to the discrete modes of the single photonic wire. For such discrete modes with energies  $0 < E_j \leq V$ , the field amplitudes  $\Psi_{a_j}(x)$  are essentially confined within the photonic wire with photon wave numbers  $\alpha_j = j\pi/a$ ,  $j = 1, 2, \dots$  and of either even or odd parity [228]. The index  $j$  gives the number of intensity maxima and



$(j - 1)$  the number of nodes of the spatial field distribution in the unit cell - as can be extracted from Fig. 6.2 (a). The corresponding discrete energies are described by Equation (2.69) [45]:

$$E_j(k_x) \cong (\pi\hbar c/n_c) \sqrt{1/L_c^2 + j^2/a^2}. \quad (6.3)$$

Here, both the cavity thickness  $L_c$  as well as the wire width  $a$  play a key role in determining the number of confined states. The angular distribution of the emission from discrete modes confined in the photonic well is given by the Fourier transform  $\tilde{\Psi}_{aj}(k)$  of the field amplitude  $\Psi_{aj}(x)$  [48]:

$$\tilde{\Psi}_{aj} \cong 2A j \pi a \frac{\cos(ak/2) \sin(j\pi/2) + \sin(ak/2) \cos(j\pi/2)}{(j\pi - ak)(j\pi + ak)}. \quad (6.4)$$

The highest below-barrier mode  $j_{\max}$  and the lowest extended mode  $j_{\max} + 1$  satisfy the following relation [229]:

$$j_{\max} < a(2m_a^*V)^{1/2}/\pi\hbar < j_{\max} + 1. \quad (6.5)$$

Of special interest is the case where the energy of the lowest extended Bloch wave precisely coincides with the barrier (i.e.  $E_{j_{\max}+1} = V, \beta = 0$ ), expressed by the condition [228]:

$$\cos(Ka) - \frac{bK}{2} \sin(Ka) = \cos(kd), \quad (6.6)$$

with the “wavevector”  $K = (m_a^*V)^{1/2}/\hbar$ . Equivalently, the lowest extended state ( $j_{\max} + 1$ ) appears at  $E = V$  when the following condition is satisfied:

$$(j_{\max} + 1)^2 \pi^2 \hbar^2 / 2m_a^* a^2 = V. \quad (6.7)$$

In that case, zero-states appear at  $Ka = 2\pi n$ , ( $n = 0, 1, 2, \dots$ ), while  $\pi$ -states appear at  $Ka = \pi(2n + 1)$ . The extended Bloch waves appear at  $E_j > V$ . Photonic bands are formed with particular subbands, continuing the discrete state index  $j$ . These subbands are separated by the bandgaps at the Brillouin zone boundaries. The extended Bloch waves consist of two parts: a wavefunction  $\cos(qx - (j + 1)\pi/2)$  with  $j$  nodes within the well, surrounded by propagating waves  $\exp(\pm ikx)$ , resulting in the energies  $\hbar^2(k \pm \pi j/d)^2 / 2m_a^*$ . They resemble either a zero- or  $\pi$ -Bogoliubov-like dispersions [225], depending on the parity of the mode  $j_{\max}$ .

Fig. 6.3 shows the analytic dispersion of such photonic Bloch waves for three different wire widths. Increasing the size of the potential well brings the states below the barrier closer together and also leads to an increase of  $j_{\max}$ . While the number of extended states above the barrier remains the same due to the constant barrier width of 3.5  $\mu\text{m}$ , their shape changes significantly, driven by the spectral shift of confined states. Especially the switching from zero- (for  $j_{\max} = 8, j_{\max} = 10$ ) to  $\pi$ -mode ( $j_{\max} = 9$ ) can be clearly distinguished. In the experimental spectra,

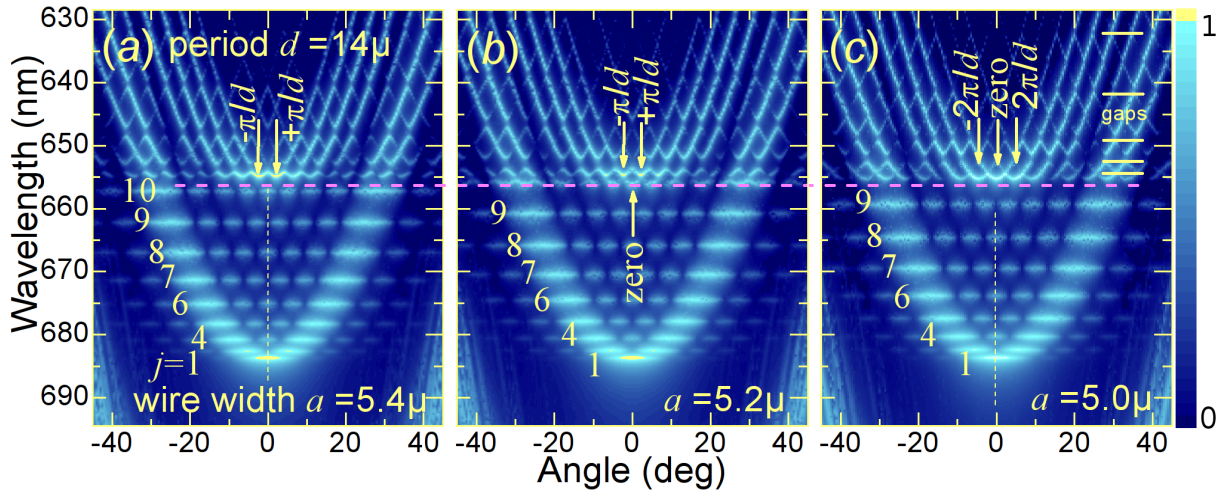


**Figure 6.4:** Calculated angle-resolved spectra of the periodic array of deep photonic wires with the potential widths  $a = 5.4 \mu\text{m}$ ,  $5.2 \mu\text{m}$ , and  $5.0 \mu\text{m}$  for (a), (b) and (c) respectively ( $L_P = 14 \mu\text{m}$  for all figures). The magenta dashed horizontal line marks resonance energy of the planar organic MC without metal at  $\lambda_c \approx 656 \text{ nm}$ , as a guide for the eye, separating discrete modes, confined in the wires, at  $\lambda \geq 656 \text{ nm}$ , from propagating extended waves above the barrier with anticrossing bands, at  $\lambda \leq 656 \text{ nm}$ . The slight decreasing of the wire width results in decreasing of the total number of localized modes from odd  $n = 9$  to even  $n = 8$ . Hence the nearest lowest extended Bloch wave-like modes switch from the odd ( $\pi$ -type) mode to the even (zero-type) mode. Reprinted with permission from reference [4].

the dispersion is enriched by highly efficient Bragg-scattering of features at the Brillouin zone boundaries. For comparison, this effect is added in Fig. 6.3 (c) by backfolding the analytically calculated spectrum at the boundaries  $n\pi/d$ .

For the lasing states, one has to consider that the density of the states in one dimension is given by the equation [230]:  $\rho(E) = 2(dk/dE)/\pi$ , which, for a  $\pi$ -state, reaches maxima at the bottoms of the  $(j_{\text{max}} + 1)$ -subband at  $k = n\pi d$  or its tops at  $k = 0$ , where the Van Hove singularity occurs due to vanishing of the group velocity. The lasing threshold for the particular state is determined by the interplay of absorption and optical gain.

While the analytical equations (6.2) - (6.7), described above, allow qualitative understanding of the formation of the state manifold and dispersions, they do not take into account effects such as metal absorption, residual absorption of the organic semiconductor, gain, polarization splitting, and so on.

In order to obtain a more realistic FF picture, numerical calculations are performed based on the Rigorous Coupled Wave Analysis method. These numerical simulations of the periodic arrays of deep photonic wires with identical periods  $L_P = 14 \mu\text{m}$  and three different widths  $a = 5.4 \mu\text{m}$ ,  $5.2 \mu\text{m}$  and  $5.0 \mu\text{m}$  are presented in Fig. 6.4 (a), (b) and (c), respectively. These calculations confirm the analytical model and show the difference between the localized, dis-

crete states below the barrier, and the extended continuous subbands above, separated by minibandgaps. For the discrete modes in the spectral range of 655 nm...685 nm, Fig. 6.4 illustrates the narrow energy levels characterized by the index  $j$ , the energy  $E_j(k)$  and their flat wavevector distribution, entirely determined by the well width  $a$ . These modes are neither influenced by the barrier width  $b$  nor the period  $L_P$ , which affect the energy band distribution above the barrier. The amplitudes of the wavevector, the distribution of the confined modes, the positions of the nodes, the main and satellite maxima and their half-widths, as well as their alternative even and odd parities, are all confirmed in the numerically calculated spectrum, exactly as predicted by the analytical relations. In particular, the decrease of the well width  $a$  from 5.4 to 5.0  $\mu\text{m}$  leads to a gradual short-wavelength shift of all levels with indices  $j \leq j_{\text{max}}$ . Moreover, the number of discrete modes changes from 9 to 8, wherein the parity of the highest localized -  $j_{\text{max}}$  - mode changes from odd to even. In addition to the analytical formulas, the numerical simulations also include the spectral broadening of the confined modes. Additionally, the numerical simulation predicts the angular and spectral distributions of the amplitudes and half-width of cosine-like dispersion curves  $E_j(k)$ .

Organic microcavities with embedded periodically distributed thin metal stripes serve as an excellent playground to experimentally demonstrate the energetic dispersions of arrays of deep photonic wires. One can observe coexisting discrete modes, confined mostly within the photonic well between the barriers, and extended continuous Bloch waves propagating above both wells and barriers. The KP model allows for a simple analytical description of the system. According to this model, the highest localized mode  $j_{\text{max}}$  can be even or odd, depending on relation (6.5).

An even or odd parity of the highest discrete mode  $j_{\text{max}}$  confined in the photonic wells determines the parity of the lowest ( $j_{\text{max}+1}$ ) extended in-phase zero- or anti-phase  $\pi$ -modes, propagating above the energy barriers. Above the barrier, the extended Bloch waves  $\Psi_{aj}(x)$  form photon bands (with  $j$  indexing the particular subband) separated by the bandgaps at the Brillouin zone boundaries. While the use of metal-organic photonic wires here opens the direct path to the electrical injection of excitons for this system, alternative routes can be found that further preserve the high optical quality and low absorption of the devices. It has to be noted that the KP model in this section, in particular the simplified approximation of the photon effective mass, is only valid when the cavity resonance is not detuned with respect to the DBR wavelength. A more in-depth quantitative analysis will follow in the next section.

## 6.2 Control of Lasing from Bloch States in SiO<sub>2</sub>-patterned Microcavities

This section addresses the spontaneous and coherent stimulated emission of SiO<sub>2</sub> photonic wires in a MC with an organic active medium. Under spatially selective excitation, the possibility to precisely control the spectral and angular position of lasing from the wire and above the potential barrier is demonstrated. Numerical simulations accompany the experimental results to further showcase the effect of a selective gain distribution. Even though the presented MCs operate in the weak coupling regime, such results are more generally applicable towards guiding, trapping, and controlling photons or polaritons in organic or inorganic MCs.

Typically, lasing in VCSELs arises in vertical direction, from the apex of the microcavity dispersion parabola. In those cases, the coherent photons or polaritons emit from this mode under an in-plane wavevector  $k = 0$  from the lower polariton branch or MC photon dispersion. Coherent emission from polaritons in non-ground states was observed under resonant pumping, explained by an incomplete polariton down-relaxation and their short life time. Coherent emission from excited states of planar MCs at resonant laser excitation has also been observed experimentally [231, 232] and explained as the reemission of the excitation laser into a ring-like distribution in  $k$ -space due to elastic resonant Rayleigh scattering at static disorder. Ring-shaped coherent emission at nonresonant excitation was reported [233] and explained in GaAs MCs where excess energy was lost before being captured into a bottle-neck trap [234]. Ring-shaped coherent emission has further been observed in CdTe [235] and organic [236] MCs, due to scattering of light into multiple cavity modes at  $k \neq 0$ .

Periodically arranged photonic wires offer a possibility for studying the formation of Bloch-states in ZnO [96] or GaAlAs MCs[56], showcasing coherent emission from non-ground gap states in the Bloch-like polariton dispersion [86] or more exotic Fibonacci-sequence patterns [237]. Cerna *et al.* [206] demonstrated the manipulation of confined polariton modes in a 0D pillar by tuning either the incidence angle of the excitation beam and/or its energy at below-threshold intensities. Moreover, optical structuring has been employed, where the formation of an exciton population in a particular pumping geometry locally increases the cavity potential and leads to emission from confined modes [238] or geometrical phase-locking of emission from several excited spots [210, 239]. Furthermore, gain-induced trapping of exciton polaritons has been utilized by Roumpos *et al.* due to the short lifetime and finite size of excitations [240].

A manipulation of coherence in ground- and excited- states could be shown in circular pillars [241] and photonic wires [93, 221] by a controlled shift of the excitation spot position. Furthermore, a switching of coherent modes was demonstrated by spatially selective excitation under nonresonant optical pumping in GaAs pillar MCs.

### 6.2.1 Coexisting of Confined and Extended Optical Bloch States in a SiO<sub>2</sub> Photonic Wire Array

For 1D confinement in organic photonic wires with micron-size widths  $L_W$  from  $\sim 1 \mu\text{m}$  to  $\sim 10 \mu\text{m}$ , optical lithography is utilised to add thin SiO<sub>2</sub> stripes ( $n_{\text{SiO}_2} = 1.45$ ) via a lift-off process. This patterning modulates the cavity thickness with an amplitude of  $d_{\text{SiO}_2} = 15 \text{ nm}$  and periods of  $3.7 - 14.8 \mu\text{m}$ , sandwiched between two similar DBRs. Each photonic wire is surrounded by barriers of only the organic cavity layer with a smaller height  $d_O = \lambda_c/2n_O$  and width  $L_B \sim 2$  to  $\sim 10 \mu\text{m}$ .

Microcavities exhibit a parabolic dispersion up to certain angles, above a constant potential determined by the cavity thickness. An additional thin layer of SiO<sub>2</sub> in this system causes a shift in the MC energy landscape, i.e. the photon potential is red-shifted according to Section 2.2.4:

$$E_{\text{Cav}} = \frac{\pi\hbar c}{n_O d_O + n_{\text{SiO}_2} d_{\text{SiO}_2}}, \quad (6.8)$$

where  $n_i$  and  $d_i$  are the refractive indices and physical thickness of the organic (O) cavity layer and the SiO<sub>2</sub> wires. Such a red shift in cavity resonance is already showcased in Chapter 4. Please note that this equation is an approximation that is valid near the center of the DBR stop-band, where the penetration into neighbouring mirror layers is minimal. A full calculation is given later in this chapter.

In photonic wires, this shift causes an index-guided confinement which discretizes the MC resonance into several standing wave modes, exhibiting flat dispersion below the potential barrier. Both red-shift and discretization are visible in the spatially-resolved  $\mu\text{-PL}$  measurement in Fig 6.5 (a). Below the barrier, non-dispersive discrete states correspond to localised modes trapped at the position of potential wells, and inner satellites (648 nm - 625 nm). Above the photonic barrier potential, the dispersion is extended, with the appearance of photonic minibands (<623 nm). Here, a multitude of Bragg-scattered extended states become visible, being repeated after each reciprocal lattice constant  $2\pi/(L_W + L_B)$ .

To compare such patterning with the use of thin silver films in the previous chapter, Figure 6.5 shows the spatially resolved emission from such photonic wires for either TPP-based (a) or dielectric (b) confinement.

In Fig. 6.5 (a), one observes a strong spatial confinement of photons in the spectral range between 658 nm to 685 nm at the position of the 40 nm-thick metal layer. The emission from photonic wires is discretized in energy and exhibits modes of increasing number of antinodes that are directly observable in the emission of our sample. As only discrete  $k$ -values are allowed

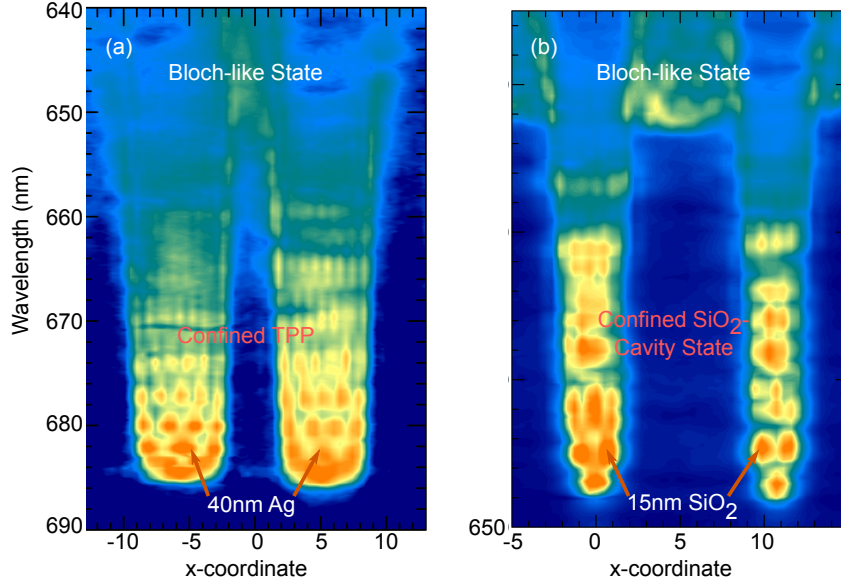


**Figure 6.5:** (a) Spatially resolved emission spectrum of a MC with 40 nm-thick metal stripes of  $\approx 7 \mu\text{m}$  in width. In the range of 658 nm - 685 nm, confined Tamm-plasmon-polaritons are visible as discrete standing waves with an increasing number of antinodes due to the strong confinement below the barrier. Above the barrier, an extended Bloch-like state becomes visible. (b) Spatially resolved emission spectrum of a MC with SiO<sub>2</sub> stripes of  $\approx 4.5 \mu\text{m}$  in width. Here, confined states are visible in the range of 649 nm - 622 nm. Despite their different physical origins, both types of structuring produce similar strong lateral confinement. Reprinted with permission from reference [7].

inside the well, the energies (at  $k_y = 0$ ) are qualitatively given by Equation (2.69):

$$E_m = \hbar c \sqrt{k_z^2 + k_y^2 + k_z^2} = \hbar c \sqrt{k_z^2 + \frac{(m+1)^2 \pi^2}{n_C^2 a^2}} = \pi \hbar c \sqrt{\frac{1}{(n_C L_C)^2} + \frac{(m+1)^2}{n_C^2 a^2}}, \quad (6.9)$$

where  $n_C$  and  $L_C$  are the effective cavity refractive index and thickness, which has to be adapted to the phase change at the metal interface, accordingly, and  $c$  is the speed of light in vacuum. The index  $m$  describes the number of confined states from ground ( $m=0$ ) to highest excited state below the barrier. Above the barrier ( $< 658$  nm), extended states fill the spectrum.

Similarly strong confinement can be observed now in SiO<sub>2</sub> stripes, where a comparably small physical thickness of only 15 nm is enough to create the deep potential of the photonic wire from 621 nm to 649 nm. In 4.5  $\mu\text{m}$  thick wires, again a discretization of modes is demonstrated below the barrier. The calculation of their energy levels follows Equation (6.9) again, where the cavity thickness  $n_C L_C$  is directly calculated from the optical thicknesses of organic and SiO<sub>2</sub> layers  $n_{\text{Alq}_3} L_{\text{Alq}_3} + n_{\text{SiO}_2} L_{\text{SiO}_2}$ . The smaller width of the wire here leads to a larger spacing between discrete states. In addition, a detuning of this particular cavity with respect to the DBR design

wavelength facilitates a splitting of each discrete mode into its respective polarization directions TE and TM, where TE modes lie lower in energy than their TM counterparts. A full calculation of these polarization-dependent mode positions requires a full consideration of the penetration of modes into adjacent DBR layers.

The types of structuring employed here serve similarly well to confine light inside of microcavities, even though the physics behind the shift of the photonic potential is completely different. Both, plasmonic and index-guided confinement, may be utilized to shape photon or polariton dispersions towards interesting new experiments.

### 6.2.2 Photonic Bloch States in Metal- or SiO<sub>2</sub>-Patterned Cavities

While the spatially-resolved near field gives a good representation of the photonic well and its corresponding modes and a direct observation of the photonic potential, the full observation of Bloch-states can only be made in angle-resolved emission spectra. Figure 6.6 shows the dispersion for both metal- (a) and SiO<sub>2</sub> (c) cavities below and above their potential barrier. Below the barrier, the discrete states exhibit a flat dispersion and  $(m - 1)$  submaxima inside the typical cavity parabola, according to the index  $m$  of discrete state. While even states ( $m = 0, 2, \dots$ ) exhibit always an antinode in the center, odd states ( $m = 1, 3, \dots$ ) show the first antinodes at  $k = \pi/(a + b)$  and thus show no emission in normal direction to the sample surface.

Above the barrier, the formation of photonic energy bands with band-gaps becomes clear in both cases. Here, the lowest above-barrier state starts, complementary to the oddity of the highest below-barrier state, either at  $k = 0$  ((c),  $m_{\text{below}} = 7$ ) or at a  $\pi$ -state ((a),  $m_{\text{below}} = 8$ ). As the intensity of light is dampened by the metal layer, the below-barrier states in the metal cavity exhibit a lower intensity than the above-barrier states, while in the SiO<sub>2</sub> cavity a more evenly distributed intensity can be observed. Nevertheless, both types of structuring do not only show the formation of localized states below, but also a clear and directly accessible Bloch-like dispersion above the photon potential barrier. Furthermore, this interaction between different optical states of several periodic wires at macroscopic distances showcases the large spatial coherence in the system, at room-temperature, even below the lasing threshold.

The formation of Bloch-like optical modes can be calculated using the modified Kronig-Penney model given in Section 2.4. The cavity dispersion is related to the dispersion of a free electron and receives an equivalent to the effective mass on the order of  $10^{-5} \cdot m_{\text{el}}$ . Utilizing this analogy, the Kronig-Penney model can be computed from the time-independent Schrödinger equation. Figure 6.6 (b) and (d) show this calculation for the corresponding samples (a) and (c), reproducing number and positioning of localized states and formation of extended Bloch-like states above the potential barrier. As the emission of microcavities is influenced by Bragg-

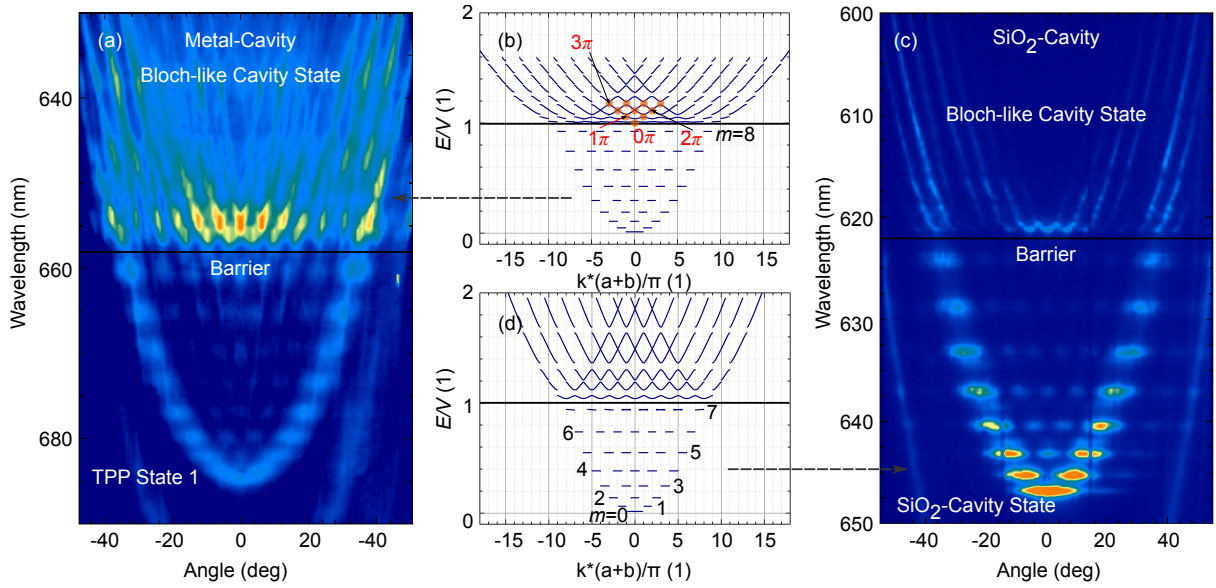


**Figure 6.6:** Spontaneous emission spectra from laterally patterned microcavities. (a) Angle-resolved emission spectrum of a MC with a 40 nm-thick silver layer of  $\approx 4 \mu\text{m}$  in width. Below the barrier at 658 nm, discrete TPP states are confined within the metal stripe, exhibiting a flat dispersion. Above the barrier, an extended Bloch-like spectrum becomes visible. (b) Kronig-Penney calculation for (a) with Bragg-scattering up to the eighth order. (c) Angle-resolved emission spectrum of a MC with a 15 nm thick  $\text{SiO}_2$  layer of  $\approx 4.5 \mu\text{m}$  in width. Again, a discrete, confined spectrum becomes visible below the barrier, albeit of higher quality owing to the low absorption of  $\text{SiO}_2$  in comparison to silver. Above the barrier, a similar Bloch-like band structure with clear bandgaps is visible. (d) Kronig-Penney calculation for (c) with Bragg-scattering up to the eighth order. Reprinted with permission from [7].

scattering at the boundaries of the Brillouin zones, this feature is included as scattered replica up to order 8 in the calculation.

The patterning with  $\text{SiO}_2$  wires enables a thorough investigation of the behaviour of light in corresponding cavities. For this purpose, different wire widths and periods are fabricated in the same sample, comparing the formation of Bloch states here. Figure 6.7 gives the angle-resolved emission spectra of different wire widths ((a) to (c)) and different periods ((d) and (e)). It becomes clear that an increase in width of the potential well decreases the spacing of discrete states, leading to an increased number of fully confined states from 8 (wire width  $5 \mu\text{m}$ ) to 17 ( $11 \mu\text{m}$ ). It is remarkable that even for such large spacings, the Bloch state formation below and above the potential barrier is still possible, owing to a large coherence length of the system even in the spontaneous emission regime. When keeping the wire width constant and changing their period, however, the localised states are not effected. Instead, the shape of the extended states above-barrier and their Bragg-scattered replica can be manipulated.



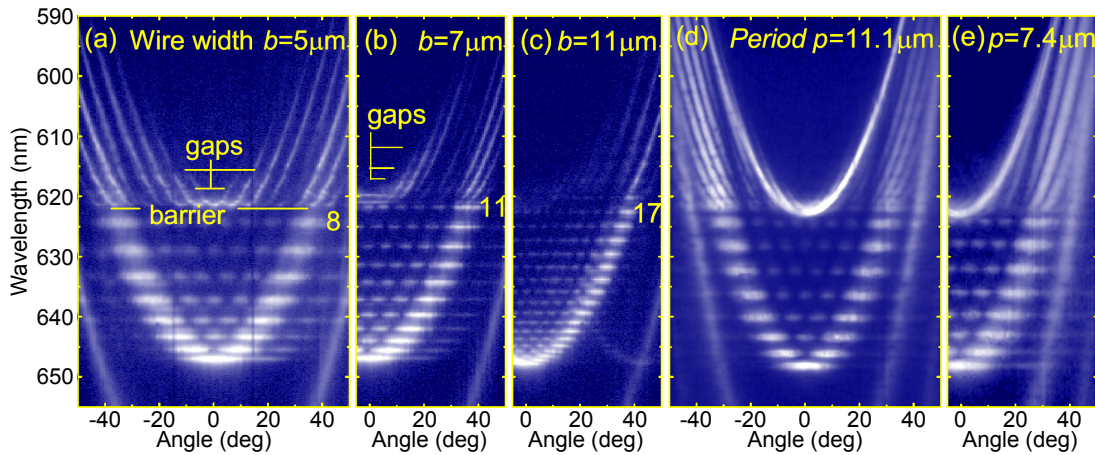


**Figure 6.7:** Experimental spectra, (a)-(e) angle resolved, (f) spatially resolved. (a) to (c): wire widths  $L_B = 5 \mu\text{m}$ ,  $7 \mu\text{m}$  and  $11 \mu\text{m}$ , respectively, and a barrier width of  $L_W = 3 \mu\text{m}$ , showing extended states above and localized states below the potential barrier. A larger wire width leads to smaller energy gaps between the levels of localized states resulting in more levels, see numbers 8, 11 and 17. (d) and (e): the same wire width  $L_B = 5.5 \mu\text{m}$  and the periods  $L_P = 11.1 \mu\text{m}$  and  $L_P = 7.4 \mu\text{m}$ , respectively, exhibiting no change in the localized states, but in the distance of the replica of extended states to each other. Figure reprinted with permission from reference [5].

Both metal and dielectric structuring facilitate an engineering of the cavity dispersion despite fundamentally different physical origins. While coupled Tamm-plasmon states enable interesting insights into the coupling of photons to plasmons and a direct route to electrical excitation, structuring via loss-less dielectric materials provides the highest optical quality of the sample and very narrow modes with high quality factors both in vertical and lateral direction.

### 6.2.3 Quantitative Description of Coexisting Localized and Extended Bloch States

Previous considerations only give an approximation regarding exact energetic positioning of modes and do not take into account polarisation of light, they however are correct if the microcavity is in tune with the stop-band of the DBRs and no polarisation splitting [77, 198] is present. In all other cases, a more involved theory has to be applied. This fact becomes clear in Figure 6.8 (a) and (b), where polarisation-dependent angle resolved spectra of a  $\text{SiO}_2$ -wire cavity are shown. Here, the spacing of TM-polarised discrete states is larger than for TE-polarisation, even leading to a different number of discrete states from 14 (TM) to 16 (TE) in total.

Such polarisation properties can be integrated into the existing theory by the concept of a polarisation-dependent effective mass. The effective mass of a photon in a microcavity can be obtained from the curvature of the derived energy dispersion. The dispersion by Equation (6.10)

for microcavities with small to zero detuning is given by Equation (2.91):

$$E(k_x) = \hbar c \sqrt{k_z^2 + k_x^2/n_c^2} \approx E_0 + \frac{\hbar^2}{2m^*} k_x^2. \quad (6.10)$$

There,  $k_x$  is the wavevector parallel and  $k_z = 2\pi/2n_c L_c$  perpendicular to the cavity plane.

More detuning between the distributed Bragg reflectors (DBRs) and the cavity layer results in the aforementioned polarisation splitting. Since Equation (6.10) does not include the polarisation, the resonance calculations by Panzarini *et al.*[77] are employed here, which consist of the cavity thickness  $L_c$ , the cavity-only resonance frequency  $\omega_c$ , the central DBR stop-band frequency  $\omega_s$ , the penetration depth into the DBR  $L_{\text{DBR}}$  and the effective cavity thickness  $L_{\text{eff}} = L_c + L_{\text{DBR}}$ :

$$\omega = \frac{L_c \omega_c + L_{\text{DBR}} \omega_s}{L_{\text{eff}}}. \quad (6.11)$$

From Panzarini *et al.*, we obtain parametrisations for each variable in Equation (6.11) depending on  $\theta$ , the angle between the direction of the light propagation, the cavity plane normal ( $z$ -direction), and even on the polarization. With the relation  $k_x = k \sin(\theta)$ , one can approximate  $\omega \approx \omega_0 + \omega_1 x^2$  to the second order of  $x = \sin(\theta)$ , resulting in Equation (6.12) for the effective mass, considering  $k \approx k_z = \omega_0/c$ :

$$m^* = \frac{\hbar \omega_0^2}{2\omega_1 c^2}. \quad (6.12)$$

A direct Taylor approximation on  $\omega$  is extensive, so Taylor approximations of all variables are considered (see Equation (6.13)) and  $\omega$  is calculated from Equation (6.11) stopping at terms of  $x^2$ :

$$\omega_c \approx \omega_{c0} + \omega_{c1} x^2, \omega_s \approx \omega_{s0} + \omega_{s1} x^2 \quad (6.13)$$

$$L_{\text{DBR}} \approx L_{D0} + L_{D1} x^2, \frac{1}{L_{\text{eff}}} \approx \frac{1}{L_{\text{eff0}}} - \frac{L_{D1}}{L_{\text{eff0}}^2} x^2 \quad (6.14)$$

$$\begin{aligned} \omega &\approx \left( L_c (\omega_{c0} + \omega_{c1} x^2) + (L_{D0} + L_{D1} x^2) (\omega_{s0} + \omega_{s1} x^2) \right) \\ &\quad \cdot \left( \frac{1}{L_{\text{eff0}}} - \frac{L_{D1}}{L_{\text{eff0}}^2} \right) \\ &\approx \frac{L_c \omega_{c0} + L_{D0} \omega_{s0}}{L_{\text{eff0}}} \\ &\quad + x^2 \left( \frac{L_c \omega_{c1} + L_{D1} \omega_{s0} + L_{D0} \omega_{s1}}{L_{\text{eff0}}} - \frac{L_{D1} (L_c \omega_{c0} + L_{D0} \omega_{s0})}{L_{\text{eff0}}^2} \right). \end{aligned} \quad (6.15)$$

Utilising this parametrisation, the effective mass of microcavity photons can be calculated with high precision from Equation (6.12), obtaining values of  $m_{\text{TE}}^* = 1.30 \cdot 10^{-5} \cdot m_{\text{el}} = 1.19 \cdot 10^{-35}$  kg and  $m_{\text{TM}}^* = 1.04 \cdot 10^{-5} \cdot m_{\text{el}} = 9.45 \cdot 10^{-36}$  kg. Such low masses aid in a multitude of interesting

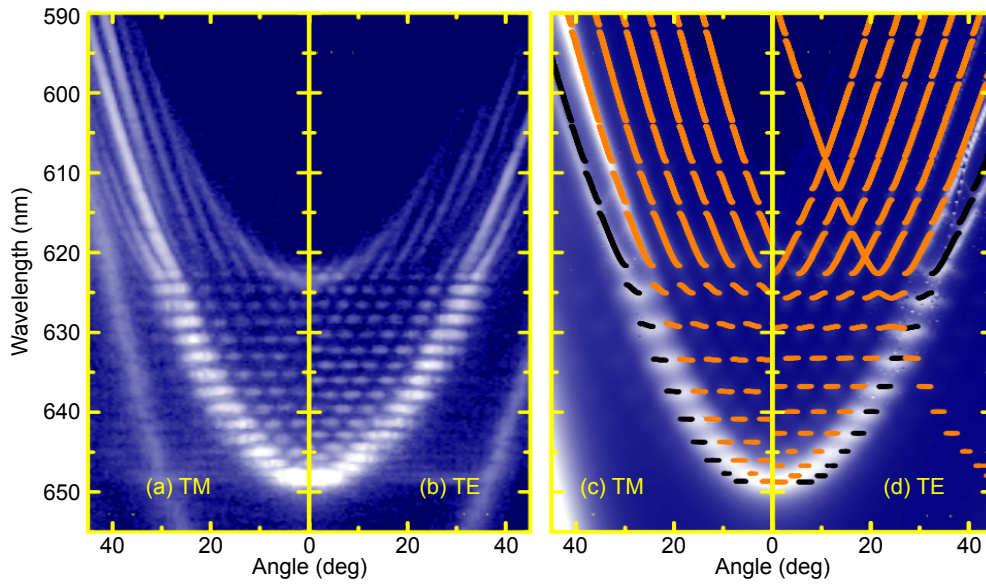


**Figure 6.8:** (a) and (b): measured angle-resolved spectra of TM- and TE-polarized emission, respectively, both with wire width  $b = 11.1 \mu\text{m}$  and period  $p = 14.8 \mu\text{m}$ , showing different energy levels depending on the polarization resulting in more discrete levels for TE than for TM-polarized light. (c) and (d): numerically simulated transmission of TM- and TE-polarized light, respectively, overlaid with the calculated energy dispersion using the KP-model and the effective mass of a photon propagating through a microcavity of the same design in black and the Bragg scattered states in orange. Reprinted with permission from reference [5].

propositions, among them the Bose-Einstein condensation of quasiparticles formed by the strong interaction between excitons and microcavity photons. While in the present case, the TE-mass is larger than the TM-mass, this relation changes when the cavity-DBR detuning changes sign as well.

Unfortunately, in the experiment, the photonic potential structure is not perfectly rectangular. Irregularities in fabrication lead to a lateral deformation of the photonic wires by few tens to a hundred nm. In turn, the Bloch state formation in the experiment does not perfectly follow the theory presented here. To verify the analytical theory presented here, numerical simulations of perfect structures are performed, closely resembling the real cavity conditions. By a commercially<sup>1</sup> implemented rigorous coupled wave analysis, a cavity with a wire width of  $7 \mu\text{m}$  and a barrier of  $1 \mu\text{m}$  is simulated and compared to the mode positions of the effective-mass-corrected Kronig-Penney model. Figure 6.8 (c) and (d) show an excellent agreement between this calculation and the numerically simulated spectrum in both TE and TM polarisation. This further validates the modelling and can aid in the prediction of further experiments exploiting the photon effective mass.

<sup>1</sup>RSoft by RSoft Design Group inc.

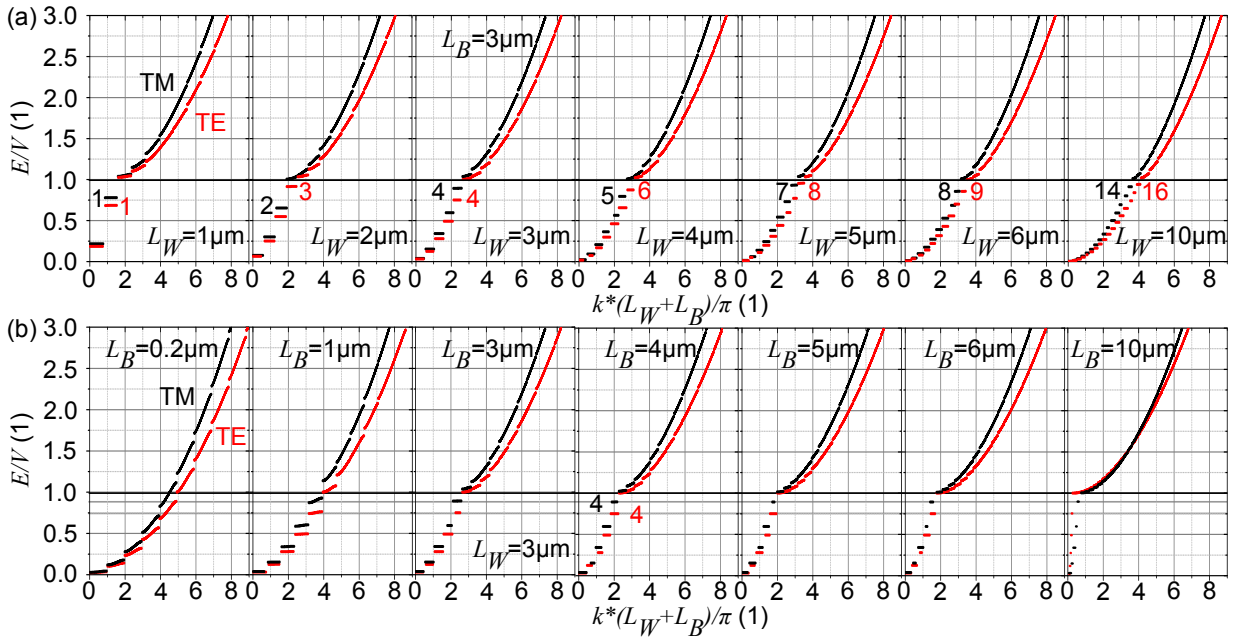


**Figure 6.9:** Bloch states calculated with effective-mass-corrected Kronig-Penney model with a potential depth of 80 meV and photon effective masses of  $m_{\text{TE}}^* = 1.30 \cdot 10^{-5} \cdot m_{\text{el}}$  and  $m_{\text{TM}}^* = 1.04 \cdot 10^{-5} \cdot m_{\text{el}}$ . The larger mass of TE-polarised photons leads to a less steep dispersion curve and red-shift of discrete states compared to TM photons. (a) Variation of photonic wire width  $L_W$  at constant barrier thickness of  $L_B = 3.0 \mu\text{m}$ . Increasing the width of the photonic well drastically increases the number of discrete states below the barrier. At large wire widths, both polarisations may exhibit a different number of discrete states. The above-barrier bands remain largely unchanged during the variation. (b) Variation of the barrier thickness  $L_B$  at constant wire width  $L_W = 3.0 \mu\text{m}$ . While the below-barrier states show the same number and spectral position of discrete states, the above-barrier bands transform into a smooth parabola with only diminutive gaps for large barrier thicknesses. Interestingly, for small barriers an interaction between photonic well states is possible and a non-flat dispersion results also for below-barrier states.

In Figure 6.9, a large variation of both barrier and well widths is performed utilising this model. Increasing the photonic wire width (Fig. 6.9 (a)), the number of discrete states rises as their spectral distance decreases as expected for a larger quantum well. Starting from only two discrete states for a wire width of  $L_W = 1 \mu\text{m}$ , a multitude of states appears in the following calculations, until the below-barrier space is almost filled by a quasi-continuum at widths  $> 10 \mu\text{m}$ . Here, only higher order states exhibit a significant spectral spacing, which increases as the mode number becomes larger. Here, also a difference in the number of discrete states can be made out for different polarisations. As in the present example the TE mass is larger than the TM mass, the corresponding curvature is more flat and in turn a higher number of discrete states may appear. This effect is visible for wire widths of  $2 \mu\text{m}$ , and  $4 \mu\text{m} \dots > 10 \mu\text{m}$ . Coincidentally, for a width of  $3 \mu\text{m}$ , the discrete state number is the same. In special cases, dispersion features of

both polarisations might overlap, as seen for a width of  $6\ \mu\text{m}$  where a degenerate state between  $m_{\text{TE}} = 9$  and  $m_{\text{TM}} = 8$  is formed. At such points, lasing in both polarisations may occur under the right conditions. While the below-barrier spectrum is drastically altered, the above-barrier states remain mostly the same. The position of photonic minibands is however influenced by the below-barrier behaviour and, as explained in the last section, their parity can facilitate the formation of zero and  $\pi$ -phase coupling in the first Brillouin zone (not depicted).

The situation changes, when the barrier width is varied at constant photonic wire thickness (see Fig. 6.9 (b)). Here, number and spectral position of the below-barrier discrete states is fixed by the constant wire width. Above the barrier, the spectrum transforms from the photon miniband structure with considerable gaps at low barrier thickness to a more or less continuous parabolic spectrum for wide barriers. Even in this calculation, where perfect coherence is assumed, a band structure is hardly visible above  $L_{\text{B}} = 10\ \mu\text{m}$ . One of the most interesting features arises here, when the barrier is very small compared to the wire thickness. Such thin barriers allow the tunneling of photons between different photonic wires and enable an interaction between discrete state also below the energy barrier. In the model, such interaction facilitates a dispersion of light also for the otherwise flat, non-dispersive states at  $E/V < 1$ . While for  $L_{\text{B}} = 1\ \mu\text{m}$ , this is the case for the higher order discrete states, for very thin barriers ( $L_{\text{B}} = 0.2\ \mu\text{m}$ ), tunneling is possible at almost all photonic energy levels. A coherent interaction between such otherwise confined optical states may enable a multitude of new experiments, including the Bloch oscillation of photons in these superstructures.

The large polarization splitting and its detailed understanding are furthermore key aspects for applications e.g. in Spin-Optronics, such as the optical spin Hall effect [57] and the recent proposal of a Z polaritonic topological insulator [58]. By adding a driving field to similar systems, optical Bloch oscillations were observed and investigated [177, 242, 243, 244, 245, 246, 247].

### 6.2.4 Above-Threshold Investigation

The low absorption of the  $\text{SiO}_2$  photonic wire and the high quality of patterning not only enable the direct observation of the spatial distribution of light, from the ground state with one antinode to higher excited trapped states with up to six antinodes visible in the experiment, but furthermore aid in the transitioning to the stimulated emission regime. For (far-) above-threshold excitation of the photonic wires, two types of lasing are observed, depending on the positioning of the single pump spot. Figure 6.10 showcases both near and far field spectra of lasing modes in such a system. While placing a single pump spot strongly focused over one photonic wire (marked as a pink circle in Fig. 6.10 (a)), the coherent emission originates from the bottom of the potential well, at  $648\ \text{nm}$  and  $k = 0$  (see Fig. 6.10 (c)), where the parabola apex would appear

in an unstructured MC. Shifting the excitation to the position of the barrier (Figs. 6.10 (b) and (d), input-output curve (e)), the strong stimulated emission is now concentrated at 623 nm, as a supermode above the left and right barriers at  $\pm 5 \mu\text{m}$ . In  $k$ -space, not only laser emission at zero angle can be observed, but a strong scattering into the hybrid well-barrier state at angles  $\pm 30^\circ$  takes place. An analogous behaviour can be observed in the formation of a Kastler ring in MCs with multiple cavity modes [236]. The extended Bloch-states are illuminated more strongly for an excitation of the barrier and show a first hint of the photon miniband structure.

Utilizing this spatially selective pump above-threshold, one can manipulate the coherent emission from discrete states confined in separated excited photonic wires, or from an extended Bloch wave, propagating through excited barriers and neighboring non-excited photonic wires.

While the gain profile of the organic  $\text{Alq}_3$ :DCM emitter system covers a broad spectral range, its peak is centered at 630 nm. Utilizing the flat dispersion in photonic wires, there exists a possibility to probe this distribution when exciting the wires only slightly above threshold. As lasing starts at points of high photonic DOS, with  $\rho(E) = 2(dk/dE)/\pi$ , each discrete mode represents a condensation point for the laser modes. In Figure 6.11, photonic wires of different widths  $L_W = 1.0 \mu\text{m}$ ,  $3.7 \mu\text{m}$ , and  $10.0 \mu\text{m}$  exhibit coherent emission only at  $630 \text{ nm} \pm 3 \text{ nm}$  for a pump intensity at or slightly above the lasing threshold. The overall high density of photonic states allows lasing from non-ground states, providing the peak gain value can overcome absorption which happens only in higher excited modes closer to the emission maximum. For larger excitation energies, the coherent emission shifts again towards the potential well or -barrier ground state, where the highest Q - values are obtained.

All angle-resolved spectra here follow the same general sample composition, i.e. showing confined wire states at 648 nm - 625 nm, while the different widths of the potential well strongly influences the appearance and number of the discrete, flat modes. The distribution of these states can be calculated using the modified Kronig-Penney model, where the particle energy and effective mass are substituted by their photonic counterparts in MCs [4, 5]. For the approximation of high barriers, the spatial mode distribution  $F_m(x)$  can then be expressed as

$$F_m(x) \approx \cos(q_m x) \text{ or } \sin(q_m x). \quad (6.16)$$

Here, the discretized modes are labelled by an integer  $m = 0, \pm 1, \pm 2, \dots$ , yielding the corresponding wavenumbers  $q_m = \pi(m + 1)/L_W$ . The analytical expression for the angular distribution (with  $k_x \propto \sin \theta$ ) of the emission intensity  $I_m(k_x)$  follows from the Fourier-transformation of the spatial distribution [48]:

$$I_m(k_x) \propto \cos\left(\frac{L_W k_x}{2} - \frac{m\pi}{2}\right)^2 \times \frac{q_m^2}{(q_m^2 - k_x^2)^2}. \quad (6.17)$$

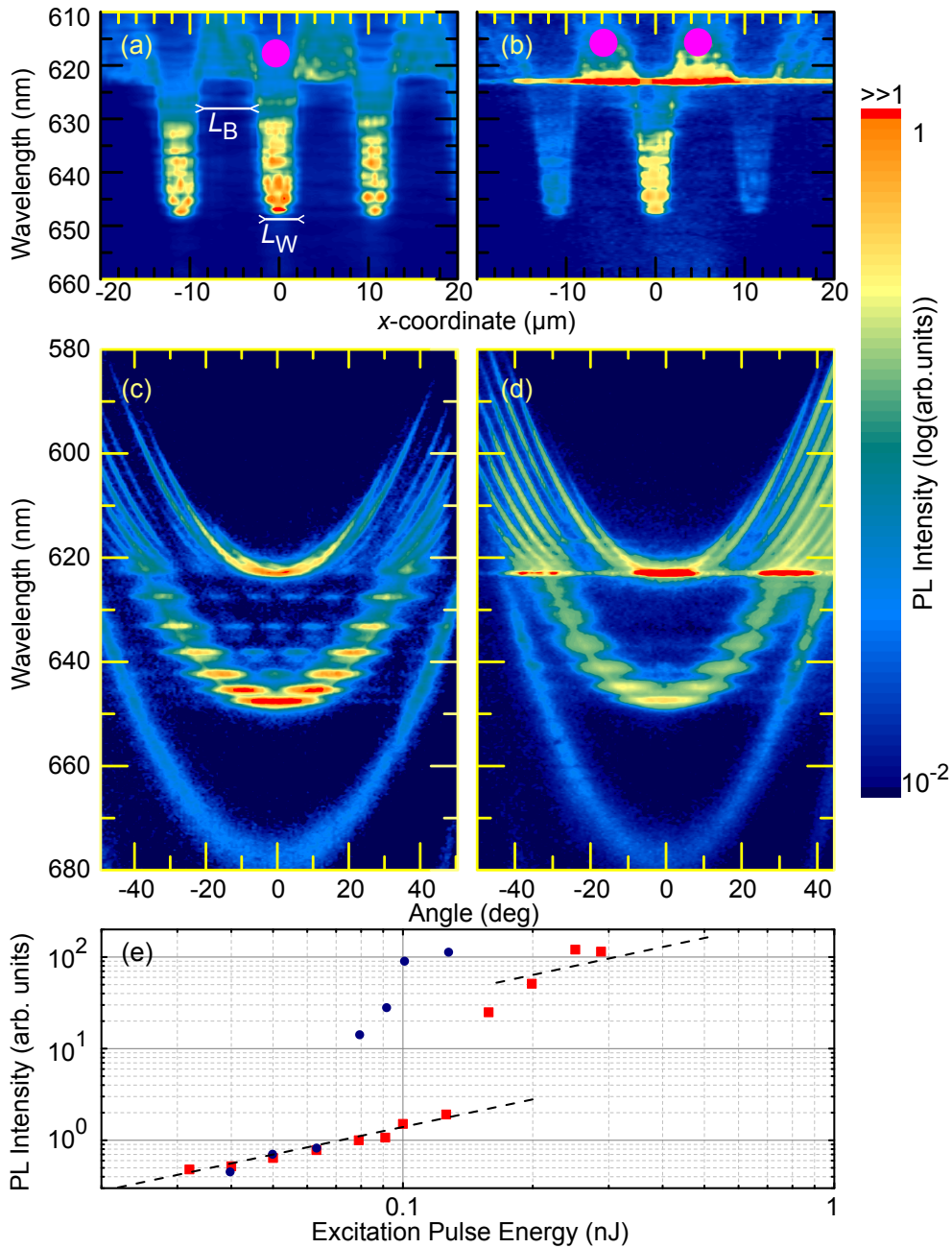


**Figure 6.10:** (a), (b): Spatially resolved emission spectrum perpendicular to a photonic wire for above-threshold excitation localized on the wire (a,  $L_W = 3.7 \mu\text{m}$ ) and of the barrier (b,  $L_B = 7.4 \mu\text{m}$ ). The potential induced by the  $\text{SiO}_2$  wire laterally traps photons in discrete standing wave modes. Lasing takes place either from the lowest confined state (a), or the lowest extended above-barrier state (b) (deep red). The excitation spot position is indicated in pink. (c), (d): Angle-resolved emission corresponding to (a) and (b). The emission from the barrier exhibits a flat dispersion, while the above-barrier states show a Bloch-like dispersion with almost continuous spectra. The intensity is color-coded in logarithmic scale in all figures. (e) Input-output curve for excitation of the barrier as in (b), (d) (red squares) with a lasing threshold of  $0.15 \text{ nJ}$  ( $\sim 20 \mu\text{J}/\text{cm}^2$ ) and for the excitation of the wire as in (a), (c) (blue circles) with a threshold of  $0.1 \text{ nJ}$ . Dashed lines with a slope of 1 are added as a guide for the eye. Reprinted with permission from reference [6].

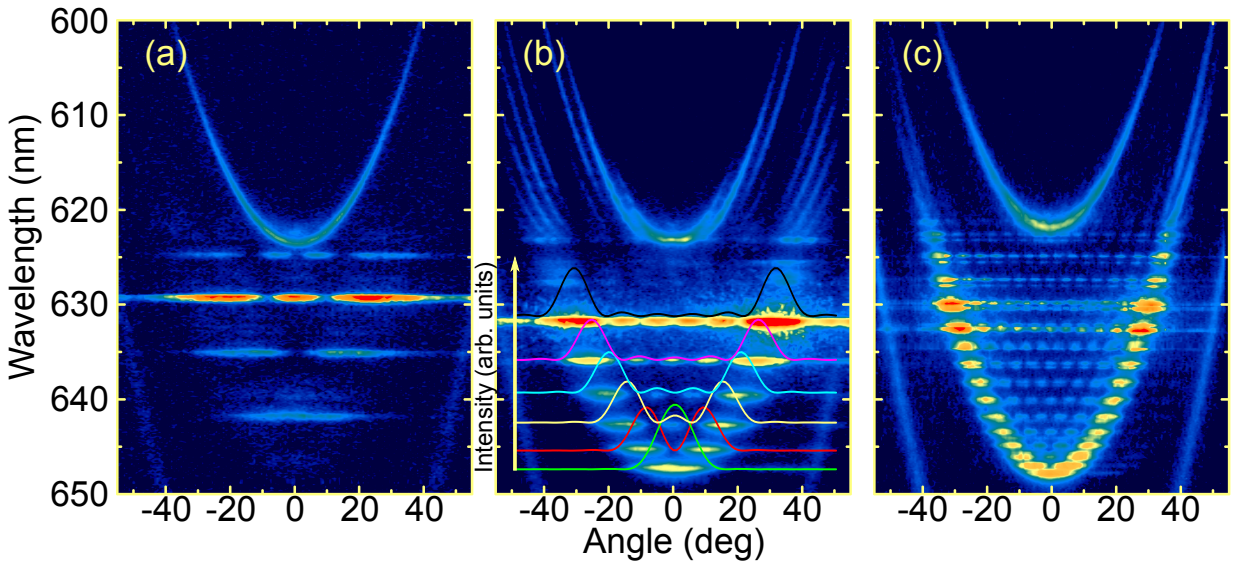


**Figure 6.11:** Angle-resolved emission from photonic wire arrays of different  $L_W = 1 \mu\text{m}$  (a),  $3.7 \mu\text{m}$  (b), and  $10.0 \mu\text{m}$  (c) for excitation on the wire. The width of the photonic wire leads to a closer or wider spacing of the discrete modes below the barrier, and a differing total number of confined states. Due to the flat dispersion of the confined states, lasing originates from the modes closest to the gain maximum of the organic emitter, even for different geometries. Intensity is color-coded as in Fig. 6.10. Solid lines in (b) represent calculations of  $k$ -spacing according to Eq.(6.17). Reprinted with permission from reference [6].

This equation yields the angle- and spectrally-resolved emission of the discrete modes in the spectral range of  $623 \text{ nm} < \lambda < 643 \text{ nm}$ .

Even though the width of the photonic wire  $L_W$  does not influence the total red-shift of the resonance (Eqn. (6.8)), it has a significant influence on the number and spacing of the discrete modes, as apparent from Eqns. (6.9) and (6.17). Figure 6.11 showcases this behaviour for the different widths of the potential well on top of the photonic wires. Here, it becomes obvious that a smaller wire width leads to larger energetical gaps between and a smaller number of the discrete states. For imperfect sample conditions, i.e. a not perfectly square potential, the spectral position of modes differs. However, the  $k$ -space distribution after Eq. (6.17) still fits remarkably well, since the lateral confinement is very strong. This is showcased in Fig. 6.11 (b) by solid lines.

### 6.2.5 Control of Lasing by Selective Excitation

The spectral alignment of gain maximum and cavity modes, however, is not the only factor to consider. In particular, the spatial position and distribution of gain can have a significant impact on the spectral and angular distribution, or even the threshold of laser emission in such photonic



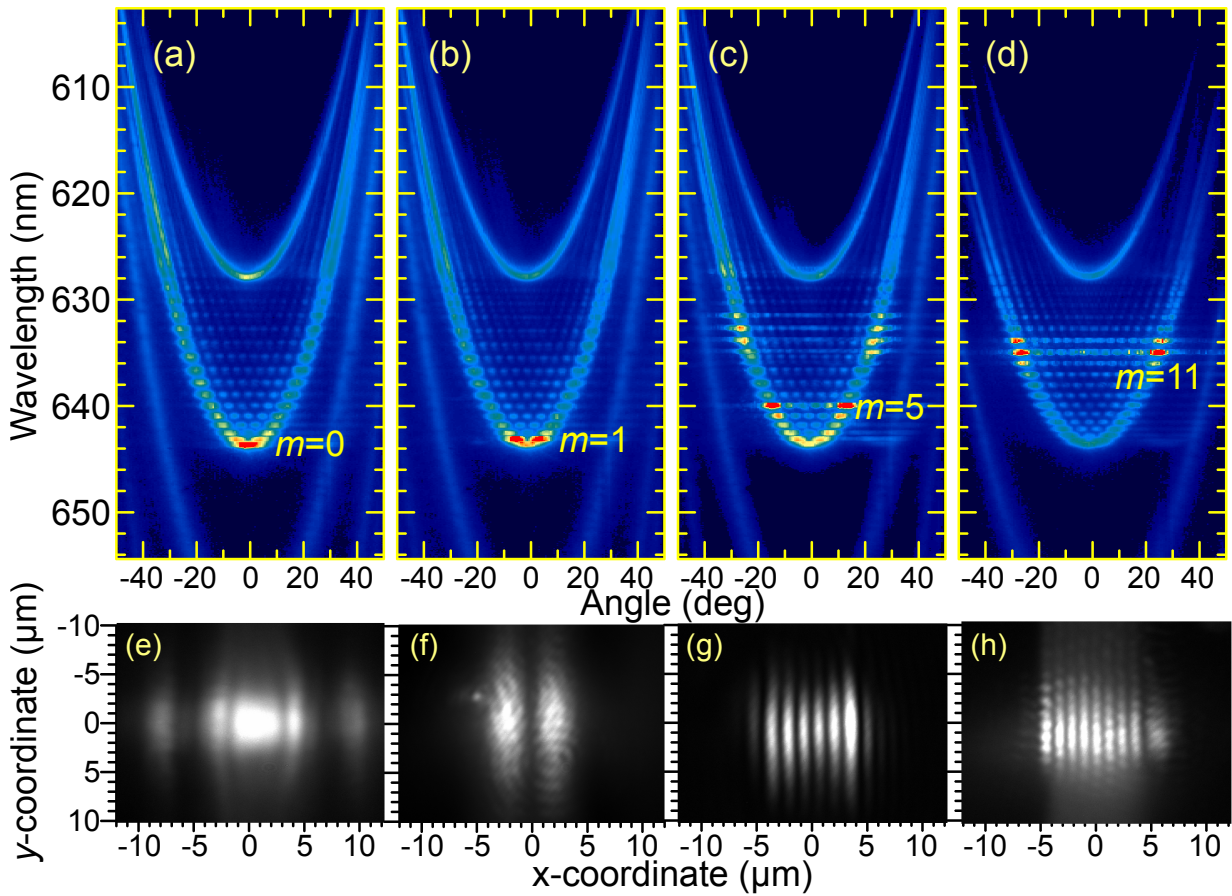


**Figure 6.12:** Lasing from a photonic wire of  $L_W = 10.0 \mu\text{m}$ , for different gain distributions created via two excitation beam interference. (a)-(d) show the angle-resolved dispersion, while (e)-(h) show the corresponding modes in near-field. Here, the  $x$ -coordinate is perpendicular, while the  $y$ -coordinate is parallel to the wire orientation. By varying the angle of two excitation beams, and thus the spatial distribution of gain, modes with a corresponding field distribution are selectively excited, from the ground state with one antinode (a), to higher excited states with  $m + 1$  antinodes (b-d). Intensity in (a)-(d) is color-coded as in Fig. 6.10. Reprinted with permission from reference [6].

wires. If a strongly focused ( $< 3 \mu\text{m}$ ) excitation spot is centered exactly in a photonic wire, only symmetric (even) modes can overcome the threshold, while all antisymmetric (odd) modes only show weaker spontaneous emission. In general, the excitation reaches the highest efficiency, when its spatial distribution overlaps with the corresponding field distribution of the laser mode. Utilizing this principle, the dependence of the near- and far-field emission spectra on spatially selective excitation of photonic wires is investigated. When the excitation spot at above-threshold intensity is focused into the center of the wire (see Figure 6.12(a)), coherent emission emerges from the center of the excited wire with a wavelength  $\lambda_0 = 643 \text{ nm}$  at  $k = 0$ . The remaining - higher - modes are still visible in spontaneous emission with significantly weaker intensity.

In the approximation (6.16), the confined modes have a periodic modulation with a period  $P = 2L_W/(m + 1)$  within a wire of the thickness  $L_W$ . For an optimal selective excitation of the  $m$ -th confined mode, the pump laser beam is split into two to utilise the interference pattern created by focusing those two beams onto the sample under an oblique angle. This scheme creates the desirable periodic population of excitons in the DCM and provides gain in the photonic wire that selectively excites certain modes. Changing the incident angles of the two excitation beams, the period of the interference pattern changes accordingly, allowing the precise control of the excitation geometry in the system and to create standing waves with a distinct transversal wavenumber  $q_m$ . This way, the occurrence of coherent emission can be switched from the wire ground state (Fig. 6.12 (a) and (e)), to higher excited states. To demonstrate this concept, laser emission from modes  $m = 1$  (Fig.6.12 (b) and (f)),  $m = 5$  (Fig.6.12 (c) and (g)), and  $m = 11$  (Fig.6.12 (d) and (h)) is shown exemplarily. Here, the micrographs (e)-(h) show the near-field emission of the confined modes in the photonic wires, where  $m$  nodes and  $m + 1$  antinodes are observed in the spatially resolved emission of the respective state. Each mode is optimized for the lowest threshold of the non-resonant excitation. This allows not only the energetic tuning of the laser, but furthermore enables a direct control over the main peak in the angular distribution of the coherent emission from  $k = 0$  in the ground state over angles of  $\pm 5^\circ$  ( $m = 1$ ),  $\pm 14^\circ$  ( $m = 5$ ), and  $\pm 23^\circ$  ( $m = 11$ ) to even higher angles. The satellite maxima of the higher excited states also provide an outcoupled laser light at exactly (for  $m$  even) or close to (for  $m$  odd)  $k = 0$ . The interference angles between the exciting beams outside of the cavity are:  $\approx 10^\circ$  ( $m=1$ , (b));  $\approx 31^\circ$  ( $m=5$ , (c));  $\approx 66^\circ$  ( $m=11$ , (d)). The weak emission centered around (645 nm,  $+25^\circ$ ) is an artifact of the optical setup.

By utilising the broadband emission of the laser dye and exhibiting a fine control over the spatial exciton distribution via a specific pump scheme, a highly tunable system results. As the tunability of the system stems mainly from the confinement of the wires, an application towards strong-coupling is straightforward by substituting the luminescent dye for a system with sufficiently strong and narrow absorption in the spectral region of interest. This will further open up fascinating new experiments such as spin-optics, the investigation of magnetic properties, and propagation of excitons in such potential landscapes.

### 6.2.6 Numerical Simulation of Selective Excitation

To quantitatively confirm the experimental spectra, a numerical simulation is performed, showing the emission from a periodic ( $P = 10 \mu\text{m}$ ) array of photonic wires with a width of  $L_W = 5 \mu\text{m}$  using a rigorous coupled wave analysis. In the angle resolved image presented in Figure 6.13, again the coexistence of confined and extended Bloch-states below and above the potential bar-

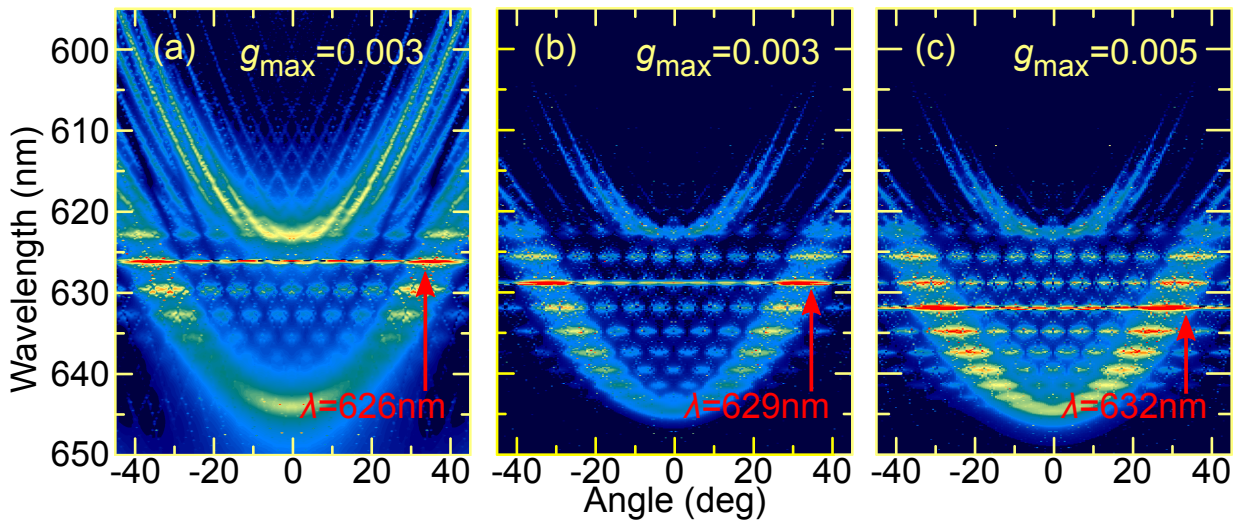


**Figure 6.13:** Calculated angle-resolved spectra of emission from photonic wires under different gain distributions. Intensity is color-coded as in Fig. 6.10. Reprinted with permission from reference [6].

rier of the SiO<sub>2</sub>-wires is confirmed. As the simulation assumes a perfect sample condition, the Bloch-like photonic miniband structure is well visible above the barrier here.

In this approach, the amplitude and spectral shape of gain is included into the consideration, both dependent on excitation intensity. For the simulation, the sample is excited by an array of different spatially distributed gain maxima amplitudes:  $g_{\max}(626 \text{ nm}) = 3 \times 10^{-3}$  (a),  $g_{\max}(629 \text{ nm}) = 3 \times 10^{-3}$  (b), and  $g_{\max}(631 \text{ nm}) = 5 \times 10^{-3}$  (c). As marked in red, lasing starts from the confined modes that closely resemble the spatial gain distribution. The wavelength and angular distribution of coherent emission can be easily tuned by switching between different confined modes utilizing the excitation scheme.

In a photonic wire microcavity, one-dimensional confinement of photons can be realised in a photonic potential well created by stripes of SiO<sub>2</sub>. The experimental observation of photonic Bloch states as a spectral discretization of the cavity dispersion below and extended quasi-continuous states above the confining potential is accompanied by a description of these modes via a Kronig-Penney model tailored to the system. Using a broadband organic emitter, its gain distribution is directly probed in differently sized wires with flat dispersion. By creating a spatial distribution of excitons in a modified pump scheme, the wide spectral range of the emitter can be taken advantage of to directly tune the laser emission from the ground state at  $k = 0$  to arbitrarily high excited states at smaller wavelengths and larger outcoupling angles. Therefore, such finely tuned experimental conditions enable a direct control over the coherent emission in the device.

## 6.3 Comparing Laser Modes in Periodically Patterned Microcavities

While both SiO<sub>2</sub> and silver photonic wires facilitate the formation of photonic Bloch states, their above-threshold behaviour showcases their different composition. By increasing the excitation intensity, both such MCs can be brought to lase at threshold energies on the order of the magnitude of a few nJ/Pulse. The laser mode characteristics however differ strongly from planar cavities, where stimulated emission takes place always at the bottom of the cavity parabola, at  $k=0$ . There, the apex provides a high density of states (DOS) and therefore an accumulation of field intensity necessary to overcome the lasing threshold.

The coherent interaction between states located in different photonic potential wells or on top of the barrier in patterned MCs severely alters the photon dispersion as seen above and provides a concentration of photon DOS  $\rho(E) = 2(dk/dE)/\pi$  [230] next to photonic bandgaps and at discrete states below the barrier. This leads to a manifold increase of possible lasing modes both on top of the structured areas and in between. Even though lasing in TPP structures has been reported recently [83, 84], the additional metal absorption even in such optimised TPP states makes lasing of this particular state difficult to observe. Here, the above-barrier extended Bloch states provide the ability to observe unusual lasing modes of the cavity state at non-zero in-plane momentum. Figure 6.14 (a) depicts a measurement above threshold, showing lasing (in red) from an excited above-barrier state. Here, the laser mode is concentrated at  $k = \pm\pi/(a + b)$  and no emission in normal direction is observed. Due to its comparably weaker intensity, the spontaneous emission of the TPP states is not visible here. By further increasing the excitation pulse energy, even multimode lasing from up to 4 different modes at increasing  $k = \pm m\pi$  can be observed, shown in Fig. 6.14 (b).

On the other hand, the almost loss-less SiO<sub>2</sub> wires provide an ideal spot for tunable lasing modes in their discrete states as described above. Fig. 6.14 (c) and (d), comparatively shows the spatially and angle-resolved spectra of lasing from a high excited discrete state. Due to polarisation splitting [5, 207], the discrete states split into TE- and TM-polarized modes and the final lasing modes is split into the 6TE and 5TM mode due to their close spatial overlap.

The lateral patterning of microcavities provides an interesting playground for engineering coherent interaction of photons and polaritons at macroscopic distances. While metallic patterning provides coherently coupled states above the potential barrier as well as a direct electrical access for future charge carrier injection, SiO<sub>2</sub> wires provide continuously tunable coherent states[6] in their deep photonic potential wells. Such patterning can be integrated into smallest devices on the micron-scale in all dimensions.

Even though conceptually very different structured interlayers are employed to produce shifts

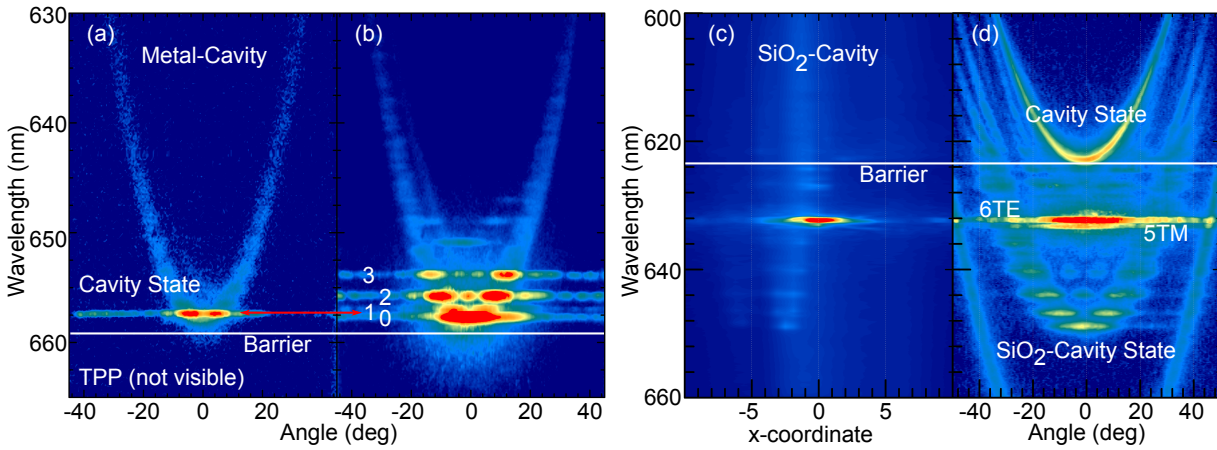


**Figure 6.14:** Lasing spectra of patterned MCs. (a) Angle-resolved lasing of the second cavity-state ( $m=1$ ) in a MC with 40 nm-thick silver stripes of  $\approx 4 \mu\text{m}$  in width. The lateral patterning enables lasing of non-ground modes in the cavity state at the position of  $\pm 1\pi$ . (b) Angle-resolved lasing of multiple states in the metal-cavity at  $k = m \times \pi$ , going up to  $m=3$ . (c) Lasing of a highly excited  $\text{SiO}_2$ -cavity state in a MC with 15 nm  $\text{SiO}_2$  of  $\approx 4.5 \mu\text{m}$  in width. Due to the low absorption of  $\text{SiO}_2$  and the flat dispersion provided by the confinement, higher order states can be excited. (d) Angle-resolved image of (c), showing lasing at high  $m$ . Due to polarization splitting in this MC, the lasing mode is split into the  $m=6$  TE- and  $m=5$  TM-modes. Reprinted with permission from reference [7].

in the cavity potential, both facilitate the formation of localized and extended Bloch-like states. In metal-organic MCs, the formation of Tamm-plasmon-polaritons is utilised, enabling the observation of photonic wells, Bloch-states and laser emission at non-zero in-plane momentum, also showcasing their macroscopic coherence at room-temperature. Patterning the cavity using the almost loss-less  $\text{SiO}_2$  the potential shifts due to an increased cavity thickness and Bloch-states of very high optical quality are observed in all directions. Continuously tunable lasing is enabled by exciting different discrete states in the system. The experimental observation of Bloch-states is assisted by a modified Kronig-Penney calculation, giving an analytical model for the complex dispersion in the cavities. Both types of structuring show promising features for shaping photonic and polaritonic states in MCs and controlling the build-up of coherence in those systems.



# 7 Hybrid Waveguide-VCSEL Resonators And Coherent Interaction

*In this chapter, a different type of in-plane structuring is employed to manipulate the microcavity dispersion. By fabricating a micrometer-scale grating on top of the substrate, a coherent coupling between the VCSEL mode and waveguided modes in the active layer is realised.*

*Section 7.1 provides an introduction to the device architecture, showing that the lateral profile is continued through to the top of the sample, facilitating efficient Bragg-scattering of modes in the active area.*

*In Section 7.2, the polarisation- and angle-resolved spontaneous emission spectra are discussed. Here, the observation of anticrossing between VCSEL and scattered waveguided modes demonstrates the coherent coupling between these regimes.*

*Finally, Section 7.3 investigates the coherent emission of such hybrid devices, showing the emergence of hybrid lasing modes with a large lateral extension in real and sharp resonances in  $k$ -space besides the typical VCSEL mode lasing.*

*The contents of this chapter have been published in parts in reference [10] © 2016 John Wiley and Sons.*

## 7.1 Hybrid Device Architecture

Two of the most successful microresonator concepts are the vertical cavity surface emitting laser (VCSEL), comprising a vertical cavity of highly reflective DBRs sandwiching an active layer, and the distributed feedback (DFB) laser, where a periodic optical grating selects laser modes from an active waveguide (WG) layer. Here, the concepts of VCSEL and waveguide are united in a single device, facilitating coherent interaction between them via a periodic optical grating at points of crossing dispersion relation.

While a first order DFB grating enables only edge emission of the device, higher order gratings [248, 249, 250] scatter light also into the vertical direction and thus enable coupling to a VCSEL mode in a combined device. Here, a  $|\sin|$ -profile with a comparably large period of  $1.1 \mu\text{m}$  and a modulation depth of  $\approx 30 \text{ nm}$  is etched into a silicon substrate providing a scattering of wave-

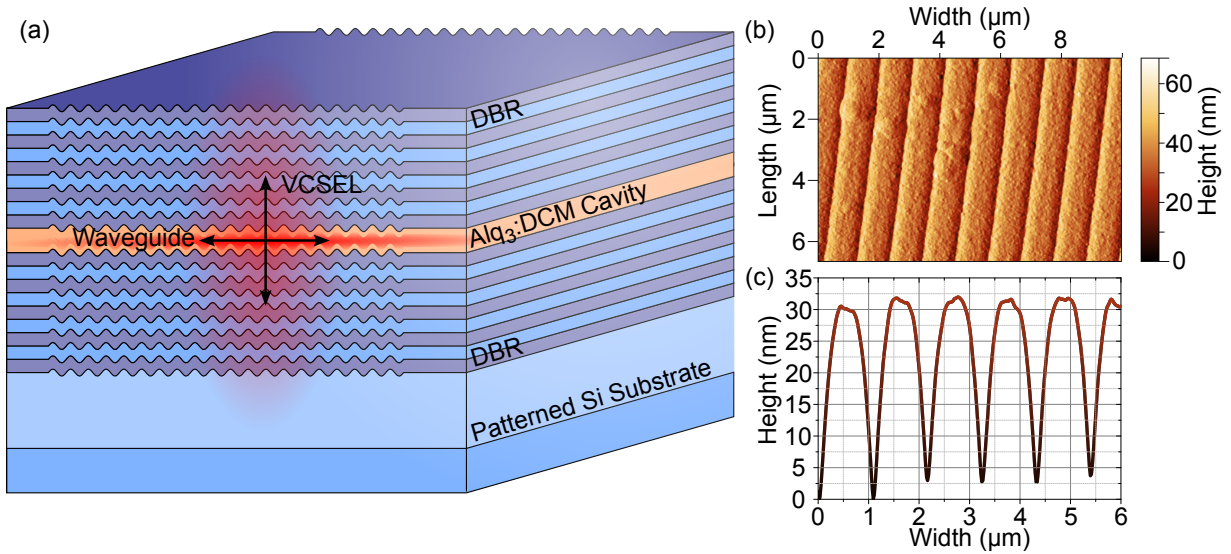


**Figure 7.1:** (a) Sample schematic for the hybrid WG-VCSEL sample. A full microcavity stack is deposited on top of a periodically patterned Si substrate, leading to a coupling of in-plane WG and vertical microcavity resonator. (b) Atomic force microscope image of the top DBR layer of the finished cavity showing that the patterning of the substrate is continued through all 43 layers. (c) Contour profile of (b) with a  $|\sin|$ -like shape. Reprinted with permission from reference [10].

guided modes into the vertical resonator. The large period provides no direct optical feedback for a DFB, but facilitates scattering of modes into surface emission. On top of this structure, a full VCSEL stack of  $2 \times 21$  layer  $\text{SiO}_2$ - $\text{TiO}_2$  DBRs encasing an active  $\text{Alq}_3$ :DCM cavity of 185 nm thickness is deposited via thermal evaporation. The sample schematic is depicted in Figure 7.1 (a). The deposition technique and rigid silicon substrate facilitate a continuation of the pattern throughout the whole device up to the top DBR layer. On top of the finished device, the morphology is scanned by atomic force microscopy (see Fig. 7.1 (b) and (c)), revealing an almost perfect continuation of the pattern despite depositing 43 different layers (total thickness  $\approx 4 \mu\text{m}$ ) on the initial structure. This fabrication provides a corrugated waveguide in the full cavity, comprising the organic active and surrounding DBR layers.

## 7.2 Emission of Hybrid WG-VCSEL Resonators

The surface emission of the hybrid device is investigated in a micro-photoluminescence setup (Section 3.3.1) with an additional polarisation filter for the emitted light. The device is excited optically with a tightly focused spot (diameter  $2 \mu\text{m}$ ) at 405 nm for below-threshold and 532 nm for below- and above-threshold investigation. For this purpose, emission and excitation are located on the same side of the sample (reflection geometry), where a beam splitter enables



incoupling of the excitation light and outcoupling of the emission through the same high-NA objective (63 $\times$ , NA=0.8), as the opaque Si substrate allows no transmission at these wavelengths.

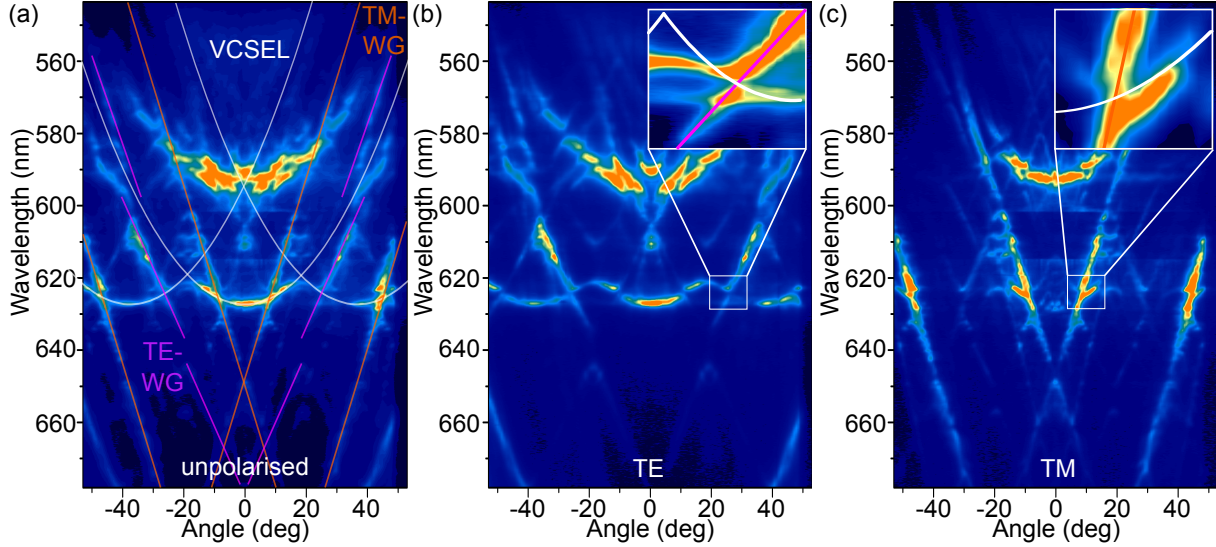


**Figure 7.2:** Angle-resolved spontaneous surface emission from hybrid cavities. (a) Unpolarised emission. Lines represent guides for the eye for parabolic VCSEL and linear WG modes. From the Bragg-scattering separation, a period of  $\approx 1.0\mu\text{m}$  is extracted. (b) TE and (c) TM polarised emission. While in TE polarisation, the VCSEL mode and Bragg-scattered replica are still visible, in TM polarisation, the linear WG modes dominate the far field picture. In all figures, a pronounced anticrossing is facilitated by a strong coherent interaction between VCSEL and WG modes. Reprinted with permission from reference [10].

While VCSEL modes exhibit parabolic dispersion, and waveguided modes show an almost linear dispersion of their surface emission, the behaviour of the hybrid device is much more complex. Figure 7.2 shows angle-resolved emission spectra below the lasing threshold in different polarisations. In both TE and TM, modes of linear dispersion represent the corresponding waveguide modes with large slopes of  $2.4\text{ nm}/1^\circ$  (TM) and  $1.85\text{ nm}/1^\circ$  (TE) cutting through the far field. While in TE polarisation, the apex of the cavity parabola is visible at  $628\text{ nm}$  and  $0^\circ$  (and Bragg-scattered to  $\pm 40^\circ$ ), in TM polarisation the VCSEL mode is dominated by the WG. The DBR sideband emission with an apex at  $595\text{ nm}$  however is still recognizable in all three figures, albeit strongly disturbed by the waveguided modes.

At crossing points of WG and VCSEL dispersion, the emission reveals a coherent interaction between both modes, as modes overlap and exhibit a pronounced anticrossing. Interestingly, this effect facilitates points of drastically increased density of states combined with the added optical feedback from both resonators leading to increased emission intensity. Note that all features are Bragg-scattered at angles:  $\vartheta = \pm \arcsin(k_{\text{Bragg}}/k_z) = \pm \arcsin(\lambda_C/a) \approx 35^\circ$  and

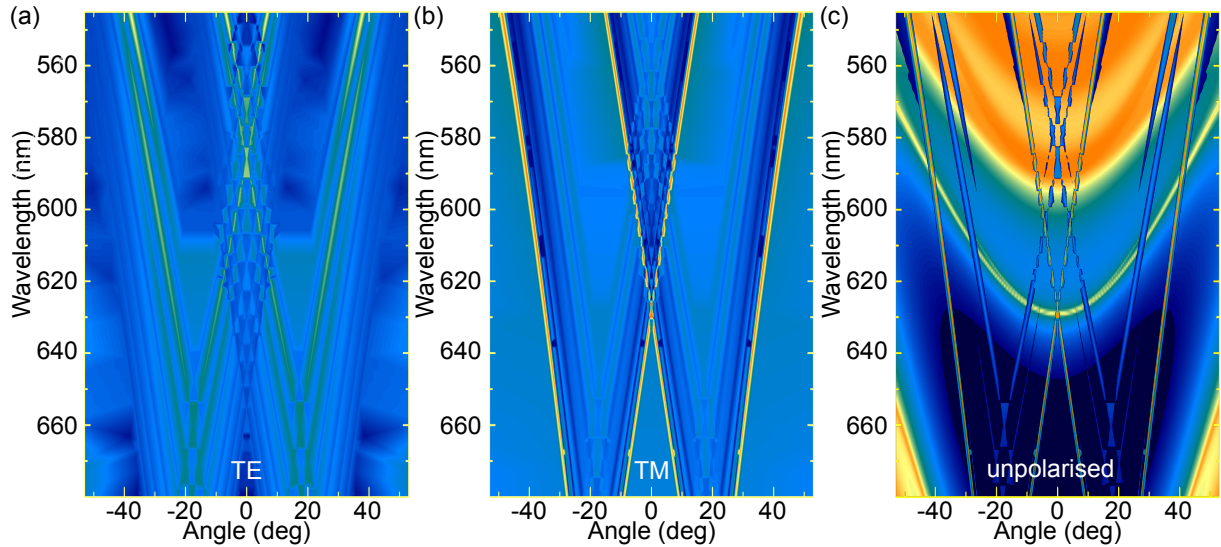


**Figure 7.3:** Calculation of scattered waveguided modes for the hybrid device. Color scale in (a) and (b) depicts the fraction of a mode residing in the active layer. (a) In TE-polarisation, only weak modes with linear dispersion populate the far field. (b) In TM-polarisation, strong and sharp WG resonances are scattered into the surface emission, coinciding with experimental observation. (c) Extracted TE and TM polarized modes and transfer-matrix calculation of VCSEL transmission. The calculated far field provides a clear explanation for all modes observed in the experiment. WG mode calculations have been performed by Tim Wagner (IAPP). Reprinted with permission from reference [10].

thus appear twice in the angular range observed. From the experiment, we obtain a scattering at  $\pm 38^\circ$  which coincides well with the calculation bearing in mind uncertainties in angle and period. Subsequently, WG modes interact with Bragg-scattered VCSEL modes and vice versa as well, and in addition anticrossing is observed between different VCSEL modes (and WG modes) themselves, facilitating a highly complex emission spectrum in the far field regime. In contrast to the manipulation of the optical potential by inserting interlayers into the cavity, the photon energy landscape is not changed here as the cavity thickness remains constant at all points. All observed effects thus stem from the coherent interaction of different resonator types.

To unambiguously identify the modes appearing in the system, we numerically calculate waveguided modes appearing in the stack. These modes are quantified by the amount of their confinement in the active layer, i.e. modes that interact with the cavity layer show emission, modes that predominantly appear in the mirror layers show none. The calculated modes are then scattered at the Bragg grating to produce a far field image of the surface emission from the WG. These calculations are depicted in Figure 7.3, showing a clear coincidence with the experimentally obtained spectra. In TE-polarisation (Fig. 7.3 (a)), only weak modes appear in the surface emission, leading to a weak modulation of the far field in the experiment. In TM-polarisation

(Fig. 7.3 (b)) however, the scattered WG modes show a significant distribution in the active layer, which can be translated to a significant contribution towards the MC emission as previously observed in the experiment (Fig. 7.2 (c)). Here, the far field image is dominated by the scattered WG modes. Fig. 7.3 (c) finally depicts a transfer-matrix calculation of the VCSEL transmission with simulation parameters corresponding to the WG calculations, producing the main resonance at 630 nm, the mirror sideband at 590 nm, and the second cavity mode in the  $3/2\lambda$  cavity, visible at large angles above 660 nm. In addition, strong WG modes above a certain threshold<sup>1</sup> are overlaid in the picture. While the VCSEL calculation provides the expected cavity mode position, it has to be noted that the WG resonances appear slightly blue-shifted when compared to the experiment. Such variations can be explained by the incomplete knowledge about the exact layer thicknesses of each mirror and cavity layer, where even small deviations have a significant effect on the calculated WG modes. For the best fit, we obtain a thickness of 105 nm for the SiO<sub>2</sub>, 86 nm for the TiO<sub>2</sub> and 511 nm for the Alq<sub>3</sub>:DCM layer. Despite those deviations, a convincing allocation of all modes observed in the system can be made.

### 7.3 Stimulated Emission of Hybrid Resonators

Increasing the excitation pulse energy, the system enters the stimulated emission regime at thresholds on the order of 1 nJ/pulse. In contrast to planar microcavities, where lasing typically originates at the single point of the parabola apex in the far field emission, the hybrid device offers a multitude of laser modes. The unpolarised picture in Figure 7.4 (a) already offers two distinct lasing wavelengths at 624 nm and 628 nm, as well as a Bragg-scattered replica at 628 nm and  $\pm 40^\circ$ . At first glance, this mode corresponds with the expected VCSEL mode of an undisturbed system and differs only in those large angle replica. Similar to the observation of the Kastler ring [236], laser light can efficiently scatter into higher angle modes, even if lasing originally only takes place in normal direction. Here, the periodic corrugation provides an additional outcoupling angle for the standard microcavity lasing.

The mode at 624 nm however can only be attributed to the hybrid system. The polarisation-resolved far field in Fig. 7.4 (b) and (c) makes this observation more clear. As in the below-threshold spectra, the TE polarisation shows the original cavity mode and corresponding lasing from it. Interestingly, the presence of the WG mode at  $\approx 25^\circ$  enables another point of scattering for the stimulated emission, not clearly resolved in the unpolarised image. The enlarged inset of 7.4 (b) shows a clear distinction between the scattered VCSEL and WG modes as the crossing WG mode unsurprisingly provides another possibility of outcoupling. Here, no lasing mode is observed at 624 nm. In TM-polarisation (Fig. 7.4 (c)), lasing of hybrid modes appears alongside

<sup>1</sup>i.e. modes that reside at least 20% inside the active layer

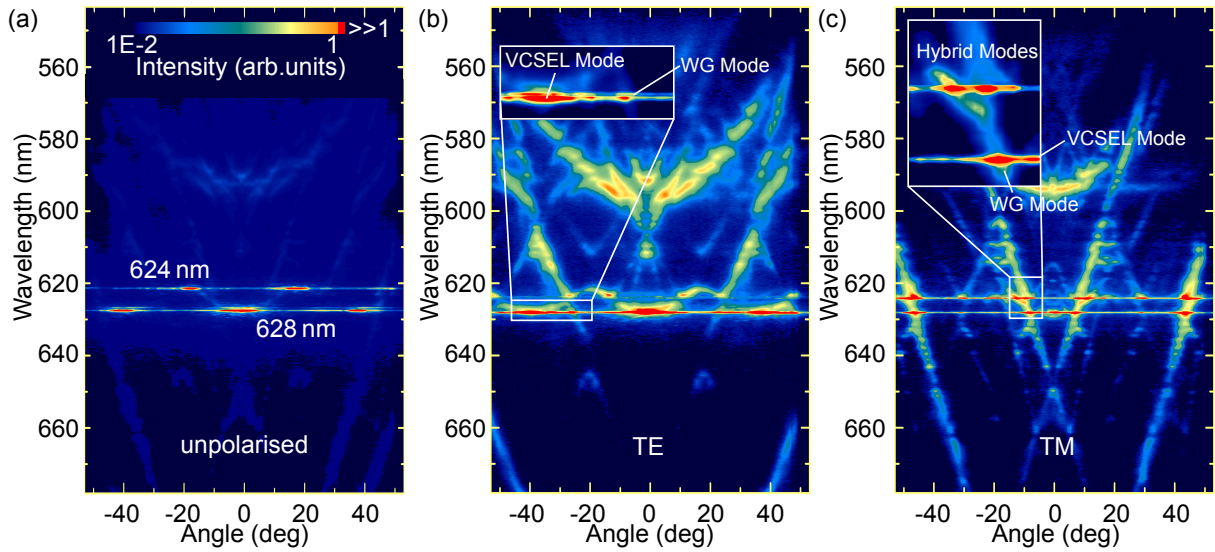


**Figure 7.4:** Angle-resolved stimulated surface emission from hybrid cavities. (a) Unpolarised emission. Laser modes are observed at 628 nm (predominantly VCSEL) at  $0^\circ$  and Bragg-scattered replica at  $\pm 40^\circ$  and at 624 nm (hybrid mode). (b) TE polarised emission with the bare VCSEL mode as the only lasing mode. (c) TM polarised emission, where lasing originates from both VCSEL and hybrid modes at crossing points between the dispersions of both resonator structures. Here, both modes at 624 nm and 628 nm lase. Reprinted with permission from reference [10].

the cavity lasing. While again the cavity mode lases and scatters into TM-WG modes, the Bragg-scattering of the bare VCSEL mode is much less pronounced than in the TE case and in fact not visible in this resolution. At 624 nm, the hybrid modes start lasing at comparable thresholds and similar peak intensity where the coupling of both resonators remains stable above threshold and facilitates a splitting of  $3^\circ$ . The laser mode forms at the position of high DOS at crossing points of the dispersion curves and scatters into different bare WG and Bragg-scattered hybrid modes at larger angles. These observations prove a clear coherent coupling of two fundamentally different propagations of light. Apart from providing an avenue of combining different directions of laser outcoupling this behaviour may facilitate additional optical feedback if a DFB laser is realised in the device. One could imagine spatially separated dedicated coupling regions in a hybrid device connected by a fully confining waveguide, enabling the transport of coherent emission from one VCSEL to another similar to optical in- and outcoupling gratings in optical waveguides [251] or surface plasmon-based devices [252].

The spatial extension of coherent emission furthermore emphasizes the different behaviour of bare VCSEL and hybrid modes. Figure 7.5 (a)-(c) show the near field spectra of stimulated emission in different polarisations showcasing a strong localisation of the VCSEL mode emission in the TE polarised case. While a strong Bragg-scattering is apparent by the far field spectrum as well as directly visible in the corresponding near field micrograph (Fig. 7.5 (e)), the mode

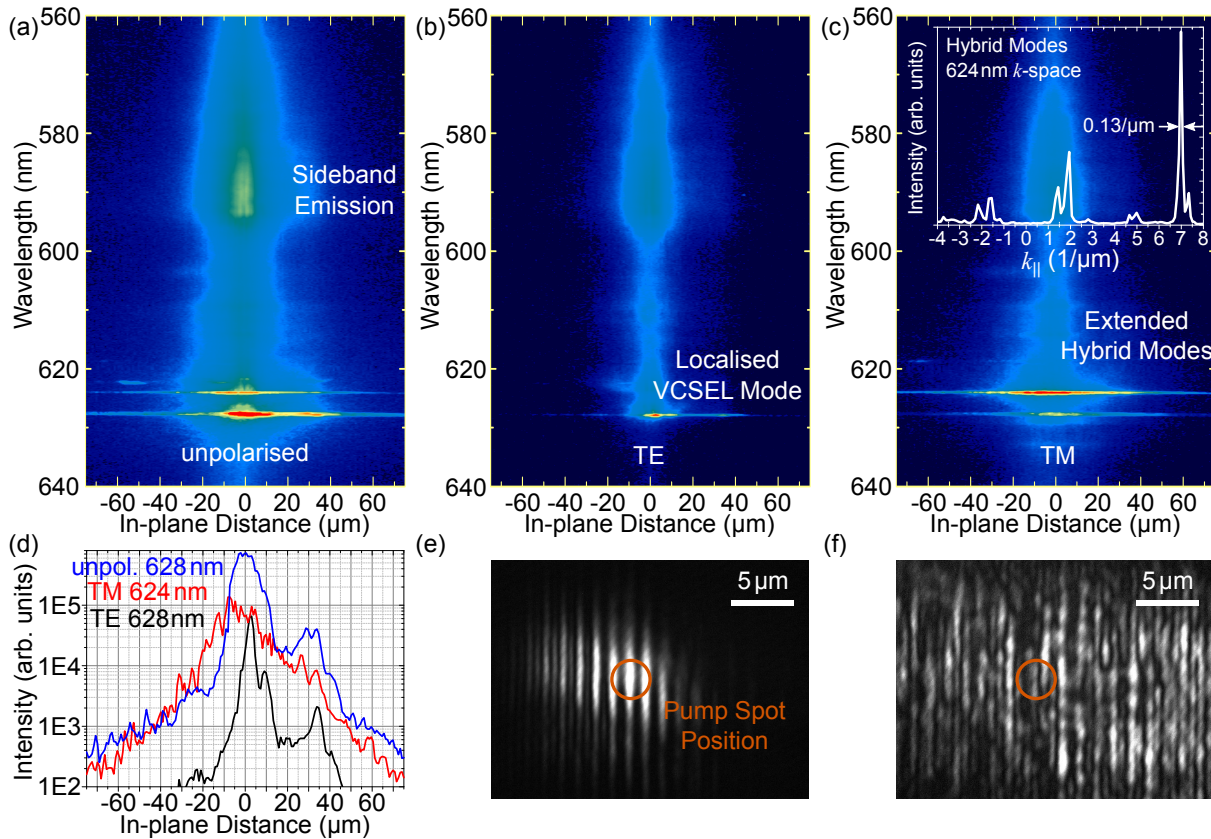


**Figure 7.5:** Spatially-resolved stimulated vertical emission from hybrid cavities. (a) Unpolarised, (b) TE polarised, and (c) TM polarised emission. (d) Extracted spatial intensity profiles of the laser modes. While the pure VCSEL mode in TM polarisation decays quickly and is barely visible 15  $\mu\text{m}$  away from the pump spot, the hybrid modes in TM polarisation show a much broader extension in space and are still visible at distances  $> 60 \mu\text{m}$ . (e) and (f) near field micrographs of TE and TM polarised emission, respectively. While the bare VCSEL mode in TE polarisation covers  $\approx 10 \mu\text{m}$  around the pump spot, the hybrid mode in TM polarisation exhibits larger spatial extension. Inset in (c) shows the momentum-resolved hybrid laser mode profile. Sharp resonances in  $k$ -space confirm the large coherent spatial extension in real space. Reprinted with permission from reference [10].

extension of  $\approx 10 \mu\text{m}$  is that of a standard microcavity mode [197, 253]. Here, the lasing mode forms in the vertical cavity around the position of the focused pump spot. For the hybrid modes however, the situation changes. While the peak intensity is still observed at the position of the pump spot (centre of Fig. 7.5 (c)), the spatial intensity decline is much more shallow than for the bare cavity lasing. Figure 7.5 (d) shows extracted intensity profiles from the different lasing modes, showing a broad mode extension of  $> 20 \mu\text{m}$  and a shallow decline after that (red line). In contrast, the VCSEL mode (black line) exhibits a sharp peak around  $0 \mu\text{m}$  and drops off almost completely in the first  $\pm 20 \mu\text{m}$ . The near field micrograph of the hybrid mode lasing (Fig. 7.5 (f)) coincides with this observation, as virtually no intensity drop-off can be seen in the spatial region

shown. To compare this behaviour with the angle-resolved spectra, the stimulated emission profile of the 624 nm hybrid mode is extracted from Fig. 7.4 (c) and plotted as an inset in 7.5 (c). In  $k$ -space, sharp laser resonances arise from the different contributing modes, confirming the large spatial extension in the real space emission. The combination of both resonators facilitates very large mode volumes of the hybrid modes, increasing the coherent area by almost an order of magnitude, opening the possibilities for interesting applications regarding the spatial transfer of coherence.

# 8 Cavity-Enhanced Charge-Transfer State Absorption for Highly Efficient NIR Detectors

*In this chapter, the optical features of organic microcavities are employed for a different purpose. Instead of aiding as a resonator for the stimulated emission in microlasers, the field enhancement inside of such devices is exploited for cavity enhanced spectrally narrow photodetectors. For this purpose, the intermolecular charge-transfer state in mixed layers of organic acceptor/donor blends is utilised and efficient photodetection in the near-infrared is realised.*

*In Section 8.1 the general concept is introduced based on simulations of the optical field distribution in such devices. By using two highly reflective silver contacts and comparably thick transport layers, a field enhancement at  $>900$  nm is realised here. Additionally, a passive filter is integrated, showing reduced optical field of undesired wavelengths inside the detector.*

*In Section 8.2, cavity-enhanced detectors are fabricated and evaluated regarding their external quantum efficiency (EQE) and current-voltage (IV) behaviour and compared to reference devices optimised for solar cell performance. Furthermore, the thickness of the top contact is varied and compared to optical simulations, showing a narrowing of the resonance for an increased reflectivity of the top mirror.*

*The concept of an optical microcavity opens possibilities of spectral tunability for the narrowband photodetection. In Section 8.3, the angular response is evaluated, showing the typical parabolic cavity dispersion, opening an avenue for spectral tunability over 100 nm on a single device. Varying the thickness of the transport layers, the resonance wavelength can be manipulated further.*

*The results in this chapter have been achieved as the result of a cooperation with different researchers. All EQE and IV measurements shown here have been performed by Bernhard Siegmund. Angle-resolved optical measurements have been done in cooperation with Mathias Böhm. Additional input towards the results in this chapter has been given by Johannes Benduhn, Donato Spoltore, Christian Körner, and Koen Vandewal (all IAPP, TU Dresden).*

## 8.1 Design and Optical Simulation of Optimised Metallic Microcavities

### 8.1.1 Concept of Cavity-Enhanced Charge-Transfer State Absorption

Today, organic solar cells are widely researched regarding material classes, fabrication techniques, and optical and electrical design, etc. In small molecule solar cells, the material combination of Buckminster fullerene ( $C_{60}$ ) and zinc-phthalocyanine (ZnPc) is well established as a lab standard for the active layer with well known properties and behaviour, despite limitations in high-end performance. Both materials show desirable properties for efficient splitting of excitons. By thermal co-evaporation, a favourable intermixing can be achieved [254] and power conversion efficiencies of  $\geq 4\%$  are possible in optimised designs [255, 256], absorbing well in the visible range of light (VIS). Here, this blend layer is utilised for the fabrication of organic photodetectors in the near-infrared (NIR), a spectrum typically not covered by the absorption of either molecule. In the mixed layer however, an intermolecular charge-transfer (CT) state forms at interfaces between  $C_{60}$  and ZnPc as an exciton can be created between a hole on the HOMO of ZnPc left by the excitation of an electron to the LUMO of  $C_{60}$  [115]. Typically, this state is populated in the process of charge carrier separation, as excitons created in the bare films diffuse to the interface and intermediately form the CT state in a non-radiative process before becoming fully separated with the electron being donated to  $C_{60}$ , the hole remaining on ZnPc [257]. In this process, the CT state can act as a pathway for direct optical transitions to the ground state, leading to a loss of the excitation and an emission of a low-energy photon and is typically undesired for solar cell operation [114, 115, 258]. The reverse process, absorbing low energy photons to directly create a CT exciton must then be possible as well, however showing low absorption coefficients on the order of  $10^4 \text{ cm}^{-1} \dots 10^3 \text{ cm}^{-1}$  [115, 116] and is thus not commonly considered. Compared to the neat materials, the CT absorption shoulder extends into the NIR for the ZnPc: $C_{60}$  blend (see Section 2.3.2 and [13]) and opens the possibility for photodetection in this spectral range, if the absorption can be enhanced.

By introducing the active blend into an optical microcavity, strong field enhancement can be achieved at the position of the active layer, leading to significant contributions of the CT absorption in the overall external quantum efficiency (EQE) of an organic solar cell. Cavity-enhanced detectors utilise such enhancement to facilitate large, spectrally selective quantum efficiency in very thin active layers. The resulting organic microcavity can be very lightweight, flexible and integrated on small as well as very large scale.



### 8.1.2 Device Design and Optical Simulation

Here, a standard small molecule solar cell represents the basis of the investigations for NIR photodetectors. The full stack is deposited via thermal evaporation under ultra-high vacuum and comprises two metallic contacts, the hole transport material N,N'-((Diphenyl-N,N'-bis)9,9,-dimethyl-fluoren-2-yl)-benzidine (BF-DPB) doped with either 2,2'-(perfluoronaphthalene-2,6-diylidene)dimalononitrile (F<sub>6</sub>TCNNQ, 10 wt%) or the proprietary dopand NDP9 (Novaled AG, 10 wt%), the active bulk heterojunction ZnPc:C<sub>60</sub> sandwiched by thin layers of either material as a neat film, and the electron transport material N,N-Bis(flouren-2-yl)-naphthalenetetracarboxylic diimide (Bis-HFI-NTCDI) doped with ditungsten-tetra(hpp) (W<sub>2</sub>(hpp)<sub>4</sub>, 7 wt%). Due to the volatility and limited availability of the n-dopand W<sub>2</sub>(hpp)<sub>4</sub>, other electron transport material combinations are used in addition, namely C<sub>60</sub>:W<sub>2</sub>(hpp)<sub>4</sub> (lower concentration, 3 wt%) and 4,7-diphenyl-1,10-phenanthroline (BPhen), doped with Cs atoms. While often conductive oxides (such as indium tin oxide) are utilised as transparent contacts, thin metal films can act as transparent contacts for efficient cells as well [185, 259, 260].

For the photodetecting device however, two reflective silver films are employed to create an optical microcavity inside the cell, enhancing the optical field of the resonant wavelength between them. For this purpose, a thick 100 nm silver layer is used as a bottom electrode and back mirror, exhibiting reflectivities >99% in the NIR. The top contact comprises another silver electrode of thicknesses between 9 nm...54 nm, acting as a semitransparent mirror on the side that will be illuminated. To enhance the optical and electrical quality of this top silver layer, a seed layer of 1 nm of gold and a diffusion barrier layer of 3 nm of MoO<sub>3</sub> is used for all top contacts.

While very thin silver layers (such as 9 nm) facilitate sufficient electrical contact, their reflectivity is low (< 50% in the NIR) and they are typically not suitable as cavity mirrors. These devices serve a comparison by varying the transport layer thicknesses from optimised solar cell to detector behaviour. A reference cell of these materials with the same stack design but optimised layer thicknesses reaches power conversion efficiencies of ≈ 2%. Surrounding the active layer of constant thickness (50 nm ZnPc:C<sub>60</sub>, volume ratio 1:1) are 5 nm of either neat material. The transport layers act not only as charge transporters, but are utilised for the optical alignment of the microcavity, meaning a variation in transport layer thickness to facilitate a spectral shift of the cavity resonance. For this purpose, both layers exhibit rather large thicknesses, typically above 60 nm, and are adjusted separately with the aim of keeping the optical field maximum of the desired wavelength centred in the BHJ. Figure 8.1 shows the sample design and electrical field distribution of the resonant wavelength in the device. Clearly, between both metal electrodes a standing wave forms and exhibits its maximum enhancement at the position of the active blend layer. As discussed in Section 2.2.4, the use of conductive mirrors facilitates a finite field strength at the metal-organic interface, as phase shifts occur here. The use of a thick, highly

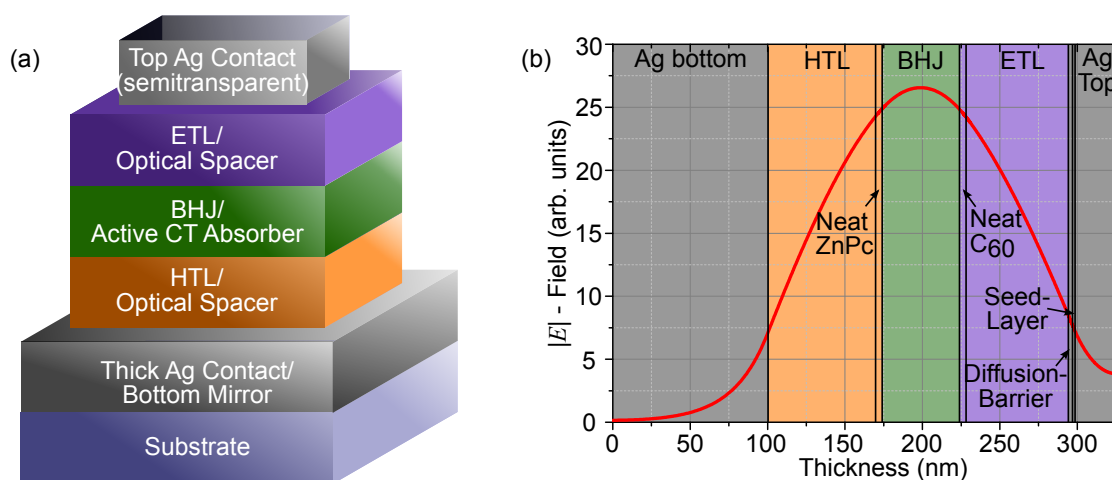


**Figure 8.1:** (a) Schematic of sample design comparable to an organic solar cell. Transport layers double as optical spacers to position the resonance in the centre of the active BHJ. (b) Optical field distribution of resonant light in the cavity-enhanced device.

reflective and a thinner, semitransparent mirror furthermore leads to an asymmetric field distribution in the device. For a well-designed device, both transport layers have therefore to be varied independently, also taking into account their respective refractive indices. Resulting in this optimisation is an uneven layer thickness distribution under simulation of all included layers. Figure 8.2 (a) shows the full optical field distribution in the VIS and NIR in an optimised device, where the resonance wavelength is centred at 900 nm. A comparably thick top contact of 30 nm Ag is chosen, resulting in a decreased field strength in the VIS, decreasing the conventional power conversion device of the device if used as a solar cell. However, a strong field enhancement can be observed at the cavity resonance facilitating a spectrally localised enhancement of electrical field at the position of the active layer. While such field enhancement and the formation of an optical cavity is not possible for a highly absorbing device and a cavity resonance will not form at the absorption maxima of either organic material, the positioning of the resonance in the region of the weakly absorbing CT state enables such optical enhancement. Consequently, the absorption of this state is strongly enhanced by the increased field strength and a direct excitation of CT excitons is made possible with high efficiency. The low initial absorption of the CT state furthermore facilitates a small spectral width (full width at half maximum, FWHM) of the resonance, which opens interesting applications such as spectroscopy in the NIR. In addition to the resonance at 900 nm, the second order resonance is visible at  $\approx 450$  nm exhibiting a field node in the centre of the active layer, but still showing strong field enhancement with two antinodes in the organic layers.

For small-band photodetectors, it is often desired to allow an unambiguous assignment of photocurrent to a small wavelength interval. For this purpose, signals from other spectral ranges,

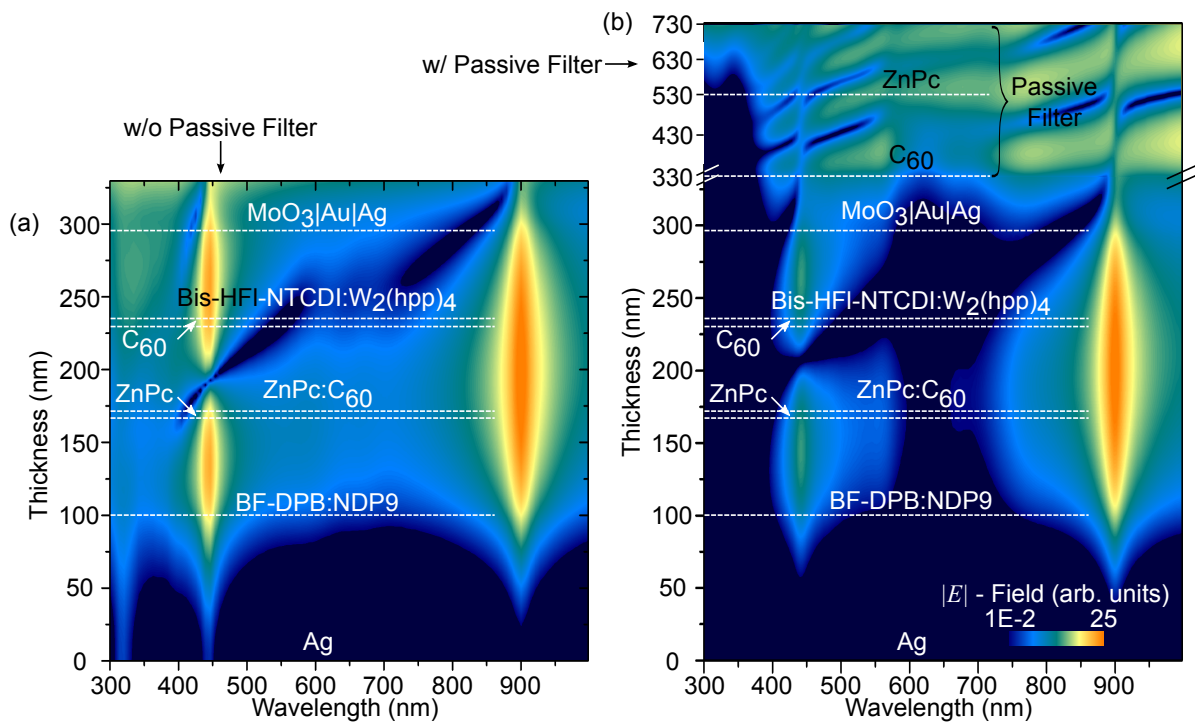


**Figure 8.2:** (a) Simulated optical field of a cavity enhanced device comprising 100 nm Ag | 71 nm BF-DPB:NDP9 | 5 nm ZnPc | 50 nm ZnPc:C<sub>60</sub> | 5 nm C<sub>60</sub> | 63 nm Bis-HFI-NTCDI:W<sub>2</sub>(hpp)<sub>4</sub> | 3 nm MoO<sub>3</sub> | 1 nm Au | 30 nm Ag. The silver electrodes double as microcavity mirrors and facilitate a strong field enhancement at 900 nm in the active BHJ region. A second order cavity state can be observed at 450 nm as well. (b) Simulated optical field of the same device with an additional 200 nm C<sub>60</sub> | 200 nm ZnPc passive absorber layer on top. The passive absorber strongly reduces the internal electrical field at lower wavelengths, leading to a suppressed signal in the region 300 nm...850 nm. The optical constants of the ETL used here are those of the undoped layer. The optical field is depicted as false colours on logarithmic scale in both figures.

especially in the VIS, should be suppressed. Fabricating such a visible-blind device with organic small molecules is typically inhibited by their broad absorption bands. The materials used here also show efficient absorption and charge carrier generation under illumination in the VIS, hence their use as solar cell absorbers, and while the thick metal top contact facilitates a suppression of visible photons entering the device, still a significant signal can be expected. Solving this challenge requires the use of spectral lowpass filters, absorbing all high energy photons above their respective bandgap and transmitting only photons of lower wavelength. While rigid filters are commonly used in spectroscopy and readily available, it is possible to directly integrate a flexible passive absorption filter of organic materials in the device. For this purpose, 200 nm of both ZnPc and C<sub>60</sub> (or any other broadband VIS absorber molecule) are deposited on top of the cavity-enhanced device as a flat heterojunction. The positioning of the filter outside of the

device makes those layers electrically inert while they provide a sufficient absorption of high-energy photons. The flat junction furthermore allows for only minimal CT state absorption in this passive layers. Figure 8.2 (b) subsequently shows a strongly decreased field strength at the position of the active BHJ in the VIS range, suppressing both intermediate wavelengths and second order cavity. Designs with and without passive filters are employed in organic microcavities with various optimisations towards their spectral and electrical behaviour.

## 8.2 Enhancing the Absorption of the C<sub>60</sub>:ZnPc Charge-Transfer State

### 8.2.1 External Quantum Efficiency of CT-NIR Detectors

The external quantum efficiency (EQE) of organic solar cells is an important measure combining the ability to absorb incident photons and generate, split, and transport charge carriers to the respective electrodes. In photodetectors, the EQE as well as the noise current of the device determine the performance in terms of specific detectivity, which depends on the wavelength of incident light. In contrast to solar cells, a broad absorption and thus broad EQE is not required for detectors and narrowband EQE spectra can be desired for spectroscopic applications or multiplexing. Here, EQE of cavity-enhanced devices is tailored to exhibit narrow resonances at wavelengths in the NIR, while inhibiting contributions from other wavelengths. Figure 8.3 (a) shows a device comprising 100 nm Ag | 79 nm BF-DPB:NDP9 | 5 nm ZnPc | 50 nm ZnPc:C<sub>60</sub> | 5 nm C<sub>60</sub> | 81 nm Bis-HFI-NTCDI:W<sub>2</sub>(hpp)<sub>4</sub> | 3 nm MoO<sub>3</sub> | 1 nm Au | 18 nm Ag, exhibiting a sharp EQE peak at 950 nm. Here, the cavity-enhancement of the optical field at this wavelength leads to an immense increase in signal from the CT absorption region, reaching a peak EQE of 18% for a charge-transfer state in this sample, far away from the optical gap of either neat material. While CT state absorption and resulting EQE has been reported multiple times before [115], at this wavelength it resides below 1% for the blend of ZnPc:C<sub>60</sub>[13]. Similarly, our reference cell<sup>1</sup> without cavity enhancement shows comparable values of ≈1% at 950 nm. The reference features a transparent ultra-thin metal top contact and its transport layer thicknesses are optimised for solar cell operation, as depicted in the inset of Fig. 8.3, reaching a PCE of 2%. Comparing EQE of both cavity-enhanced devices and reference (Fig. 8.3 (b)), an overall drastic decrease of EQE (and thus performance as a solar cell) is observed as thick mirrors and transport layers are not suited for the broadband conversion of light. However, at the resonance wavelength, the cavity-enhanced detectors show a superior signal, more than one order of mag-

<sup>1</sup>100 nm Ag | 31 nm BF-DPB:NDP9 | 5 nm ZnPc | 50 nm ZnPc:C<sub>60</sub> | 5 nm C<sub>60</sub> | 36 nm Bis-HFI-NTCDI:W<sub>2</sub>(hpp)<sub>4</sub> | 3 nm MoO<sub>3</sub> | 1 nm Au | 9 nm Ag

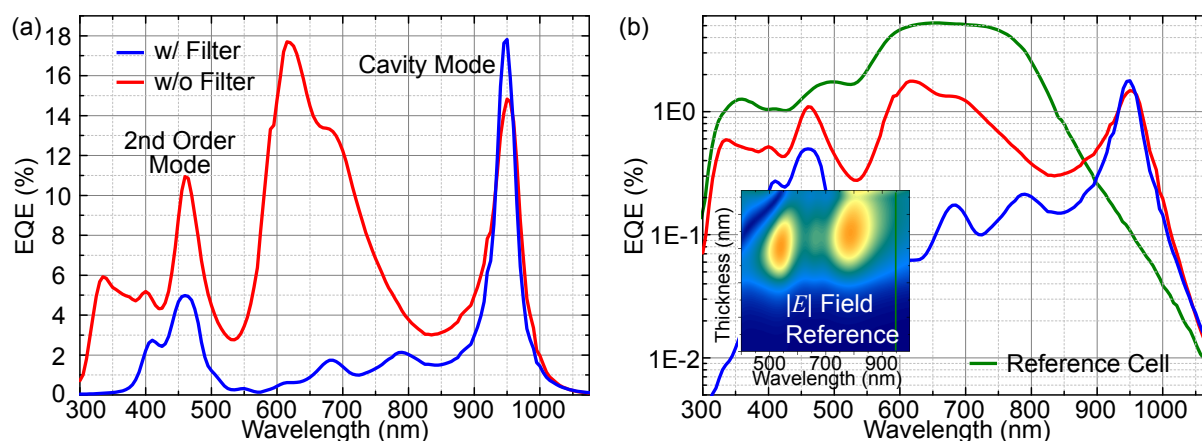


**Figure 8.3:** (a) External quantum efficiency (EQE) of a cavity-enhanced device (layer composition in text) with (blue) and without (red) passive filter. The EQE shows a strong signal for enhanced CT state absorption at 950 nm. The passive filter is able to suppress the signal in the VIS, while not harming the desired detector signal. (b) EQE on logarithmic scale compared with a reference device (green). The reference EQE shows a strong drop off above 850 nm and no significant contribution at 950 nm. Inset shows the optical field distribution of the reference device. EQE measurements performed by Bernhard Siegmund.

nitude above the reference. Here, it becomes clear that the optical field enhancement works as desired and is able to boost the CT state absorption into a region suitable for application.

The inclusion of the passive filter layers of 200 nm ZnPc, and 200 nm of P4-Ph4-DIP<sup>2</sup> (instead of C<sub>60</sub>) on top show furthermore the desired strong suppression of any signal from the VIS. While the unfiltered sample shows EQE contributions up to 18% at 620 nm (absorption maximum of ZnPc) even though the top mirror already decreases the illumination of organic layers outside of cavity resonances, the passive filter manages to keep the EQE below 2% for all off-resonance wavelengths. The remaining main peaks are the desired cavity resonance at 950 nm and the second order mode at 475 nm which was already predicted in the optical simulation. Here, a dedicated absorber in the blue can aid to further suppress this signal. For 18 nm of silver as the top mirror, the CT-state resonance exhibits a full width at half maximum (FWHM) of 30 nm, coinciding well with simulation, while mirrors with higher reflectivities can facilitate even narrower resonances. Remarkably, all values are reached without any bias voltage and thus reliable photodetection is made possible without an external power source.

The diode behaviour of the devices can be seen in the current-voltage (IV) behaviour, plotted in Figure 8.4. Here, a device with a cavity resonance centered at 910 nm<sup>3</sup> is illuminated either by a sun simulator (Xe arc lamp, 100 mW/cm<sup>2</sup>) or a narrowband light emitting diode (905 nm,

<sup>2</sup>2,3,10,11-tetrapropyl-1,4,9,12-tetraphenyl-diindeno[1,2,3-cd:1',2',3'-lm]perylene

<sup>3</sup>100 nm Ag | 70 nm BF-DPB:NDP9 | 5 nm ZnPc | 50 nm ZnPc:C<sub>60</sub> | 5 nm C<sub>60</sub> | 71 nm Bis-HFI-NTCDI:W<sub>2</sub>(hpp)<sub>4</sub> | 3 nm MoO<sub>3</sub> | 1 nm Au | 18 nm Ag,

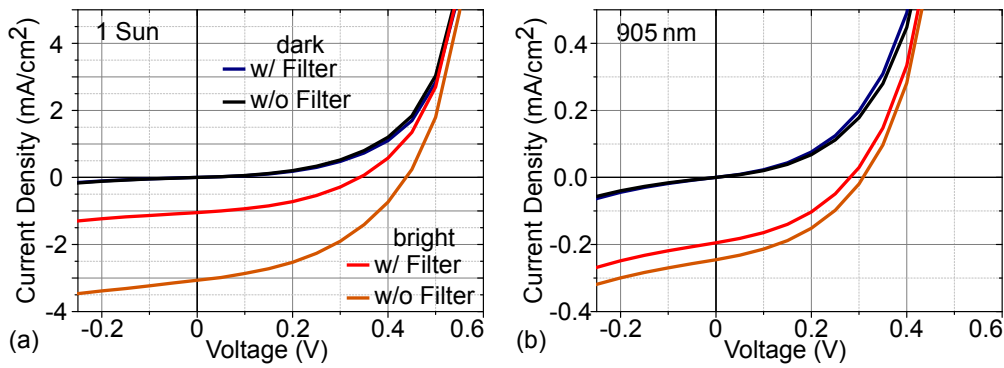


**Figure 8.4:** (a) Current-voltage characteristics of a cavity enhanced device optimised for 910 nm (layer composition see <sup>3</sup>) at illumination of (a) a sun simulator at 1 sun ( $100 \text{ mW/cm}^2$ ) (b) a narrowband light emitting diode at 905 nm and  $3.6 \text{ mW/cm}^2$ . IV measurements performed by Bernhard Siegmund.

FWHM $\approx 50 \text{ nm}$ ,  $P \approx 3.6 \text{ mW/cm}^2$ ). In both cases, diode-like IV curves can be observed without illumination (dark), shifting to negative current densities when exposed by light (bright). While the unfiltered sample absorbs the broadband spectrum fully and reach short circuit current densities of  $j_{\text{SC}} = -3 \text{ mA/cm}^2$  under 1 sun, the sample with passive filter is spectrally selective to CT absorption at the resonance and thus exhibits a current density of  $j_{\text{SC}} = -1 \text{ mA/cm}^2$ , reaching an on-off ratio of  $\sim 10^4$  here. Under illumination of the narrowband LED, both devices show similar short circuit currents, showing that the passive filter has no significant detrimental impact on the detection at the resonance wavelength. Compared to illumination under 1 sun ( $\approx 18 \text{ mW/cm}^2$  between 880 nm and 930 nm,  $j_{\text{SC}} = -1 \text{ mA/cm}^2$ ), the filtered device shows a similar response under LED illumination ( $3.6 \text{ mW/cm}^2$ ,  $j_{\text{SC}} = -0.2 \text{ mA/cm}^2$ ), again emphasizing the functionality of the monolithically integrated passive filtering.

In subsequent devices, different electron and hole transport layers are tested to test the adaptability of the design. For electron transport materials, C<sub>60</sub>:W<sub>2</sub>(hpp)<sub>4</sub> as well as Bis-HFI-NTCDI:-W<sub>2</sub>(hpp)<sub>4</sub> show comparable diode behaviour. Using BPhen:Cs as the electron transport layer can even improve the saturation of the device. All ETLs show similar performance in the EQE. On the p-side, BF-DPB can also be doped by the non-proprietary F6-TCNNQ, yielding working devices with albeit slightly reduced EQE ( $0.8 \times$  EQE at resonance of devices with NDP9 dopand).

### 8.2.2 Dependence on Top Mirror Thickness

Cavity-enhanced device strongly depend on the quality of mirrors employed and the reflectivities reached by them. Here, a trade-off between high mirror reflectivity and complete optical isolation has to be found to optimise various parameters. While the bottom mirror is not being illuminated

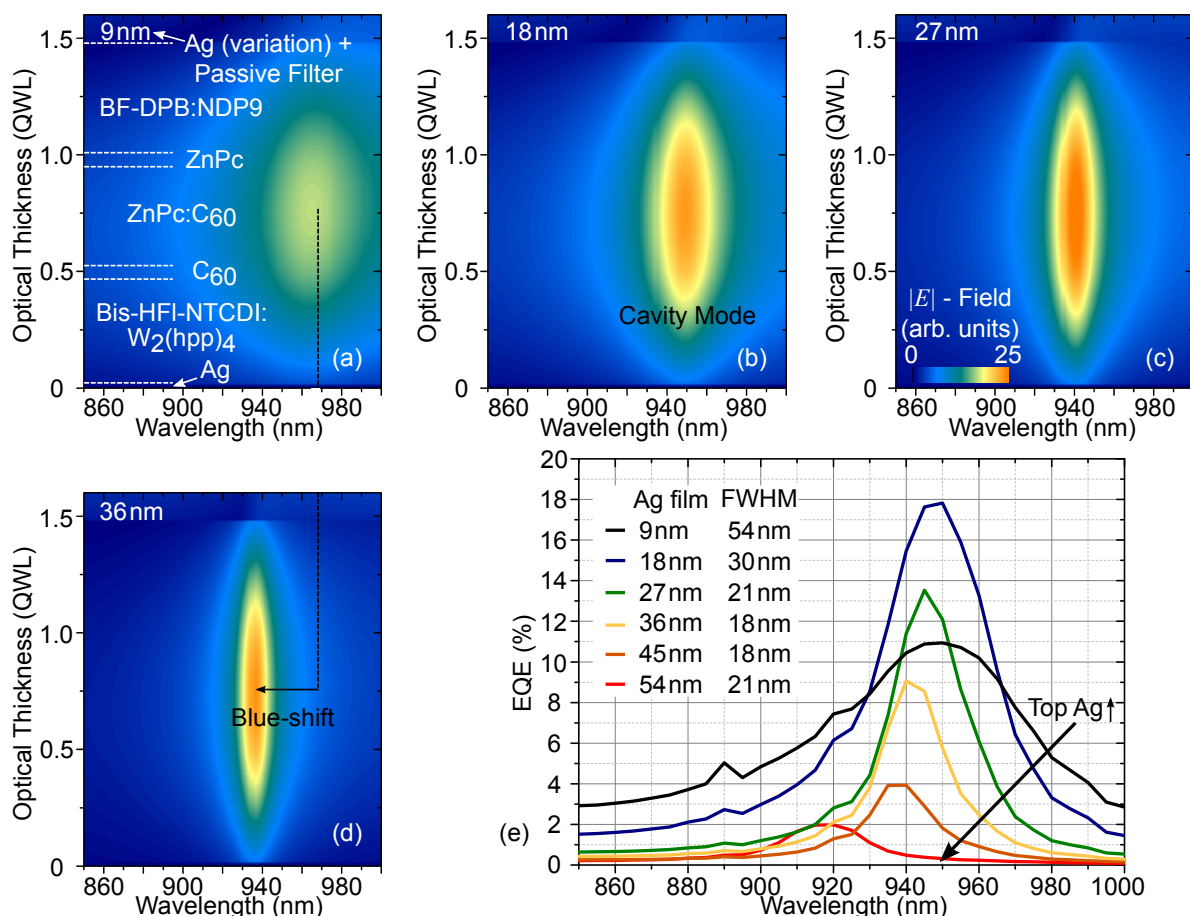


**Figure 8.5:** (a)-(d) Simulated optical field of a cavity enhanced device (composition as in Fig. 8.3) with varying top contact thicknesses. The top contact comprises 3 nm MoO<sub>3</sub> | 1 nm Au and 9 nm (a), 18 nm (b), 27 nm (c), and 36 nm (d) of Ag. Increasing the top mirror thickness leads to an increased  $Q$ -factor and blue shift of the resonance. (e) Measured EQE of devices with varying top contact thicknesses. As expected from simulation, increasing the silver film thickness leads to a narrowing and blue-shift of the resonance. Best performance is achieved between 18 nm and 27 nm. EQE measurements performed by Bernhard Siegmund.

and can be chosen arbitrarily thick, the top mirror still has to exhibit a certain transmittivity in order for photons to enter the resonator. While dielectric resonators greatly benefit from increased reflectivities, the additional absorption of metal layers limit the achievable peak EQE and FWHM.

Figure 8.5 (a)-(d) shows the optical field distributions of a cavity enhanced device for different thicknesses of the top contact. Here, the higher reflectivities of thicker silver films lead to a spectral narrowing of the resonance as well as a blue-shift which can be explained by the phase change of light at the organic - top silver interface (see Section 2.2.4), which varies considerably with the thickness. In the simulation, a maximum field enhancement can be achieved for

27 nm of silver (corresponding to  $\mathcal{R} = 92.5\%$ ), while further narrowing is possible for thicker layers. Comparing the simulation to measured EQE values of corresponding devices, the general trends can be confirmed. Both spectral narrowing and blue-shift are observed in the experimental spectra, while here the maximum EQE is achieved for only 18 nm of silver ( $\mathcal{R} = 83\%$ ). This difference might stem from an additional parasitic absorption caused by the doped electron and hole transport layers. As discussed in [169, 170] and Equation (2.86), higher parasitic absorption of transport layers causes a broadening of the resonance and different optimal conditions for maximum signal. Increasing the parasitic absorption requires a lowering of the top mirror reflectivity, as more light has to enter the device to make up for it, which is exactly what is observed in the experiment. The optical effects of molecular doping are difficult to accurately measure and include in the simulation, explaining the slight discrepancy between experiment and simulation. Increasing the top mirror thickness further, quality factors of  $Q = 53$  can be achieved in the experiment.

## 8.3 Spectral Tunability

One of the major advantages of combining cavity based effects with a broad shoulder of charge-transfer state absorption is the ability to spectrally tune the response by various means. While the variation of the silver film thickness has already shown a blue-shift of the resonance, more controllable options are sought. The use of a microcavity for field enhancement opens the obvious possibilities of tuning via either an increase of the cavity thickness or an exploitation of the angular dispersion. Both methods shall be considered in the following.

### 8.3.1 Angular Response

The interference-based nature of microcavity effects makes them susceptible to variations in the illumination or outcoupling angle, as discussed in Section 2.2.4. Cavity-enhanced detectors show a similar behaviour, as long as the inherent absorption band is broad enough to support the change in wavelength. As CT absorption extends as a broad shoulder next to the absorption bands of the neat materials, such effects have to be taken into account. For extended light sources, a collimation of light can aid in the narrowing of the measured signal, suppressing contributions from larger angles which additionally measure smaller wavelengths in the same setup. However, such a tunability can even be exploited for spectroscopic purposes. Here, we rotate a cavity enhanced device with respect to the plane of incident light and measure corresponding absorption and EQE spectra.

Figure 8.6 shows the angle-resolved absorption ((a) and (b)) and EQE ((c) and (d)) of such a



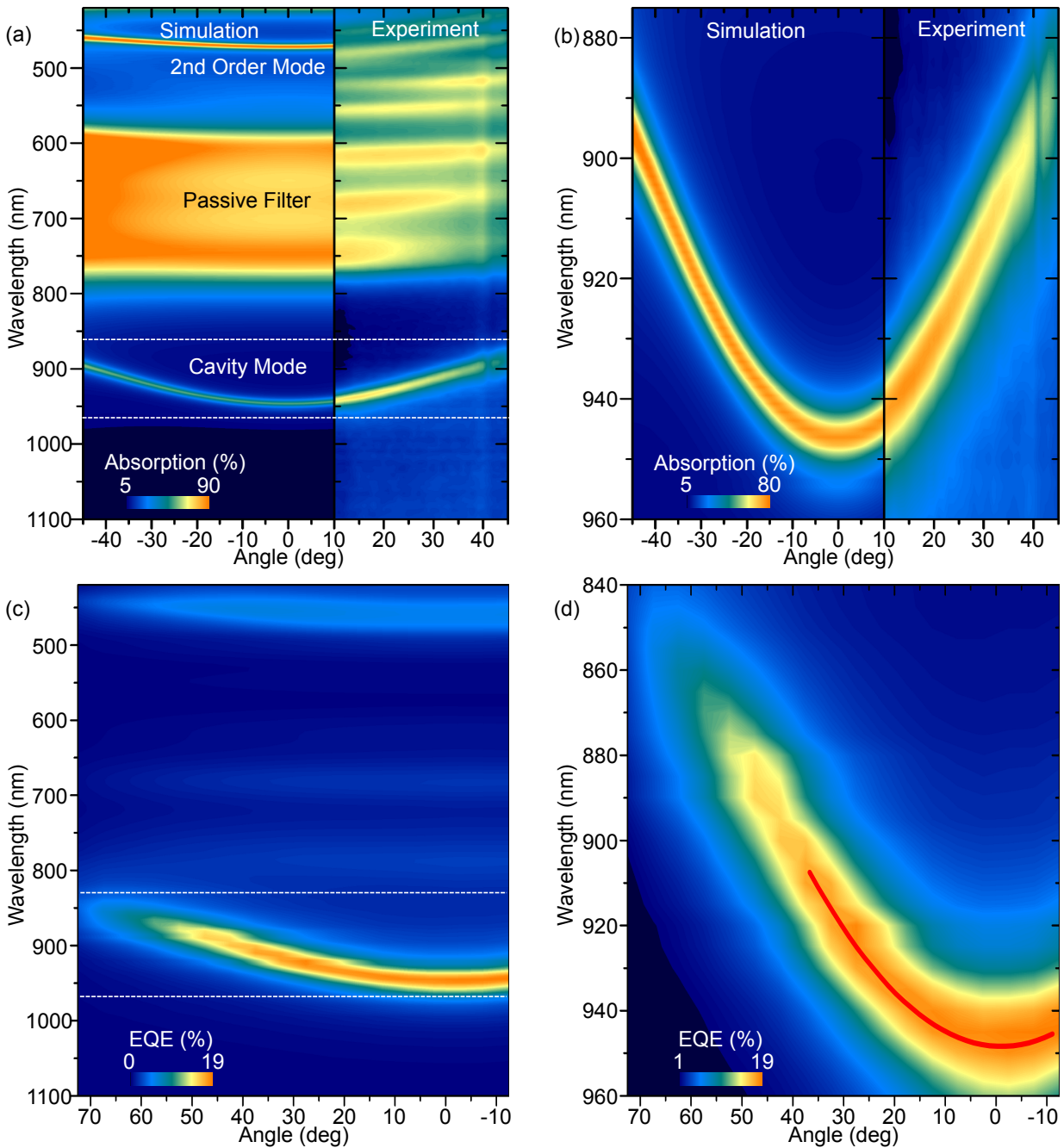


**Figure 8.6:** (a) Simulated (left) and measured (right) angle-resolved absorption spectrum of the cavity-enhanced device. The spectrally narrow cavity mode around 950 nm shows strong absorption, in addition to the passive filter region between 550 nm...800 nm and the second order mode at 480 nm. (b) Enhanced view of the cavity mode (dashed region in (a)), exhibiting the typical parabolic dispersion. (c) Angle-resolved external quantum efficiency (EQE) of the device. The passive filter suppresses all EQE signal apart from the cavity mode and a smaller contribution of the second order mode. (d) Enhanced view of the cavity mode (dashed region in (c)), showcasing spectral tunability of the EQE signal over 100 nm. Red line represents the cavity mode extracted from (b). EQE measurements performed by Bernhard Siegmund.

sample, exhibiting a strong cavity resonance at 950 nm under normal incidence. The absorption spectra reveal a multitude of absorption peaks, from the actual cavity mode (950 nm...890 nm), the second order cavity (490 nm...450 nm), to the absorption of the passive filter evaporated on top (800 nm...550 nm). While all features are well represented in both simulation (left) and experiment (right), the experimental spectra show slightly smaller absolute values due to additional scattering in the reflection measurement of the small-scale device in the goniometer setup. The cavity mode shows strongly enhanced absorption compared to its spectral neighbourhood and exhibits the typical parabolic dispersion curve of a microcavity. By turning the sample from  $0^\circ$  to  $45^\circ$ , the resonant absorption peak shifts by  $\approx 60$  nm and shows only a slight drop-off in intensity for larger angles (which is in part due to the measurement setup). Also, second order cavity modes and passive absorption peaks exhibit a slight angle-dependence, agreeing in simulation and experiment. Here, it has to be noted that the passive filter absorption will not be detected in the actual electrical measurement.

The angle-dependent EQE in Fig. 8.6 (c) shows a similar image of parabolic cavity behaviour. By measuring angles up to  $70^\circ$ , a tunability of almost 100 nm is realised, supported by the broad CT absorption band. While for large angles, the illumination reduces proportional to  $\cos(\theta)$  and a drop in signal is observed, for angles below  $50^\circ$  an almost constant signal with corresponding narrow FWHM can be observed. Here, the actual cavity resonance is the only significant contribution to the signal, with only a slight addition by the second order cavity mode at 450 nm. While the passive filtering obviously absorbs wide ranges of visible light, the actual detector signal shows only the desired mode. The EQE coincides well with the absorption data, added as a red contour line in Fig. 8.6 (d).

While such angle-dependent behaviour is unique to cavity-based devices, it has to be well understood in applications and in the best case can aid finely tunable spectrally resolved photodetection.

### 8.3.2 Variation of Transport Layer Thicknesses for Spectral Tunability

The nature of microcavity optics directly relates the cavity mode as a standing wave between to mirrors to the distance between them. Consequently, a variation in their distance brings with it a variation also in resonance wavelength. The cavity-enhanced organic photodetectors presented here provide a very straightforward way of tuning the cavity thickness by changing the thickness of the transport layers that, apart from charge carrier transport, act as optically inert spacer layers. To preserve the position of the optical field maximum in the optical center of the cavity, and thus at the position of the active BHJ, both transport layers have to be varied independently. As the active volume in the cavity stays the same, no significant difference in signal is expected, as long

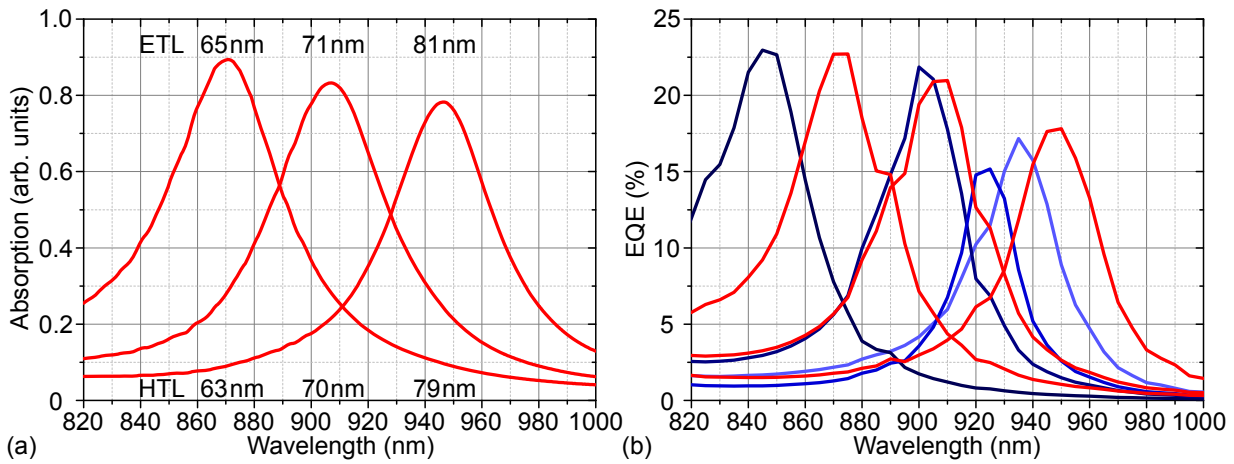


**Figure 8.7:** (a) Simulation of cavity-enhanced device absorption for the design: 100 nm Ag | (63, 70, 79) nm BF-DPB:NDP9 | 5 nm ZnPc | 50 nm ZnPc:C<sub>60</sub> | 5 nm C<sub>60</sub> | (65, 71, 81) nm Bis-HFI-NTCDI:W<sub>2</sub>(hpp)<sub>4</sub> | 3 nm MoO<sub>3</sub> | 1 nm Au | 18 nm Ag. The detection wavelength is tunable by changing the cavity thickness, varying both HTL and ETL separately to keep the cavity mode in the centre of the device. (b) EQE of various detectors with different wavelengths. Design for red devices according to (a), blue devices show varying materials and top mirror thicknesses. Red devices show a good agreement with theoretically expected mode positions and spectral widths. EQE measurements performed by Bernhard Siegmund.

as the underlying absorption of the active material stays constant upon variation of the excitation wavelength.

Figure 8.7 (a) shows the simulation of sample absorption while for a tunable device comprising 100 nm Ag | (63, 70, 79) nm BF-DPB:NDP9 | 5 nm ZnPc | 50 nm ZnPc:C<sub>60</sub> | 5 nm C<sub>60</sub> | (65, 71, 81) nm Bis-HFI-NTCDI:W<sub>2</sub>(hpp)<sub>4</sub> | 3 nm MoO<sub>3</sub> | 1 nm Au | 18 nm Ag. Increasing the transport layer thicknesses brings about a red-shift of the cavity resonance, coinciding well with the measured EQE spectra of actual devices in Fig. 8.7 (b). Here, the red curves correspond to the simulation in (a), while other spectra are achieved with different transport materials or a variation of top metal film thicknesses. Due to their comparably high refractive indices ( $n_{\text{ETL}} \approx n_{\text{HTL}} \approx 1.7$ ) and the use of a  $\lambda/2$  cavity, the cavity resonance increases by a factor of  $\Delta\lambda = \Delta d \cdot 2 \cdot n_{\text{ETL}} \approx \Delta d \cdot 3.4$  corresponding to the increase of transport layer thicknesses, as observed in the experiment. This can be exploited not only in different samples, but opens the path to a quasi-continuously tunable device by evaporating thickness-wedged layers onto an array of independent contacts. This way, fully functioning IR spectrometers can be fabricated on a very small scale.

Overall, the utilisation of microcavities for enhancing an otherwise very weakly absorbing state opens a multitude of tunability via variation of mirror, active, or transport layers as well as angle of incidence. Extending the CT state further into the NIR by exchanging the active BHJ

or constituents thereof will enable a further red-shift of observable resonances, as the underlying cavity concept is universal for all wavelengths.

## 8.4 Distributed Bragg Reflector Cavities for High- $Q$ Photodetectors

Cavity-enhanced photodetectors based on thin-film metal mirrors allow for easy fabrication as the mirrors double as electrodes for the device. However, the use of absorbing materials as cavity mirrors leads to drawbacks in optical quality. The superior performance of distributed Bragg reflectors (DBRs) can significantly enhance the quality factor (for  $Q > 100$ ) due to their high reflectance at the position of the stop band and vanishing absorption overall. Utilising this enhancement, the specific detectivity could be shifted further into the infrared, as the decrease in CT state absorption can be compensated by high quality factors. For this purpose, it is however essential to decrease the parasitic absorption of all non-active materials, namely contacts and transport layers, to very low values ( $k < 10^{-2}$ ). An elegant way to incorporate an electrical contact directly into the DBR structure would be the use of transparent conductive oxides, which can additionally serve as spacer layers, decreasing the thickness of the transport layers. Alternatively, highly n-doped  $C_{60}$  has been investigated as a stand-alone electrode [261] and might serve for a similar purpose due to its low sheet resistance and low absorption in the NIR. As a third option, ultra-thin metal films show high conductivities above percolation threshold but influence the cavity optics due to the formation of Tamm-plasmon-polaritons. It has to be noted that such considerations only work if parasitic absorption of all layers can be kept at a minimum.

Here, the use of DBR mirrors for cavity-enhanced CT detectors is explored in optical simulations for different design concepts. Figure 8.8 shows the distribution of the optical field around the cavity resonance for a DBR-metal cavity (a) and a two-DBR cavity (b). The use of a metal top mirror provides advantages in sample fabrication. A DBR of design wavelength 950 nm can be prepared on a glass substrate and subsequently, a detector stack be prepared on top, finishing with a silver contact. This way, any harmful exposure of sensible organic molecules to UV radiation and/or heat during DBR processing can be avoided completely. By electron beam evaporation, such a DBR can be fabricated by adding quarter-wavelength (qwl) layers of  $TiO_2$  (high refractive index) and  $SiO_2$  (low refractive index) on top of each other. Less harmful ways of producing a DBR might facilitate top mirrors, such as solution processing of  $TiO_2$  and  $SiO_2$  nanoparticles to form qwl layers [262, 263], or DBRs made completely of organic materials [264]. As depicted in Fig. 8.8 (a), such a device already facilitates a sharp resonance as field strength is accumulated with increasing amplitude in every  $SiO_2$ - $TiO_2$  pair. In this structure, the bottom contact comprises an ultra-thin 9 nm silver film combined with a 3 nm  $MoO_3$  layer and a 1 nm gold seed layer as utilised before. The organic stack follows similar considerations as in the previous sections. A resonant mode forms at 970 nm exhibiting exceptional sharpness ( $FWHM \approx 4.2$  nm,  $Q \approx 220$ ) in the detector area, compared to the measured  $Q$  values of the

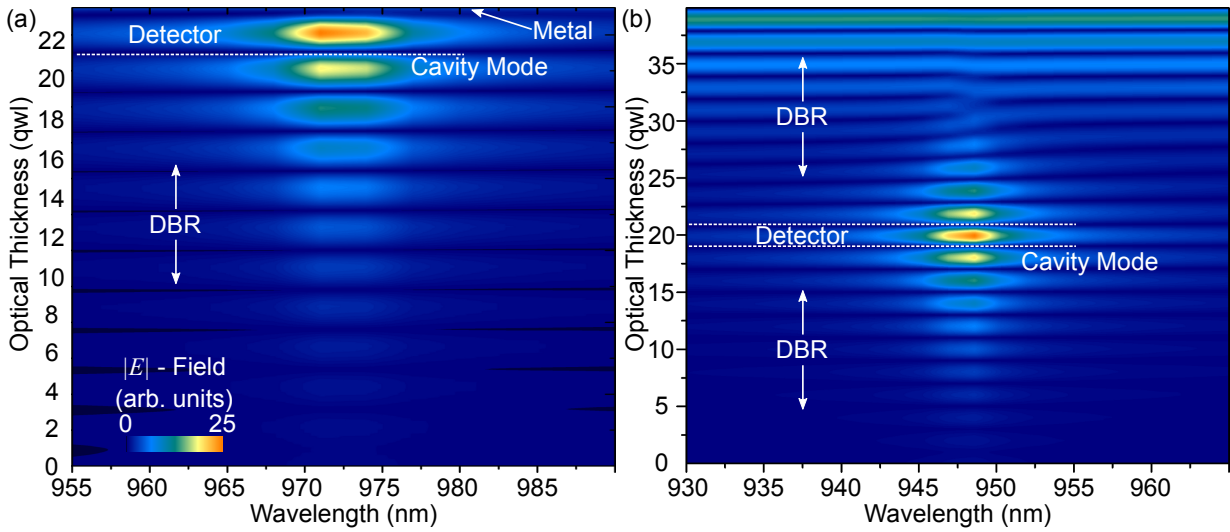


**Figure 8.8:** (a) Simulated optical field of a cavity-enhanced detector comprising a DBR bottom and a 50 nm metal top mirror. In addition, a thin metal contact of 9 nm thickness is added on top of the bottom DBR. A high-quality cavity mode ( $Q \approx 220$ ) is observed in the active detector area. (b) Simulated optical field of a cavity-enhanced detector comprising two DBRs and ITO contacts. The high quality mirror and low-loss ITO contacts facilitate a sharp ( $Q \approx 330$ ) cavity mode in the detector area in the centre of the device.

previous all-silver-mirror devices of 53. However, due to the use of metal in this system, this is not the only resonant mode developing. As discussed in previous chapters, the combination of periodic photonic crystals such as DBRs and plasmonic interlayers leads to the build-up of two Tamm-plasmon-polariton (TPP) resonances. Figure 8.9 (a) shows the absorption spectrum of the device, clearly depicting both TPP1 mode as desired cavity resonance at 970 nm and a TPP2 resonance at 1089 nm. Here, the formation of both resonances is facilitated by the interaction of light in the photonic structure with either metal-organic (TPP1) and metal-DBR (TPP2) interface. The field distribution for both modes can be seen in Fig. 8.9 (b), showing the resonances with maxima in the active area of the detector part. Note that this two-resonance behaviour is caused by the bottom metal contact on the DBR and not by the top contact as the second surface of the top mirror is not part of the optical resonator. Instead, only a TPP1 resonance is expected for a device without plasmonic bottom contact. Nevertheless, the depicted device provides a viable route for further enhancement of the CT-absorption based devices. While a parasitic signal might be expected from the TPP2 resonance, its significant red-shift limits the overall impact.

Instead of a silver top contact, a second DBR can be utilised, if parasitic absorption in the detector can be controlled. Figures 8.8 (b) and 8.9 (c) show field simulations of a device incorporating two DBR mirrors and transparent indium tin oxide (ITO) contacts, as commonly employed in solar cell fabrication. Here, the use of two high-quality mirrors facilitates even

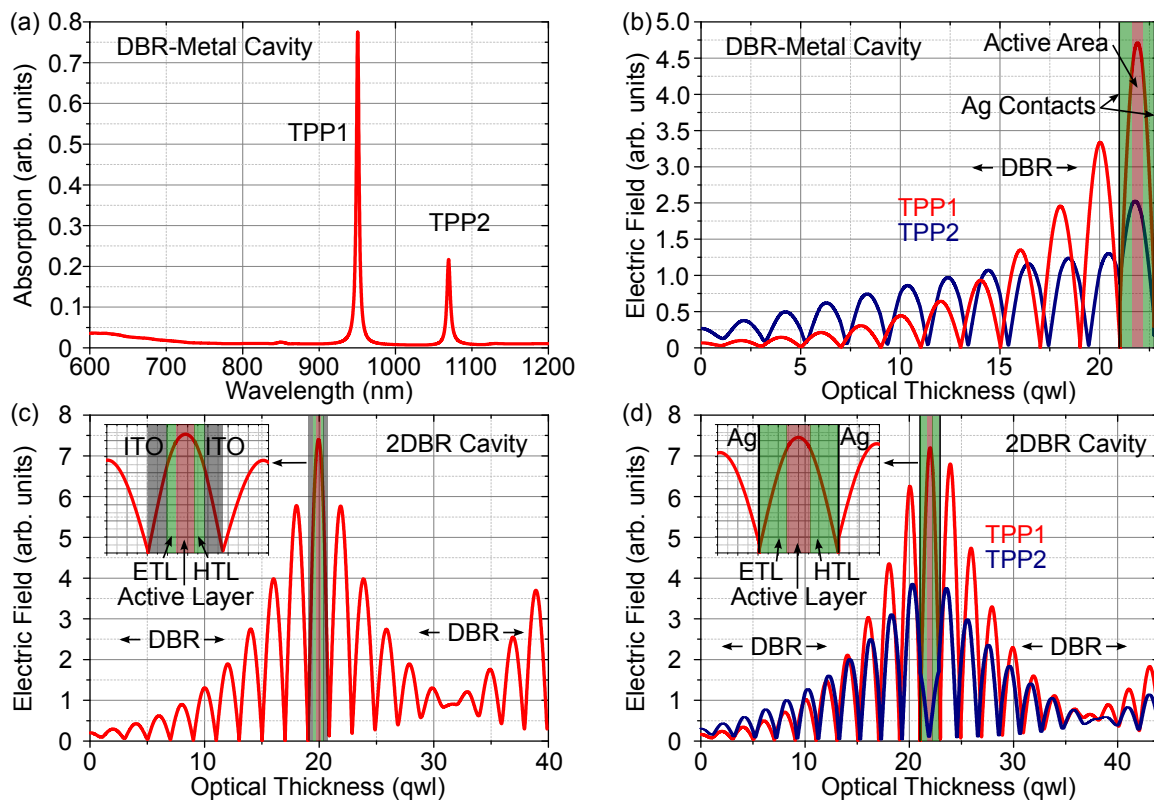


**Figure 8.9:** (a) Simulated absorption spectrum of a DBR-metal cavity-enhanced detector. The formation of Tamm-plasmon-polaritons when combining periodic photonic crystals and metal layers facilitates two resonances in the spectrum. (b) Simulated optical field distribution of TPP1 (970 nm) and TPP2 (1089 nm), both showing enhanced field strength in the detector area. (c) Simulated optical field at 947 nm of a 2DBR cavity-enhanced detector with ITO contacts. Inset shows detailed view of the active detector area. (d) Simulated optical field of TPP1 (950 nm) in a 2DBR cavity-enhanced detector with 9 nm Ag contacts. Inset shows detailed view of the active detector area. In this structure, TPP2 (1050 nm) is suppressed as it exhibits a minimum in the centre of the device.

higher  $Q$ -factors ( $> 300$ ) and increased field strength in the detector area. The use of 80 nm thick ITO contacts instead of silver facilitates a largely plasmon-free behaviour and thus no TPP resonances are observed here. While the use of ITO layers as both contact and spacer layers reduces the necessary transport layer thickness, ITO exhibits finite absorption in the NIR as well and thus contributes to losses in the system. Here, other oxides could be utilised for even higher performance. Nevertheless, such devices show promising features if technological challenges in preparation can be overcome.

As an intermediate concept, a two-DBR cavity can be combined with ultra-thin metal contacts (3 nm  $\text{MoO}_3$ , 1 nm Au, 9 nm Ag on both sides), surpassing even the performance of the ITO-device and exhibiting quality factors  $Q > 500$ . Figure 8.9 (d) shows the optical field distribution

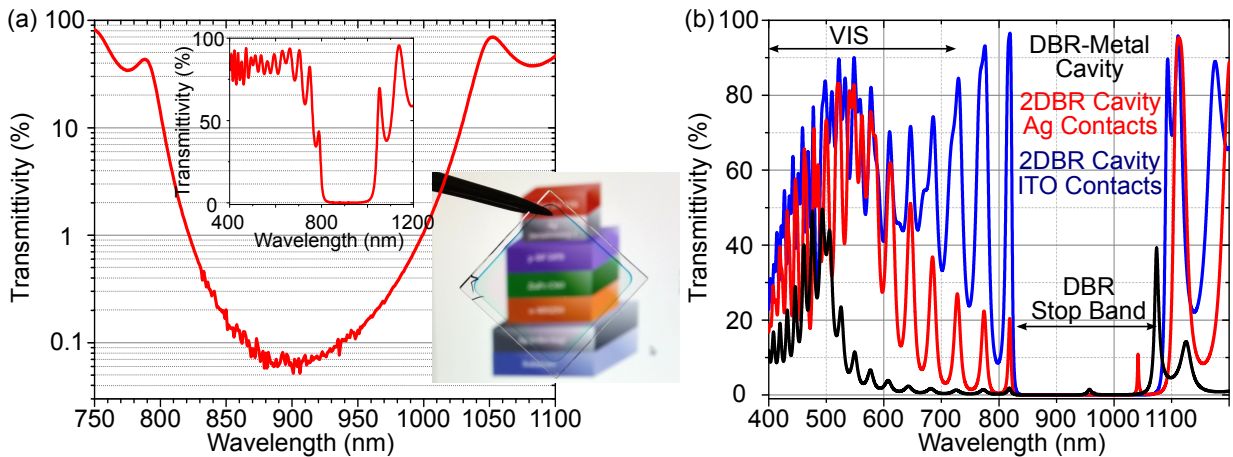


**Figure 8.10:** (a) Experimental transmission spectrum of a DBR with a design wavelength of 900 nm and photograph of said DBR. Inset shows the transmission spectrum over a wide spectral range, indicating a transmission  $\geq 80\%$  in the VIS. (b) Simulated transmission spectra of full cavity-enhanced devices comprising a DBR and 25 nm Ag top mirror (black line), a 2DBR cavity with 9 nm Ag contacts (red line), and a 2DBR cavity with ITO contacts (blue line). Optimised IR detectors can exhibit a transmission of  $\approx 60\%$  in the VIS for the materials used here.

of the device, at the resonance positions of TPP1 at 950 nm and TPP2 at 1050 nm. Again, the interaction of metal contacts and DBR facilitates the formation of both TPP states. In this design however, the influence of TPP2 is greatly reduced. The symmetric design of the sample leads to the formation of only one degenerate TPP2 state for both metals which in addition exhibits a minimum of the optical field between them, in the detector volume. This way, only the TPP1 resonance will be harnessed for photodetection.

While metal mirrors used previously show high reflectance in a broad spectral range, the use of interference-based mirrors in a smaller range provides considerable transmission outside of the stop band, especially in the VIS. Figure 8.10 (a) shows the measured transmission spectrum of a NIR-DBR, exhibiting a stop band between 800 nm and 1000 nm of  $\mathcal{R} \gtrsim 99.9\%$  and a transmission of  $\mathcal{T} \gtrsim 80\%$  in the visible range of the spectrum. The photograph shows said DBR providing wavelength-neutral high transmission of all colours. Thus, utilising the right organic materials, a visible-transparent NIR detector can be realised. For this purpose, the DBR concepts are evaluated in transfer-matrix simulations regarding their full transmission spectrum. All concepts introduced above exhibit a finite transmission in the visible (see 8.10 (b)). While the DBR-metal cavity (with 25 nm top Ag mirror) shows rather low transmission only in the blue and green regions of the spectrum, cavities with two DBRs and transparent contacts can still transmit a significant amount of light. Utilising two 9 nm Ag contacts, the transmitted spectrum broadens and shows values  $\gtrsim 50\%$  between 500 nm and 600 nm. Finally, the ITO-based device exhibits broad transmission above 60% over almost the whole visible range. Here, the transmittivity is



essentially limited by the band to band absorption of ZnPc and can be enhanced further, if other materials with desirable properties are found.

The use of DBR mirrors for high-quality cavity enhanced CT detectors promises enhanced functionality of devices with high spectral selectivity and provides a route to visible-transparent NIR detection. Resulting from this concepts, cost-efficient, lightweight, and high quality spectroscopic applications can be envisioned.



# 9 Conclusion and Outlook

## Conclusion

In this dissertation, the behaviour of light in microcavity structures is investigated regarding two main applications: The control and manipulation of stimulated, coherent emission from organic microlasers, and the spectrally sensitive absorption of NIR photons in cavity-enhanced organic photodetectors. The central point revolves around the application of dielectric microcavity resonators in combination with organic fluorescent emitters to facilitate lasers over a broad spectral range and the direct intervention into their mode structure with in-plane microstructures.

Chapter 4 introduces the concept of organic microlasers, demonstrating the tunability of such devices by introducing a wedge-shaped  $3/2\lambda$  cavity layer to facilitate lasing over a broad spectral range of 90 nm in a single device using the same emitter system. Furthermore, the concept of planar interlayers directly between DBR mirror and organic cavity layer is introduced, allowing a shifting of the cavity resonance within the mirror stop band. In metal-organic microcavities, Tamm-plasmon-polaritons are formed when thin silver films interact with the photonic crystal structure of a microcavity laser, showing a significant redshift of the original cavity resonance due to the interaction with plasmons based in the metal and the resulting phase-shift of light. In thin non-absorbing dielectric interlayers, such as  $\text{SiO}_2$ , similar resonance shifts are observed, however based on the increase of the optical cavity thickness by the added low refractive index layer next to the organics. Interestingly, both conceptually very different types of interlayers show similar behaviour and offer complementary routes of manipulating the cavity mode.

Finally, the growth of thin silver films for the application in organic microcavities is investigated. Here, concepts first realised in the fabrication of ultra-thin metal contacts – namely the use of growth-enhancing seed layers and diffusion barrier layers – are employed to significantly enhance the optical quality of silver films in the system. The use of  $\text{MoO}_3$  diffusion barrier layers and Au seed layers directly shows reduced absorption induced by localised surface plasmons in in-situ transmission spectroscopy during fabrication and facilitates a doubling of the quality factor for thin silver films deposited on top of the organic layer in a metal-organic microcavity.

In Chapter 5 patterned interlayers are first utilised in organic microlasers. By locally changing the cavity, areas of different resonances are brought spatially close to each other, resulting in the formation of in-plane standing waves. Such multidimensional photonic confinement is

investigated in dielectric photonic wires and plasmonic photonic dots, both showing discretisation of modes in the direction perpendicular to the patterning. To facilitate a full picture of both in-plane components of the momentum vector, the concept of dispersion tomography is introduced. Here, the  $k_x$ -component is directly measured, while the  $k_y$ -component is scanned by means of sample rotation or shifting of the far-field lens in the micro-photoluminescence setup. In the resulting tomograms, the two-dimensional photonic confinement in SiO<sub>2</sub>-wires and the full three-dimensional confinement in silver photonic dots can be depicted vividly.

Finally, the confinement enabled by such metallic microstructures is applied to significantly reduce the lasing threshold in the system. In elliptic holes in a silver film embedded in an organic microcavity, the formation of coherent standing Mathieu-modes is observed at thresholds three times lower than in a planar cavity. Even further, the fabrication of triangular structures in such metal films enables the gradual observation of confinement in relation to the mode positioning in the triangle. Here, lasing thresholds of one order of magnitude below the ones in planar systems can be realised. Such advantageous metal patterning can be employed to introduce electrical contacts in the system, opening a pathway for the realisation of electrically driven solid state organic lasers.

In Chapter 6, periodic stripes of either silver or SiO<sub>2</sub> are utilised for the observation of photonic Bloch states in organic microcavities. As vertically confined photons show a parabolic dispersion above a potential energy defined by the cavity thickness, a red-shift of the resonance can be analogously interpreted as a shift of this photonic potential. Thus, in periodic structures, a Kronig-Penney potential is realised enabling the direct observation of Bloch-states in both spatially and momentum-resolved spectroscopy. The deep photonic wires used here show a coexistence of localised modes at the position of wires as well as extended modes above the photonic potential, corresponding to energy bands in condensed matter. The parity of confined modes is investigated in metal-organic Kronig-Penney structures and correlates to the formation of either zero- or  $\pi$ - phase coupled modes of the first above-barrier band. In dielectric periodic structures, the high optical quality of the non-absorbing wires enables a detailed investigation of different widths of the photonic potential well and barrier as well as the observation of lasing from Bloch-states. Exciting the system with two interfering beams, a preferred in-plane momentum vector is selected, enabling a direct control over lasing wavelength and outcoupling direction of confined and extended Bloch-states. The experiments are accompanied by an analytical modified Kronig-Penney theory which introduces a polarisation-dependent effective photon mass to quantitatively compute mode positions in these and related systems. All investigations are additionally accompanied by numerical simulations using the rigorous-coupled-wave-analysis and showing excellent agreement with both experiment and analytic modelling.

Chapter 7 introduces a different kind of in-plane patterning for such microlasers. Here, instead

of manipulating the photonic potential landscape, all microcavity layers are deposited on top of a periodically structured substrate. As a result, waveguided modes in the cavity plane are scattered into the vertical direction and exhibit linear dispersion curves in addition to the original parabolic cavity mode. A sufficient in-plane coherence length even below threshold enables a coherent interaction of both resonators as observed in a pronounced anticrossing of waveguided and VCSEL modes in the far-field spectrum. Resulting from this coupling, both original VCSEL modes as well as hybrid WG-VCSEL modes show stimulated emission, where hybrid modes exhibit a macroscopically increased spatial extension of the coherent laser mode, proven by both spatially resolved spectra as well as sharp modes in  $k$ -space. The coherent coupling of two conceptually different devices with perpendicular propagation directions facilitates a multitude of new applications.

In Chapter 8, the microcavity concept is expanded towards absorbing systems to facilitate the cavity-enhanced photodetection by utilising the intermolecular charge-transfer state in donor-acceptor blends of organic materials. Organic bulk-heterojunctions exhibit optically accessible charge transfer states when the electron is excited from the HOMO of the donor directly to the LUMO of the acceptor. While the absorption coefficients for this transition are typically very low, the optical field in the corresponding spectral range can be dramatically enhanced by the use of an optical microcavity. Here, spectrally sensitive NIR photodetection is facilitated by enhancing the charge transfer state absorption in ZnPc:C<sub>60</sub> solar cells, reaching external quantum efficiencies above 20% (18% at 950 nm) and spectral widths significantly below 50 nm. The detector is tunable in wavelength by means of the angular dispersion or by changing the thickness of the charge transport layers that double as optical spacers. Finally, concepts for further enhancement utilising high-quality DBR mirrors are illustrated. The devices shown here present an accessible way to reliably detect light in a wavelength range very interesting for application. In contrast to using filters or gratings, here all necessary elements providing an electrical signal as readout are already integrated on an extremely small scale which can be further minimised laterally. Furthermore, the novel concept of directly accessing the charge transfer state absorption provides a methodology for interesting fundamental experiments in the future.

### Outlook

In this dissertation, it could be shown how microcavities offer an extensive playground to investigate light with varying degrees of confinement as well as extended macroscopic coherence and the ability to directly observe analogies to quantum behaviour with optical waves. For organic microlasers, multiple pathways of future investigation open.

Pursuing the goal of an electrically driven organic solid state laser, metal-organic microcavities can be utilised in different geometries to minimise optical losses while maintaining an efficient

charge carrier injection. Here, patterned metal layers can sufficiently confine photons on small lateral scales while acting as electrical contacts. Furthermore, by utilising lift-off techniques to deposit a patterned silver layer in combination with an insulating layer above, the current flow can be directed into small areas of metal-free holes, where optical confinement additionally complements the performance (see Fig. 9.1). For this purpose, lateral conductivity can be enhanced by transparent conductive layers such as conductive oxides or highly doped organic transport layers. In addition, exciting extended photonic Bloch states provides the ability to couple photons between metallic contacts and in metal-free areas above the photonic potential barrier. These patternings facilitate a spatial separation of charge carrier injection, inevitably connected to optical losses, and the actual lasing modes in a future device.

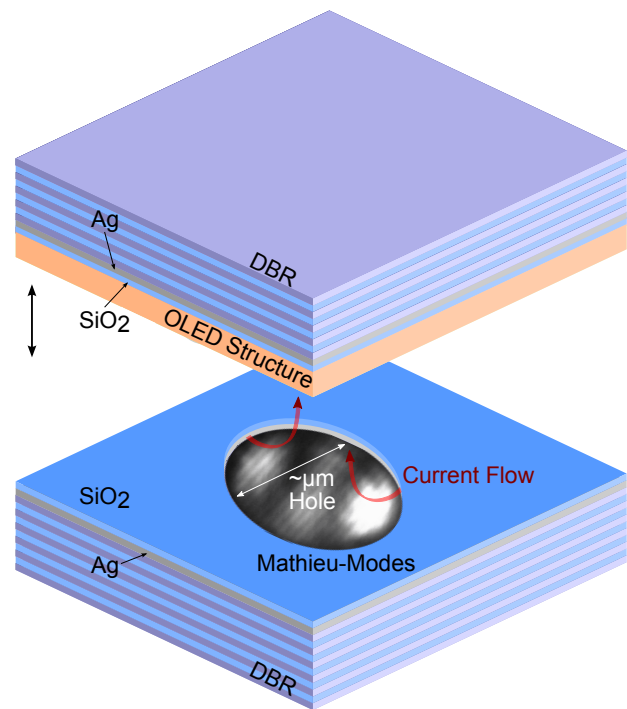


**Figure 9.1:** Scheme for organic MC with directed current flow in confined hole.

The investigations on selective excitation of a multitude of different lasing modes can be harnessed for tunable lasing on ultra-small scale. Unlike other tunable organic microcavities, where gradual wedges provide tunability over a macroscopic lateral distance, with this concept a wavelength-tunable laser can be realised on an area smaller than  $10\ \mu\text{m} \times 10\ \mu\text{m}$ . Unlike most other studies, the present experiments are performed at room-temperature under ambient conditions, and are therefore easily accessible and adaptable to real-world applications. The precise control over lasing wavelength and main outcoupling angle of coherent emission are highly desired in applications. With the rise of new active material systems with broader gain profiles, such as colloidal quantum dots [265, 266], nanoplatelets [28, 267], or hybrid organic-inorganic perovskites [24, 25], a fine control of lasing seems more and more necessary. Furthermore, one could imagine a precise screening of material gain profiles, as the high density of photonic modes of discrete states allows for lasing at the gain maximum first, and not necessarily at the apex of a cavity parabola.

While interesting applications arise from the investigation of patterned microcavities, opportunities for more fundamental research are present as well. By adding a periodic photonic wire superlattice, an additional periodicity is brought into the system. While breaking the

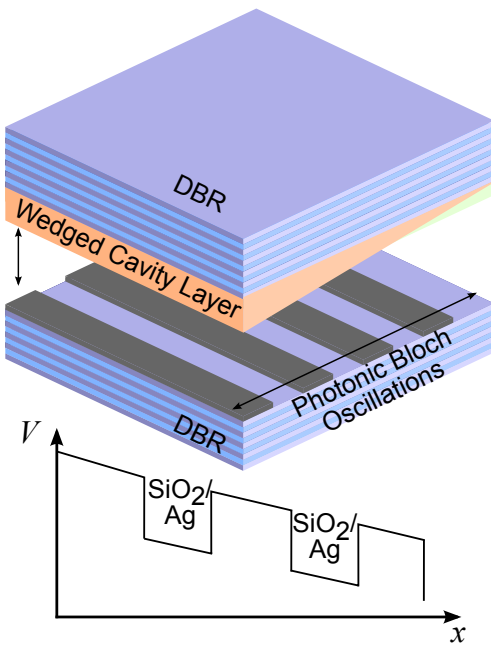


**Figure 9.2:** Sample schematic for the observation of photonic Bloch oscillations.

vertical symmetry when inserting a  $\lambda/2$  cavity layer leads to the formation of the cavity mode as a kind of optical trap state, the in-plane symmetry can be manipulated as well. By adding a driving field to a periodic potential well structure, Bloch oscillations occur as investigated in semiconductor superlattices [176, 268] and optical systems [243]. Here, such a driving field can be realised by evaporating a wedge-shaped cavity layer on top of a photonic wire array. The change of cavity layer thickness in turn leads to a change in resonant or base photonic energy in the system. The resulting potential landscape, depicted in Figure 9.2, offers the possibility to observe the Wannier-Stark ladder in micro-photoluminescence spectroscopy as well as the direct observation of spatially, spectrally, and temporally resolved oscillation using an ultrafast up-conversion setup.

Coherently coupling two fundamentally different types of light propagation such as waveguided and surface-emitted laser modes has been shown to produce macroscopically coherent modes. It is possible to imagine an even further transport of coherence in the sample plane. For this purpose, first order DFB gratings can be utilised to transport light between coupling gratings of higher order to facilitate coherent transmission of information. Coupling VCSEL and DFB resonators can result in higher optical feedback of the hybrid device and consequently can increase critical properties such as the  $\beta$  factor of micro-lasers.

The introduction of a strongly coupled active system into the photonic structures presented here is straightforward (e.g. with organic strongly coupled systems [138, 139]) and facilitates the observation of confinement, Bloch states and -oscillations, and selective excitation of different modes in coherent polariton condensates.

In addition, by further breaking the symmetry and creating a multi-cavity system with a varying detuning, an angular selectivity can be

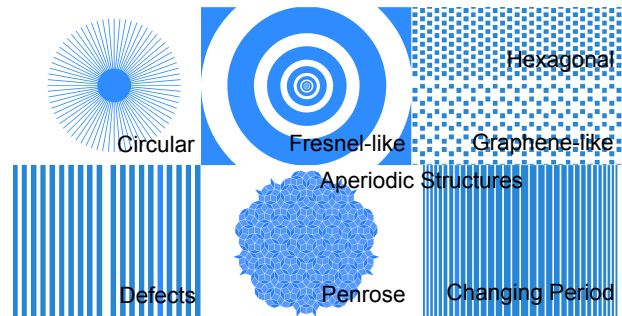


**Figure 9.3:** Selection of photonic structures including defects and aperiodic patterning.

introduced. Light-guiding aperiodic patterning might furthermore be applied to concentrate light, with future possibilities of non-linear interaction or incoupling to small fibre apertures in small scale devices. Continuing this result, defect states in otherwise periodic lattices can be investigated to create additional lateral field enhancement and strong confinement, similar to the vertical confinement in the cavity layer between DBRs. Tuning these defect states enables a high degree of control over the lasing wavelength. By more sophisticated lateral patterning, a full 3D confinement can be achieved, enhancing the field in all three dimensions by preventing and trapping wave-guided and leaky modes travelling in the sample plane.

Fabrication and investigation of metal-organic microcavities with spatially periodic patterning and the systematic transition to aperiodic 2D- and 3D-microstructures, including quasicrystals, spiral-like and Fresnel lenses, and defects in periodic patterns, and observation and characterization of the corresponding lasing modes. In similar systems, graphene-like patterns [99, 269] and their edge states [270, 271], quasicrystal Fibonacci- [237, 272, 273], Penrose- [274, 275, 276, 277], and Lieb-like [278, 279] patterns are already under investigation.

The application of microcavities for the cavity-enhanced charge transfer state absorption as presented in this work is directly transferable to application. Large area, flexible, and lightweight detectors can be realised with the proposed system, and high spatial resolution might be achieved on a pixel grid of perpendicular top- and bottom electrodes as the lateral optical mode extension remains on the single micrometer-scale for quality factors below 200. Utilising similar electrode arrays, spectroscopic applications can be realised by creating wedged cavities, gradually varying the thicknesses of transport layers as demonstrated in principle in this work. Finally, prospects of further enhancement by using DBR mirrors have been explored in simulation in this work already. Here, higher detectivity, sensitivity and visible transparent devices can be realised. Apart from photodetection applications, the direct observation of charge transfer state absorption opens up new ways to investigate in detail a fundamental process in organic semiconductors.



# Abbreviations

AFM	...	Atomic Force Microscopy
Alq <sub>3</sub>	...	Tris(8-hydroxyquinolato)aluminium, matrix material
$\beta$	...	$\beta$ -factor, fraction of spontaneous emission coupled into the lasing mode
CCD	...	charge-coupled device
$d_C$	...	cavity thickness
DBR	...	distributed Bragg reflector
DCM	...	Dicyanomethylene-2-methyl-6-p-dimethylaminostyryl-4H-pyran, laser dye, emitter material
DFB	...	distributed feedback
$\vec{E}$	...	electric field
$\epsilon_0$	...	vacuum permittivity, $\epsilon_0 = 8.854 \cdot 10^{-12} \text{F/m}$
$\epsilon; \epsilon', \epsilon''$	...	relative permittivity; real, and imaginary part of $\epsilon$
$F_P$	...	Purcell-factor, factor of spontaneous emission rate in a cavity compared to the same transition in vacuum
FRET	...	Förster resonant energy transfer
$\vec{k}, k, k_{\parallel}, k_{\perp}$	...	wavevector, wavenumber, parallel and perpendicular components
$L_W,$	...	photonic wire/ metal stripe thickness, optical thickness
$l$	...	angular mode number of Mathieu-modes
$\lambda, \lambda_D, \lambda_C$	...	wavelength, DBR design wavelength, cavity resonance
MC	...	microcavity
$\mu\text{-PL}$	...	micro-photoluminescence
$\tilde{n}(\omega); n(\omega), k(\omega)$	...	complex refractive index; real part: refractive index, imaginary part: extinction coefficient
$n$	...	radial mode number of Mathieu-modes
ND, OD	...	neutral density, optical density
OLED	...	organic light emitting diode
OSOL	...	organic solar cell
(O)VCSEL	...	(organic) vertical cavity surface emitting laser

PVD, EBPVD, TPVD	...	physical vapour deposition, electron beam PVD, thermal PVD
$L_P, p$	...	photonic wire period
$q$	...	surface plasmon wavenumber
$Q$	...	quality factor
$\mathcal{R}, \mathcal{T}$	...	reflectivity, transmittivity
TE	...	transversal electric
TM	...	transversal magnetic
TS1, TS2	...	Tamm state 1, Tamm state 2
TPP	...	Tamm-plasmon-polariton
$\vartheta$	...	cavity outcoupling angle
$\varphi$	...	sample rotation angle/ double Dove prism rotation angle
$\omega_p$	...	plasma frequency

# Bibliography

- [1] A. Mischok, F. Lemke, C. Reinhardt, R. Brückner, A. Zakhidov, S. Hintschich, H. Fröb, V. Lyssenko, and K. Leo, “Dispersion tomography of an organic photonic-wire microcavity,” *Applied Physics Letters*, vol. 103, no. 18, p. 183302, 2013.
- [2] A. Mischok, R. Brückner, C. Reinhardt, M. Sudzius, V. G. Lyssenko, H. Fröb, and K. Leo, “Threshold reduction by multidimensional photonic confinement in metal-organic microcavities,” in *SPIE Photonics Europe*, pp. 91370D–91370D, International Society for Optics and Photonics, 2014.
- [3] A. Mischok, R. Brückner, M. Sudzius, C. Reinhardt, V. G. Lyssenko, H. Fröb, and K. Leo, “Photonic confinement in laterally structured metal-organic microcavities,” *Applied Physics Letters*, vol. 105, no. 5, p. 051108, 2014.
- [4] A. Mischok, V. G. Lyssenko, R. Brückner, F. Löchner, R. Scholz, A. A. Zakhidov, H. Fröb, and K. Leo, “Zero- and  $\pi$ -states in a periodic array of deep photonic wires,” *Advanced Optical Materials*, vol. 2, no. 8, pp. 746–750, 2014.
- [5] F. J. Löchner, A. Mischok, R. Brückner, V. G. Lyssenko, A. A. Zakhidov, H. Fröb, and K. Leo, “Coexisting localized and extended optical Bloch states in a periodic deep wire array microcavity,” *Superlattices and Microstructures*, vol. 85, pp. 646–652, 2015.
- [6] A. Mischok, R. Brückner, H. Fröb, A. Zakhidov, V. Lyssenko, and K. Leo, “Control of lasing from Bloch states in microcavity photonic wires via selective excitation and gain,” *Physical Review Applied*, vol. 3, no. 6, p. 064016, 2015.
- [7] A. Mischok, R. Brückner, H. Fröb, V. G. Lyssenko, and K. Leo, “Photonic lattices in organic microcavities: Bloch states and control of lasing,” *Proc. SPIE*, vol. 9566, pp. 95660T–95660T–11, 2015.
- [8] I. Slowik, Y. Zhang, A. Mischok, R. Brückner, V. Lyssenko, H. Fröb, N. Kronenberg, M. Gather, and K. Leo, “Fano-like interference in the emission spectra of a multimode organic microcavity,” *Selected Topics in Quantum Electronics, IEEE Journal of*, vol. 22, pp. 1–6, Jan 2016.

- [9] C. Tzschaschel, M. Sudzius, A. Mischok, H. Fröb, and K. Leo, “Net gain in small mode volume organic microcavities,” *Applied Physics Letters*, vol. 108, p. 023304, 2015.
- [10] A. Mischok, T. Wagner, R. Brückner, M. Sudzius, H. Fröb, V. G. Lyssenko, and K. Leo, “Lasing and macroscopic coherence of hybridized modes in coupled 2D waveguide-vcSEL resonators,” *Advanced Optical Materials*, DOI:10.1002/adom.201600282, 2016.
- [11] T. Wagner, , M. Sudzius, A. Mischok, H. Fröb, V. G. Lyssenko, and K. Leo, “Hybrid DFB-VCSEL resonators for enhanced optical feedback,” *in preparation*, 2016.
- [12] T. Wagner, , M. Sudzius, A. Mischok, H. Fröb, V. G. Lyssenko, and K. Leo, “Lasing from hybrid DFB-VCSEL resonators,” *in preparation*, 2016.
- [13] B. Siegmund, A. Mischok, J. Benduhn, D. Spoltore, H. Fröb, C. Körner, K. Leo, and K. Vandewal, “Narrowband near infrared detection via the intermolecular charge transfer state,” *in preparation*, 2016.
- [14] F. Nehm, A. Mischok, J. Jördening, S. Schubert, H. Fröb, V. G. Lyssenko, L. Müller-Meskamp, and K. Leo, “Metal diffusion barriers for organic optoelectronics,” *in preparation*, 2016.
- [15] C. Kropla, F. Lemke, V. G. Lyssenko, A. Mischok, R. Brückner, H. Fröb, and K. Leo, “Lasing from hybrid DFB-VCSEL resonators,” *in preparation*, 2016.
- [16] B. Siegmund, A. Mischok, J. Benduhn, D. Spoltore, H. Fröb, C. Körner, K. Leo, and K. Vandewal, “Verfahren zur Detektion und Umwandlung von infraroter elektromagnetischer Strahlung.” German Patent Office, Aktenzeichen 102015215581.1.
- [17] A. Einstein, “Strahlungs-Emission und Absorption nach der Quantentheorie,” *Verhandlungen der Deutschen Physikalischen Gesellschaft*, vol. 18, pp. 318–323, 1916.
- [18] A. Einstein, “Zur Quantentheorie der Strahlung,” *Physikalische Zeitschrift*, vol. 18, pp. 121–128, 1917.
- [19] J. P. Gordon, H. J. Zeiger, and C. H. Townes, “The maser – new type of microwave amplifier, frequency standard, and spectrometer,” *Physical Review*, vol. 99, no. 4, p. 1264, 1955.
- [20] T. Maiman, “Stimulated emission of radiation in ruby,” *Nature*, vol. 187, pp. 493–494, 1960.

- [21] M. C. Gather and S. H. Yun, "Single-cell biological lasers," *Nature Photonics*, vol. 5, no. 7, pp. 406–410, 2011.
- [22] M. Schubert, A. Steude, P. Liehm, N. M. Kronenberg, M. Karl, E. C. Campbell, S. J. Powis, and M. C. Gather, "Lasing within live cells containing intracellular optical microresonators for barcode-type cell tagging and tracking," *Nano letters*, vol. 15, no. 8, pp. 5647–5652, 2015.
- [23] M. Oxborrow, J. D. Breeze, and N. M. Alford, "Room-temperature solid-state maser," *Nature*, vol. 488, pp. 353+, AUG 16 2012.
- [24] G. Xing, N. Mathews, S. S. Lim, N. Yantara, X. Liu, D. Sabba, M. Grätzel, S. Mhaisalkar, and T. C. Sum, "Low-temperature solution-processed wavelength-tunable perovskites for lasing," *Nature materials*, vol. 13, no. 5, pp. 476–480, 2014.
- [25] F. Deschler, M. Price, S. Pathak, L. E. Klintberg, D.-D. Jarausch, R. Higler, S. Hüttner, T. Leijtens, S. D. Stranks, H. J. Snaith, *et al.*, "High photoluminescence efficiency and optically pumped lasing in solution-processed mixed halide perovskite semiconductors," *The Journal of Physical Chemistry Letters*, vol. 5, no. 8, pp. 1421–1426, 2014.
- [26] M. M. Adachi, F. Fan, D. P. Sellan, S. Hoogland, O. Voznyy, A. J. Houtepen, K. D. Parrish, P. Kanjanaboos, J. A. Malen, and E. H. Sargent, "Microsecond-sustained lasing from colloidal quantum dot solids," *Nature communications*, vol. 6, 2015.
- [27] B. Guzelturk, Y. Kelestemur, K. Gungor, A. Yeltik, M. Z. Akgul, Y. Wang, R. Chen, C. Dang, H. Sun, and H. V. Demir, "Stable and low-threshold optical gain in CdSe/CdS quantum dots: An all-colloidal frequency up-converted laser," *Advanced Materials*, vol. 27, no. 17, pp. 2741–2746, 2015.
- [28] B. Guzelturk, Y. Kelestemur, M. Olutas, S. Delikanli, and H. V. Demir, "Amplified spontaneous emission and lasing in colloidal nanoplatelets," *ACS nano*, vol. 8, no. 7, pp. 6599–6605, 2014.
- [29] R. N. Hall, G. E. Fenner, J. D. Kingsley, T. J. Soltys, and R. O. Carlson, "Coherent light emission from GaAs junctions," *Phys. Rev. Lett.*, vol. 9, pp. 366–368, Nov 1962.
- [30] D. Sanvitto, A. Daraei, A. Tahraoui, M. Hopkinson, P. W. Fry, D. M. Whittaker, and M. S. Skolnick, "Observation of ultrahigh quality factor in a semiconductor microcavity," *Applied Physics Letters*, vol. 86, no. 19, p. 191109, 2005.

- [31] C. W. Tang, “Two-layer organic photovoltaic cell,” *Applied Physics Letters*, vol. 48, no. 2, pp. 183–185, 1986.
- [32] Heliatek. <http://www.heliatek.com/de/presse/pressemitteilungen/details/neuerweltrekord-fuer-organische-solarzellen-heliatek-behauptet-sich-mit-12-zelleffizienz-als-technologiefuehrer> 2015-09-30.
- [33] S. Mathew, A. Yella, P. Gao, R. Humphry-Baker, B. F. Curchod, N. Ashari-Astani, I. Tavernelli, U. Rothlisberger, M. K. Nazeeruddin, and M. Grätzel, “Dye-sensitized solar cells with 13% efficiency achieved through the molecular engineering of porphyrin sensitizers,” *Nature chemistry*, vol. 6, no. 3, pp. 242–247, 2014.
- [34] H. Zhou, Q. Chen, G. Li, S. Luo, T.-b. Song, H.-S. Duan, Z. Hong, J. You, Y. Liu, and Y. Yang, “Interface engineering of highly efficient perovskite solar cells,” *Science*, vol. 345, no. 6196, pp. 542–546, 2014.
- [35] C. W. Tang and S. A. VanSlyke, “Organic electroluminescent diodes,” *Applied Physics Letters*, vol. 51, no. 12, pp. 913–915, 1987.
- [36] S. Reineke, F. Lindner, G. Schwartz, N. Seidler, K. Walzer, B. Lüssem, and K. Leo, “White organic light-emitting diodes with fluorescent tube efficiency,” *Nature*, vol. 459, no. 7244, pp. 234–238, 2009.
- [37] H. Koezuka, A. Tsumura, and T. Ando, “Field-effect transistor with polythiophene thin film,” *Synthetic Metals*, vol. 18, no. 13, pp. 699 – 704, 1987. Proceedings of the International Conference of Science and Technology of Synthetic Metals.
- [38] B. Soffer and B. McFarland, “Continuously tunable, narrow-band organic dye lasers,” *Applied physics letters*, vol. 10, no. 10, p. 266, 1967.
- [39] N. Tessler, G. Denton, and R. Friend, “Lasing from conjugated-polymer microcavities,” *Nature*, vol. 382, no. 6593, pp. 695–697, 1996.
- [40] F. Hide, M. A. Daz-Garca, B. J. Schwartz, M. R. Andersson, Q. Pei, and A. J. Heeger, “Semiconducting polymers: A new class of solid-state laser materials,” *Science*, vol. 273, no. 5283, pp. 1833–1836, 1996.
- [41] V. Kozlov, V. Bulović, P. Burrows, and S. Forrest, “Laser action in organic semiconductor waveguide and double-heterostructure devices,” *Nature*, vol. 389, no. 6649, pp. 362–364, 1997.

- [42] R. Brückner, M. Sudzius, S. Hintschich, H. Fröb, V. Lyssenko, and K. Leo, “Hybrid optical Tamm states in a planar dielectric microcavity,” *Physical Review B*, vol. 83, no. 3, p. 033405, 2011.
- [43] C. Reinhardt, R. Brückner, J. Haase, M. Sudzius, S. Hintschich, H. Fröb, V. Lyssenko, and K. Leo, “Mode discretization in an organic microcavity including a perforated silver layer,” *Applied Physics Letters*, vol. 100, no. 10, p. 103306, 2012.
- [44] R. Loudon, *The quantum theory of light*. Oxford university press, 2000.
- [45] J. P. Reithmaier, M. Röhner, H. Zull, F. Schäfer, A. Forchel, P. A. Knipp, and T. L. Reinecke, “Size dependence of confined optical modes in photonic quantum dots,” *Phys. Rev. Lett.*, vol. 78, pp. 378–381, Jan 1997.
- [46] A. Tartakovskii, V. Kulakovskii, A. Forchel, and J. Reithmaier, “Exciton-photon coupling in photonic wires,” *Physical Review B*, vol. 57, no. 12, p. R6807, 1998.
- [47] M. Bayer, T. Gutbrod, J. Reithmaier, A. Forchel, T. Reinecke, P. Knipp, A. Dremin, and V. Kulakovskii, “Optical modes in photonic molecules,” *Physical review letters*, vol. 81, no. 12, p. 2582, 1998.
- [48] T. Gutbrod, M. Bayer, A. Forchel, P. A. Knipp, T. L. Reinecke, A. Tartakovskii, V. D. Kulakovskii, N. A. Gippius, and S. G. Tikhodeev, “Angle dependence of the spontaneous emission from confined optical modes in photonic dots,” *Phys. Rev. B*, vol. 59, pp. 2223–2229, Jan 1999.
- [49] C. Weisbuch, M. Nishioka, A. Ishikawa, and Y. Arakawa, “Observation of the coupled exciton-photon mode splitting in a semiconductor quantum microcavity,” *Physical Review Letters*, vol. 69, no. 23, p. 3314, 1992.
- [50] H. Deng, G. Weihs, C. Santori, J. Bloch, and Y. Yamamoto, “Condensation of semiconductor microcavity exciton polaritons,” *Science*, vol. 298, no. 5591, pp. 199–202, 2002.
- [51] H. Deng, H. Haug, and Y. Yamamoto, “Exciton-polariton Bose-Einstein condensation,” *Reviews of modern physics*, vol. 82, no. 2, p. 1489, 2010.
- [52] A. Amo, T. Liew, C. Adrados, R. Houdré, E. Giacobino, A. Kavokin, and A. Bramati, “Exciton–polariton spin switches,” *Nature Photonics*, vol. 4, no. 6, pp. 361–366, 2010.
- [53] J. Berger, O. Lyngnes, H. Gibbs, G. Khitrova, T. Nelson, E. Lindmark, A. Kavokin, M. Kaliteevski, and V. Zapasskii, “Magnetic-field enhancement of the exciton-polariton

- splitting in a semiconductor quantum-well microcavity: The strong coupling threshold,” *Physical Review B*, vol. 54, no. 3, p. 1975, 1996.
- [54] C. Sturm, D. Solnyshkov, O. Krebs, A. Lemaître, I. Sagnes, E. Galopin, A. Amo, G. Malpuech, and J. Bloch, “Driven-dissipative confined polariton condensate under magnetic field,” *arXiv preprint arXiv:1409.5112*, 2014.
- [55] C. Sturm, D. Solnyshkov, O. Krebs, A. Lemaître, I. Sagnes, E. Galopin, A. Amo, G. Malpuech, and J. Bloch, “Nonequilibrium polariton condensate in a magnetic field,” *Physical Review B*, vol. 91, no. 15, p. 155130, 2015.
- [56] K. Winkler, J. Fischer, A. Schade, M. Amthor, R. Dall, J. Geßler, M. Emmerling, E. A. Ostrovskaya, M. Kamp, C. Schneider, *et al.*, “A polariton condensate in a photonic crystal potential landscape,” *New Journal of Physics*, vol. 17, no. 2, p. 023001, 2015.
- [57] A. Kavokin, G. Malpuech, and M. Glazov, “Optical spin hall effect,” *Physical review letters*, vol. 95, no. 13, p. 136601, 2005.
- [58] A. Nalitov, D. Solnyshkov, and G. Malpuech, “Polariton Z topological insulator,” *Physical review letters*, vol. 114, no. 11, p. 116401, 2015.
- [59] M. Born and E. Wolf, *Principles of Optics*. Cambridge University Press, 7. ed., 1999.
- [60] S. A. Maier, *Plasmonics: Fundamentals and Application*. Springer Science + Business Media LLC, 1. ed., 2007.
- [61] P. B. Johnson and R. W. Christy, “Optical Constants of the Noble Metals,” *Phys. Rev. B*, vol. 6, pp. 4370–4379, Dec 1972.
- [62] E. Petryayeva and U. J. Krull, “Localized surface plasmon resonance: Nanostructures, bioassays and biosensingA review,” *Analytica Chimica Acta*, vol. 706, no. 1, pp. 8 – 24, 2011.
- [63] M. Zinke-Allmang, L. C. Feldman, and M. H. Grabow, “Clustering on surfaces,” *Surface Science Reports*, vol. 16, no. 8, pp. 377 – 463, 1992.
- [64] C. Sönnichsen, *Plasmons in metal nanostructures*. PhD thesis, Ludwig-Maximilians Universität München, 2001.
- [65] K. J. Vahala, “Optical microcavities,” *Nature*, vol. 424, no. 6950, pp. 839–846, 2003.
- [66] F. Koyama, “Recent advances of VCSEL photonics,” *Lightwave Technology, Journal of*, vol. 24, no. 12, pp. 4502–4513, 2006.



- [67] J. J. Degnan, “The waveguide laser: a review,” *Applied physics*, vol. 11, no. 1, pp. 1–33, 1976.
- [68] D. Armani, T. Kippenberg, S. Spillane, and K. Vahala, “Ultra-high-Q toroid microcavity on a chip,” *Nature*, vol. 421, no. 6926, pp. 925–928, 2003.
- [69] B. Gayral, J. M. Gerard, A. Lematre, C. Dupuis, L. Manin, and J. L. Pelouard, “High-Q wet-etched GaAs microdisks containing InAs quantum boxes,” *Applied Physics Letters*, vol. 75, no. 13, pp. 1908–1910, 1999.
- [70] K. Srinivasan, P. E. Barclay, O. Painter, J. Chen, A. Y. Cho, and C. Gmachl, “Experimental demonstration of a high quality factor photonic crystal microcavity,” *Applied Physics Letters*, vol. 83, no. 10, pp. 1915–1917, 2003.
- [71] H. Altug, D. Englund, and J. Vučković, “Ultrafast photonic crystal nanocavity laser,” *Nature Physics*, vol. 2, no. 7, pp. 484–488, 2006.
- [72] H. Stoll and A. Yariv, “Coupled-mode analysis of periodic dielectric waveguides,” *Optics Communications*, vol. 8, no. 1, pp. 5–8, 1973.
- [73] H. Kogelnik and C. Shank, “Coupled-wave theory of distributed feedback lasers,” *Journal of applied physics*, vol. 43, no. 5, pp. 2327–2335, 1972.
- [74] E. Popov and L. Mashev, “Dispersion characteristics of multilayer waveguides,” *Optics communications*, vol. 52, no. 6, pp. 393–396, 1985.
- [75] M.-S. Kwon, “A numerically stable analysis method for complex multilayer waveguides based on modified transfer-matrix equations,” *Journal of Lightwave Technology*, vol. 27, no. 20, pp. 4407–4414, 2009.
- [76] E. M. Purcell, “Spontaneous emission probabilities at radio frequencies,” *Physical Review*, vol. 69, p. 681, 1946.
- [77] G. Panzarini, L. C. Andreani, A. Armitage, D. Baxter, M. Skolnick, V. Astratov, J. Roberts, A. V. Kavokin, M. R. Vladimirova, and M. Kaliteevski, “Exciton-light coupling in single and coupled semiconductor microcavities: Polariton dispersion and polarization splitting,” *Physical Review B*, vol. 59, no. 7, p. 5082, 1999.
- [78] A. Yariv and P. Yeh, *Optical waves in crystals*, vol. 10. Wiley, New York, 1984.
- [79] H. A. Macleod, *Thin-film optical filters*. CRC Press, 2010.

- [80] M. Kaliteevski, I. Iorsh, S. Brand, R. Abram, J. Chamberlain, A. Kavokin, and I. Shelykh, “Tamm plasmon-polaritons: Possible electromagnetic states at the interface of a metal and a dielectric Bragg mirror,” *Physical Review B*, vol. 76, no. 16, p. 165415, 2007.
- [81] M. Kaliteevski, S. Brand, R. Abram, I. Iorsh, A. Kavokin, and I. Shelykh, “Hybrid states of Tamm plasmons and exciton polaritons,” *Applied Physics Letters*, vol. 95, no. 25, p. 251108, 2009.
- [82] R. Brückner, M. Sudzius, S. Hintschich, H. Fröb, V. Lyssenko, M. Kaliteevski, I. Iorsh, R. Abram, A. Kavokin, and K. Leo, “Parabolic polarization splitting of Tamm states in a metal-organic microcavity,” *Applied Physics Letters*, vol. 100, no. 6, p. 062101, 2012.
- [83] C. Symonds, G. Lheureux, J. Hugonin, J. Greffet, J. Laverdant, G. Brucoli, A. Lemaitre, P. Senellart, and J. Bellessa, “Confined Tamm plasmon lasers,” *Nano letters*, vol. 13, no. 7, pp. 3179–3184, 2013.
- [84] R. Brückner, V. Lyssenko, S. Hofmann, and K. Leo, “Lasing of Tamm states in highly efficient organic devices based on small-molecule organic semiconductors,” *Faraday discussions*, vol. 174, pp. 183–201, 2014.
- [85] C. Constantin, E. Martinet, D. Oberli, E. Kapon, B. Gayral, and J. Gérard, “Quantum wires in multidimensional microcavities: Effects of photon dimensionality on emission properties,” *Physical Review B*, vol. 66, no. 16, p. 165306, 2002.
- [86] D. Tanese, H. Flayac, D. Solnyshkov, A. Amo, A. Lemaître, E. Galopin, R. Braive, P. Senellart, I. Sagnes, G. Malpuech, *et al.*, “Polariton condensation in solitonic gap states in a one-dimensional periodic potential,” *Nature communications*, vol. 4, p. 1749, 2013.
- [87] C. Schneider, T. Heindel, A. Huggenberger, P. Weinmann, C. Kistner, M. Kamp, S. Reitzenstein, S. Höfling, and A. Forchel, “Single photon emission from a site-controlled quantum dot-micropillar cavity system,” *Applied Physics Letters*, vol. 94, no. 11, p. 111111, 2009.
- [88] Y. Zhang and M. Lončar, “Submicrometer diameter micropillar cavities with high quality factor and ultrasmall mode volume,” *Optics letters*, vol. 34, no. 7, pp. 902–904, 2009.
- [89] S. Reitzenstein, A. Bazhenov, A. Gorbunov, C. Hofmann, S. Münch, A. Löffler, M. Kamp, J. Reithmaier, V. Kulakovskii, and A. Forchel, “Lasing in high-Q quantum-dot micropillar cavities,” *Applied physics letters*, vol. 89, no. 5, p. 1107, 2006.

- [90] C. W. Lai, N. Y. Kim, S. Utsunomiya, G. Roumpos, H. Deng, M. D. Fraser, T. Byrnes, P. Recher, N. Kumada, T. Fujisawa, and Y. Yamamoto, “Coherent zero-state and  $\pi$ -state in an exciton-polariton condensate array,” *Nature*, vol. 450, pp. 529–U8, Nov 22 2007.
- [91] P. V. Santos *et al.*, “Modulation of photonic structures by surface acoustic waves,” *Reports on progress in physics*, vol. 68, no. 7, p. 1639, 2005.
- [92] E. Cerda-Méndez, D. Krizhanovskii, M. Wouters, R. Bradley, K. Biermann, K. Guda, R. Hey, P. Santos, D. Sarkar, and M. Skolnick, “Polariton condensation in dynamic acoustic lattices,” *Physical review letters*, vol. 105, no. 11, p. 116402, 2010.
- [93] L. Ferrier, E. Wertz, R. Johne, D. D. Solnyshkov, P. Senellart, I. Sagnes, A. Lemaître, G. Malpuech, and J. Bloch, “Interactions in confined polariton condensates,” *Phys. Rev. Lett.*, vol. 106, p. 126401, Mar 2011.
- [94] O. El Daif, A. Baas, T. Guillet, J.-P. Brantut, R. I. Kaitouni, J. L. Staehli, F. Morier-Genoud, and B. Deveaud, “Polariton quantum boxes in semiconductor microcavities,” *Applied Physics Letters*, vol. 88, no. 6, pp. –, 2006.
- [95] R. Schmidt-Grund, H. Hilmer, A. Hinkel, C. Sturm, B. Rheinländer, V. Gottschalch, M. Lange, J. Zúñiga-Pérez, and M. Grundmann, “Two-dimensional confined photonic wire resonators—strong light–matter coupling,” *physica status solidi (b)*, vol. 247, no. 6, pp. 1351–1364, 2010.
- [96] L. Zhang, W. Xie, J. Wang, A. Poddubny, J. Lu, Y. Wang, J. Gu, W. Liu, D. Xu, X. Shen, *et al.*, “Weak lasing in one-dimensional polariton superlattices,” *Proceedings of the National Academy of Sciences*, vol. 112, no. 13, pp. E1516–E1519, 2015.
- [97] N. Y. Kim, K. Kusudo, C. Wu, N. Masumoto, A. Löffler, S. Höfling, N. Kumada, L. Worschech, A. Forchel, and Y. Yamamoto, “Dynamical d-wave condensation of exciton-polaritons in a two-dimensional square-lattice potential,” *Nature Physics*, vol. 7, no. 9, pp. 681–686, 2011.
- [98] B. Zhang, S. Brodbeck, Z. Wang, M. Kamp, C. Schneider, S. Höfling, and H. Deng, “Coupling polariton quantum boxes in sub-wavelength grating microcavities,” *Applied Physics Letters*, vol. 106, no. 5, p. 051104, 2015.
- [99] T. Jacqmin, I. Carusotto, I. Sagnes, M. Abbarchi, D. Solnyshkov, G. Malpuech, E. Galopin, A. Lemaître, J. Bloch, and A. Amo, “Direct observation of Dirac cones and a flat-band in a honeycomb lattice for polaritons,” *Physical review letters*, vol. 112, no. 11, p. 116402, 2014.

- [100] J. C. Gutiérrez-Vega, R. M. Rodríguez-Dagnino, M. A. Meneses-Nava, and S. Chávez-Cerda, “Mathieu functions, a visual approach,” *American Journal of Physics*, vol. 71, no. 3, pp. 233–242, 2003.
- [101] B. E. Cherrington, *Gaseous electronics and gas lasers*, vol. 94. Elsevier, 2014.
- [102] F. J. Duarte, P. Kelley, L. W. Hillman, and P. F. Liao, *Dye laser principles*. Academic Press, 1990.
- [103] K. F. Renk, “Titanium–sapphire laser,” in *Basics of Laser Physics*, pp. 75–80, Springer, 2012.
- [104] G. H. B. Thompson, “Physics of semiconductor laser devices,” *Chichester, Sussex, England and New York, Wiley-Interscience, 1980. 572 p.*, vol. 1, 1980.
- [105] R. Brückner, M. Sudzius, H. Fröb, V. Lyssenko, and K. Leo, “Saturation of laser emission in a small mode volume organic microcavity,” *Journal of Applied Physics*, vol. 109, no. 10, p. 103116, 2011.
- [106] H. Yokoyama and S. D. Brorson, “Rate equation analysis of microcavity lasers,” *Journal of Applied Physics*, vol. 66, no. 10, pp. 4801–4805, 1989.
- [107] P. R. Rice and H. Carmichael, “Photon statistics of a cavity-QED laser: A comment on the laser–phase-transition analogy,” *Physical Review A*, vol. 50, no. 5, p. 4318, 1994.
- [108] H. Yokoyama, “Physics and device applications of optical microcavities,” *Science*, vol. 256, no. 5053, pp. 66–70, 1992.
- [109] G. Björk and Y. Yamamoto, “Analysis of semiconductor microcavity lasers using rate equations,” *Quantum Electronics, IEEE Journal of*, vol. 27, no. 11, pp. 2386–2396, 1991.
- [110] M. Knupfer, “Exciton binding energies in organic semiconductors,” *Applied Physics A*, vol. 77, no. 5, pp. 623–626, 2003.
- [111] K. Leo, “Benzol,” 1999. <http://www.orgworld.de> 2015-09-30.
- [112] M. Born, “Born-Oppenheimer approximation,” *Quantum*, vol. 2, no. 2014/12, p. 4, 1927.
- [113] B. Maennig, M. Pfeiffer, A. Nollau, X. Zhou, K. Leo, and P. Simon, “Controlled p-type doping of polycrystalline and amorphous organic layers: Self-consistent description of conductivity and field-effect mobility by a microscopic percolation model,” *Physical Review B*, vol. 64, no. 19, p. 195208, 2001.

- [114] C. Deibel, T. Strobel, and V. Dyakonov, “Role of the charge transfer state in organic donor-acceptor solar cells,” *Advanced Materials*, vol. 22, no. 37, pp. 4097–4111, 2010.
- [115] K. Vandewal, S. Albrecht, E. T. Hoke, K. R. Graham, J. Widmer, J. D. Douglas, M. Schubert, W. R. Mateker, J. T. Bloking, G. F. Burkhard, *et al.*, “Efficient charge generation by relaxed charge-transfer states at organic interfaces,” *Nature materials*, vol. 13, no. 1, pp. 63–68, 2014.
- [116] K. Vandewal, *Charge transfer complexes in polymer:fullerene bulk heterojunction solar cells*. PhD thesis, Universiteit Hasselt, 2008.
- [117] K. Vandewal, A. Gadisa, W. D. Oosterbaan, S. Bertho, F. Banishoeib, I. Van Severen, L. Lutsen, T. J. Cleij, D. Vanderzande, and J. V. Manca, “The relation between open-circuit voltage and the onset of photocurrent generation by charge-transfer absorption in polymer: Fullerene bulk heterojunction solar cells,” *Advanced Functional Materials*, vol. 18, no. 14, pp. 2064–2070, 2008.
- [118] B. Schütte, H. Gothe, S. Hintschich, M. Sudzius, H. Fröb, V. Lyssenko, and K. Leo, “Continuously tunable laser emission from a wedge-shaped organic microcavity,” *Applied Physics Letters*, vol. 92, no. 16, p. 163309, 2008.
- [119] F. P. Schäfer, W. Schmidt, and J. Volze, “Organic dye solution laser,” *Applied Physics Letters*, vol. 9, no. 8, pp. 306–309, 1966.
- [120] O. Peterson, S. Tuccio, and B. Snavely, “CW operation of an organic dye solution laser,” *Applied Physics Letters*, vol. 17, no. 6, pp. 245–247, 1970.
- [121] T. Riedl, T. Rabe, H. Johannes, W. Kowalsky, J. Wang, T. Weimann, P. Hinze, B. Nehls, T. Farrell, and U. Scherf, “Tunable organic thin-film laser pumped by an inorganic violet diode laser,” *Applied Physics Letters*, vol. 88, no. 24, pp. 241116–241116, 2006.
- [122] S. Schauer, X. Liu, M. Worgull, U. Lemmer, and H. Hölscher, “Shape-memory polymers as flexible resonator substrates for continuously tunable organic dfb lasers,” *Optical Materials Express*, vol. 5, no. 3, pp. 576–584, 2015.
- [123] X. Liu, S. Lebedkin, W. Pfleging, H. Besser, M. Wissmann, I. Nazarenko, T. Mappes, S. Koeber, C. G. Koos, M. Kappes, *et al.*, “Surface-enhanced Raman spectroscopy (SERS) using nanopillar arrays as functional substrates and an organic semiconductor DFB laser as excitation source,” in *CLEO: Science and Innovations*, pp. STh4H–8, Optical Society of America, 2014.

- [124] X. Liu, *Organic Semiconductor Lasers and Tailored Nanostructures for Raman Spectroscopy*. KIT Scientific Publishing, 2015.
- [125] T. Grossmann, S. Klinkhammer, M. Hauser, D. Floess, T. Beck, C. Vannahme, T. Mappes, U. Lemmer, and H. Kalt, “Strongly confined, low-threshold laser modes in organic semiconductor microcavities,” *Optics express*, vol. 19, no. 10, pp. 10009–10016, 2011.
- [126] M. Langner, M. Sudzius, S. I. Hintschich, H. Fröb, V. G. Lyssenko, and K. Leo, “Sub-nanojoule threshold lasing in  $5 \times 5 \mu\text{m}^2$  organic photonic boxes,” in *Photonics Europe*, pp. 699902–699902, International Society for Optics and Photonics, 2008.
- [127] C. Karnutsch, C. Gÿrtner, V. Haug, U. Lemmer, T. Farrell, B. Nehls, U. Scherf, J. Wang, T. Weimann, G. Heliotis, *et al.*, “Low threshold blue conjugated polymer lasers with first- and second-order distributed feedback,” *Applied physics letters*, vol. 89, no. 20, p. 201108, 2006.
- [128] G. Strangi, V. Barna, R. Caputo, A. De Luca, C. Versace, N. Scaramuzza, C. Umeton, R. Bartolino, and G. N. Price, “Color-tunable organic microcavity laser array using distributed feedback,” *Physical review letters*, vol. 94, no. 6, p. 063903, 2005.
- [129] X. Liu, P. Stefanou, B. Wang, T. Woggon, T. Mappes, and U. Lemmer, “Organic semiconductor distributed feedback (DFB) laser as excitation source in Raman spectroscopy,” *Optics express*, vol. 21, no. 23, pp. 28941–28947, 2013.
- [130] Y. Yang, G. A. Turnbull, and I. D. Samuel, “Sensitive explosive vapor detection with polyfluorene lasers,” *Advanced Functional Materials*, vol. 20, no. 13, pp. 2093–2097, 2010.
- [131] Y. Wang, Y. Yang, G. A. Turnbull, and I. D. Samuel, “Explosive sensing using polymer lasers,” *Molecular Crystals and Liquid Crystals*, vol. 554, no. 1, pp. 103–110, 2012.
- [132] Q. Liao, Z. Xu, X. Zhong, W. Dang, Q. Shi, C. Zhang, Y. Weng, Z. Li, and H. Fu, “An organic nanowire waveguide exciton–polariton sub-microlaser and its photonic application,” *Journal of Materials Chemistry C*, vol. 2, no. 15, pp. 2773–2778, 2014.
- [133] S. Chénais and S. Forget, “Recent advances in solid-state organic lasers,” *Polymer International*, vol. 61, no. 3, pp. 390–406, 2012.
- [134] D. Lidzey, D. Bradley, T. Virgili, A. Armitage, M. Skolnick, and S. Walker, “Room temperature polariton emission from strongly coupled organic semiconductor microcavities,” *Physical review letters*, vol. 82, no. 16, p. 3316, 1999.

- [135] P. Michetti and G. La Rocca, “Polariton states in disordered organic microcavities,” *Physical Review B*, vol. 71, no. 11, p. 115320, 2005.
- [136] R. Holmes and S. Forrest, “Strong exciton–photon coupling in organic materials,” *Organic Electronics*, vol. 8, no. 2, pp. 77–93, 2007.
- [137] R. Holmes, S. Kéna-Cohen, V. Menon, and S. Forrest, “Strong coupling and hybridization of Frenkel and Wannier-Mott excitons in an organic-inorganic optical microcavity,” *Physical Review B*, vol. 74, no. 23, p. 235211, 2006.
- [138] J. D. Plumhof, T. Stöferle, L. Mai, U. Scherf, and R. F. Mahrt, “Room-temperature Bose–Einstein condensation of cavity exciton–polaritons in a polymer,” *Nature materials*, vol. 13, no. 3, pp. 247–252, 2014.
- [139] K. Daskalakis, S. Maier, R. Murray, and S. Kéna-Cohen, “Nonlinear interactions in an organic polariton condensate,” *Nature materials*, vol. 13, no. 3, pp. 271–278, 2014.
- [140] S. Kéna-Cohen and S. Forrest, “Room-temperature polariton lasing in an organic single-crystal microcavity,” *Nature Photonics*, vol. 4, no. 6, pp. 371–375, 2010.
- [141] S. Riechel, U. Lemmer, J. Feldmann, S. Berleb, A. Mückl, W. Brütting, A. Gombert, and V. Wittwer, “Very compact tunable solid-state laser utilizing a thin-film organic semiconductor,” *Optics letters*, vol. 26, no. 9, pp. 593–595, 2001.
- [142] Z. Xie, L. Hung, and S. Lee, “High-efficiency red electroluminescence from a narrow recombination zone confined by an organic double heterostructure,” *Applied Physics Letters*, vol. 79, no. 7, pp. 1048–1050, 2001.
- [143] M. Koschorreck, R. Gehlhaar, V. Lyssenko, M. Swoboda, M. Hoffmann, and K. Leo, “Dynamics of a high-Q vertical-cavity organic laser,” *Applied Physics Letters*, vol. 87, no. 18, p. 181108, 2005.
- [144] M. Tian, J. Luo, and X. Liu, “Highly efficient organic light-emitting devices beyond theoretical prediction under high current density,” *Optics express*, vol. 17, no. 24, pp. 21370–21375, 2009.
- [145] V. Kozlov, V. Bulovic, P. Burrows, M. Baldo, V. Khalfin, G. Parthasarathy, S. Forrest, Y. You, and M. Thompson, “Study of lasing action based on Förster energy transfer in optically pumped organic semiconductor thin films,” *Journal of applied physics*, vol. 84, no. 8, pp. 4096–4108, 1998.

- [146] S. Riechel, *Organic semiconductor lasers with two-dimensional distributed feedback*. PhD thesis, Ludwig Maximilians Universität München, 2002.
- [147] K. Shaklee and R. Leheny, “Direct determination of optical gain in semiconductor crystals,” *Applied Physics Letters*, vol. 18, no. 11, pp. 475–477, 1971.
- [148] L. Dal Negro, P. Bettotti, M. Cazzanelli, D. Pacifici, and L. Pavesi, “Applicability conditions and experimental analysis of the variable stripe length method for gain measurements,” *Optics communications*, vol. 229, no. 1, pp. 337–348, 2004.
- [149] B. W. Hakki and T. L. Paoli, “Gain spectra in GaAs double- heterostructure injection lasers,” *Journal of Applied Physics*, vol. 46, no. 3, pp. 1299–1306, 1975.
- [150] A. Köhler and H. Bässler, *Electronic Processes in Organic Semiconductors: An Introduction*. John Wiley & Sons, 2015.
- [151] B. Maennig, J. Drechsel, D. Gebeyehu, P. Simon, F. Kozlowski, A. Werner, F. Li, S. Grundmann, S. Sonntag, M. Koch, *et al.*, “Organic pin solar cells,” *Applied Physics A*, vol. 79, no. 1, pp. 1–14, 2004.
- [152] J. Huang, M. Pfeiffer, A. Werner, J. Blochwitz, K. Leo, and S. Liu, “Low-voltage organic electroluminescent devices using pin structures,” *Applied Physics Letters*, vol. 80, no. 1, pp. 139–141, 2002.
- [153] K. Walzer, B. Maennig, M. Pfeiffer, and K. Leo, “Highly efficient organic devices based on electrically doped transport layers,” *Chemical reviews*, vol. 107, no. 4, pp. 1233–1271, 2007.
- [154] P. Peumans, A. Yakimov, and S. R. Forrest, “Small molecular weight organic thin-film photodetectors and solar cells,” *Journal of Applied Physics*, vol. 93, no. 7, pp. 3693–3723, 2003.
- [155] K.-J. Baeg, M. Binda, D. Natali, M. Caironi, and Y.-Y. Noh, “Organic light detectors: Photodiodes and phototransistors,” *Advanced Materials*, vol. 25, no. 31, pp. 4267–4295, 2013.
- [156] G. Azzellino, A. Grimoldi, M. Binda, M. Caironi, D. Natali, and M. Sampietro, “Fully inkjet-printed organic photodetectors with high quantum yield,” *Advanced Materials*, vol. 25, no. 47, pp. 6829–6833, 2013.



- [157] G. Pace, A. Grimoldi, D. Natali, M. Sampietro, J. E. Coughlin, G. C. Bazan, and M. Caironi, "All-organic and fully-printed semitransparent photodetectors based on narrow bandgap conjugated molecules," *Advanced Materials*, vol. 26, no. 39, pp. 6773–6777, 2014.
- [158] A. Pierre, I. Deckman, P. B. Lechêne, and A. C. Arias, "High detectivity all-printed organic photodiodes," *Advanced Materials*, pp. n/a–n/a, 2015.
- [159] T. N. Ng, W. S. Wong, M. L. Chabynyc, S. Sambandan, and R. A. Street, "Flexible image sensor array with bulk heterojunction organic photodiode," *Applied Physics Letters*, vol. 92, no. 21, p. 213303, 2008.
- [160] H. Zhang, S. Jenatsch, J. De Jonghe, F. Nüesch, R. Steim, A. C. Véron, and R. Hany, "Transparent organic photodetector using a near-infrared absorbing cyanine dye," *Scientific reports*, vol. 5, 2015.
- [161] S.-h. Wu, W.-l. Li, B. Chu, C. S. Lee, Z.-s. Su, J.-b. Wang, F. Yan, G. Zhang, Z.-z. Hu, and Z.-q. Zhang, "High response deep ultraviolet organic photodetector with spectrum peak focused on 280 nm," *Applied Physics Letters*, vol. 96, no. 9, p. 093302, 2010.
- [162] H.-W. Lin, S.-Y. Ku, H.-C. Su, C.-W. Huang, Y.-T. Lin, K.-T. Wong, and C.-C. Wu, "Highly efficient visible-blind organic ultraviolet photodetectors," *Advanced Materials*, vol. 17, no. 20, pp. 2489–2493, 2005.
- [163] Y. Fang, Q. Dong, Y. Shao, Y. Yuan, and J. Huang, "Highly narrowband perovskite single-crystal photodetectors enabled by surface-charge recombination," *Nature Photonics*, 2015.
- [164] Q. Lin, A. Armin, P. L. Burn, and P. Meredith, "Filterless narrowband visible photodetectors," *Nature Photonics*, 2015.
- [165] D. Ray and K. Narasimhan, "High response organic visible-blind ultraviolet detector," *Applied Physics Letters*, vol. 91, no. 9, p. 3516, 2007.
- [166] F. Boroumand, M. Zhu, A. Dalton, J. Keddie, P. Sellin, and J. Gutierrez, "Direct x-ray detection with conjugated polymer devices," *Applied Physics Letters*, vol. 91, no. 3, 2007.
- [167] J. Qi, L. Ni, D. Yang, X. Zhou, W. Qiao, M. Li, D. Ma, and Z. Y. Wang, "Panchromatic small molecules for UV-Vis-NIR photodetectors with high detectivity," *Journal of Materials Chemistry C*, vol. 2, no. 13, pp. 2431–2438, 2014.

- [168] N. Joshi, *Photoconductivity: Art: Science & Technology*, vol. 25. CRC Press, 1990.
- [169] M. Ünü, G. Ulu, and M. Gökkavas, “Resonant cavity enhanced photodetectors,” *Photodetectors and Fiber Optics*, 2001.
- [170] K. Kishino, M. S. Ünü, J.-I. Chyi, J. Reed, L. Arsenault, and H. Morkoc, “Resonant cavity-enhanced (RCE) photodetectors,” *Quantum Electronics, IEEE Journal of*, vol. 27, no. 8, pp. 2025–2034, 1991.
- [171] J. Heroux, X. Yang, and W. Wang, “GaInNAs resonant-cavity-enhanced photodetector operating at 1.3  $\mu\text{m}$ ,” *Applied physics letters*, vol. 75, no. 18, 1999.
- [172] O. I. Dosunmu, D. D. Cannon, M. K. Emsley, L. C. Kimerling, and M. S. Unlu, “High-speed resonant cavity enhanced Ge photodetectors on reflecting Si substrates for 1550-nm operation,” *Photonics Technology Letters, IEEE*, vol. 17, no. 1, pp. 175–177, 2005.
- [173] M. Furchi, A. Urich, A. Pospischil, G. Lilley, K. Unterrainer, H. Detz, P. Klang, A. M. Andrews, W. Schrenk, G. Strasser, *et al.*, “Microcavity-integrated graphene photodetector,” *Nano letters*, vol. 12, no. 6, pp. 2773–2777, 2012.
- [174] M. S. Ünü and S. Strite, “Resonant cavity enhanced photonic devices,” *Journal of Applied Physics*, vol. 78, no. 2, pp. 607–639, 1995.
- [175] W. van Haeringen and D. Lenstra, *Analogies in Optics and Micro Electronics*. Springer, 1990.
- [176] K. Leo, P. H. Bolivar, F. Brüggemann, R. Schwedler, and K. Köhler, “Observation of Bloch oscillations in a semiconductor superlattice,” *Solid State Communications*, vol. 84, no. 10, pp. 943–946, 1992.
- [177] A. Kavokin, G. Malpuech, A. Di Carlo, P. Lugli, and F. Rossi, “Photonic Bloch oscillations in laterally confined bragg mirrors,” *Physical Review B*, vol. 61, no. 7, p. 4413, 2000.
- [178] P. Wilkinson, “Photonic Bloch oscillations and wannier-stark ladders in exponentially chirped bragg gratings,” *Physical Review E*, vol. 65, no. 5, p. 056616, 2002.
- [179] H. Trompeter, W. Krolikowski, D. N. Neshev, A. S. Desyatnikov, A. A. Sukhorukov, Y. S. Kivshar, T. Pertsch, U. Peschel, and F. Lederer, “Bloch oscillations and Zener tunneling in two-dimensional photonic lattices,” *Physical review letters*, vol. 96, no. 5, p. 053903, 2006.

- [180] S. Pfuetzner, C. Mickel, J. Jankowski, M. Hein, J. Meiss, C. Schuenemann, C. Elschner, A. A. Levin, B. Rellinghaus, K. Leo, *et al.*, “The influence of substrate heating on morphology and layer growth in C60:ZnPc bulk heterojunction solar cells,” *Organic Electronics*, vol. 12, no. 3, pp. 435–441, 2011.
- [181] D. R. Lide, *CRC handbook of chemistry and physics*. CRC press, 2004.
- [182] P. Šmilauer, “Thin metal films and percolation theory,” *Contemporary Physics*, vol. 32, no. 2, pp. 89–102, 1991.
- [183] R. Sennett and G. Scott, “The structure of evaporated metal films and their optical properties,” *JOSA*, vol. 40, no. 4, pp. 203–210, 1950.
- [184] G. Jeffers, M. Dubson, and P. Duxbury, “Island-to-percolation transition during growth of metal films,” *Journal of applied physics*, vol. 75, no. 10, pp. 5016–5020, 1994.
- [185] S. Schubert, J. Meiss, L. Müller-Meskamp, and K. Leo, “Improvement of transparent metal top electrodes for organic solar cells by introducing a high surface energy seed layer,” *Advanced Energy Materials*, vol. 3, no. 4, pp. 438–443, 2013.
- [186] N. Eustathopoulos, M. G. Nicholas, and B. Drevet, *Wettability at high temperatures*, vol. 3. Elsevier, 1999.
- [187] L. Vitos, A. Ruban, H. L. Skriver, and J. Kollar, “The surface energy of metals,” *Surface Science*, vol. 411, no. 1, pp. 186–202, 1998.
- [188] F. Nehm, S. Schubert, L. Müller-Meskamp, and K. Leo, “Observation of feature ripening inversion effect at the percolation threshold for the growth of thin silver films,” *Thin Solid Films*, vol. 556, pp. 381–384, 2014.
- [189] S. Schubert, M. Hermenau, J. Meiss, L. Müller-Meskamp, and K. Leo, “Oxide sandwiched metal thin-film electrodes for long-term stable organic solar cells,” *Advanced Functional Materials*, vol. 22, no. 23, pp. 4993–4999, 2012.
- [190] C.-W. Chu, S.-H. Li, C.-W. Chen, V. Shrotriya, and Y. Yang, “High-performance organic thin-film transistors with metal oxide/metal bilayer electrode,” *Applied Physics Letters*, vol. 87, no. 19, pp. 193508–193508, 2005.
- [191] S. Krotkus, F. Ventsch, D. Kasemann, A. A. Zakhidov, S. Hofmann, K. Leo, and M. C. Gather, “Photo-patterning of highly efficient state-of-the-art phosphorescent OLEDs using orthogonal hydrofluoroethers,” *Advanced Optical Materials*, vol. 2, no. 11, pp. 1043–1048, 2014.

- [192] A. A. Zakhidov, J.-K. Lee, H. H. Fong, J. A. DeFranco, M. Chatzichristidi, P. G. Taylor, C. K. Ober, and G. G. Malliaras, "Hydrofluoroethers as orthogonal solvents for the chemical processing of organic electronic materials," *Advanced Materials*, vol. 20, no. 18, pp. 3481–3484, 2008.
- [193] S. Shatalin, J. Tan, R. Juškaitis, and T. Wilson, "Polarisation contrast imaging of thin films in scanning microscopy," *Optics communications*, vol. 116, no. 4, pp. 291–299, 1995.
- [194] C. Körner, *Oligothiophene Materials for Organic Solar Cells - Photophysics and Device Properties*. PhD thesis, Institut für Angewandte Photophysik, Technische Universität Dresden, 2012.
- [195] M. Langner, *Laterally modified microcavity systems containing organic emitters*. PhD thesis, Dresden, Technische Universität Dresden, Diss., 2011, 2011.
- [196] B. Schütte, H. Gothe, M. Sudzius, V. G. Lyssenko, S. I. Hintschich, H. Fröb, and K. Leo, "Lower limit of the lasing threshold in an organic microcavity," *Proc. SPIE Photonics Europe*, pp. 699930–699930, 2008.
- [197] K. Ujihara, "Spontaneous emission and the concept of effective area in a very short optical cavity with plane-parallel dielectric mirrors," *Japanese journal of applied physics*, vol. 30, no. 5B, p. L901, 1991.
- [198] F. Becker, M. Langner, H. Fröb, V. Lyssenko, K. Leo, and C. Adachi, "Dependence of polarization splitting on mode tuning in microcavities," *Applied Physics Letters*, vol. 95, no. 19, p. 191106, 2009.
- [199] A. C. Dürr, F. Schreiber, M. Kelsch, H. D. Carstanjen, and H. Dosch, "Morphology and thermal stability of metal contacts on crystalline organic thin films," *Advanced Materials*, vol. 14, no. 13-14, pp. 961–963, 2002.
- [200] S. Lenk and S. Reineke, "Application of ultrathin metal electrodes in OLEDs," in *Solid-State and Organic Lighting*, pp. DW3D–2, Optical Society of America, 2015.
- [201] S. Lenk, T. Schwab, S. Schubert, L. Müller-Meskamp, K. Leo, M. C. Gather, and S. Reineke, "White organic light-emitting diodes with 4 nm metal electrode," *Applied Physics Letters*, vol. 107, no. 16, p. 163302, 2015.
- [202] D. Godbey, L. Buckley, A. Purdy, and A. Snow, "Copper diffusion in organic polymer resists and inter-level dielectrics," *Thin Solid Films*, vol. 308, pp. 470–474, 1997.

- [203] S. Olthof, J. Meiss, B. Lüssem, M. Riede, and K. Leo, “Photoelectron spectroscopy investigation of thin metal films employed as top contacts in transparent organic solar cells,” *Thin Solid Films*, vol. 519, no. 6, pp. 1872–1875, 2011.
- [204] K. Hennessy, A. Badolato, M. Winger, D. Gerace, M. Atatüre, S. Gulde, S. Fält, E. L. Hu, and A. Imamoğlu, “Quantum nature of a strongly coupled single quantum dot–cavity system,” *Nature*, vol. 445, no. 7130, pp. 896–899, 2007.
- [205] N. Gippius and S. Tikhodeev, “Polariton effect in a chain of coupled photonic dots,” *physica status solidi (a)*, vol. 178, no. 1, pp. 587–592, 2000.
- [206] R. Cerna, D. Sarchi, T. Paraíso, G. Nardin, Y. Léger, M. Richard, B. Pietka, O. El Daif, F. Morier-Genoud, V. Savona, *et al.*, “Coherent optical control of the wave function of zero-dimensional exciton polaritons,” *Physical Review B*, vol. 80, no. 12, p. 121309, 2009.
- [207] F. Becker, R. Brückner, M. Langner, S. I. Hintschich, M. Sudzius, H. Fröb, V. G. Lyssenko, and K. Leo, “Coherent quasimodes and supermodes in a planar microcavity,” *Superlattices and Microstructures*, vol. 49, no. 3, pp. 193–202, 2011.
- [208] M. Bass, E. W. Van Stryland, D. R. Williams, and W. L. Wolfe, *Handbook of optics*, vol. 2. McGraw-Hill, 2001.
- [209] I. Tamm, “Über eine mögliche art der elektronenbindung an kristalloberflächen,” *Zeitschrift für Physik*, vol. 76, no. 11-12, pp. 849–850, 1932.
- [210] R. Brückner, A. A. Zakhidov, R. Scholz, M. Sudzius, S. Hintschich, H. Fröb, V. Lyssenko, and K. Leo, “Phase-locked coherent modes in a patterned metal-organic microcavity,” *Nature photonics*, vol. 6, no. 5, pp. 322–326, 2012.
- [211] J. Haase, S. Shinohara, P. Mundra, G. Risse, V. Lyssenko, H. Fröb, M. Hentschel, A. Eychmüller, and K. Leo, “Hemispherical resonators with embedded nanocrystal quantum rod emitters,” *Applied Physics Letters*, vol. 97, no. 21, p. 211101, 2010.
- [212] F. Ding, T. Stöferle, L. Mai, A. Knoll, and R. F. Mahrt, “Vertical microcavities with high Q and strong lateral mode confinement,” *Physical Review B*, vol. 87, no. 16, p. 161116, 2013.
- [213] L. Mai, F. Ding, T. Stöferle, A. Knoll, B. J. Offrein, and R. F. Mahrt, “Integrated vertical microcavity using a nano-scale deformation for strong lateral confinement,” *Applied Physics Letters*, vol. 103, no. 24, p. 243305, 2013.

- [214] J. C. Gutiérrez-Vega, R. Rodríguez-Dagnino, M. Meneses-Nava, and S. Chávez-Cerda, “Mathieu functions, a visual approach,” *American Journal of Physics*, vol. 71, no. 3, pp. 233–242, 2003.
- [215] A. M. Angulo, C. Noguez, and G. C. Schatz, “Electromagnetic field enhancement for wedge-shaped metal nanostructures,” *The Journal of Physical Chemistry Letters*, vol. 2, no. 16, pp. 1978–1983, 2011.
- [216] M. R. Disfani, M. S. Abrishamian, and P. Berini, “Electromagnetic fields near plasmonic wedges,” *Optics letters*, vol. 37, no. 10, pp. 1667–1669, 2012.
- [217] A. Kavokin and G. Malpuech, “Thin films and nano structures. cavity polaritons,” 2003.
- [218] M. Bayer, T. Gutbrod, A. Forchel, T. Reinecke, P. Knipp, R. Werner, and J. Reithmaier, “Optical demonstration of a crystal band structure formation,” *Physical Review Letters*, vol. 83, no. 25, p. 5374, 1999.
- [219] G. Guttroff, M. Bayer, J. Reithmaier, A. Forchel, P. Knipp, and T. Reinecke, “Photonic defect states in chains of coupled microresonators,” *Physical Review B*, vol. 64, no. 15, p. 155313, 2001.
- [220] A. Tartakovskii, V. Kulakovskii, P. Dorozhkin, A. Forchel, and J. Reithmaier, “Far-field emission pattern and photonic band structure in one-dimensional photonic crystals made from semiconductor microcavities,” *Physical Review B*, vol. 59, no. 15, p. 10251, 1999.
- [221] E. Wertz, L. Ferrier, D. Solnyshkov, R. Johné, D. Sanvitto, A. Lemaître, I. Sagnes, R. Grousson, A. V. Kavokin, P. Senellart, *et al.*, “Spontaneous formation and optical manipulation of extended polariton condensates,” *Nature physics*, vol. 6, no. 11, pp. 860–864, 2010.
- [222] N. Y. Kim, C.-W. Lai, S. Utsunomiya, G. Roumpos, M. Fraser, H. Deng, T. Byrnes, P. Recher, N. Kumada, T. Fujisawa, *et al.*, “GaAs microcavity exciton-polaritons in a trap,” *physica status solidi (b)*, vol. 245, no. 6, pp. 1076–1080, 2008.
- [223] N. Y. Kim, K. Kusudo, A. Löffler, S. Höfling, A. Forchel, and Y. Yamamoto, “Exciton-polariton condensates near the Dirac point in a triangular lattice,” *New Journal of Physics*, vol. 15, no. 3, p. 035032, 2013.
- [224] K. Kusudo, N. Y. Kim, A. Löffler, S. Höfling, A. Forchel, and Y. Yamamoto, “Stochastic formation of polariton condensates in two degenerate orbital states,” *Physical Review B*, vol. 87, no. 21, p. 214503, 2013.

- [225] S. Utsunomiya, L. Tian, G. Roumpos, C. Lai, N. Kumada, T. Fujisawa, M. Kuwata-Gonokami, A. Löffler, S. Höfling, A. Forchel, *et al.*, “Observation of Bogoliubov excitations in exciton-polariton condensates,” *Nature Physics*, vol. 4, no. 9, pp. 700–705, 2008.
- [226] V. Kohnle, Y. Léger, M. Wouters, M. Richard, M. Portella-Oberli, and B. Deveaud, “Four-wave mixing excitations in a dissipative polariton quantum fluid,” *Physical Review B*, vol. 86, no. 6, p. 064508, 2012.
- [227] C. Kittel, *Introduction to solid state physics*. Wiley, 2005.
- [228] H.-S. Cho and P. R. Prucnal, “New formalism of the Kronig-Penney model with application to superlattices,” *Physical Review B*, vol. 36, no. 6, p. 3237, 1987.
- [229] P. Carpena, V. Gasparian, and M. Ortuño, “Number of bound states of a Kronig-Penney finite-periodic superlattice,” *The European Physical Journal B-Condensed Matter and Complex Systems*, vol. 8, no. 4, pp. 635–641, 1999.
- [230] J. Wolfe, “Summary of the kronig-penney electron,” *American Journal of Physics*, vol. 46, no. 10, pp. 1012–1014, 1978.
- [231] T. Freixanet, B. Sermage, J. Bloch, J. Marzin, and R. Planel, “Annular resonant rayleigh scattering in the picosecond dynamics of cavity polaritons,” *Physical Review B*, vol. 60, no. 12, p. R8509, 1999.
- [232] R. Houdré, C. Weisbuch, R. Stanley, U. Oesterle, P. Pellandini, and M. Ilegems, “Measurement of cavity-polariton dispersion curve from angle-resolved photoluminescence experiments,” *Physical Review Letters*, vol. 73, no. 15, p. 2043, 1994.
- [233] P. Savvidis, J. Baumberg, D. Porras, D. Whittaker, M. Skolnick, and J. Roberts, “Ring emission and exciton-pair scattering in semiconductor microcavities,” *Physical Review B*, vol. 65, no. 7, p. 073309, 2002.
- [234] R. Houdré, C. Weisbuch, R. Stanley, U. Oesterle, and M. Ilegems, “Coherence effects in light scattering of two-dimensional photonic disordered systems: Elastic scattering of cavity polaritons,” *Physical Review B*, vol. 61, no. 20, p. R13333, 2000.
- [235] M. Richard, J. Kasprzak, R. Romestain, R. André, and L. S. Dang, “Spontaneous coherent phase transition of polaritons in CdTe microcavities,” *Physical review letters*, vol. 94, no. 18, p. 187401, 2005.

- [236] P. Schneeweiss, M. Sudzius, R. Gehlhaar, M. Hoffmann, V. Lyssenko, H. Fröb, and K. Leo, “Observation of Kastler ring stimulated emission from an organic microcavity,” *Applied Physics Letters*, vol. 91, no. 5, p. 1118, 2007.
- [237] D. Tanese, E. Gurevich, F. Baboux, T. Jacqmin, A. Lemaître, E. Galopin, I. Sagnes, A. Amo, J. Bloch, and E. Akkermans, “Fractal energy spectrum of a polariton gas in a Fibonacci quasiperiodic potential,” *Physical review letters*, vol. 112, no. 14, p. 146404, 2014.
- [238] A. Dreismann, P. Cristofolini, R. Balili, G. Christmann, F. Pinsker, N. G. Berloff, Z. Hatzopoulos, P. G. Savvidis, and J. J. Baumberg, “Coupled counterrotating polariton condensates in optically defined annular potentials,” *Proceedings of the National Academy of Sciences*, vol. 111, no. 24, pp. 8770–8775, 2014.
- [239] G. Tosi, G. Christmann, N. Berloff, P. Tsotsis, T. Gao, Z. Hatzopoulos, P. Savvidis, and J. Baumberg, “Geometrically locked vortex lattices in semiconductor quantum fluids,” *Nature communications*, vol. 3, p. 1243, 2012.
- [240] G. Roumpos, W. H. Nitsche, S. Höfling, A. Forchel, and Y. Yamamoto, “Gain-induced trapping of microcavity exciton polariton condensates,” *Physical review letters*, vol. 104, no. 12, p. 126403, 2010.
- [241] D. Bajoni, P. Senellart, E. Wertz, I. Sagnes, A. Miard, A. Lemaître, and J. Bloch, “Polariton laser using single micropillar GaAs-GaAlAs semiconductor cavities,” *Physical review letters*, vol. 100, no. 4, p. 047401, 2008.
- [242] T. Pertsch, P. Dannberg, W. Elflein, A. Bräuer, and F. Lederer, “Optical Bloch oscillations in temperature tuned waveguide arrays,” *Physical Review Letters*, vol. 83, no. 23, p. 4752, 1999.
- [243] G. Malpuech, A. Kavokin, G. Panzarini, and A. Di Carlo, “Theory of photon Bloch oscillations in photonic crystals,” *Physical Review B*, vol. 63, no. 3, p. 035108, 2001.
- [244] V. Agarwal, J. Del Río, G. Malpuech, M. Zamfirescu, A. Kavokin, D. Coquillat, D. Scalbert, M. Vladimirova, and B. Gil, “Photon Bloch oscillations in porous silicon optical superlattices,” *Physical review letters*, vol. 92, no. 9, p. 097401, 2004.
- [245] A. Szameit, T. Pertsch, S. Nolte, A. Tünnermann, U. Peschel, and F. Lederer, “Optical Bloch oscillations in general waveguide lattices,” *JOSA B*, vol. 24, no. 10, pp. 2632–2639, 2007.



- [246] J. O. Estevez, J. Arriaga, A. Mendez-Blas, E. Reyes-Ayona, J. Escorcia, and V. Agarwal, "Demonstration of photon Bloch oscillations and Wannier-Stark ladders in dual-periodical multilayer structures based on porous silicon," *Nanoscale research letters*, vol. 7, no. 1, pp. 1–7, 2012.
- [247] G. Corrielli, A. Crespi, G. Della Valle, S. Longhi, and R. Osellame, "Fractional Bloch oscillations in photonic lattices," *Nature communications*, vol. 4, p. 1555, 2013.
- [248] H. Ghafouri-Shiraz and B. Lo, *Distributed feedback laser diodes: principles and physical modelling*. John Wiley & Sons, Inc., 1997.
- [249] L. Zhang, S. Yu, M. Nowell, D. Marcenac, J. Carroll, and R. Plumb, "Dynamic analysis of radiation and side-mode suppression in a second-order DFB laser using time-domain large-signal traveling wave model," *Quantum Electronics, IEEE Journal of*, vol. 30, no. 6, pp. 1389–1395, 1994.
- [250] W. Schrenk, N. Finger, S. Gianordoli, L. Hvozdar, G. Strasser, and E. Gornik, "First- and second-order distributed feedback AlGaAs/GaAs quantum cascade lasers," in *Lasers and Electro-Optics Europe, 2000. Conference Digest. 2000 Conference on*, pp. 1–pp, IEEE, 2000.
- [251] A. W. Snyder and J. Love, *Optical waveguide theory*. Springer Science & Business Media, 2012.
- [252] P. Berini and I. De Leon, "Surface plasmon-polariton amplifiers and lasers," *Nature Photonics*, vol. 6, no. 1, pp. 16–24, 2012.
- [253] G. Björk, H. Heitmann, and Y. Yamamoto, "Spontaneous-emission coupling factor and mode characteristics of planar dielectric microcavity lasers," *Physical Review A*, vol. 47, no. 5, p. 4451, 1993.
- [254] T. Mönch, P. Guttman, J. Murawski, C. Elschner, M. Riede, L. Müller-Meskamp, and K. Leo, "Investigating local (photo-) current and structure of znpc: C 60 bulk-heterojunctions," *Organic Electronics*, vol. 14, no. 11, pp. 2777–2788, 2013.
- [255] W. Zeng, K. S. Yong, Z. M. Kam, F. Zhu, and Y. Li, "Effect of blend layer morphology on performance of ZnPc:C60-based photovoltaic cells," *Appl. Phys. Lett*, vol. 97, no. 13, p. 133304, 2010.

- [256] Y. Zhou, T. Taima, T. Miyadera, T. Yamanari, M. Kitamura, K. Nakatsu, and Y. Yoshida, "Phase separation of co-evaporated ZnPc:C60 blend film for highly efficient organic photovoltaics," *Applied Physics Letters*, vol. 100, no. 23, p. 233302, 2012.
- [257] K. Vandewal, Z. Ma, J. Bergqvist, Z. Tang, E. Wang, P. Henriksson, K. Tvingstedt, M. R. Andersson, F. Zhang, and O. Inganäs, "Quantification of quantum efficiency and energy losses in low bandgap polymer: Fullerene solar cells with high open-circuit voltage," *Advanced Functional Materials*, vol. 22, no. 16, pp. 3480–3490, 2012.
- [258] K. Vandewal, K. Tvingstedt, A. Gadisa, O. Inganäs, and J. V. Manca, "On the origin of the open-circuit voltage of polymer–fullerene solar cells," *Nature materials*, vol. 8, no. 11, pp. 904–909, 2009.
- [259] W. Cao, Y. Zheng, Z. Li, E. Wrzesniewski, W. T. Hammond, and J. Xue, "Flexible organic solar cells using an oxide/metal/oxide trilayer as transparent electrode," *Organic Electronics*, vol. 13, no. 11, pp. 2221–2228, 2012.
- [260] H. Jin, C. Tao, M. Velusamy, M. Aljada, Y. Zhang, M. Hamsch, P. L. Burn, and P. Meredith, "Efficient, large area ITO-and-PEDOT-free organic solar cell sub-modules," *Advanced Materials*, vol. 24, no. 19, pp. 2572–2577, 2012.
- [261] S. Schubert, Y. H. Kim, T. Menke, A. Fischer, R. Timmreck, L. Müller-Meskamp, and K. Leo, "Highly doped fullerene C60 thin films as transparent stand alone top electrode for organic solar cells," *Solar Energy Materials and Solar Cells*, vol. 118, pp. 165–170, 2013.
- [262] K. Jiang, A. Zakutayev, J. Stowers, M. D. Anderson, J. Tate, D. H. McIntyre, D. C. Johnson, and D. A. Keszler, "Low-temperature, solution processing of TiO<sub>2</sub> thin films and fabrication of multilayer dielectric optical elements," *Solid State Sciences*, vol. 11, no. 9, pp. 1692–1699, 2009.
- [263] S. Colodrero, M. Ocaña, and H. Míguez, "Nanoparticle-based one-dimensional photonic crystals," *Langmuir*, vol. 24, no. 9, pp. 4430–4434, 2008.
- [264] N. Valappil, M. Luberto, V. Menon, I. Zeylikovich, T. Gayen, J. Franco, B. Das, and R. Alfano, "Solution processed microcavity structures with embedded quantum dots," *Photonics and Nanostructures-Fundamentals and Applications*, vol. 5, no. 4, pp. 184–188, 2007.

- [265] B. L. Wehrenberg, C. Wang, and P. Guyot-Sionnest, “Interband and intraband optical studies of PbSe colloidal quantum dots,” *The Journal of Physical Chemistry B*, vol. 106, no. 41, pp. 10634–10640, 2002.
- [266] Y. Shirasaki, G. J. Supran, M. G. Bawendi, and V. Bulović, “Emergence of colloidal quantum-dot light-emitting technologies,” *Nature Photonics*, vol. 7, no. 1, pp. 13–23, 2013.
- [267] S. Ithurria, M. Tessier, B. Mahler, R. Lobo, B. Dubertret, and A. L. Efros, “Colloidal nanoplatelets with two-dimensional electronic structure,” *Nature materials*, vol. 10, no. 12, pp. 936–941, 2011.
- [268] V. Lyssenko, G. Valušis, F. Löser, T. Hasche, K. Leo, M. Dignam, and K. Köhler, “Direct measurement of the spatial displacement of Bloch-oscillating electrons in semiconductor superlattices,” *Physical review letters*, vol. 79, no. 2, p. 301, 1997.
- [269] A. Szameit, M. C. Rechtsman, O. Bahat-Treidel, and M. Segev, “PT-symmetry in honeycomb photonic lattices,” *Physical Review A*, vol. 84, no. 2, p. 021806, 2011.
- [270] Y. Plotnik, M. C. Rechtsman, D. Song, M. Heinrich, J. M. Zeuner, S. Nolte, Y. Lumer, N. Malkova, J. Xu, A. Szameit, *et al.*, “Observation of unconventional edge states in photonic graphene,” *Nature materials*, vol. 13, no. 1, pp. 57–62, 2014.
- [271] M. C. Rechtsman, Y. Plotnik, J. M. Zeuner, D. Song, Z. Chen, A. Szameit, and M. Segev, “Topological creation and destruction of edge states in photonic graphene,” *Physical review letters*, vol. 111, no. 10, p. 103901, 2013.
- [272] T. Hattori, N. Tsurumachi, S. Kawato, and H. Nakatsuka, “Photonic dispersion relation in a one-dimensional quasicrystal,” *Physical Review B*, vol. 50, no. 6, p. 4220, 1994.
- [273] M. Vasconcelos and E. Albuquerque, “Plasmon-polariton fractal spectra in quasiperiodic multilayers,” *Physical Review B*, vol. 57, no. 5, p. 2826, 1998.
- [274] M. Notomi, H. Suzuki, T. Tamamura, and K. Edagawa, “Lasing action due to the two-dimensional quasiperiodicity of photonic quasicrystals with a penrose lattice,” *Physical review letters*, vol. 92, no. 12, p. 123906, 2004.
- [275] Z. V. Vardeny, A. Nahata, and A. Agrawal, “Optics of photonic quasicrystals,” *Nature Photonics*, vol. 7, no. 3, pp. 177–187, 2013.

- [276] L. Dal Negro and S. V. Boriskina, “Deterministic aperiodic nanostructures for photonics and plasmonics applications,” *Laser & Photonics Reviews*, vol. 6, no. 2, pp. 178–218, 2012.
- [277] S. V. Boriskina, “Quasicrystals: Making invisible materials,” *Nature Photonics*, vol. 9, no. 7, pp. 422–424, 2015.
- [278] R. A. Vicencio, C. Cantillano, L. Morales-Inostroza, B. Real, C. Mejía-Cortés, S. Weimann, A. Szameit, and M. I. Molina, “Observation of localized states in Lieb photonic lattices,” *Phys. Rev. Lett.*, vol. 114, p. 245503, Jun 2015.
- [279] S. Mukherjee, A. Spracklen, D. Choudhury, N. Goldman, P. Öhberg, E. Andersson, and R. R. Thomson, “Observation of a localized flat-band state in a photonic Lieb lattice,” *Phys. Rev. Lett.*, vol. 114, p. 245504, Jun 2015.

# Acknowledgements

The writing of a thesis including all the work leading up to this point is an effort that can not be achieved by working alone. I would like to thank all the people who have joined me on the way. First, I would like to thank Prof. Karl Leo for giving me the opportunity of working in an extremely interesting field combining both fundamental and applied research and giving important insights into my work and all connected publications. His comments and analysis have always encouraged me in pursuing new ideas and his way of directing the institute has provided an enjoyable and fruitful working environment. I thank Prof. Malte Gather for taking over the second review and many interesting and friendly discussions.

My doctoral work was performed in the OLASER group headed by Dr. Hartmut Fröb, whom I am thankful for his guidance as well as many tips regarding all facets of science and life, in- and out-of-uni. His supervision provided a relaxed and uncomplicated but nevertheless efficient working atmosphere for me.

Most of the results in this work would not have been possible without the help of the "living laser lab", Prof. Vadim Lyssenko. His enormous theoretical and experimental knowledge as well as boundless enthusiasm and infectious love of science have inspired me to give my best. Thank you for providing a perfectly aligned laser on monday morning. Thank you for countless long, sometimes frustrating, but always extremely prosperous discussions. Thank you for pushing me. Thank you, Vadim!

In the same vein, I want to thank Dr. Robert Brückner for his insights, explanations, and help regarding sample preparation and interpretation of data. Without his knowledge and tips, many of the results achieved in this thesis would have already failed before the measurements began. Thank you for proof-reading almost every single word I wrote.

I wish to thank Prof. Alex Zakhidov for his assistance, explanations, and many practical hints regarding photolithography. With a smile, he was always able to help out with this delicate technique.

I am grateful to Tim Wagner as my office- and group-mate as well as good friend for many discussions on large and small questions regarding science as well as writing and presentation style. I enjoyed our talks and the fruitful work we did together.

Many thanks to Dr. Markas Sudzius, who has always had an open and critical ear for scientific

disputes and has helped me in perfecting our joint manuscripts.

I want to thank Bernhard Siegmund for our close collaboration, especially regarding the CT-NIR detectors. I am happy to be a part of this exciting work. I owe him gratitude for reading large parts of this thesis and many corrections that have improved the quality of the finished product greatly. Thank you for being an amazing friend for many years now. For the interesting discussions and contributions regarding the CT-detector work I also want to thank Prof. Koen Vandewal, Johannes Benduhn, Dr. Donato Spoltore, and Dr. Christian Körner.

I am very grateful to Frederik Nehm for his work on improving the growth of metal layers in organic optoelectronics as well as many conversations regarding all facts of life, and for beating me at the Kicker on a regular basis. Thank you for being a great friend as well.

For his assistance in programming, especially regarding the 3D visualisations, I thank Matthias Böhm. Thank you as well for ion-etching some of the metal samples. *skrrt*.

My Master and Bachelor students Franz Löchner, Michael Bretschneider, Daniel Wetzel, and Jendrik Jördening I thank for our work together as well as your contributions and help towards my own work. I have learned a lot from teaching others. Thanks to Franz also for our joint publications.

All coauthors of my publications as well as current and former OLASER members that have not been mentioned otherwise: Christoph Reinhardt, Felix Lemke, Susanne Hintschich, Reinhard Scholz, Irma Slowik, Yiyang Zhang, Nils Kronenberg, Stefan Meister, Christian Tzschaschel, Christian Kropla, Ron Hildebrandt, Klara Mosshammer, Stefan Gutsche, Svjatoslav Hladki, Jens Ludwig, Maik Langner, and Daniel Kasemann. Thank you for our exciting and extremely interesting time together.

Thanks to Franz Selzer, Simonas Krotkus, Florian Wölzl, Kathrin Ortstein, and Felix Dollinger for joining me in conference travels, in the office, for the daily lunch, or at the Kicker. Thanks to the many interesting people I met and discussed physics with all over the world.

A big thank you to Sven Kunze, Andreas Büst, Tobias Günther, and Andreas Wendel for technical assistance. Many thanks to Johanna Katzschner, Carla Schmidt, Annette Polte, Angelika Wolf, Christian Zschalig, Eva Schmidt, and Jutta Hunger for all organisational trouble and to Kai Schmidt and Peter Leumer for their IT service. As a two-time record coffee drinker, it is obvious that this energising liquid has played an important role in my work. I owe gratitude towards the various responsible persons and authorities: Dr. Alexander Haussmann, Dr. Tobias Mönch, Ralf Raupach, Vera Fiehler, Tino Uhlig, and Bernhard Nell.

As much time and effort as I spent working, this thesis as well as all of my studies would not have been possible without the amazing support at home, of all my friends, my family, and Tatjana. Thank you all so much!

# Erklärung

Diese Arbeit wurde am Institut für Angewandte Photophysik der Fakultät Mathematik und Naturwissenschaften an der Technischen Universität Dresden unter wissenschaftlicher Betreuung von Prof. Dr. Karl Leo angefertigt.

Hiermit versichere ich, dass ich die vorliegende Arbeit ohne unzulässige Hilfe Dritter und ohne Benutzung anderer als der angegebenen Hilfsmittel angefertigt habe; die aus fremden Quellen direkt oder indirekt übernommenen Gedanken sind als solche kenntlich gemacht.

Die Arbeit wurde bisher weder im Inland noch im Ausland in gleicher oder ähnlicher Form einer anderen Prüfungsbehörde vorgelegt.

Weiterhin versichere ich, dass bisher keine Promotionsverfahren stattgefunden haben.

Ich erkenne die Promotionsordnung der Fakultät Mathematik und Naturwissenschaften der Technischen Universität Dresden vom 23.02.2011 an.

Dresden, 17. Dezember 2015

Andreas Mischok